Smart Sensors, Measurement and Instrumentation 23

Subhas Chandra Mukhopadhyay
Octavian Adrian Postolache
Krishanthi P. Jayasundera
Akshya K. Swain *Editors*

Sensors for Everyday Life

Environmental and Food Engineering

Springer

Smart Sensors, Measurement and Instrumentation

Volume 23

Series editor

Subhas Chandra Mukhopadhyay
Department of Engineering, Faculty of Science and Engineering
Macquarie University
Sydney, NSW
Australia
e-mail: S.C.Mukhopadhyay@massey.ac.nz

More information about this series at http://www.springer.com/series/10617

Subhas Chandra Mukhopadhyay
Octavian Adrian Postolache
Krishanthi P. Jayasundera
Akshya K. Swain
Editors

Sensors for Everyday Life

Environmental and Food Engineering

Springer

Editors
Subhas Chandra Mukhopadhyay
Department of Engineering, Faculty of Science and Engineering
Macquarie University
Sydney, NSW
Australia

Octavian Adrian Postolache
Instituto de Telecomunicações
Lisbon
Portugal

and

ISCTE-IUL
Lisbon
Portugal

Krishanthi P. Jayasundera
Institute of Fundamental Sciences
Massey University
Palmerston North
New Zealand

Akshya K. Swain
Department of Electrical and Computer Engineering
University of Auckland
Auckland
New Zealand

ISSN 2194-8402 ISSN 2194-8410 (electronic)
Smart Sensors, Measurement and Instrumentation
ISBN 978-3-319-47321-5 ISBN 978-3-319-47322-2 (eBook)
DOI 10.1007/978-3-319-47322-2

Library of Congress Control Number: 2016953322

Printed on acid-free paper

This Springer imprint is published by Springer Nature
The registered company is Springer International Publishing AG
The registered company address is: Gewerbestrasse 11, 6330 Cham, Switzerland

Preface

Sensors play a pivotal role in our everyday life. They gather data on environment, and information on weather, traffic congestion, air pollution, water pollution, etc. is obtained; they gather data on human body, and information on health, treatment or therapy outcomes is obtained; they gather data on objects, and information for monitoring and control of these objects is obtained; they gather data on subjects or objects functions, and information for better decisions, control and action is obtained. For instance, the weather information is used to choose adequate clothes, the battery level sensor permits smartphone power management optimization, and the level of blood glucose allows better healthcare management. Data collected through sensors enhance our lives and our connections to each other and with our environment, allow real-time monitoring of many phenomena around us, provide information about quality of products and services, improve the equipment control based on sensorized interfaces and contribute to increase knowledge on physical and chemical world.

The advances in electronics, embedded controller, technology for communication as well as the progress towards a better informed, knowledge based society increase the demand for small size, affordable sensors that allow accurate and reliable data recording, processing, storing and communication. The work contains invited chapters from renowned experts, working in sensors' field, and it is split into two books that present several technologies and applications of sensors in *Environmental and Food Engineering* (ISBN 978-3-319-47322-2) and for *Healthcare Settings* (ISBN 978-3-319-47319-2).

The book *Sensors for Everyday Life—Environmental and Food Engineering* describes novel sensors and sensing systems developed for environment monitoring and food production and quality assessment.

Environmental quality refers to characteristics from natural environment as well as from the built environment (i.e. city air and/or water pollution, concentration of nitrate from the soil in cultivated fields). Environmental quality plays an important role in health and well-being of the populations. Degraded environmental quality as produced by air and water pollution may affect our lives, directly or through the food we eat. In food engineering various sensors are used for assessment of

contaminants, adulterants, naturally occurring toxins or any other substance that may make food injurious to health on an acute or chronic basis as well as sensors that contribute for quality improvement of food. New developed sensors and technology trend related air, water, food quality monitoring as well as for modern agronomy and food production are presented in this book.

How This Book is Organized

In Chap. 1, a novel method for the simultaneous determination of NOx and soot in the exhaust of diesel engines during the periodical technical inspection roadworthiness test is presented. A multi-wavelength light extinction measurement, in a setup similar to an opacimeter with high sensitivity, and a mathematical inversion algorithm are used to obtain the concentrations from the extinction readings.

Analytical technique of the fine particles using atomic emission spectroscopy system for an environmental pollution monitoring is presented in Chap. 2. Laser-induced breakdown spectroscopy (LIBS) system and the helium-microwave-induced plasma-atomic emission spectroscopy (He-MIP-AES) system are used for characterizations and real-time measurement of the air chemical compositions and particle size.

Chapter 3 presents sensors and method for automatic fault detection in heating ventilating and air conditioning (HVAC) systems. This is important mainly in smart buildings context as the indoor condition in these buildings is mainly related with the capabilities and reliability of HVAC systems.

New optical fiber humidity sensor is described in Chap. 4. Different humidity sensors that have been developed by now are presented focusing in the different optical structures and materials that have been used for improving sensitivity and resolutions of these sensors.

The measurement of air gas concentration represents an important field of application of sensing technologies. In Chap. 5 of the book, a review on the oxygen gas sensing technologies is presented with focus on potentiometric, amperometric, paramagnetic and tunable diode laser spectroscopy (TDLS) sensors. Theoretical aspects and operational basic of these technologies, system requirements as well as limitations of the methods are discussed in this chapter.

A low-cost sensor node based on interdigital capacitive sensor for nitrate and nitrite in surface and ground water concentration detection is presented in Chap. 6. This sensor is important for agronomy as well as for water pollution assessment. Nitrates may be present in high concentration in ground and surface water as a result of intensive agriculture, disposal of human and animal sewage and industrial wastes.

In Chap. 7 an intelligent wireless sensor network system designed to monitor various parameter in palm oil plantation for improvement in the controlled pollination process is presented. The system helps in making decision related to best time for pollination process. The inaccuracy in determining pollination readiness

of the oil palm flower could potentially cause a detrimental effect on the palm oil industry in the long run.

The following two chapters present sensors for determination of quality and quantity of water for drinking purpose. In Chap. 8, a reflectometer and a Doppler radar systems for detection of water level in septic tank is described. A novel S3 (Small Sensor System) nanowire device for the detection of complex mixtures of bacteria in potable water is presented in Chap. 9.

Next three chapters describe sensors used in food productions and quality assessment. A novel approach to monitor the quality of milk products, based on electromagnetic wave spectroscopy is presented in Chap. 10. The system use vector network analyser to capture spectral signatures in the form of scattering parameters from electromagnetic wave sensors. Data on reliability testing is presented. A new, rapid, portable, easy-to-use, economic and non-destructive fouling based on nanowire technology device to control the presence of false grated Parmigiano Reggiano cheese is described in Chap. 11. A review on the conventional techniques and dielectric spectroscopy for analyzing food products is presented in Chap. 12, focusing on the application of dielectric spectroscopy in fats and oils adulteration detection.

Different wireless sensor network architecture is implemented nowadays to perform distributed measurement tasks for environment monitoring with increase in space resolution. Big challenge in these implementations continues to be wireless interference and radio-frequency (RF) spectrum crowding. Chapter 13 focuses on a technique for optical-based RF interference cancellation. In this chapter several system architectures are presented and a sample of their experimental performance and the key characteristics of this technique and the future prospects for this technology, focusing specifically on photonic integrated circuits are discussed. A scheme is proposed in Chap. 14 that can reduce the performance difference between cluster heads (CHs) involved in inter-cluster communication on IEEE 802. 15.4 cluster-based wireless sensor networks (WSNs) under spatial non-uniform traffic condition where the CHs have various amount of traffic. This reduced the energy consumption and simplified processing mechanism to achieve long WSNs lifetime under limited network resource condition.

We do sincerely hope that the readers will find this special issue interesting and useful in their research on sensors and wireless sensor networks for environment monitoring, food production and quality assessment.

We want to acknowledge all the authors for their contribution and for sharing of their knowledge. We hope that the works presented in this book will stimulate further research related to sensors for everyday life.

Sydney, Australia — Subhas Chandra Mukhopadhyay
Lisbon, Portugal — Octavian Adrian Postolache
Palmerston North, New Zealand — Krishanthi P. Jayasundera
Auckland, New Zealand — Akshya K. Swain

About the Editors

Dr. Subhas Chandra Mukhopadhyay (M'97, SM'02, F'11) graduated from the Department of Electrical Engineering, Jadavpur University, Calcutta, India with a **Gold medal** and received the Master of Electrical Engineering degree from Indian Institute of Science, Bangalore, India. He has Ph.D. (Eng.) degree from Jadavpur University, India and Doctor of Engineering degree from Kanazawa University, Japan.

Currently he is working as Professor of Mechanical/Electronics Engineering and Discipline Leader of the Mechatronics Degree Programme of the Department of Engineering, Macquarie University, Sydney, Australia. He has over 26 years of teaching and research experiences.

His fields of interest include smart sensors and sensing technology, wireless sensor networks, internet of things, electromagnetics, control engineering, magnetic bearing, fault current limiter, electrical machines and numerical field calculation.

He has authored/co-authored over **400** papers in different international journals, conferences and book chapter. He has edited **thirteen** conference proceedings. He has also edited **fifteen** special issues of international journals as lead guest editor and **twenty-five** books with Springer-Verlag.

He was awarded numerous awards throughout his career and attracted over NZ $4.2 M on different research projects.

He has delivered **272** seminars including keynote, tutorial, invited and special seminars.

He is a **Fellow** of IEEE (USA), a **Fellow** of IET (UK) and a Fellow of IETE (India). He is a Topical Editor of IEEE Sensors Journal and an Associate Editor IEEE Transactions on Instrumentation. He has organized many international conferences either as general chair or technical programme chair. He is the

Ex-**Chair** of the IEEE Instrumentation and Measurement Society New Zealand Chapter. He chairs the IEEE IMS Technical Committee 18 on Environmental Measurements.

Dr. Octavian Adrian Postolache (M'99, SM'2006) graduated in Electrical Engineering at the Gh. Asachi Technical University of Iasi, Romania, in 1992 and he received the Ph.D. degree in 1999 from the same university, and university habilitation in 2016 from Instituto Superior Tecnico, Universidade de Lisboa, Portugal. In 2000 he became principal researcher of Instituto de Telecomunicações where he is now Senior Researcher. Since 2012 he joined Instituto Universitario de Lisboa/ISCTE-IUL Lisbon where he is currently Aux. Professor.

His fields of interests include smart sensors for biomedical and environmental applications, pervasive sensing and computing, wireless sensor networks, signal processing with application in biomedical and telecommunications, non-destructive testing and diagnosis based on eddy currents smart sensors, computational intelligence with application in automated measurement systems.

He is active member of national and international research teams involved in Portuguese and EU and International projects. He was principal researcher of different projects including EHR-Physio regarding the implementation of Electronic Health Records for Physiotherapy and he is currently principal researcher of TailorPhy project Smart Sensors and Tailored Environments for Physiotherapy.

Dr. Postolache is author and co-author of 9 patents, 4 books, 16 book chapters, 66 papers in international journals with peer review, more than 220 papers in proceedings of international conferences.

He is IEEE Senior Member I&M Society, Distinguished Lecturer of IEEE IMS, chair of IEEEI&MSTC-13 Wireless and Telecomunications in Measurements, member of IEEEI&MSTC-17, IEEEI&MSTC-18, IEEEI&MSTC-25, IEEE EMBS Portugal Chapter and chair of IEEE IMS Portugal Chapter. He is Associate Editor of IEEE Sensors Journal, and IEEE Transaction on Instrumentation and Measurements, he was general chair of IEEE MeMeA 2014, and TPC chair of ICST 2014, Liverpool and ICST 2015 in Auckland. He received IEEE best reviewer and the best associate editor in 2011 and 2013 and other awards related to his research activity in the field of smart sensing.

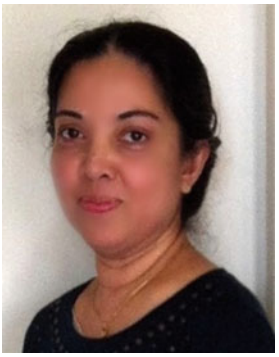

Dr. Krishanthi P. Jayasundera graduated from University of Peradeniya, Sri Lanka with honors degree in Chemistry. She obtained her both Master and Ph.D. in Organic Chemistry from Kanazawa University, Japan. She worked as postdoctoral researcher at Massey University nearly 14 years in New Zealand involving various projects focused on the chemical synthesis of architecturally interesting molecules which have biological, environmental and/or medicinal significance. Currently, she is an independent research consultant. She specializes in organic chemistry, biosciences, sensitivity analysis using NMR, HPLC, SPR and so on. She has published over 30 papers in different international journals and conference proceedings.

Akshya K. Swain received the B.Sc. degree in Electrical Engineering and the M.Sc. degree in Electronic Systems and Communication from Sambalpur University, Sambalpur, India, in 1985 and 1988, respectively, and the Ph.D. degree from the Department of Automatic Control and Systems Engineering, University of Sheffield, Sheffield, U.K., in 1997. From 1994 to 1996, he was a Commonwealth Scholar in the United Kingdom. Since September 2002, he has been with the Department of Electrical and Computer Engineering, the University of Auckland, Auckland, New Zealand. He has published over 150 papers in International Journals and conferences. His current research interests include nonlinear system identification and control, fault tolerant control, biomedical signal processing, sensor networks, and control applications to power system and wireless power transfer system. Dr. Swain is an Associate Editor of IEEE Sensors Journal and Member of the Editorial Board of International Journal of Automation and Control and International Journal of Sensors, Wireless Communications and Control.

Contents

Determination of NO_X and Soot Concentrations Using a Multi-wavelength Opacimeter

H. Axmann, A. Bergmann and B. Eichberger

Abstract A novel approach to measure both the particle and the NO_2 concentration in the exhaust of diesel engines during the roadworthiness test in the periodical technical inspection is presented. It is based on a multi-wavelength extinction measurement and a mathematical inversion algorithm to obtain the concentrations from the extinction readings. Such individual concentration values can deliver valuable insight into the cause of engine or exhaust aftertreatment defects. Furthermore the extended opacimeter provides future-proofness, if nitrous gas emissions are incorporated in the roadworthiness regulations. In addition to a detailed description of the multi-wavelength approach this chapter provides an overview of particle and nitrous gas emissions by diesel engines, the related legislation, the extinction measurement using standard opacimeters, and the physical background for this optical measurement method. The applicability of the multi-wavelength method is derived mathematically and validated with first experimental results as well as with simulations.

1 Introduction

The emissions of vehicles equipped with internal combustion engines pose a significant environmental problem and cause severe health effects. A big portion of the engines run on diesel fuel. In some European countries they even surpass the amount of gasoline vehicles with a relation of 70 to 30 % [1]. Across Europe the average fraction of newly registered diesel cars reached 58 % in 2011 [2]. While the main pollutant in the exhaust of gasoline engines is carbon dioxide (CO_2), the most

H. Axmann (✉)
AVL DiTEST GmbH, Alte Poststraße 156, 8020 Graz, Austria
e-mail: harald.axmann@avl.com

A. Bergmann · B. Eichberger
Institute of Electronic Sensor Systems, University of Technology,
Inffeldgasse 10/II, 8010 Graz, Austria

S. Mukhopadhyay et al. (eds.), *Sensors for Everyday Life*, Smart Sensors,
Measurement and Instrumentation 23, DOI 10.1007/978-3-319-47322-2_1

relevant pollutants of diesel engines are particulate matter (PM) and nitrous gases (NO_X). CO_2 is a green house gas, whereas particles and NO_2 are toxic components.

Diesel particulate matter consists mainly of carbonaceous particles, ashes and unburned fuel and oil droplets [3]. It has been lately proven to be carcinogenic [4]. Furthermore the black carbon (BC) fraction of the particles contributes to global warming, and when deposited on snowpacks the particles lead to accelerated melting through absorption of the sunlight [5].

Nitrous gases consist of nitrogen monoxide (NO) and nitrogen dioxide (NO_2). During the combustion process of diesel fuel mostly NO is produced. By the catalyzed particle filter systems in modern vehicles a significant amount of NO is oxidized to NO_2 [6–8]. NO_2 is a brown, toxic gas, which may lead to mucosal irritation. It is a main contributor to smog in big cities [9] and is—in aqueous solution—a strong acid leading to acid rain [10].

Governments all over the world reacted to this threat by introducing limits for the allowed concentration of said pollutants in the exhaust of internal combustion engines. Since the first emission regulations in the early 1970s the limit values have been significantly reduced [10–12]. This is shown in Fig. 1 using the European Emission Standards (EURO 1-6) as an example. To conform to these emission limits the engine manufacturers have to optimize the combustion process and to add new exhaust aftertreatment systems. Still the efficiency of these measures can deteriorate over time. Accordingly periodic emission checks are necessary to ensure the compliance of the vehicles to the emission limits. Such emission checks are typically performed during the periodical technical inspection (PTI) in garages or vehicle inspection institutions.

For the case of diesel vehicles the regulation-compliant functionality of the engine and the exhaust system is determined from the opacity of the exhaust gases. The corresponding measurement device is the opacity meter, commonly just called opacimeter, which is based on an optical measurement. Just as the first emission

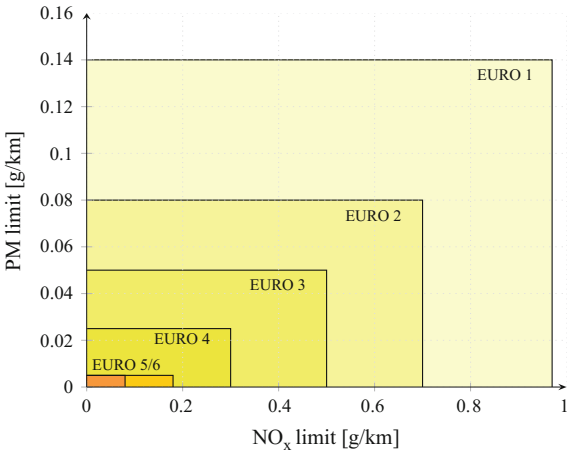

Fig. 1 PM and NO_X limits of EURO 1-6

limits its measurement principle dates back to the 1970s [13]: A measurement chamber of defined length is filled with exhaust gas, and the attenuation of light by the sample is measured. While this was working perfectly for the older diesel vehicles emitting tight black clouds of soot, it is reaching its limits for modern models [14]. Equipped with diesel particle filters (DPFs) they emit much less, very small particles. Accordingly the exhaust plumes are effectively transparent, only with a very small amount of opacity. Therefore updated or new measurement technologies are needed in order to perform meaningful and reliable measurements.

An example for a new technology is light scattering. It is also an optical measurement method, measuring the amount of light deflected by the particles in the exhaust gases. Due to its measurement principle it is mainly sensitive to particles [15]. Although it proved to be well applicable for PTI exhaust measurements, it has not been approved by the governments yet. Some other new measurement methods have been proposed, but without success [16, 17]. As an alternative researchers focused on updated versions of the opacimeter featuring an increased sensitivity. Generally it is possible to lower the detection limit by at least one order of magnitude with moderate means.

However opacimeters measure the combinational absorbing effect of all exhaust components within the green wavelength range, where the human eye has its maximum sensitivity. Originally this was by intention. It was the goal to measure an overall visual obstruction produced by the vehicle. Besides, for older vehicles, most of the effect could be attributed to the PM part. With the reduction of the particle emissions the attenuating effect of the brown NO_2 can surpass that of the particles. In such a case it might often be desirable to obtain additional information about the source of the measured signal in order to quickly identify the related defects in the exhaust system. Furthermore getting individual figures for PM and NO_X or NO_2 can be advantageous regarding the individual limitation of these two criteria pollutants. A one year study performed by the International Motor Vehicle Inspection Committee (CITA) in 2011 already investigated PTI test equipment for individual measurement of said components [13].

As shown in the following sections such extended measurement results can be achieved by an opacimeter enhanced with a multi-wavelength light source.

2 The Opacimeter

A standard opacimeter consists of a measurement chamber of defined length, a single-color, typically green light source on one side of the chamber and a light detector on the opposite side (see Fig. 2). As long as the measurement chamber contains clean air, the light emitted by the light source (e.g. a light emitting diode, LED) does not get attenuated and a nominal light intensity I_0 is measured on the detector (e.g. a photo diode). During the measurement the chamber is filled with the exhaust sample, which attenuates the light, resulting in a decreased light intensity

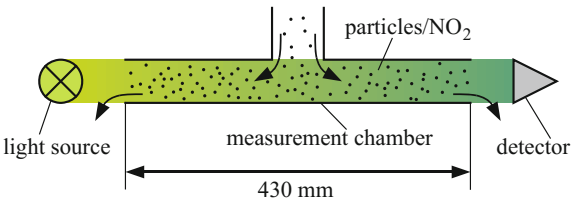

Fig. 2 Measurement principle of an opacimeter

I at the detector. By relating the two intensities I and I_0 to each other the opacity N can be calculated as

$$N = 1 - (I/I_0). \tag{1}$$

The opacity N is given in %. It depends on the length of the measurement chamber. Typically a length of 430 mm is used, but differing values are possible. Generally a length-independent measurement value is preferred. Therefore the so-called extinction coefficient k is typically determined along with or instead of the opacity. It is given in 1/m and can be calculated from I, I_0 and the effective measurement length L_{eff} using Lambert's Law [19]:

$$I/I_0 = \exp(-kL_{\text{eff}}) \tag{2}$$

In the literature this equation is also often called Lambert-Beer or Beer-Lambert law. However the name Lambert-Beer law designates a slightly different variation of (2), where the extinction coefficient is replaced by the product of the concentration c of the absorbing material and its extinction efficiency σ_{ext} [18]:

$$I/I_0 = \exp(-c\sigma_{\text{ext}}L_{\text{eff}}) \tag{3}$$

Accordingly one can determine the concentration of the absorbing material from the opacity measurement, if the extinction coefficient σ_{ext} is known and constant. The following section describes the physical background of said values and shows typical values for PM and NO_2.

3 Absorption of Particles and Gases

When light travels through a medium, energy is partly removed from the light beam by the obstacles (particles, gas molecules and atoms) in the medium. This results in an attenuation of the light beam. Such an effect is called extinction [19]. It is the combination of absorption, where energy is transferred from the incident beam to the obstacles, and scattering, where some parts of the light beam are deflected from the original path and thereby also removed from the incident beam. Mathematically this can be described in terms of the cross sections

$$\sigma_{ext} = \sigma_{abs} + \sigma_{sca}, \tag{4}$$

where σ_{abs} and σ_{sca} are the absorption and the scattering cross sections respectively [20]. The concept of a cross section is used to describe the ability of an obstacle to remove light from an incident beam in a simple way. It can be understood as the area shadowed from the incident beam. For the case of exhaust the main contributor to extinction is absorption. This is attributable to the strong absorbing effects of the primary components of the exhaust. Soot particles have a scattering share of only 10–30 % [21, 22]. Gases like NO_2 even have a negligible scattering effect [23]. This is the reason why, although physically incorrect, it has become customary to call k absorption coefficient rather than extinction coefficient.

The total extinction coefficient of a mixture of substances with differing extinction coefficients k_i can be determined by summation [24]. As in (3) k_i can be expressed by the products of the individual cross sections $\sigma_{ext,i}$ and the respective concentrations c_i. Accordingly the total extinction coefficient k can be calculated as

$$k = \sum_i k_i = \sum_i c_i \sigma_{ext,i}. \tag{5}$$

In principal the extinction cross section of the essential components in the exhaust of diesel engines, PM and NO_2, can be calculated with well-known formulas. For species very small compared to the incident wavelength, e.g. gas molecules, the shape of the object can be approximated as a sphere. In such a case the Rayleigh model can be used to calculate scattering, absorption and extinction effects. The Rayleigh model is valid, as long as the elements are smaller than approximately one tenth of the wavelength. For bigger elements, like accumulation mode exhaust particles [3], the shape must be taken into account. The behavior of spherical objects can be calculated using the Mie theory, which is applicable for any sphere diameter. Exact formulas also exist for some other well-defined shapes. For irregular objects like the fractal-like soot particles, one typically uses approximative models like the Rayleigh-Debye-Gans model for fractal aggregates (RDG-FA) [15].

For the purpose of this work it is important to understand the influence of the wavelength on the extinction behavior. Accordingly the extinction spectrum over a wide wavelength range is needed. The exact quantum-chemical calculation of such a spectrum is yet not possible [25]. Fortunately especially for gases there exists elaborate measurement data of the absorption behavior. For diesel soot particles there exists extinction data, too, though not to the same amount.

3.1 Absorption of NO_2

As said before the scattering effect of gases like NO_2 is negligible. Its extinction cross section is therefore almost identical to the absorption cross section, which is shown in Fig. 3 for the wavelength range from 250 to 800 nm, given in

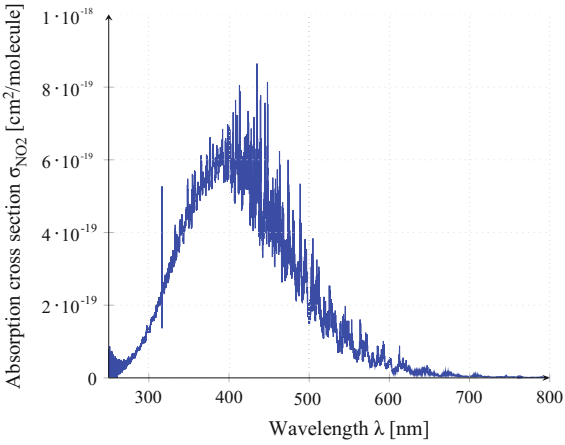

Fig. 3 Absorption cross section of NO_2

cm^2/molecule [26]. It has been measured at a pressure of 1000 mbar and a temperature of 293 K.

Generally the uncertainty is in the order of a few percent. Near 250 nm the uncertainty increases, as oscillations occur that are physically implausible. The peak around 316 nm seems to be an artefact, too. Both phenomena are not of importance for the actual work. The high oscillations around the peak at approximately 400 nm however are factious. Thus it is crucial to utilize data with high wavelength resolution in this area in order to achieve proper results. Temperature and pressure also have a notable influence on the absorption behavior. Those influences can be compensated using empirical models [25, 27].

3.2 Extinction of Soot Particles

The extinction behavior of particles is shown in Fig. 4 based on the example of a Volkswagen turbo diesel engine (TDI Type 1Z, 1.9 l, 66 kW). It is given for the wavelength range from 230 to 1000 nm in m^2/g [28, 29]. In contrast to NO_2 the spectrum is rather smooth. According to their black color the soot particles absorb light quite equally in the whole visible wavelength range. The measurement uncertainty of the given data is in the order of 5 %. It has however not been measured directly at the tailpipe. The particles had already grown to a median mobility diameter (MMD) of 250–300 nm due to coagulation, which is approximately three times bigger than the MMD of tailpipe particles. The actual effect of particle size on the extinction is rather small. The bigger particles will result in a slightly stronger extinction. This is due to an increased scattering cross section, the absorption cross section of fractal-like soot aggregates with constant volume is independent of the particle size [30]. Simulations performed with typical particle

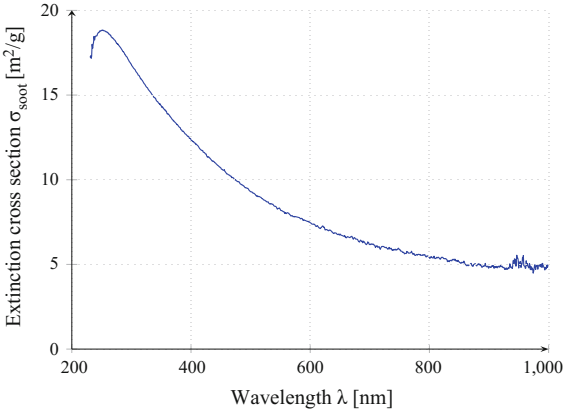

Fig. 4 Extinction cross section of diesel soot

size distributions of diesel exhaust [3, 31] predict deviations in the order of a few percent.

The absorption spectrum of NO_2 and the extinction spectrum of soot are very different, as obvious from Figs. 3 and 4. Accordingly their corresponding extinction effects differ substantially for e.g. red, green and blue light. This is used in the multi-wavelength approach presented in the following section.

4 The Multi-wavelength Approach

An examination of smoke samples using light at multiple wavelengths has already been performed in the past. Aspey and Brazier for example have investigated the particle mass fraction and mean particle size in exhaust [32]. Sharma et al. performed optical characterizations of aerosols using a multi-wavelength photoacoustic-nephelometer spectrometer [33]. Haisch and Niessner presented a photoacoustic analyzer for the simultaneous quantification of soot and NO_2 in engine exhaust [34]. In this work a similar approach is adopted for an opacimter: Using a multi-wavelength light source the individual contributions of soot and NO_2 to the opacity are determined and the respective concentration values are derived.

For this purpose the extended opacimeter performs multiple consecutive measurements of the smoke sample using different wavelengths. Any wavelengths for which the extinction differs sufficiently could be used. Standard opacimeters are equipped with a green light source. To support normal opacity measurements the green light source can be retained and a red and blue light source added. The according measurement setup is shown in Fig. 5. In each measurement *i*, where one of the light sources is enabled at a time, the equation

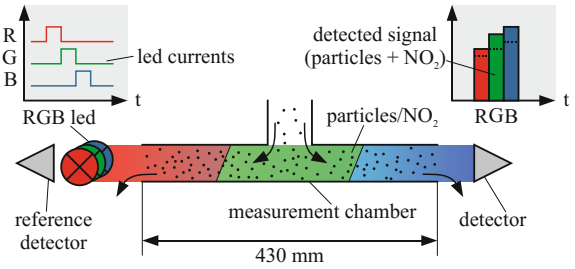

Fig. 5 Three wavelength measurement setup

$$k_i = k_{NO_2}(\lambda_i) + k_{soot}(\lambda_i) + k_{other}(\lambda_i) \tag{6}$$

holds. Herein λ_i is the wavelength of each light source, k_{NO_2}, k_{soot}, k_{other} and k_i are the individual extinction coefficients of NO_2, soot particles and other components and the total extinction coefficient at the given wavelength λ_i respectively. The equation can be rewritten as in (5) using the product of the concentrations c_x and the extinction cross sections σ_x, leading to

$$k_i = c_{NO_2}\sigma_{NO_2}(\lambda_i) + c_{soot}\sigma_{soot}(\lambda_i) + c_{other}\sigma_{other}(\lambda_i). \tag{7}$$

When performing three measurements of the same sample (i.e. the concentrations c_x remain constant during the whole measurement time) an equation system with three equations and also three unknowns is obtained. This of course requires knowledge of all extinction cross sections. In such a case, the matrix equation

$$\begin{pmatrix} k_1 \\ k_2 \\ k_3 \end{pmatrix} = \begin{pmatrix} \sigma_{NO_2}(\lambda_1) & \sigma_{soot}(\lambda_1) & \sigma_{other}(\lambda_1) \\ \sigma_{NO_2}(\lambda_2) & \sigma_{soot}(\lambda_2) & \sigma_{other}(\lambda_2) \\ \sigma_{NO_2}(\lambda_3) & \sigma_{soot}(\lambda_3) & \sigma_{other}(\lambda_3) \end{pmatrix} \begin{pmatrix} c_{NO_2} \\ c_{soot} \\ c_{other} \end{pmatrix} \tag{8}$$

can ideally be solved by simple matrix inversion.

For σ_{other} a representative absorber besides soot and NO_2 should be chosen. In practice the composition of the exhaust samples might vary to such a degree that the selection of a single representative absorber is not possible. In that case it can be omitted, leading to an over-determined system. Such a system can be solved using a least-squares algorithm to calculate the best fit for the remaining two components.

5 Technical Realization

5.1 Physical Setup

The multi-wavelength opacimeter is built from the basis of a highly sensitive single-pass opacimeter, as depicted in Fig. 5. In order to achieve a sufficiently high

sensitivity in the order of $\Delta k = 0.001\ m^{-1}$ the optical path length and hence the measurement chamber should not be too small. We used a cylindrical cell with a diameter of 2.4 cm and a length of 400 mm, where the axis of the cylinder coincides with the optical axis of the system. The inlet for the smoke sample is placed in the middle of the chamber. The exhaust is filled into the chamber by the dynamic pressure in the exhaust pipe. It leaves the chamber through the in-/outlet for the light beam.

A flow of sheath air transports the exhaust sample to the smoke outlet. The sheath air flow is produced from ambient air by filtration using a high-efficiency particulate air (HEPA) filter. On the one hand the sheath air protects the optical setup from contamination, on the other hand it defines the length of the optical path. As the optical path length directly influences the measurement value, it is crucial to keep the optical path length constant. Therefore the sheath air flow needs proper fluid dynamical considerations.

In Fig. 6 a multiphysical complex fluid dynamic simulation result is shown. The ratio of exhaust gas entering through the middle section of the measurement cell to the air flow rate through the sheath air channels defines the optical path. In order to quantify a representative exhaust gas sample within the measurement cell, the distribution of the analytes should be homogeneous, independently of the dynamic pressure in the exhaust pipe. A proper fluid dynamic design and hence an iterative optimization approach by means of complex fluid dynamics is a necessary prerequisite to obtain meaningful measurement results.

For the light source it is advantageous to use a realization that combines the three colors into a single housing. That ensures comparable optical behavior of the

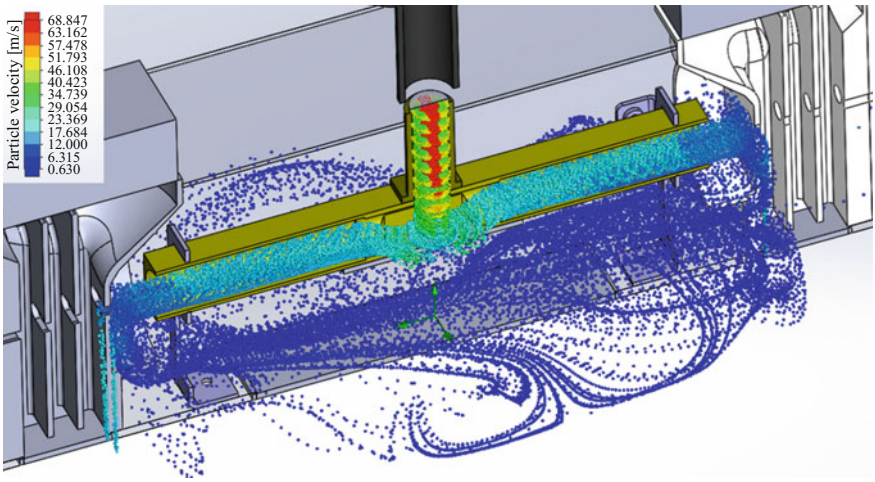

Fig. 6 Multiphysical complex fluid dynamic simulation of the measurement cell. The points represent particle ensembles with particle velocities scaled by the color. A homogeneous velocity distribution within the optical path guarantees representative samples of the exhaust gas portion to be quantified

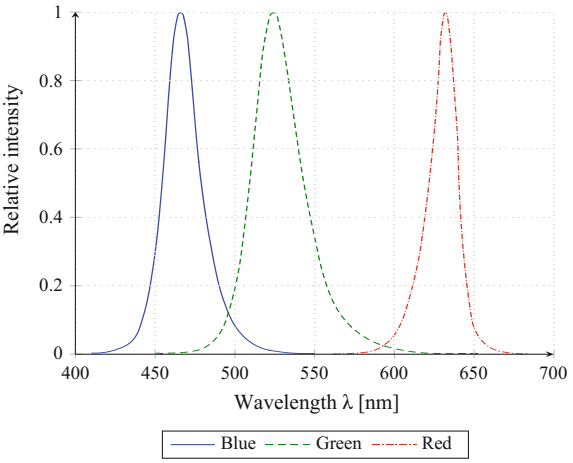

Fig. 7 Relative intensities of the used multi-color LED

different colors due to their proximity. To increase signal-to-noise ratio and reduce the challenges for amplification on the receiver side, the light source should have a high intensity. This is achievable with a commercially available high power LED, like for instance the OSRAM LRTB. Its three dominant wavelengths are at 632, 523 and 455 nm for the red, the green and the blue color respectively (see Fig. 7).

The incident light is collimated by means of an aspherical lens (optical parameters: $d = 18$ mm, $f = 15$ mm, $bfl = 11.10$ mm, $Md = 6$ mm), resulting in a beam divergence of typically less than 8°. If needed the beam divergence can be adapted by changing the distance between the lens and the LED.

On the receiver side an optical detector converts the incident light into the electrical domain. For this purpose a PIN photodiode with a large optical area of 7 mm^2 is used. A collimating lens, identical to the one on the transmitter side, is placed in front of the photodiode, to maximize the incident intensity and overcome losses due to misalignments produced by vibrations and shocks. As the measurement signal is directly proportional to the source light intensity, a stable source is of high importance. Nevertheless if fluctuations occur they can be compensated via a reference photodiode, measuring the current source intensity.

5.2 Electronic Measurement Circuitry

The optical measurement principle is based on the attenuation of light in the measurement chamber. An absence of particles or light absorbent gases corresponds to a full scale reading at the optical receiver. As a consequence, any gain or offset error/drift of the optical measurement directly and significantly influences the reading.

Numerical post-processing involves the subtraction of the actual optical output level from the reference output level and scaling this difference by the appropriate sensitivity coefficient. Both resolution and accuracy of the optical detector, its associated transconductance amplifier and the analog-to-digital converter (ADC) have to be adequately high, such as to compensate for the loss of significant digits in the following calculations.

The opacity as a ratio of I/I_0 is a dimensionless quantity, which naturally suggests a fully ratiometric measurement setup. Second order effects would still have an influence, such as gain and offset errors of the amplifiers or nonlinearities of the ADC. However, these can be kept well within allowable limits by careful circuit design.

Figure 8 shows an idealistic approach of a fully ratiometric light absorption measurement setup. The light emitted by the LED at the transmitter side is divided into two paths: The first illuminates the measurement cell containing the analyte, the second serves as a reference. An optical multiplexer at the receiver side alternately lets one of the two signals pass to the optical receiver diode. Errors related to the electronic instrumentation would largely cancel out, since the measurement and reference phase use the same optical detector and signal conditioning circuitry. Some nonlinearity would still remain, in the first instance related to the ADC.

Such an approach is not feasible for some reasons: the mechanical construction including the optical multiplexer is costly and moderately reliable, and both the optical transmitter and the optical receiver have a linear relationship between optical power and electrical current, not voltage. In contrast, the electrical signal conditioning is based on a reference voltage. It is the reference for the ADC at the receiver side and the digital-to-analog converter (DAC) for adjusting the LED

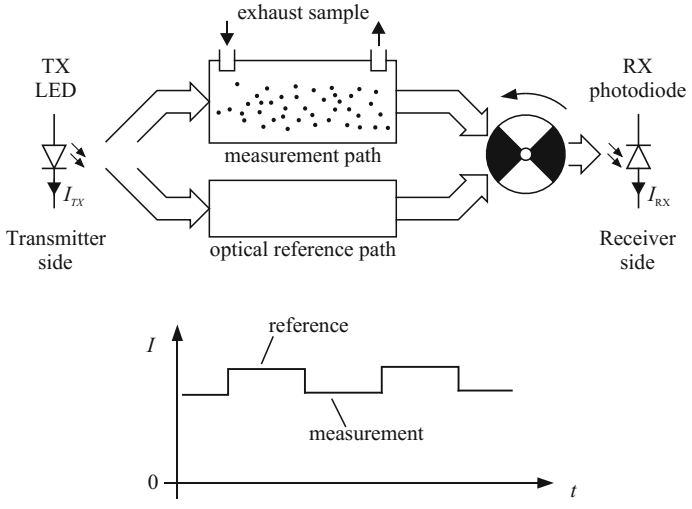

Fig. 8 Ideal approach of a fully ratiometric light absorption measurement

power at the transmitter side. As a consequence, at least two precision resistors are needed: one is part of the voltage controlled current source for the transmitter LED, another one is part of the transimpedance amplifier, converting the current output of the photodiode into a voltage output for the ADC.

Figure 9 represents the actual setup. The electronic instrumentation relies on the ratiometric principle to a great extent. A set of two identical optical receivers replaces the optical chopper of Fig. 8, each one including its dedicated transimpedance converter. A total of three precision resistors ($R_{\mathrm{REF,TX}}$, $R_{\mathrm{REF,RX,1}}$ and $R_{\mathrm{REF,RX,2}}$) are required, which is acceptable because these parts are available with excellent specifications for tolerance, temperature coefficient and long-term stability.

The optical output power of the LED correlates with its forward current. It is adjusted by the setting of the DAC, its reference voltage and the transconductance of the voltage controlled current source. A digital control loop, implemented in the firmware of the microcontroller, uses the output voltage $V_{\mathrm{RX,2}}$ of the optical reference path to set the LED current I_{TX} and keep it at the desired set level.

At the receiver side there are two photodiodes, each with its dedicated transimpedance amplifier for the current-to-voltage conversion. A critical part for the overall performance of the measurement setup is the matching of the optical receivers and their interface electronics. The photodiodes operate in current (short circuit) mode. Their light-to-current transfer ratio is therefore highly linear over several decades of intensity. Thermal influences are low and further reduced by keeping both photodiodes at the same temperature.

The influence of dark current and bias currents at the receiver side are compensated by a reference measurement with the transmitter LED turned off. Minor deviations are canceled out by digital post processing; abnormally high deviations indicate a fault situation and are handled by self-diagnostic functions.

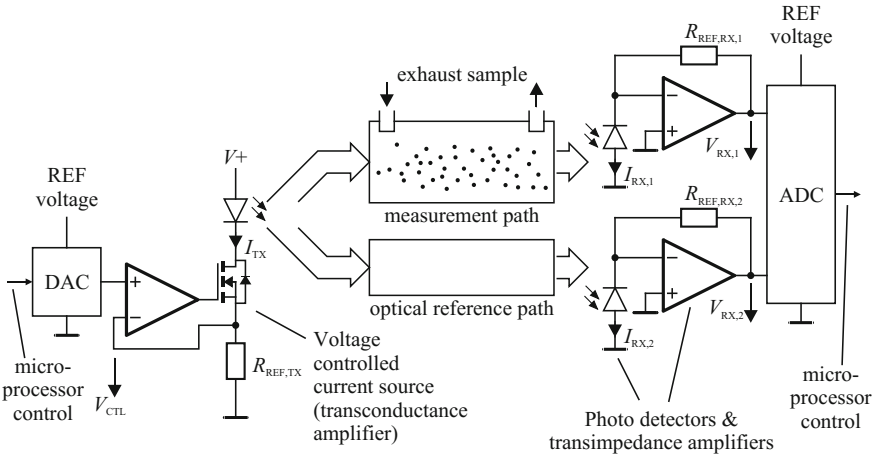

Fig. 9 Actual measurement setup

5.3 Mathematical Model

The measurement setup provides three extinction coefficients, each for one of the three used wavelengths λ_i. Equation (8) provides the equation system for determining the concentrations of three absorbing species from such a measurement. As mentioned above there is generally no exact solution for this equation system. Furthermore the third typical absorber in addition to soot and NO_2 can often not easily be identified. We therefore use the reduced equation system

$$\begin{pmatrix} k_1 \\ k_2 \\ k_3 \end{pmatrix} = \begin{pmatrix} \sigma_{NO_2}(\lambda_1) & \sigma_{soot}(\lambda_1) \\ \sigma_{NO_2}(\lambda_2) & \sigma_{soot}(\lambda_2) \\ \sigma_{NO_2}(\lambda_3) & \sigma_{soot}(\lambda_3) \end{pmatrix} \begin{pmatrix} c_{NO_2} \\ c_{soot} \end{pmatrix}, \tag{9}$$

which focusses on the two criteria pollutants particles and NO_2. In the discussion section we will show that this generally delivers good results for diesel engine exhaust.

The concentrations can be determined from (9) by inversion. This can be most easily achieved by multiplication with the pseudo inverse

$$A^+ = (A^T A)^{-1} A^T, \tag{10}$$

where A denotes the cross section matrix and A^T its transpose. It will yield the best fit for the solution in a least squares sense.

The cross section values $\sigma_x(\lambda_i)$ for NO_2 and soot can be taken from Figs. 3 and 4 respectively, as long as monochromatic light sources are used. The graphs however use different units for the cross section values. So a conversion of one of the cross sections to the unit of the other one is needed. We chose to use the unit m^2/g and converted the cross section for NO_2 as follows:

$$\sigma_{NO_2}\left[\frac{m^2}{g}\right] = \frac{1}{10^4}\sigma_{NO_2}\left[\frac{cm^2}{molecule}\right]\frac{N_A}{M_{NO_2}}\left[\frac{molecules/mol}{g/mol}\right] \tag{11}$$

Herein $M_{NO_2} = 46.005$ g/mol is the molar mass of NO_2 and $N_A = 6.022\ 10^{23}$ molecules/mol is the Avogadro constant.

Since we use a LED as a light source, the single colors are clearly not monochromatic. In this case the corresponding nominal intensities I_0 at the wavelengths λ_i have to be replaced by continuous nominal intensity spectra $I_0(\lambda)$ from Fig. 7, where at each wavelength λ (2) holds:

$$I(\lambda) = I_0(\lambda)\exp(-kL_{eff}) \tag{12}$$

On the detector the single intensities $I(\lambda)$ are integrated with respect to the spectral efficiency $\gamma(\lambda)$ of the detector:

$$I = \int \gamma(\lambda) I(\lambda) \mathrm{d}\lambda = \int \gamma(\lambda) I_0(\lambda) \exp(-kL_{\mathrm{eff}}) \mathrm{d}\lambda \tag{13}$$

The total nominal light intensity I_0 can be calculated accordingly. By relating I and I_0 a mean extinction coefficient $\bar{k}(\lambda_i)$ can be determined, as before, for each color λ_i:

$$\exp(-\bar{k}(\lambda_i) L_{\mathrm{eff}}) = \frac{\int \gamma(\lambda) I_0(\lambda) \exp(-k(\lambda) L_{\mathrm{eff}}) \mathrm{d}\lambda}{\int \gamma(\lambda) I_0(\lambda) \mathrm{d}\lambda} \tag{14}$$

In order to set up the equation system, the extinction coefficient is again replaced by the product of cross section and concentration, now denoted as $\overline{\sigma_x}(\lambda_i)$ and $\hat{c}$ respectively. However in the case of a polychromatic light source the strict proportionality does not hold for the mean values. This is obvious from the following equation:

$$\exp(-\hat{c}\overline{\sigma_x}(\lambda_i) L_{\mathrm{eff}}) = \frac{\int \gamma(\lambda) I_0(\lambda) \exp(-c\sigma_x(\lambda) L_{\mathrm{eff}}) \mathrm{d}\lambda}{\int \gamma(\lambda) I_0(\lambda) \mathrm{d}\lambda} \tag{15}$$

Despite the limited proportionality the model in (9) provides a good approximation to the real behavior, as shown by the simulations in the following discussion section.

6 Results and Discussion

The multi-wavelength approach has been evaluated using simulations and basic measurements. The results are presented and discussed in the following sections.

6.1 Sensitivity Measurements

Our first measurements have been performed with a new, highly sensitive opacimeter, to ensure that reliable measurements of the extinction produced by NO_2 are possible even at low concentrations. The opacimeter was equipped with a single color light source (green light with Gaussian intensity spectrum, $\mu = 560$ nm, $\sigma = 8$ nm). The resolution was 0.001 m^{-1}. The results are shown in Fig. 10.

Conforming to theory the measured extinction value is linearly related to the NO_2 concentration. The smallest resolvable NO_2 concentration is in the order of 10 ppm. Compared to simulations the measured extinction coefficient is a bit lower. The simulated value at 1000 ppm was approximately 0.2 m^{-1}, whereas the

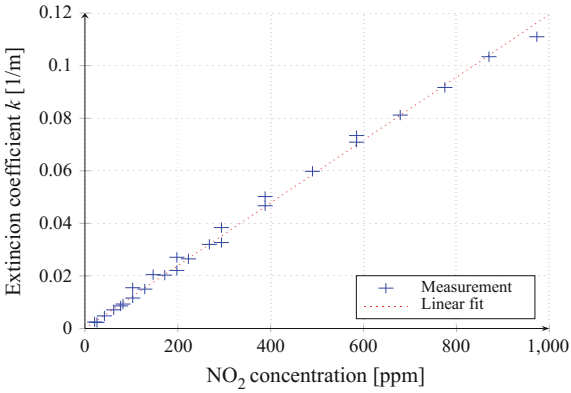

Fig. 10 NO_2 measurements with a new opacimeter

measured value is 0.12 m^{-1}. The deviations can probably be attributed to different ambient conditions (pressure and temperature).

6.2 *Mathematical Simulations*

The simulations have been performed in MATLAB using the model from (9) with the cross section spectra presented in Figs. 3 and 4. Combinations of NO_2 at concentrations from 100 to 1000 ppm and soot particles at concentrations from 1 to 1000 mg/m^3 have been tested. The results for the estimation of the NO_2 concentration from the simulated values are depicted in Fig. 11 for the noise-free case in the form of the relative deviation from the actual concentration.

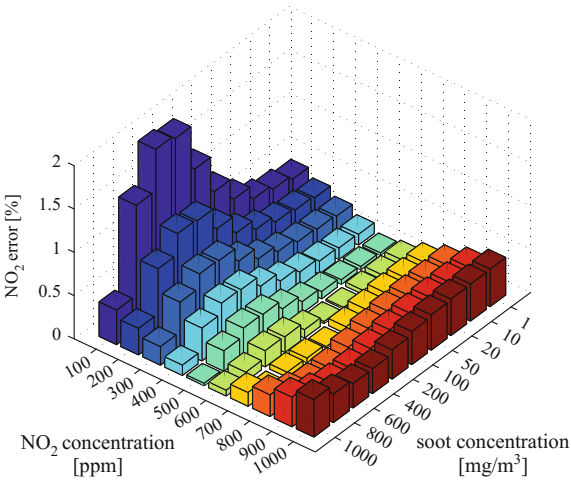

Fig. 11 Error in calculated NO_2 concentrations (simulation without noise)

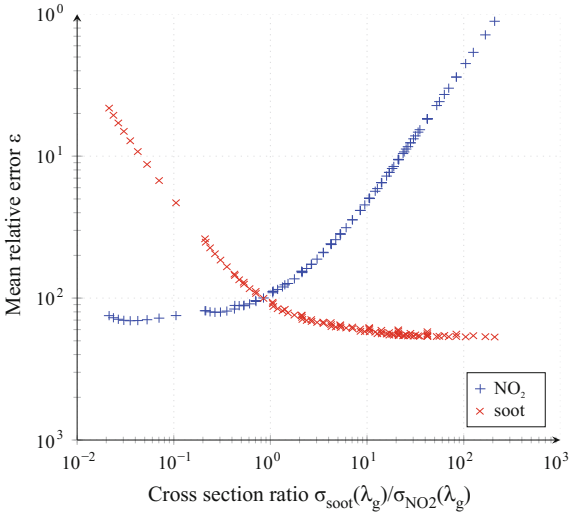

Fig. 12 Mean error in calculated NO_2 and soot concentrations (simulation with 1 % of noise)

For most combinations the error is below 1 %. Only if the contribution of one component is very low, e.g. 100 ppm of NO_2, the error can increase to almost 2 %. The reason for this error in the noise-free system is the limited proportionality due to polychromatic light. Consequently the systematic error can be reduced, when light sources with a narrow wavelength spectrum or quasi-monochromatic light sources like lasers are used.

If noise is applied the errors generally rise to a few percent. The relative error for 1 % of noise is depicted in Fig. 12. Larger errors between 10 % to 40 % for the NO_2 concentrations are only found when the contribution of soot is at least twenty times higher than that of NO_2. Solely if the share of NO_2 is smaller than 1/100 and hence negligible the mean error rises above 40 %. For the particle concentration small errors below 2.5 % can be achieved for all combinations where $c_{soot} \geq 10$ mg/m^3.

6.3 Discussion

Both preliminary measurements and simulations indicate a good applicability of the described multi-wavelength approach. Further measurements are planned for the future to investigate the performance on both laboratory mixtures of particles and NO_2 and real-world exhaust samples.

As our measurements have shown so far, it is advantageous to perform calibration measurements to acquire the cross section matrix for concentration measurements. The simulations can be a great tool for evaluating the method in theory but may result in somewhat deviating numbers.

With a calibration based on practical measurements we except good results for the determination of the concentrations of NO_2 and particles, as long as they are the

primary contributors to the extinction. Other strong absorbers present in the exhaust sample might lead to deteriorated results. For diesel exhaust this is a rare case. Known examples of additional absorbers are white and blue smoke. White smoke, produced by condensed water, can be eliminated by proper conditioning of the engine prior to the PTI and by heated sample lines. By keeping the exhaust temperature above the due point of exhaust gases, which is in the area of 45–55 °C [14], water is hindered from condensing. When using a temperature above 100 °C already condensed droplets can be evaporated again. Blue smoke is typically related to an engine defect. It can occur for instance, if oil leaks into the cylinder [35–38]. If required, such hydrocarbon emissions can be eliminated by integration of an oxidation catalyst ("catalytic stripper") into the heated sample line [39]. Hence, when implementing such measures, an overall good applicability to real engine emissions can be assumed.

For the real-world exhaust samples comparison measurements with dedicated NO_2 sensors are planned to gain insights into the quality of the measurement results. Although such dedicated devices will of course yield more accurate results [40], the proposed method can provide at least valuable qualitative results without the need for extra measurement equipment. Furthermore little or no additional conditioning of the exhaust sample is needed in comparison to a standard opacimeter. Finally the main functionality of the opacimeter, i.e. measuring the exhaust opacity, is not degraded in any way.

7 Conclusion

Emission regulation covering the whole lifetime of vehicles is a key for a clean and healthy environment. Two of the main pollutants of combustion engines, namely soot and nitrous oxides, depend strongly on the state of health of the combustion engine as well as of the exhaust aftertreatment system. Within this chapter a novel method for the simultaneous determination of NO_2 and soot in the exhaust of diesel engines with emphasis on periodical technical inspection (PTI) was elaborated in detail. It is based on a spectroscopic multi-wavelength light extinction measurement in a setup similar to an opacimeter with high sensitivity. Preliminary experimental results have proven its ability to reliably detect small concentrations of NO_2 with a limit of detection (LOD) as low as 10 ppm. The experimental research with the focus on the simultaneous determination of the second pollutant soot is ongoing. The overall results are promising and indicate the potential to gain further information on the pollutants contained in exhaust without the need for an additional dedicated sensor in PTI applications.

References

1. J. Linn, *Explaining the adoption of diesel fuel passenger cars in europe* (RFF, Washington, 2014)
2. M. Cames, E. Helmers, Critical evaluation of the european diesel car boom—global comparison, environmental effects and various national strategies. Environ. Sci. Eur. **25**(15), 1–22 (2013)
3. D.B. Kittelson, Engines and nanoparticles: a review. J. Aerosol Sci. **29**(5/6), 575–588 (1998)
4. International Agency for Research on Cancer, World Health Organization, Diesel engine exhaust carcinogenic. Press Release No. 213 (2012)
5. Y. Qian, T.J. Yasunari, S.J. Doherty, M.G. Flanner, W.K.M. Lau, J. Ming et al., Light-absorbing particles in snow and ice: measurement and modeling of climatic and hydrological impact. Adv. Atmos. Sci. **32**(1), 64–91 (2015)
6. G.P. Merker, C. Schwarz, R. Teichmann, in *Grundlagen Verbrennungsmotoren: Funktionsweise, Simulation, Messtechnik*, 7th edn. (Springer Vieweg, Wiesbaden, 2014)
7. G.A. Bishop, D.H. Stedman, Emissions of nitrogen dioxide from modern diesel vehicles, WIT Trans. Ecol. Environ. **116** (2008)
8. T.R. Dallmann, R.A. Harley, T.W. Kirchstetter, Effects of diesel particle filter retrofits and accelerated fleet turnover on drayage truck emissions at the port of Oakland. Environ. Sci. Technol. **45**(24), 10773–10779 (2011)
9. N.K. Verma, S.K. Khanna, B. Kapila, *Comprehensive Chemistry*, vol. I. Class XI. (Laxmi Publications, New Delhi, 2010)
10. K. Mollenhauer, H. Tschöke, *Handbook of Diesel Engines*, 3rd edn. (Springer, Berlin Heidelberg, 2007)
11. C.D. Rakopoulos, E.G. Giakoumis, *Diesel Engine Transient Operation: Principles of Operation and Simulation Analysis* (Springer, London, 2009)
12. European Commission: Commission regulation (EC) No 692/2008 of 18 July 2008 implementing and amending regulation (EC) No 715/2007 on type-approval of motor vehicles with respect to emissions from light passenger and commercial vehicles (Euro 5 and Euro 6) and on access to vehicle repair and maintenance information. OJ L 199, (2008), pp. 1–136
13. P. Boulter, P. Buekenhoudt, P. Stricker, H.-J. Mäurer, C. Nolte, T. Ost et al., TEDDIE—A new roadworthiness emission test for diesel vehicles involving NO, NO2, and PM measurements, final report, (CITA, 2011)
14. P. Eastwood, *Particulate Emissions from Vehicles* (Wiley, Chichester, 2008)
15. H. Axmann, A. Bergmann, B. Eichberger, Measurement of ultrafine exhaust particles using light scattering, in *2013 Seventh International Conference on Sensing Technology (ICST2013)* (IEEE, 2008), pp. 937–941
16. G. Hauser, G. Hauser, *Entwicklung eines Rußmessgerätes für Kfz-Werkstätten und AU-Prüfung, final report, phase 1* (E.A.S.T. Solutions GbR, Twieflingen, Germany, 2009)
17. I. Bennett, J. Tikkanen, L. Ntziachristos, A new sensor for long term monitoring of ultrafine particles in a number of applications, in *Annual Aerosol Science Conference* (The Aerosol Society, 2010)
18. L. Bergmann, C. Schaefer, H. Niedrig, *Lehrbuch der Experimentalphysik*, vol. 3: Optik. Wellen- und Teilchenoptik. Berlin: de Gruyter, 10 ed., 2004
19. H.C. van de Hulst, *Light scattering by small particles* (Dover Publications, New York, 1981)
20. C.F. Bohren, D.R. Huffman, *Absorption and scattering of light by small particles* (Wiley, New York, 1998)
21. C.M. Sorensen, Light scattering by fractal aggregates: a review. Aerosol Sci. Technol. **35**(2), 648–687 (2001)
22. A.C. Szkarlat, S.M. Japar, Optical and chemical properties of particle emissions from on-road vehicles. J. Air Pollut. Control Assoc. **33**(6), 592–597 (2012)

23. J. Fenger, O. Hertel, F. Palmgren, *Urban Air pollution—European Aspects* (Springer, Dortrecht, 1998)
24. M. Pitchford, W. Malm, B. Schichtel, N. Kumar, D. Lowenthal, J. Hand, Revised algorithm for estimating light extinction. J. Air Waste Manag. Assoc. **57**(11), 1326–1336 (2012)
25. J. Orphal, A critical review of the absorption cross-sections of O3 and NO2 in the ultraviolet and visible. J. Photochem. Photobiol. A Chem. **157**(2–3), 185–209 (2003)
26. S. Voigt, J. Orphal, J.P. Burrows, The temperature and pressure dependence of the absorption cross-sections of NO2 in the 250–800 nm region measured by fourier-transform spectroscopy. Photochem. Photobiol. A Chem. **149**(1–3), 1–7 (2002)
27. J. Orphal, *A critical review of the absorption cross-sections of O3 and NO2 in the 240–790 nm region* (ESA technical note, Laboratoire de Photophysique Moléculaire, CNRS, Orsay, France, 2002)
28. M. Schnaiter, H. Horvath, O. Möhler, K.-H. Naumann, H. Saathoff, O.W. Schöck, UV-VIS-NIR spectral optical properties of soot and soot-containing aerosols. J. Aerosol Sci. **34**(10), 1421–1444 (2003)
29. H. Saathoff, O. Moehler, U. Schurath, B. Kamm, S. Amd Dippel, D. Mihelcic, The AIDA soot aerosol characterisation campaign 1999. J. Aerosol Sci. **34**(10), 1277–1296 (2003)
30. R.A. Dobbins, G.W. Mulholland, N.P. Bryner, Comparison of a fractal smoke optics model with light extinction measurements. Atmos. Environ. **28**(5), 889–897 (1994)
31. S.J. Harris, M.M. Maricq, Signature size distributions for diesel and gasoline engine exhaust particulate matter. J. Aerosol Sci. **32**(6), 749–764 (2001)
32. R.A. Aspey, K.J. Brazier, In situ optical sensing of diesel exhaust particulates using a polychromatic led source. Meas. Sci. Technol. **14**, 751–758 (2003)
33. N. Sharma, I.J. Arnold, H. Moosmüller, W.P. Arnott, C. Mazzoleni, Photoacoustic and nephelometric spectroscopy of aerosol optical properties with a supercontinuum light source. Atmos. Meas. Tech. **6**, 3501–3513 (2013)
34. C. Haisch, R. Niessner, Photoacoustic analyzer for the artifact-free parallel detection of soot and NO2 in engine exhaust. Anal. Chem. **84**(17), 7292–7296 (2012)
35. S. Bhandarkar, Vehicular pollution, their effect on human health and mitigation measures. VE **1**(2), 3340 (2013)
36. E. Bocci, L. Rambaldi, Soot emission modelization of a diesel engine from experimental data. ICCSA **6785**, 317–327 (2011)
37. M. Lapuerta, F.J. Martos, M.D. Cárdenas, Determination of light extinction efficiency of diesel soot from smoke opacity measurements. Meas. Sci. Technol. **16**(10), 2048–2055 (2005)
38. A. Faiz, C. S. Weaver, M. P.Walsh, *Air pollution from motor vehicles: standards and technologies for controlling emissions* (The World Bank, Washington, D.C., 1996)
39. S. Amanatidis, L. Ntziachristos, B. Giechaskiel, D. Katsaounis, Z. Samaras, A. Bergmann, Evaluation of an oxidation catalyst ("catalytic stripper") in eliminating volatile material from combustion aerosol. J. Aerosol. Sci. **57**, 144–155 (2013)
40. Analytical and Advanced Solutions (ABB), Limas 11HW Gas Analyzer. Brochure, Online (2004). Available: http://www.abb.com

Development of the Atomic Emission Spectroscopy System Using Helium-Microwave-Induced Plasma for Fine Particles on Environmental Monitoring

Satoshi Ikezawa, Jun Yamamoto and Toshitsugu Ueda

Abstract This chapter describes the elemental analytical technique of the fine particles using atomic emission spectroscopy system for an environmental pollution monitoring. Based on our previous measurement reports, differences of the usage between the laser-induced breakdown spectroscopy (LIBS) system and the helium-microwave-induced plasma-atomic emission spectroscopy (He-MIP-AES) system are explained. Both systems were developed to allow to fulfil the criteria prescribed by the Ministry of Environment, Japan, for measuring the chemical components of particulate matter (PM) by introducing additional original sampling systems. In current environmental monitoring systems, PMs are typically collected on trapping filters placed across Japan and classified as either suspended particulate matter (SPM) or PM2.5 depending on the size. The collected PMs are subsequently analysed with automated measurement instruments such as a piezo balance and with methods such as beta ray attenuation and light scattering. While these measurement methods allow the mass concentration of PMs in the air to be obtained at hourly intervals, the chemical composition of individual particles is analysed with time-intensive laboratory procedures. In contrast, the LIBS and He-MIP-AES measurement system allow the chemical compositions and particle sizes to be measured simultaneously in real time.

1 Introduction

Recently, regional atmospheric environment issues around Japan have produced an increase in particulate matter (PM), which is considered to be a transboundary pollutant [1]. While domestically produced PM that is less than 2.5 μm in size

S. Ikezawa (✉) · J. Yamamoto · T. Ueda
Graduate School of Information Production and Systems, Waseda University, Kitakyushu, Japan
e-mail: ikezawa@y.fuji.waseda.jp

S. Mukhopadhyay et al. (eds.), *Sensors for Everyday Life*, Smart Sensors, Measurement and Instrumentation 23, DOI 10.1007/978-3-319-47322-2_2

(PM2.5) has been reported to be decreasing in cities [2], high concentrations of PM2.5 that exceed the allowable limits set by the Ministry of Environment, Japan, have been frequently observed in the western parts of the country. This PM is considered to be transported through diffusion by the westerlies. The inhalation of fine PM is known to cause a range of health problems [3–6]. PM2.5 can penetrate the gas-exchange region of the lungs. Thus, information on the size of particulates (e.g., distinguishing particulates based on size) is as important as information on their elemental components and density. However, it is difficult to obtain real-time information on the size and composition of nano-sized suspended particulate matter (SPM) simultaneously. The beta-ray absorption system is the most commonly used automatic measuring instrument for SPM in Japan. The main advantages of the beta-ray absorption method are that the mass absorption coefficient is constant with regard to the particulate composition, the method does not require frequent cleaning like the piezo balance-type dust monitoring method, and it does not require standard calibration steps that use a reference material like the light scattering method. However, recent attention has been focused on designing environmental monitoring systems that can detect particulates smaller than 2.5 μm. In order to meet the requirement of being able to measure the chemical composition of fine particulates in real time, we developed and proposed a laser-induced breakdown spectroscopy (LIBS) system, laser-induced incandescence (LII) and helium-microwave-induced plasma-atomic emission spectroscopy (He-MIP-AES) measuring system for environmental monitoring [7–13]. The LIBS is a useful tool for determining the elemental composition of various materials, and it does not require any chemical or physical preprocessing steps. However, because the entire volume of the laser-irradiation area is broken down without individually resolved particles, the LIBS technique is not sufficient for obtaining information on specific particulate sizes, just on the intensity value. The quantitative values obtained by LIBS only relate to the total volume of particulates per unit volume; in other words, these values relate to the weight/volume density. To overcome the weakness of the LIBS system for fine particle quantitative measurement, the LII technique was introduced. The most salient feature of the combined LIBS and LII system is its ability to perform real-time measurements with noncontact and nonguiding particulates into the measurement spot. He-MIP-AES system allows a larger and continuous volume of atmospheric gases to be measured compared to LIBS and LII. The radiofrequency (RF) of a capacitively coupled plasma (CCP) operating at various frequencies has long been used as an excitation source for analysis by optical emission spectrometry (OES) [14–17] since Cristescu and Grigorovici experimented on the discharge produced by the application of the output of a high-frequency oscillator to two circular plates in 1941 [18]. Microwave-induced plasma (MIP) is formed in a discharge tube placed in a cavity to which power is transmitted via a coaxial line [19]. MIP supported by an inert gas has been applied as a versatile selective OES detector in gas chromatography [20, 21]. Argon or helium is preferred as the plasma support gas because of the absence of molecular background spectra. In typical OES analysis like inductively coupled plasma (ICP), argon gas is frequently used because argon plasma is more stable under atmospheric conditions or when the

measurement sample is wet than helium plasma. However, helium is the ideal support gas because the organic compounds eluted from the gas chromatograph are then almost completely atomized in the plasma, which produces a line emission spectrum. In contrast to the Ar-ICP system, the He-MIP-AES system employs helium as the ionized gas for excitation. The metastable level of helium (19.8 eV) is greater than argon (11.5 eV), and its high excitation energy allows the analysis of a wide range of elements, including high-energy ionizing elements such as the halogen family.

2 Motivation

With the rapid growth and industrialization of Asia's economy, fossil fuel emissions from factories, power plants and automobile are emitting into the atmosphere. For preventing growing aerosol pollution and global climate change problems, numerous organizations are actively involved in research programs for the development of processes that utilize biodiesel sources. It is known that a diesel engine is more fuel efficient than a gasoline engine, and further, electronically controlled common-rail injection contribute to clean burning. Hence, cleaner-burning engine often produce smaller soot; nanosized particles as a byproduct. It is well known that inhalation of fine particle matter causes several health problems. Particles that are smaller than 2.5 μm in size (PM2.5) can penetrate the gas-exchange region of the lung. However, it is difficult to obtain the size and composition information of the fine particles in real time. We have developed and conducted experiments using following measuring methods to overcome the difficulty. Laser-induce breakdown spectroscopy (LIBS) is one of the useful methods for the determination of the elemental composition of the fine particles. Our research group has been developing LIBS techniques that have potential applications in various fields. However LIBS itself is not enough to obtain the particle size information. Figure 1 shows photograph of the MEMS fabrication room and SEM images of the particles deposited on Si membrane porous filter which gathered in the clean room.

Figure 2 illustrates for one example of the reason why LIBS particle size measurement with the range smaller than laser spot size is hard to do. In case LIBS measurement are conducted for fine particles, we only know the plasma intensity information. Because of the intensity means total amount of the particles, it may be only one particle, otherwise the plasma emission irradiated from number of particles.

Based on the requirement for particle size information, we applied laser-induced incandescence (LII) technique with LIBS. In previous our researches, the LII decay simulation model was based on one of the most detailed studies provided by Michelsen [22] (Fig. 3).

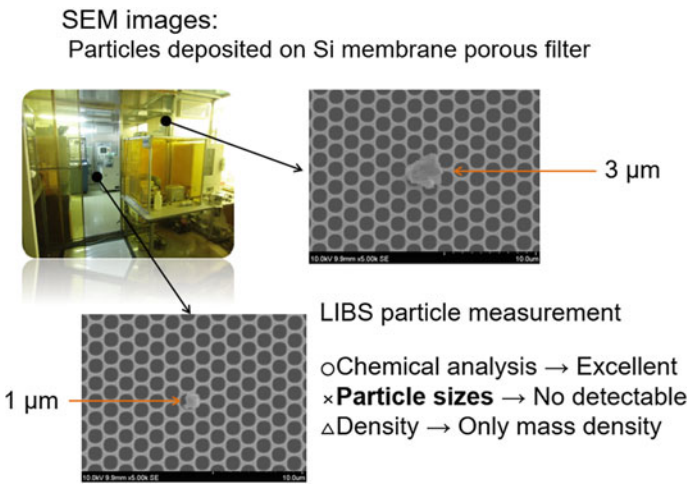

Fig. 1 Fine particles in the air and disadvantage of LIBS measurement

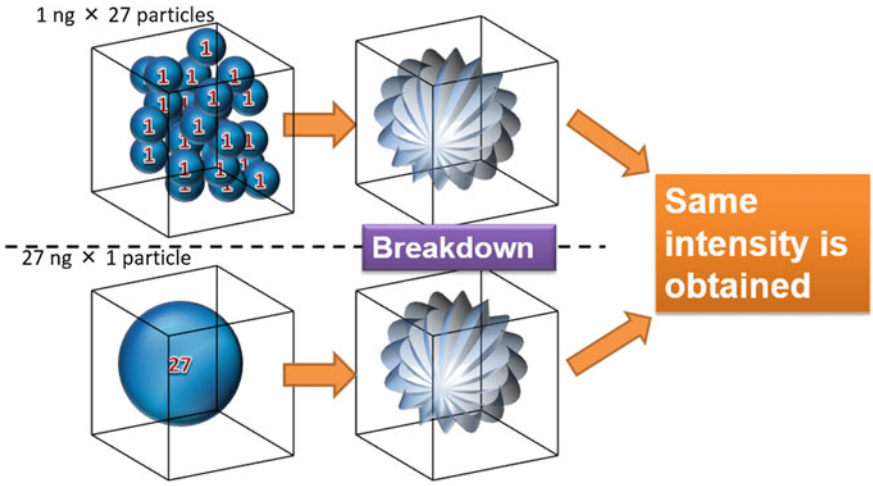

Fig. 2 Difficulty of the particle size information detection on LIBS measurement

When using the LII technique, laser pulse was irradiated on particles then thermal radiation was recorded. LII technique is based on the analysis of cooling behaviour of particles after irradiation with the laser pulse. By using Stefan-Boltzmann law for a black body, the LII signal; profile of the intensity decay time depending on the particle size. Figure 4 shows solution algorism to obtain the LII signal as a function of time-temperature curve.

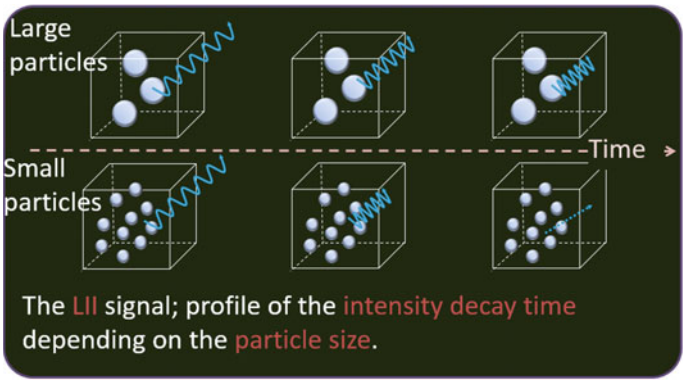

Fig. 3 Difference of the radiation cooling time associated with the radiation rate as a function of surface to volume ratio

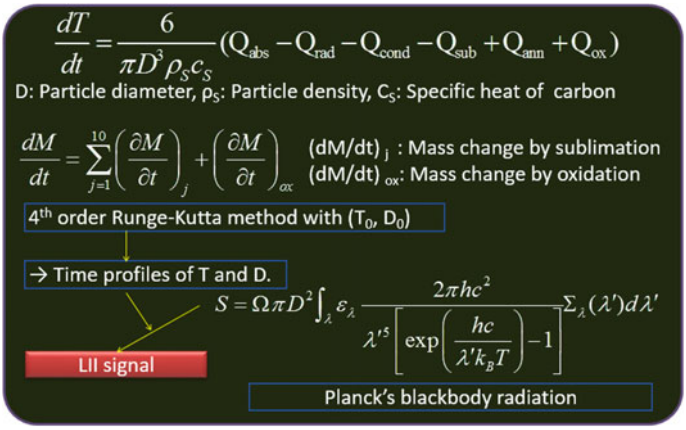

Fig. 4 Solution algorism to obtain the LII signal as a function of time-temperature curve

According to the Michelsen's model, the energy balance for the interaction of a particle with laser is given by

$$Q_{Int} = Q_{abs} - Q_{rad} - Q_{cond} - Q_{sub} + Q_{ann} + Q_{ox} \quad (1)$$

where Q_{Int} represents the sensible energy storage in particle, Q_{abs} is the rate of the laser energy absorption, Q_{rad} is the radiation rate by blackbody emission, Q_{cond} represents the energy dissipation rate by conduction, Q_{sub} represents the rate of energy loss by sublimation of carbon clusters and accounts for the energy consumption during photodesorption of the annealed particle to form small carbon clusters, Q_{ann} represents the energy production rate by particle annealing, and Q_{ox} represents the energy generation rate by oxidation. Each terms of this energy flow

rate equation were accounted for by laser beam temporal intensity profile, time dependence of the particle temperature, and initial states of the particle.

Time-derivative term of the particle temperature yields

$$\frac{dT}{dt} = \frac{6}{\pi D^3 \rho_S c_S}(Q_{abs} - Q_{rad} - Q_{cond} - Q_{sub} + Q_{ann} + Q_{ox}) \tag{2}$$

where T is the particle temperature, D is the primary particle diameter, ρ_s is density of the particle c_s is specific heat of solid carbon.

From Planck equation from blackbody, LII signal at wavelength λ' is given by

$$S = \Omega \pi D^2 \int_{\lambda} \varepsilon_{\lambda} \frac{2\pi hc^2}{\lambda'^5 \left[\exp\left(\frac{hc}{\lambda' k_B T}\right) - 1\right]} \Sigma_{\lambda}(\lambda') d\lambda' \tag{3}$$

where Ω is normalization constant, ε_λ is emissivity at wavelength λ for a Rayleigh particle, h is Planck constant, c is speed of light, k_B is Boltzmann constant, Σ_λ is accounted for by including it in the integration of the Plank function over wavelength. Solving the differential Eq. (2), each terms of energy flow ratio were calculated from the laser beam intensity profile which obtained from actual measurement.

Particle size measurement had been successfully accomplished with the help of LII technique on our LIBS system. Despite the good agreement between calculation and measured temporal profiles, calibrations using several size of particle are required for the correction to the real particle size.

In our latest research, new measuring device using He-MIP-AES technique was additionally introduced [13]. He-MIP-AES system allows a larger and continuous volume of atmospheric gases to be measured compared to LIBS and LII.

3 Device Designs

A. LIBS and LII Analysis Method

Figure 5 represents the schematic of the LIBS and LII system. When using the LIBS technique, a higher energy laser pulse was focused on particles to create plasma then atomic specific emissions were dispersed by spectrograph and then recorded with a streak camera by separating from predomination of bremsstrahlung spectra. When using the LII technique, unfocused laser pulse was irradiated on particles then thermal radiation was dispersed by spectrograph and then recorded with a streak camera.

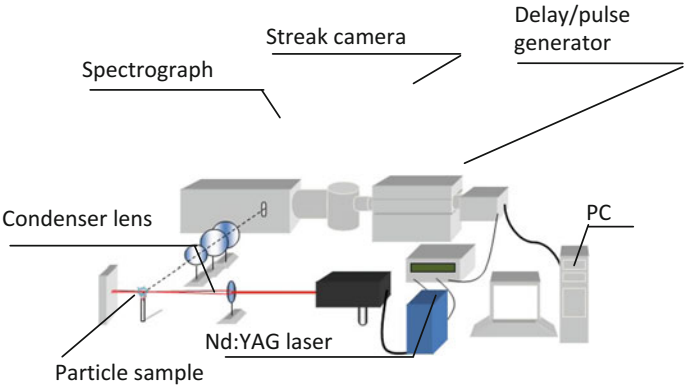

Fig. 5 Schematic of the LIBS and LII combination system

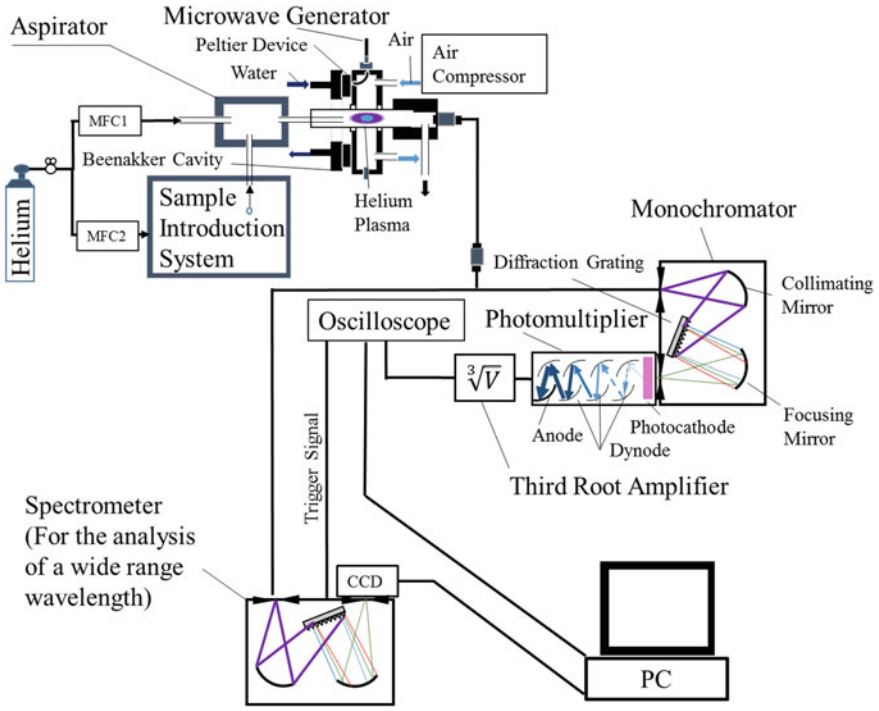

Fig. 6 Schematic of the MIP system using Beenakker cavity and two-way spectroscopic analysis system

B. He-MIP-AES Method

Figure 6 shows a schematic of the MIP system. The He-MIP-AES system is a reconstruction of an existing particle analyzer system (PT1000, Yokogawa Electric Co., Tokyo, Japan) [23]. The He-MIP system utilizes microwaves with a frequency of 2.45 GHz in TM_{010} mode. The microwaves are introduced into a Beenakker-type cylindrical cavity resonator. Electromagnetic energy at 70–200 W is condensed at the quartz discharge tube, which is set at the center of the cavity. The plasma stability depends on the temperature stability of the cavity. In order to keep the cavity temperature at 20 °C, a laminar airflow at 20 L/min is formed on the surface of the discharge tube for cooling, and a Peltier device is attached to the discharge tube for fine control. Preventing the introduction of other gases into the cavity is also important for plasma stability. Helium gas is introduced to the sampling introduction system at 45 ± 10 mL/min and to the aspirator at 300 mL/min for optimal operation. Contaminating gases lead to shrinking of the plasma and electromagnetic polarization. This may cause insufficient plasma processing of the samples, which may lead to failure of the quantitative analysis from the matrix effect, molecular ion effect, and quenching phenomenon. In order to maintain plasma purity, special techniques need to be carefully applied to collecting samples and introducing particulates. Therefore, the particle is exposed under a helium atmosphere at the sample introduction area of the system.

The particle is then aspirated with helium gas, and the aggregate is unpacked at the point of the inflow area into the fast-flowing helium gas. Considering the location and velocity of the sample particles, the fastest helium flow of the centre axis for the cylinder (inner diameter is 3.5 mm) reaches 1.108 m/s. The flow velocity at the centre is twice the average flow speed at a 300 mL/min flow rate. This means that the minimum transit time of particles inside the helium plasma over a distance of 10 mm is about 9 ms. The minimum transit time requires the optical system to measure each particle within 9 ms. The optical system employs an originally designed switching module to detect particles in order to reveal their chemical composition at high sensitivities (0.33 nm resolution) or to detecting particles with unknown chemical compositions over broad wavelength ranges (250–680 nm, 3.3 nm resolution). The optical system for the plasma emission spectrum combines a monochromator and photomultiplier; these are used in the high-sensitivity detection mode. In the high-sensitivity mode, the wavelength of the spectrum peak should be a narrow band around a known spectral line when presetting the photomultiplier. The intensity signal of the plasma emission produced from each particle is converted to the third root value by the electrical circuit to obtain a diameter-equivalent value. When detecting the chemical composition of the particles, a multi-channel spectrometer is used, and the spectra are recorded with the charged-coupled device (CCD) array. The trigger signal output has a delay at the oscilloscope of 20 ns. The CCD requires 8–9 μs to reset its operation and 1.9 ms to process data. Thus, if the gate time of the spectrometer is 1 ms, one measuring cycle takes 2.909 ms (344 Hz). The system operation time is clearly within 9 ms.

4 Calibration and Evaluation

A. Wavelength Calibration of Monochromator

Wavelength calibration tests of the monochromator were conducted by using a mercury lump with several spectrum wavelengths: 253.65, 313.16, 365.02, 435.84, and 546.07 nm. In these calibration tests, the measurement scanning direction was set from both wavelength sides to find the backlash effect between turning table gears. The results are shown (Figs. 7, 8, 9, 10, and 11).

These experimental results for the monochromator indicate that spectrum peek data obtained both direction have a certain of error toward true value, and these error difference at comparable level means that the backlash had almost no effect at these calibration wavelengths. Figure 12 shows the peak shift trend toward the measured wavelength. It shows that the monochromator had a margin of error for the wavelength of ±0.3 nm, and the peak shift showed a linear trend toward the wavelength. Thus, the calibration curve allowed the correct value to be obtained in actual measurements.

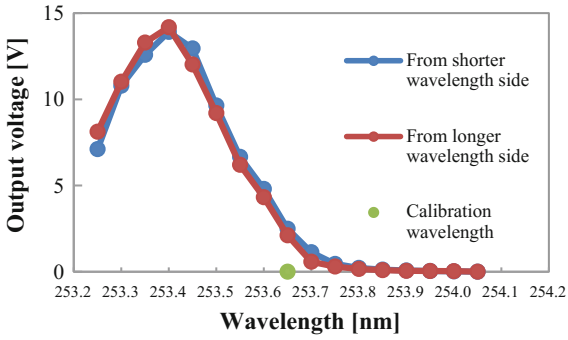

Fig. 7 Measurement results at 253.65 nm wavelength

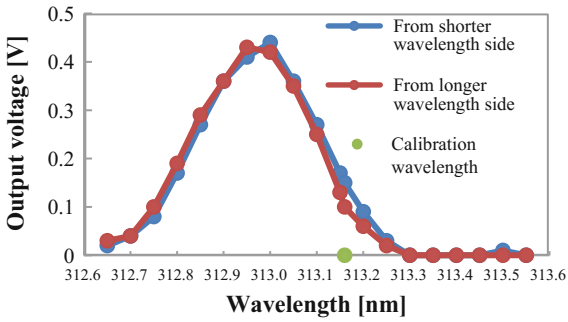

Fig. 8 Measurement results at 313.16 nm wavelength

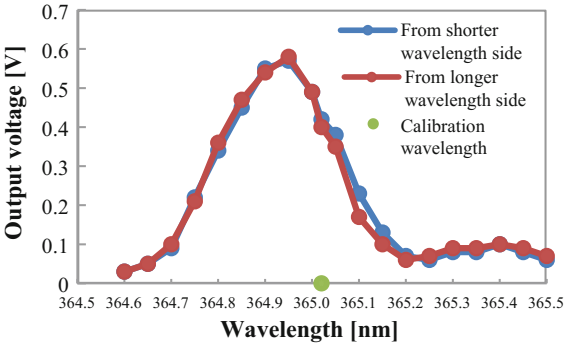

Fig. 9 Measurement results at 365.02 nm wavelength

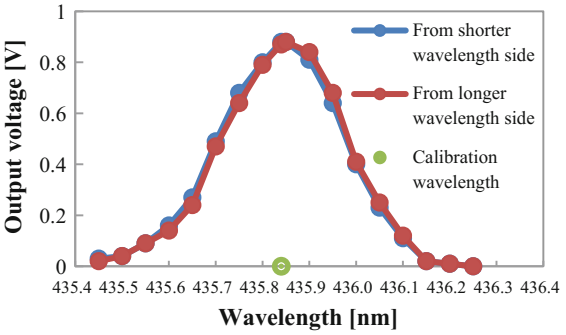

Fig. 10 Measurement results at 435.84 nm wavelength

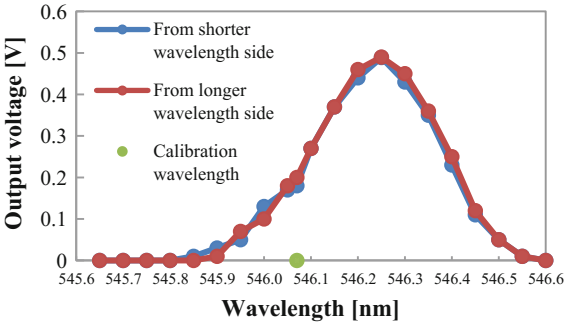

Fig. 11 Measurement results at 546.07 nm wavelength

B. Equivalent Grain Size Identification

To evaluate the performance of the MIP system for quantitative particle size analysis, the particle size was identified from the output intensity signal. Spherical and uniform-size silicon dioxide particles were used as standard particles of a known size (Fig. 13).

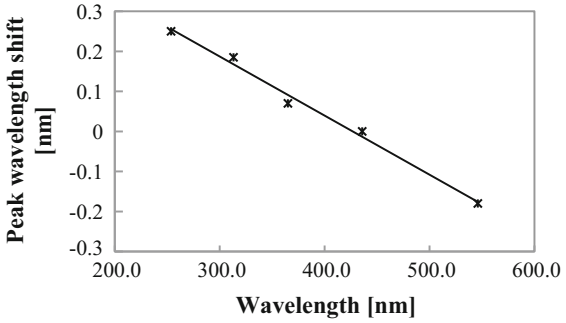

Fig. 12 Peak shift trend toward measurement wavelength

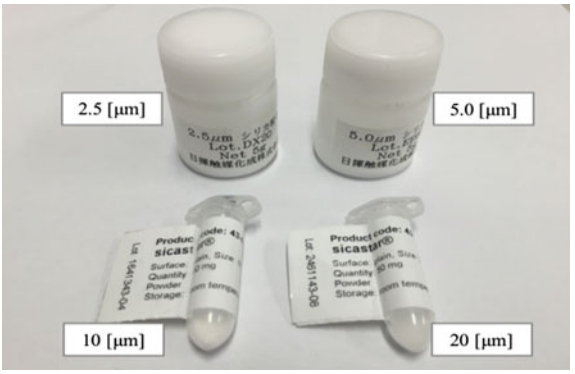

Fig. 13 Silicon dioxide standard particles

Four particle sizes (diameter: 2.5, 5.0, 10, and 20 μm) were used in the experiment (Table 1). For conversion to the size of a pure silicon particle, the conversion factor from the silicon dioxide particle was set to 0.7615 based on the volume fractions of the constituent elements. The detection wavelength for silicon was set to 288.18 nm.

C. Introduction of Intensity Correction Factor for Other Elements

The equivalent particle diameter D has a proportional relationship to the output voltage of the third root amplifier V. However, the intensity correction factor K for other elements with different wavelengths should be as given in (4) b
ased on previous research works [23].

$$D = KV \tag{4}$$

Table 1 Experimental results for output voltage at greatest frequency of third root amplifier and particle diameter

	Particle diameter variation			
SiO_2 (μm)	2.5	5.0	10.0	20.0
Si (μm)	1.9	3.8	7.6	15.2
Output voltage of third root amplifier (V)	1.7	3.8	7.5	14.7

D. Limit of Detection

The limit of detection (LOD) for a particle size in the system is defined according to the relative intensity of the atomic spectrum (intensity correction factor) and the ground noise level. Table 2 presents a reference chart for several elements.

Table 2 List of correction factors and LOD

Element	Selected spectrum wavelength (nm)	Intensity correction factor K	Noise level (V)	He-MIP-AES LOD of particle size (μm)
Si	288.18	1	0.76	0.98
Ag	328.07	0.270	0.66	0.23
Al	396.15	0.622	0.63	0.51
As	234.98	0.276	0.58	0.21
Au	267.60	0.360	0.65	0.30
B	294.77	0.421	0.62	0.34
Ba	493.41	0.355	0.59	0.27
C	247.86	0.631	0.51	0.42
Ca	393.37	0.103	2.47	0.33
Ce	401.24	1.550	0.61	1.24
Cl	479.45	2.494	0.23	0.75
Cr	520.84	0.426	0.60	0.33
Cu	324.75	0.293	0.70	0.27
F	685.60	4.704	0.54	3.28
Fe	238.20	0.257	2.63	0.88
Ga	294.36	0.158	0.67	0.14
K	766.49	1.905	0.50	1.25
Mg	285.21	0.278	0.84	0.30
Mn	293.31	0.492	0.70	0.45
Mo	277.54	0.483	0.65	0.41
N	744.26	2.450	0.50	1.58
Na	588.99	0.274	0.58	0.21
Ni	341.48	0.482	0.65	0.41
P	255.33	0.529	0.63	0.43
Pb	405.78	0.167	4.32	0.94
S	527.89	2.849	0.59	2.19
V	298.88	0.415	0.73	0.39
W	400.87	1.448	0.62	1.18
Zn	334.50	0.327	0.69	0.29
Zr	343.82	0.533	0.69	0.48

5 Measurement and Analysis of Suspended Particles in Atmosphere Using MIP System for Environmental Monitoring

The measurements was taken on the rooftop deck of a building at our university campus in Kitakyushu, Japan. The height of the roof top deck is about 10 m from the ground. Suspended particles were collected over a 7-h period from 10:00 to 17:00 with a flow rate of 5 L/min and deposited on a filter with a pore diameter of 0.4 μm.

Figure 14 shows the premeasurement plasma spectrum of the He-MIP system with a multi-channel spectrometer being used for wide-range spectrum finding. Besides the helium carrier gas (He), hydrogen (H), oxygen (O) and hydroxyl radical (•OH) were also observed. This is because of the measurement was conducted under atmospheric pressure conditions, and moisture in the air or adhering to the inner tube wall was introduced.

The measurement results for particles suspended in air using the He-MIP-AES instrument are reported in Figs. 15, 16, 17, and 18. These figures show the event number of plasma emissions with respect to individual particle sizes for elemental

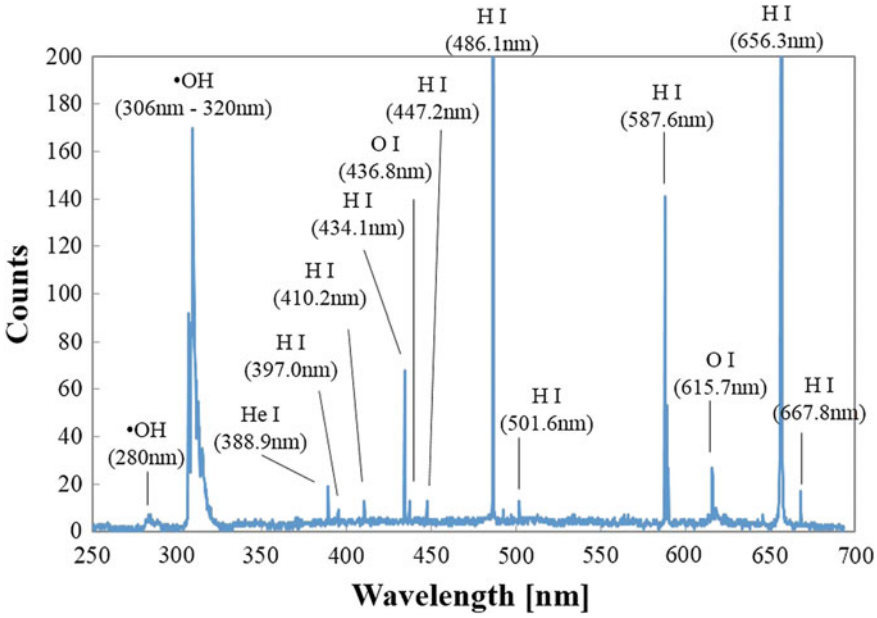

Fig. 14 Plasma spectrum of He-MIP system using multi-channel spectrometer without measured particles

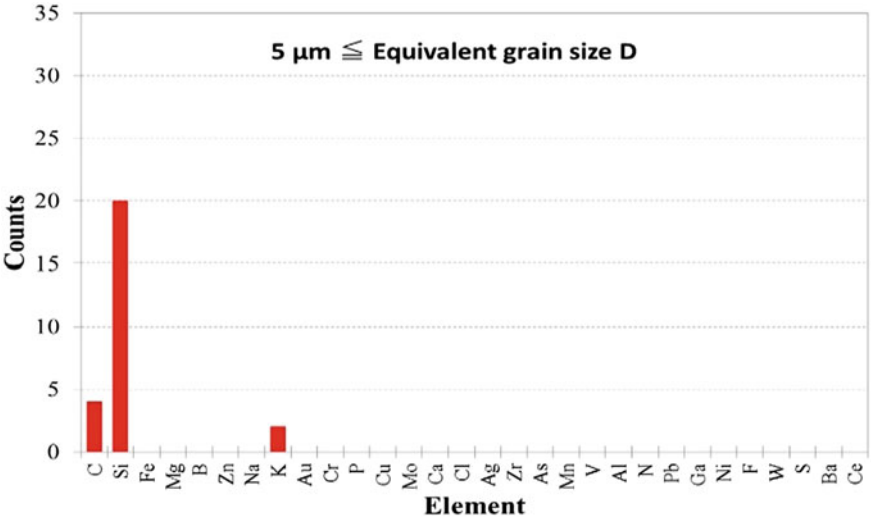

Fig. 15 Counts of particles greater than 5 μm in size for elemental signals obtained from plasma spectral emissions

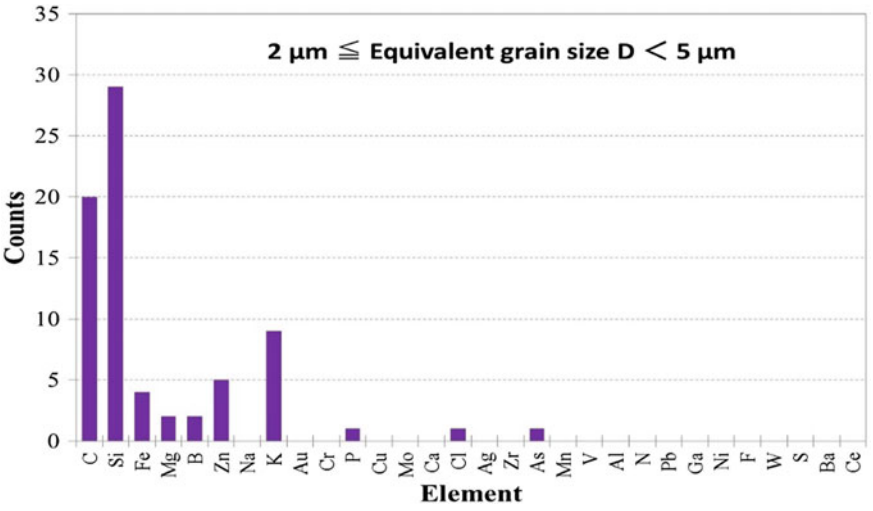

Fig. 16 Counts of particles greater than 2 μm and less than 5 μm in size for elemental signals obtained from plasma spectral emissions

signals classified by the equivalent grain size diameter D. The diameter was derived from the output voltage of the third root amplifier with an intensity correction factor.

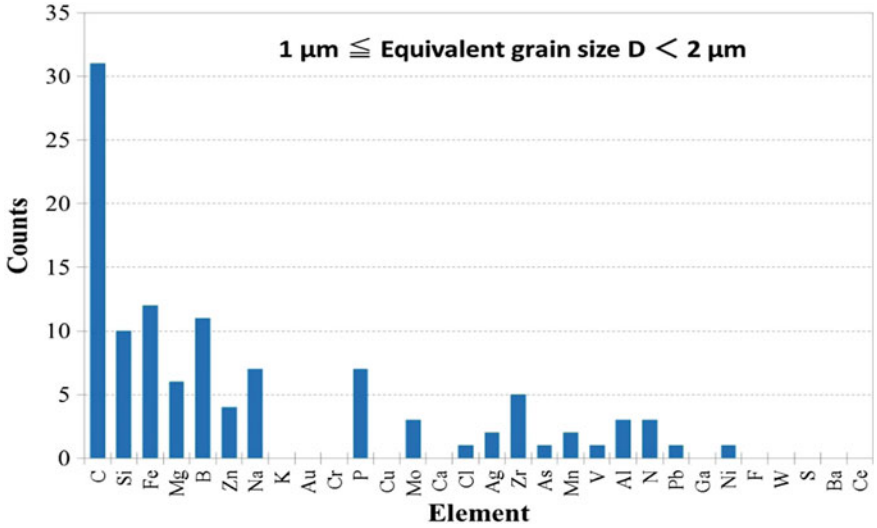

Fig. 17 Counts of particles greater than 1 μm and less than 2 μm in size for elemental signals obtained from plasma spectral emissions

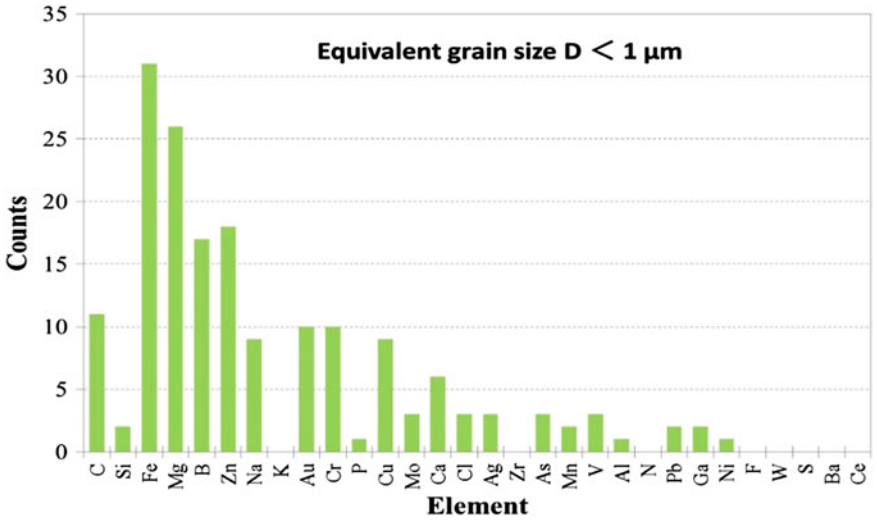

Fig. 18 Counts of particles less than 1 μm in size for elemental signals obtained from plasma spectral emissions

6 Conclusions

Suspended particle measurement was demonstrated using the He-MIP system with two-way spectroscopic analysis. The measurement results can be explained as follows. For the particles with a diameter of over 5 μm, silicon (Si) was the most often observed element followed by carbon (C) and potassium (K). For particles in the size range of 2–5 μm, Si was the most often observed element followed by C, K, zinc (Zn), iron (Fe), magnesium (Mg), and boron (B). In the size range of 1–2 μm, C was the most often observed element followed by Fe, B, Si, sodium (Na), phosphorus (P), Mg, zirconium (Zr), Zn, molybdenum (Mo), aluminum (Al), nitrogen (N), silver (Ag), and manganese (Mn). Nanoparticles with diameters in the sub-micrometer range were also detected. A large number of elements were detected, e.g., Fe, Mg, Zn, B, C, Au, chromium (Cr), Na, copper (Cu), calcium (Ca), Mo, chlorine (Cl), Ag, arsenic (As), vanadium (V), Si, Mn, lead (Pb), and gallium (Ga). The results obtained with the He-MIP system confirmed that the nanoparticles contained rare and precious metals that are not produced around the location where measurements were conducted. This indicates that many of the nanoparticles were either related to industrial activities or had been transported over several thousands of kilometers. While primary particles remain suspended for a few days and then diffuse over several kilometers, secondary particles remain in suspension for a few weeks to a few months. Thus, it was inferred that the measured nanoparticles had undergone reactions, in contrast to other micro-sized particles, over repeated cycles of aggregation and disaggregation. The above method allows the sizes and chemical compositions of the PM to be detected simultaneously; this may aid in gaining an understanding regarding the interactions between yellow sand and nanoparticles and the adhesive properties of carbonaceous materials in terms of nanoparticles deposited on micro-sized particles.

Acknowledgment We are grateful to JGC Catalysts and Chemicals Ltd. for providing us with silicon dioxide particles.

References

1. The National Institute for Environmental Studies (NIES) (2013) No. 345, 2013.2.21 <https://www.nies.go.jp/whatsnew/2013/20130221/20130221.html>
2. K. Hara, J. Homma, K. Tamura, M. Inoue, K. Karita, E. Yano, Decreasing trends of suspended particulate matter and PM2.5 concentrations in Tokyo, 1990-2010. J. Air Waste Manag. Assoc. **63**(6), 737–748 (2013)
3. J.H. Brown, K.M. Cook, F.G. Ney, T. Hatch, Influence of particle size upon the retention of particulate matter in the human lung. Am. J. Public Health Nations Health, 450–458 (1950)
4. U.P. Kodavanti, M.C. Schladweiler, A.D. Ledbetter, W.P. Watkinson, M.J. Campen, D.W. Winsett et al., The spontaneously hypertensive rat as a model of human cardiovascular disease: evidence of exacerbated cardiopulmonary injury and oxidative stress from inhaled emission particulate matter. Toxicol. Appl. Pharmacol. **164**(3), 250–263 (2000)

5. G.L. Squadrito, C. Rafael, B. Dellinger, W.A. Pryor, Quinoid redox cycling as a mechanism for sustained free radical generation by inhaled airborne particulate matter. Free Radical Biol. Med. **31**(9), 1132–1138 (2001)
6. A.P. Carll, N. Haykal-Coates, D.W. Winsett, W.H. Rowan III, M.S. Hazari, A.D. Ledbetter et al., Particulate matter inhalation exacerbates cardiopulmonary injury in a rat model of isoproterenol-induced cardiomyopathy. Inhalation Toxicol. **22**, 355–368 (2010)
7. S. Ikezawa, T. Ueda, Basic research on elemental and size analytical system for nano-sized suspended particulate matter using contactless optical measurement techniques. Int. J. Meas. Technol. Instrum. Eng. **3**(1), 16–27 (2013)
8. S. Ikezawa, M. Wakamatsu, T. Ueda, Optical analytical technique for carbonaceous particles using laser-induced electro-avalanche fluorescence and laser-induced incandescence. Sens. Mater. **25**(1), 57–77 (2013)
9. S. Ikezawa, M. Wakamatsu, T. Ueda, Development of semi-quantitative analytical system for metal nanoparticle ink using laser-induced breakdown spectroscopy. Int. J. Smart Sens. Intell. Syst. **5**(1), 215–232 (2012)
10. S. Ikezawa, M. Wakamatsu, T. Ueda, Diesel particulate analysis using SEM-EDX and laser-induced breakdown spectroscopy. Int. J. Smart Sens. Intell. Syst. **4**(2), 174–188 (2011)
11. S. Ikezawa, M. Wakamatsu, Y. L'vovich Zimin, J. Pawlat, T. Ueda, Development of carbonaceous particle size analyzer using laser-induced incandescence technology. IEEJ. Trans. Sens. Micromach. **131**(5), 171–177 (2011)
12. M. Wakamatsu, S. Ikezawa, T. Ueda, Particle element and size simultaneous measurement using LIBS. IEEJ Trans. Sens. Micromach. **127**(9), 397–402 (2007)
13. S. Ikezawa, J. Yamamoto, T. Ueda, Development of Helium-microwave-induced plasma-atomic emission spectroscopy system with two-way spectroscopic analysis, in *Proceedings of the 9th International Conference on Sensing Technology*, pp. 786–791 (2015)
14. J.D. Cobine, D.A. Wilbur, The electronic torch and related high frequency phenomena. J. Appl. Phys. **22**(6), 835–841 (1951)
15. M. Yamamoto, S. Murayama, UHF torch discharge as an excitation source. Spectrochim. Acta **25A**, 773–776 (1967)
16. H. Goto, K. Hirokawa, M. Suzuki, Spectrometric detection of various metals by high-frequency plasma torch. Fresenius' Zeitschrift fur analytische Chemie **225**(2), 130–137 (1967)
17. R. Nakashima, S. Sasaki, Determination of iron, manganese, and magnesium in high-purity molybdenum by high-frequency plasma torch emission spectrometry. Anal. Chim. Acta **85** (1), 75–81 (1976)
18. G. Cristescu, R. Grigorovici, Optische temperaturbestimmungen an der hochfrequenten fackelentladung. Naturwissenschaften **29**(38), 571–572 (1941)
19. C.I.M. Beenakker, A cavity for microwave-induced plasmas operated in helium and argon at atmospheric pressure. Spectrochimica Acta Part B **31**(8–9), 483–486 (1976)
20. A.J. McCormack, S.C. Tong, W.D. Cooke, Sensitive selective gas chromatography detector based on emission spectrometry of organic compounds. Anal. Chem. **37**(12), 1470–1476 (1965)
21. S. Greenfield, H.D. McGeachin, P.B. Smith, Plasma emission sources in analytical spectroscopy II. Talantn **22**, 553–562 (1975). Pergamon Press
22. H.A. Michelsen, Understanding and predicting the temporal response of laser-induced incandescence from carbonaceous particles. J. Chem. Phys. **118**, 7012–7045 (2003)
23. H. Takahara, M. Iwasaki, Y. Tanibata, Particle analyzer system based on microwave-induced plasma technology. IEEE Trans. Instrum. Meas. **44**(3), 819–823 (1995)

Real-Time HVAC Sensor Monitoring and Automatic Fault Detection System

Ying Guo, Josh Wall, Jiaming Li and Sam West

Abstract Real-time monitoring of heating, ventilation, and air conditioning (HVAC) systems is crucial to maintaining optimal performance such as providing thermal comfort and acceptable indoor air quality, guaranteeing energy saving, and assuring system reliability. In a realistic situation, HVAC systems can degrade in performance or even fail due to a variety of operational problems, such as stuck open or closed air dampers and water valves, supply or exhaust air fan faults, hot or chilled water pump faults, and inefficiencies in the way HVAC systems or pieces of equipemnt are controlled. This paper presents automatic fault detection techniques, as well as a key sensor sets selection approach that can help to maintain the performance of HVAC systems, and optimise fault detection results. One key step to make sure the approach succeeds is the sensor feature selection process. This paper implements the ensemble rapid centroid estimation (ERCE) as the data-driven sensor and feature selection algorithm, which is the core method to assure the automatic fault detection can function correctly. Instead of choosing sensors manually, ERCE method can automatically select representative features that are unique and relevant to the faults in a HVAC system. The methodology presented is implemented in real-world commercial buildings with experimental results showing that different types of faults are detected successfully.

1 Introduction

Heating, ventilation, and air conditioning (HVAC) systems are designed to provide thermal comfort and acceptable indoor air quality in a range of commercial buildings [1]. HVAC systems consume a large amount of energy throughout the world. For

Y. Guo (✉) · J. Li
Data61, CSIRO (Commonwealth Scientific and Industrial Research Organisation), Marsfield, NSW 2122, Australia
e-mail: ying.guo@csiro.au

J. Wall · S. West
Energy, CSIRO (Commonwealth Scientific and Industrial Research Organisation), Mayfield West, NSW 2304, Australia

S. Mukhopadhyay et al. (eds.), *Sensors for Everyday Life*, Smart Sensors, Measurement and Instrumentation 23, DOI 10.1007/978-3-319-47322-2_3

example, in Australia, it is estimated that the installed base of non-residential HVAC systems consumes 9 % of electricity produced, representing more than 3.6 % of Australia's greenhouse gas emissions; and they create more than 55 % of electrical peak demand in commercial business district (CBD) buildings [2]. The Australia government recognizes that large efficiency gains can be achieved through ongoing maintenance and more optimal operation of HVAC systems in existing building stock, and seeks to establish national system standards of documentation for design, installation, operation and maintenance of HVAC equipment/systems.

As well as the mechanical and electrical components and pieces of equipement, a HVAC system comprises some form of control logic to regulate the operation of the components and system as a whole. Usually a sensing device is used to compare the actual state (e.g. temperature or humidity) with a target state. Then the control logic draws a conclusion of what action has to be taken (e.g. provide more heating or cooling). Modern HVAC systems not only have fundamental sensors and actuating devices in addition to some basic control logic to perform their required function, but often include a more advanced building management and control system (BMCS) that provides multiple levels of control, data monitoring and analytics, user interfaces and even interfaces to other building energy systems.

A variety of sensing devices (such as temperature, humidity, velocity, or pressure) are installed in the HVAC systems. Sensors measure the actual value of a controlled variable such as temperature, humidity or flow and provides information to the BMCS. In a realistic situation, the building HVAC system can fail to satisfy performance expectations envisioned because of problems caused by improper installation of sensors, inadequate maintenance, and equipment or sensor failures. These problems, or "faults," include mechanical failures such as stuck, broken, or leaking valves, dampers, or actuators; control problems related to failed or drifting sensors, poor feedback loop tuning or incorrect sequencing logic; fouled heat exchangers; design errors; or inappropriate operator intervention. Such faults often go unnoticed for extended periods of time until the deterioration in performance becomes great enough to trigger comfort complaints, equipment failure or excessive power consumption.

Automated fault detection and sensor monitoring techniques for HVAC systems can identify these types of faults, with the potential energy-saving of avoiding these faults is estimated at 10–40% of HVAC system energy consumption, depending on the age and condition of the equipment, maintenance practices, climate, and building use [3–6]. By sensing and identifying minor problems before they become major problems, the useful service life of equipment can be extended. Also, repairs can be scheduled when convenient, avoiding downtime and overtime work. Depending on the building use, better control of the temperature, humidity, and ventilation rate of the occupied spaces can improve employee productivity, occupant comfort, and/or product quality control.

Most of the current commercially available solutions in HVAC sensor monitoring and fault detection systems use rule-based methods, where most solutions integrate and interpret incoming sensor data in accordance with the pre-determined set of rules, produce a risk profile, and initiate a response to a breach of these rules [7–10].

Another class of solutions use model-based methods, which use analytical mathematical models to compare and identify faults based on the sensor data sets [11–13].

Since every building is unique, it is not a simple task to set these rules or to generate these analytical mathematical models. In addition, the task of setting these thresholds used by such solutions to raise alarms is quite involved, and prone to producing false alarms. Hence, we developed a statistical machine learning algorithm based approach for the automated monitoring and fault detection in HVAC systems [14–17]. Our approach uses probabilistic models that are constructed on the probabilistic links between variables. Meanwhile, the probabilities are learnt from the stored sensor monitoring data sets. It is an ideal representation for combining prior knowledge and data, and can have much better flexibility and adaptability when applied to HVAC system.

For a complex HVAC system, the number of sensors and actuators can number in their thousands, and the selection of key sensors and actuators containing the main feature of the system and reflect to important system faults, is crucial for the success of our approach. This paper presents automated monitoring and fault detection techniques, and a key sensor sets selection approach to optimise the fault detection results. This methodology has been implemented and tested in real-world commercial buildings and experimental results show that different types of faults are detected successfully.

2 Overview on HVAC Systems, Sensor Monitoring and Fault Detection

A HVAC system normally includes central plant consisting of a hydronic heater, a hydronic chiller, a pump system, a valve system, a heat exchange system (which includes dedicated heated and chilled water coils), and an air distribution system for supplying occupants with conditioned air. It also includes a sensing system that includes a number of sensors located throughout the system, such as temperature, humidity, air velocity, volumetric flow, pressure, gas concentration, position, and occupancy detection sensors. The BMCS includes a computing system which interfaces with various sensory signals in the HVAC system. Using feedback from various components and sensors of the HVAC system, the environmental conditions for the inhabitancy or functional purpose of the building can be regulated. Figure 1 shows a simple schematic of a HVAC system. It consists of three main parts: air handling unit (AHU), the chiller (cooling) and boiler (heating) systems, and the control system. When a HVAC system is operational, a supply air fan as part of the AHU draws air from either outside, return air from the indoor area, or a mix of both, and past the cooling/heating coil heat exchange to achieve the desired temperature and humidity before being supplied to the indoor area. A trade off among exhaust, fresh and recirculation air is decided by the BMCS, based on the real-time sensor signals.

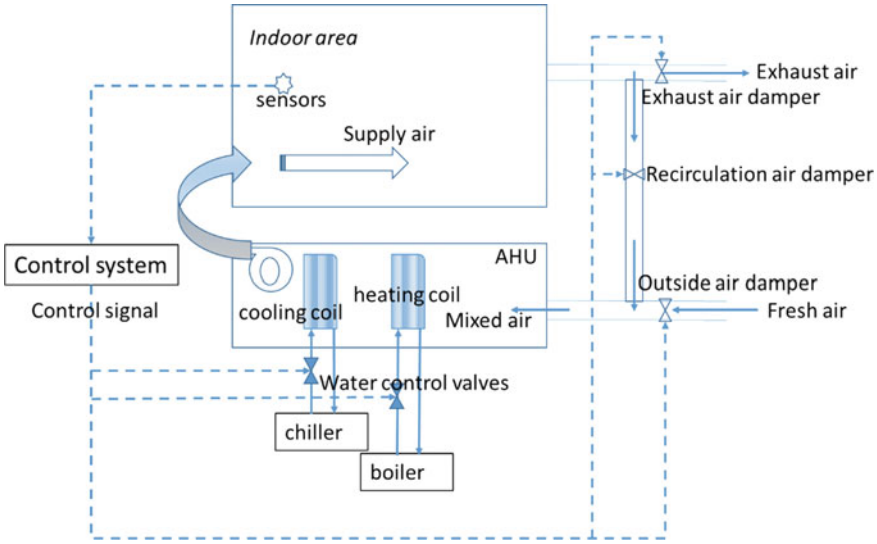

Fig. 1 General schematic diagram of a typical HVAC system

In a typical multiple storey commercial building, there can be tens to hundreds of zones. A large high rise commercial office building needs to be divided into multiple zones, in order to satisfy and maintain desired temperature and air quality conditions. Figure 2 shows a screenshot of a single zone from a BMCS interface. Some sensors such as the damper positions, valve positions are marked in the figure, while some other sensors' readings are listed in the top right corner, such as the supply air temperature set point, return fan speed set point, etc.

Thousands of sensors read real-time status of the equipment in a large HVAC system. The abundance of sensor data makes it difficult and expensive for human operators to continuously monitor the system and identify faults or operational inefficienies quickly.

One solution is to develop an intelligent automated sensor monitoring and fault detection system which can continuously monitor sensor data from various system components and identify unusual or inefficient behaviours.

Our approach is to use statistic machine learning algorithms based on key sensor selection and monitoring technique. Firstly, historical sensor data is logged during normal operation of the HVAC system. Secondly, suitable sensor combinations and their features are chosen to train HVAC system status models. These self-learnt models can build up the time-varying relationships between monitored sensors and/or sensor features of normal operation in a HVAC system.

Finally, ongoing real-time sensor data is read in, and the likelihood of this data matching with learnt historical behaviour indicates whether the HVAC system is running as normal or not. Figure 3 shows the overview of this real-time monitoring and fault detection approach.

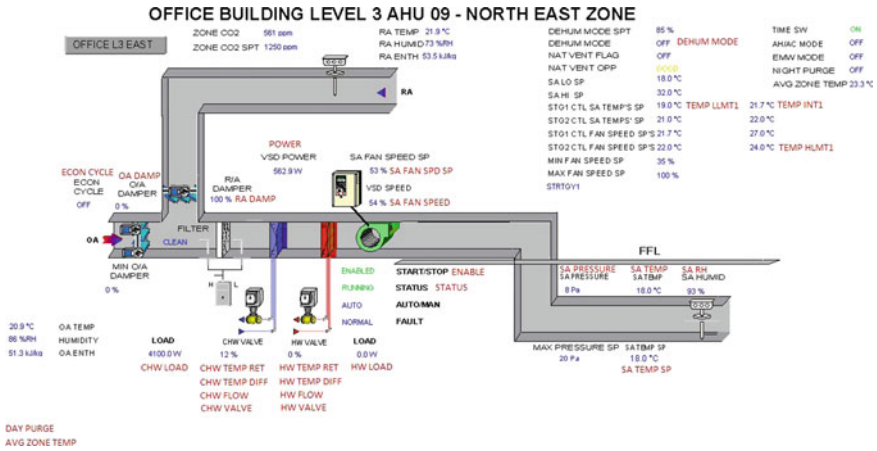

Fig. 2 The view of an Air Handling Unit (AHU) of a HVAC system from the Building Management & Control System interface.

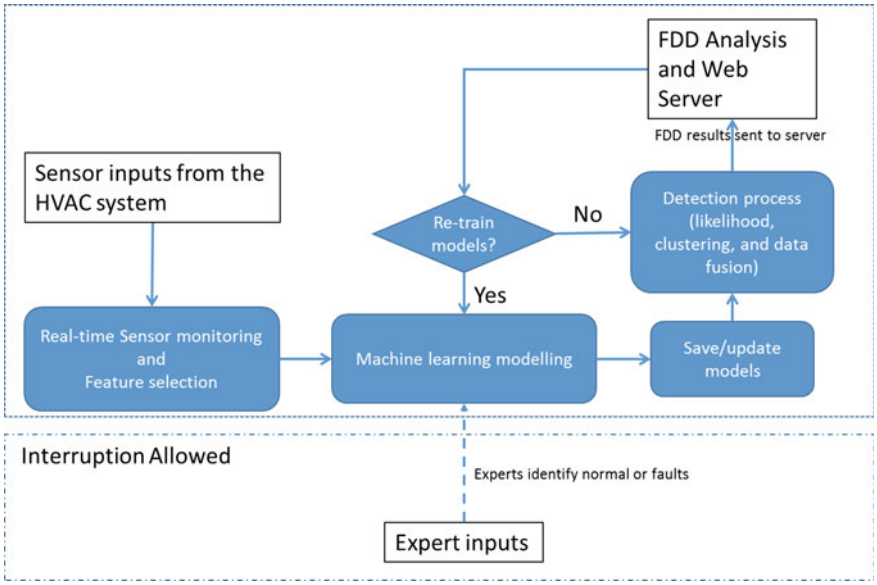

Fig. 3 Overview of the real-time sensor monitoring and fault detection approach

3 Sensor Monitoring and Fault Detection Approach in Detail

To overcome or ameliorate some of the limitations of existing fault detection methods, our approach is a combination of the state-of-the-art machine learning algorithms, including dynamic Bayesian networks (DBNs), Hidden Markov Models (HMMs), as well as swarm intelligence and consensus clustering methods. This section overviews our approach in details. Subsection A will present the key sensor selection for efficient real-time monitoring, the second subsection will show the architecture of the machine learning based methods, and the third subsection will list the main faults that are detected for HVAC systems.

Sensor and feature selection: As explained in Sect. 2, thousands of sensors are sending data to the database, and some of them are very crucial for proper system monitoring, modelling, and correct fault detection results. Proper sensor and/or sensor feature selection is essential for the whole model-based approach.

The aim of sensor selection is minimising redundancies between sensors so that the important system features are not undermined. HVAC system's performance may change dynamically depending on many conditions such as weather condition, seasonal condition, and occupancy of the building. Hence the sensors and their features need to be constantly monitored. Moreover, some sensors may contain little dynamic information, and can adversely affect the final model to an extent that some faults are missed. One way to decide the sensor combination is to depend on the HVAC technician's experience, but this is not an efficient way when it is applied to different structured buildings.

In our approach, we applied the rapid centroid estimation (RCE) as the key data-driven sensor and feature selection algorithm, which specifically performs well under varying seasonal conditions [18]. The feature extraction process from the sensor data involves statistical analysis [19–21] and dimensionality reduction [19, 21]. This is a crucial step, as inappropriate features could reduce the capability of the fault detection result.

We implemented an approach for sensor/feature selection using an ensemble clustering algorithm, which allows the natural recovery of clusters without having a priori knowledge regarding the optimum number of clusters. The method is Ensemble Rapid Centroid Estimation (ERCE) [22] based on the RCE algorithm [23]. ERCE exploits the fact that the quality of a clustering ensemble depends on the degree of diversity of the provided clusters. It shows better performance than conventional clustering algorithms such as complete linkage, ensemble k-means and ensemble fuzzy c-means.

The ERCE is a sequential process including clustering, fuzzification, and ensemble aggregation. In the clustering stage, various unique voronoi tessellations of the data is discovered; in the fuzzification stage, the voronoi tessellations are converted into fuzzy partitions; and in the ensemble aggregation stage, the final partition is recovered using the weighted fuzzy co-association-tree by hybrid

method [22, 23]. An overview of ERCE is presented as following, where a detailed description is available in [22, 23].

Given a data matrix Y,

$$Y = \left[y_1 \ldots y_j \ldots y_{n_j} \right],$$

where j denotes the observation index, n_j denotes the number of data (volume), and a particle position matrix X

$$X = [x_1 \ldots x_i \ldots x_{n_i}],$$

where i denotes the particle index, n_i denotes the number of particles, high dimensional voronoi tessellations are performed on the data such that each observation in Y is mapped to the nearest particle. In other words, each particle x_i governs a voronoi cell of the set C_i:

$$C_X = [C_1 \ldots C_i \ldots C_{n_i}], \ \varnothing \subseteq C_{1,\ldots,n_i}$$

which may contain empty sets. The clustered set,

$$C_X = C_{r,\ldots,n_c} \cap C_{i,\ldots,n_i}, \ \varnothing \subseteq C_X,$$

is the sets in $C_{i,\ldots,n_i}$ which partitions Y to n_c non-empty clusters.

The ERCE contains n_m swarms working in parallel such that

$$C_{\text{ERCE}} = \left\{ C_{X_1} \ldots C_{X_{n_m}} \right\}.$$

Using the concept of charged particles [22], the possibility of creating duplicate partitions is minimised. Ideally each C_{X_m} would then return a unique partition of the data such that

$$C_{X_1} \neq C_{X_2} \neq \ldots \neq C_{X_m},$$

where each partition C_{X_m} denotes an optimal partition returned by the mth swarm.

After the clustering process, the label matrix is fuzzified based on the distance between particles and data $D = D(X, Y)$. The fuzzy membership value for the jth observation with respect to the ith cluster, u_{ij}, can be calculated as followings:

$$u_{ij} = \frac{e^{-d_{ij}/(2\lambda_i)}}{\sum_{i=1}^{n_i} e^{-d_{ij}/(2\lambda_i)}} \tag{1}$$

where d_{ij} is the distance between the ith particle to the jth observation, and λ_i denotes the ith bandwidth of the cluster centre. Here $\lambda_{1,\ldots,n}$ can be optimised using a compromise between the partition's fuzzified dissimilarity

$$D_{ij} = u_{ij} d_{ij},$$

and Shannon entropy

$$H(u_{ij}) = -u_{ij} log\, u_{ij}$$

for each i and j. In other words, for each cluster, C_i, the optimum λ_i can be found by solving a convex optimisation problem:

$$\min_{s.t. \forall i, \lambda_i > 0} \|H - D\|^2, \tag{2}$$

which optimised λ_i for all cells, $i = 1, \ldots, n_i$, that the Gaussian probability distribution of the data governed in each corresponding voronoi cell is best described. In this approach, we use non-linear least square to optimise Eq. (2).

The examples in Sect. 4 will show that the feature selection is a powerful tool which can not only determine the feature cluster number, but also rank each feature within each cluster. The feature with the highest ranking in each cluster is then chosen as the key feature for fault detection.

Intelligent fault detection methods: The main processes of fault detection algorithm work as two steps, **training process step** (or called learning), and **fault detection step** (or called testing).

The historical sensor data which measures the **normal operation status** of the system was collected for **training process**. The intelligent sensor and feature selection process (as in Sect. 3A) is firstly implemented to prepare the training datasets. A statistical machine learning approach then learns the relativity between sensor measurements and system performance through these data. This approach uses probabilistic models that consist of variables and probabilistic links, which can denote the physical relationship between the sensor readings. Because of the complexity of the HVAC system, multiple models are learnt during the training process. The training process can be done during nights or weekends, and it normally takes about ten minutes over one week's datasets for one building. Because the system performance might change slowly because of season, weather, or other conditions, the training process can be repeated at a regular basis. For instance, the current training process can be done every week on tested buildings.

The **fault detection process** is to detect whether there is a fault in the system or not (binary classification problem). After the training process, a learnt normality model of the HVAC system can be used to detect system faults automatically. The collected sensor data is periodically detected with the models built based on the sensor features, and the similarity between current measurement and the historical feature is calculated. If the algorithm finds that the difference is obvious, a fault alarm is raised.

As the training process is a binary classification problem on time-series sensor features, we implemented a methodology which is based on a combination of the HMMs and the Support Vector Machines (SVM) algorithms [24]. HMMs are used

to denote the physical relationship between the sensor data in a dynamic system. Meanwhile, SVM can handle the nonlinear behavior very well, and requires small amount of training samples [16, 25, 26].

Furthermore, while the faults are detected as deviations in the normal operation, they can be the input data for training one or more of the fault detection models to learn patterns of faulty operation of the HVAC system wherein normal operation is detected as deviations in the faulty operation. As a dynamic process, the normality model and the fault models are adapted while the HVAC BMS dataset increases, hence the performance of real-time monitoring and fault detection improves.

The selected features of the sensor data are tested on different pre-trained HVAC normality models. Then the likelihood matrix is calculated as the indicator of the similarity between current sensor readings and normal system sensor readings. A couple of methodologies such as clustering and data fusion algorithms are also implemented as the final stage in the analysis of the likelihood matrix, and make the final decision as a sequence of binary value (e.g. Yes for normal, and No for abnormal). More details of the training methodologies are in [6, 15, 27].

Main faults for HVAC systems: It is reported that a few top listed faults are the major faults for HVAC systems [28]. Properly detect these faults can avoid up to 30% of energy waste in HVAC systems [29]. A short description of each fault is listed as following, and our sensor monitoring and fault detection approach will mainly focus on them.

- Hot water valve leaking or stuck: If the hot water valve stuck, hot air cannot be provided properly. If an internal valve leaks, it can be very difficult to troubleshoot and is often confused with a compressor that is not pumping to capacity. Both a leaking valve and a failing compressor have the same symptoms—both the heating and cooling capacity of the system are diminished. This is because the compressor continues to pump the air around and around inside the leaking valve.
- Supply-air fan belt slipping: The supply-air fan belt slipping can lead to the supply-air fan not running at setting speed.
- Outside air damper leaking or stuck: Damper not in the proper position. Outside air cannot circulate properly.
- Return air damper leaking or stuck: Return air cannot circulate properly.
- Individual zone temperature sensor fault: The temperature sensor reading in a zone is wrong.

4 Experimental Results

The intelligent real-time sensor monitoring and fault detection system has been tested on several buildings. In this section, we will show the results in one of these buildings, a large commercial building in Newcastle, Australia. The sensors are sending real-time data to the monitoring and fault detection system with a 1-min

interval which is typical of the resolution of trended sensor data from a BMS database [13]. Figure 4 shows an example of 15 sensors for an air handling unit (AHU).

Fault detection experimental results: During August and September 2013, 35 faults in four different fault types were generated for one AHU. Most faults last over six hours.

Table 1 listed the summary of the experimental results. Two types of faults, hot water valve stuck and individual zone air temperature failure are 100 % detected. But the success rate for the slipping supply-air fan belt fault is low. The lowest, though, is the return air/outdoor air damper point stuck fault, where only one third faults are detected. One of the main reasons is the measurement of the effects of each fault. For some faults, the return air qualities are affected directly, and corresponding sensor measurements are collected, such as return air temperature. For the return air damper, when it stuck at 70 %, the main facts that can change accordingly should be outdoor air fraction or indoor air CO2. These facts were not measured or saved in the datasets for modelling.

Sensor monitoring and feature selection results: We have also analyzed the sensitivity of the sensor features for the fault detection in HVAC systems. The parameters that we judge include the data sample rate, training window size,

Fig. 4 An example of the sensor data for an air handling unit in the Newcastle building

Table 1 Summary of fault detection experimental results

Generated faults in Aug/Sep 2013	Detected	Not detected	Detection rate (%)	Comments
Hot water valve stuck	11	0	100	
Return air/outdoor air damper stuck	3	6	33	For the return air damper, when it stuck at 70 %, the main facts that can change accordingly should be outdoor air fraction or indoor air CO2. These data were not measured or saved in the datasets hence not selected for modelling
Slipping supply-air fan belt fault	7	4	63.6	
Individual zone air temperature failure	4	0	100	

missing data tolerance, and minimal sensor subset performance. We chose the high frequency datasets for comparison experiments. The original dataset's sample rate is at one reading per 5 s, which is higher than most real HVAC systems. From the original trials, we observed that the training/testing window size is relevant to the sample rate. Hence we analyze the effects of the combination of these two parameters. We changed the sample rate to the following: 5 s, 20 s, 30 s, 40 s, 50 s, 60 s, 80 s, and 90 s. The training/testing window size changes between the following values: 10, 20, 50, 80, and 100. The combination of sensors is the same as default (six sensors).

Table 2 summarize the performance of the combination of these two parameters. Tick for successful detection, cross for unsuccessful detection. As we can see, when the sample rate increases, the window size need to be shorter to get the successful results. For the 90 s sample rate, the window size should be 20, which means that the training and testing data covers a 30–min period.

Table 2 Sensitivity of the sample rate versus window size of the sensor monitoring rate. Ticks for successful fault detection

Sample rate → / Window size ↓	5 s	20 s	30 s	40 s	50 s	60 s	80 s	90 s
10	×	×	×	×	×	×	×	×
20	×	×	×	√	√	√	√	√
50	×	×	√	√	√	√	√	×
80	×	√	√	×	×	×	×	×
100	√	√	×	×	×	×	×	×

Case study for sensor selection and its effect on fault detection: In this subsection, we will present one example to show the effect of sensor selection on fault detection results. The detail of this fault is as following:

- Date: 20/11/2009
- Location: All AHUs for Newcastle building
- Description: This is an actual fault that occurred when the chilled water system was under heavy load. Chiller 2 failed due to an overheating safety cut-out, and Chiller 1 failed to ramp up due to some misconfigured set-points, causing the chilled water temperature to rise to around 23 °, and in turn causing the chilled water valves on many zones (AHU9 included) to open up to near 100 %.

This type of faults is relatively common for HVAC systems, and can lead to a large waste of energy. The sensors that are selected to build the HMMs by the intelligent algorithms described in Sect. 3. A are: hot water valve sensor, chilled water valve sensor, supply air relative humidity sensor, supply air temperature sensor, return air relative humidity sensor, return air temperature sensor.

HMMs are trained on normal fault-free historical data. Then the real-time sensor monitoring data is fed in to calculate the likelihood. The lower the likelihood value, the higher possibility a fault exists.

The fault detection results are shown in Figs. 5 and 6. Figure 5 is the likelihood curves for the data on 20th Nov 2009, and the corresponding fault detection results after a classification and clustering process is shown in Fig. 6. It is clear that the fault, occurring after 12:00 pm, is convincingly detected, as shown by the likelihood curves.

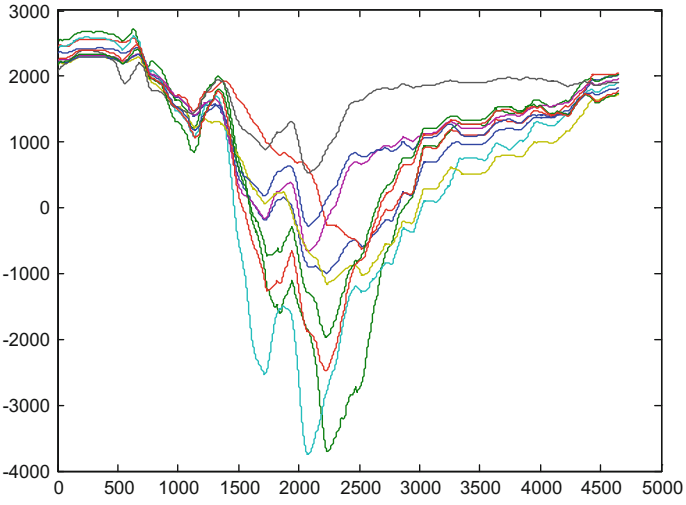

Fig. 5 A family of likelihood curves from a detected fault prior to clustering

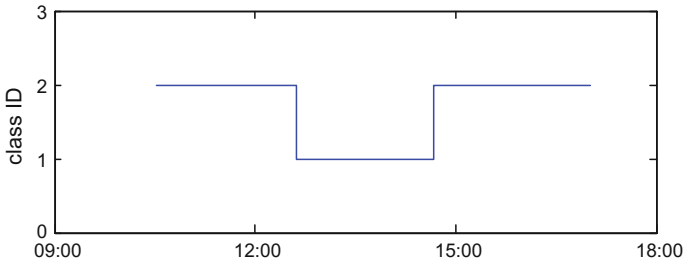

Fig. 6 Detection results for the fault after clustering and classification on the likelihood curves

If we manually remove one sensor feature from the optimized sensor combination, the fault would then become difficult to be detected. One example is shown in Figs. 7 and 8, for the same fault datasets—where the supply air temperature sensor data is not used for the HMM learning process. The likelihood curves drop to lower levels earlier that day, and the classified fault period is not correct. This example shows the importance of proper sensor features. Our approach can automatically select suitable sensor features rather than depend on domain expert, and assure successful detection results.

The above example proves that ERCE, as the data-driven sensor and feature selection algorithm, is crucial for the fault detection results. In fact, ERCE specifically performs well under varying seasonal conditions. The ERCE method selects features that are unique and relevant to the faults in the HVAC system. For different seasons, ERCE selects different combination of sensor data as the key features. Pattern for the winter dataset is different from the pattern for the summer dataset. The experimental results show that the sensor and feature selection process can ensure

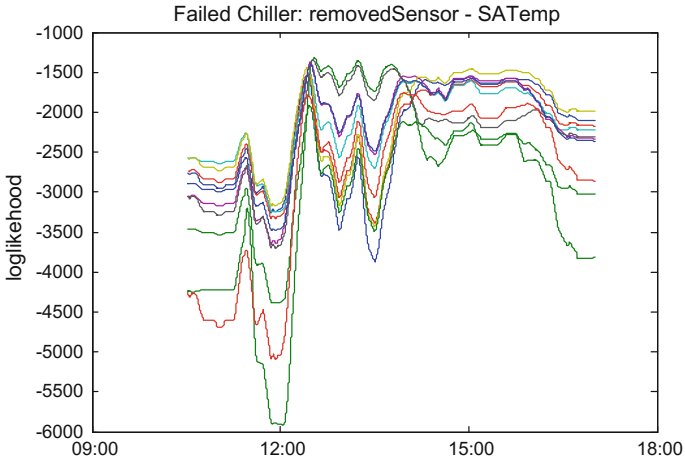

Fig. 7 A family of likelihood curves without using optimal sensor combination

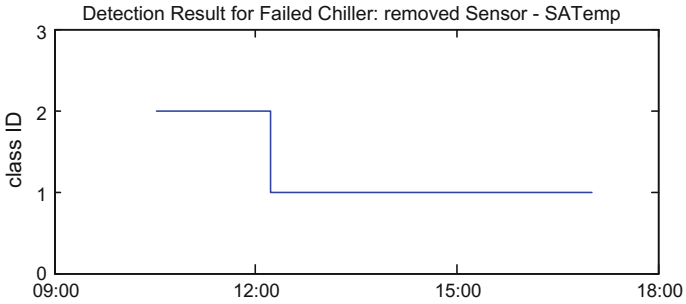

Fig. 8 Corresponding fault detection results

the success of the fault detection results for the HVAC system. It is proven that the ERCE method can improve the fault detection results, comparing to the results based on other feature selection clustering method, such as EAC k-means [18].

5 Conclusion and Discussion

This paper presents dynamic, machine-learning based techniques for automated sensor monitoring and fault detection in HVAC systems. This approach can be seen as a good combination of model-based methods and data-based methods. The main approaches are based on graphical modelling techniques such as HMMs, which encode probabilistic relationships among variables of interest. This approach is an ideal representation for combining prior knowledge and data. It does not need very detailed understanding of the physical system as in model-based approaches. It also does not need huge data sets as in the black-box approaches. Comparing with pure model-based or data-based approaches, it combines the strengths in both areas and can overcome their shortfalls by balancing the dependency on physical models and datasets.

One critical step to ensure the approach succeeds is that of the sensor feature selection process. This paper implements the ensemble rapid centroid estimation (ERCE) as the data-driven sensor and feature selection algorithm, which is the core method to ensure automated fault detection is achieved. Instead of choosing sensors manually, the ERCE method can automatically select representative features that are unique and relevant to the faults in the HVAC system. It also discards redundant sensors that are less crucial or have less system features. The experimental results show that this sensor and feature selection process can ensure the success of the fault detection results for HVAC systems. It is proven that the ERCE method can improve the fault detection results, comparing to the results based on other feature selection clustering methods, such as EAC k-means.

Planned future work includes comparing the selected sensor features from different buildings, and identifing the common features for multiple types of buildings.

By improving the generalizability of the sensor monitoring and fault detection approach, less modelling time can be saved, and more improvements in performance, such as fault detection accuracy, can be achieved.

References

1. M. Rolloos, HVAC systems and indoor air quality. Indoor Built Environ. **2**(4), 204–212 (1993)
2. A.G. Department of industry, innovation and science, in *Heating, Ventilation and Air-conditioning* (2016). http://industry.gov.au/Energy/EnergyEfficiency/Non-residentialBuildings/HVAC/Pages/default.aspx
3. K.W. Roth, J. Dieckmann, S.D. Hamilton, W. Goetzler, in *Energy Consumption Characteristics of Commercial Building HVAC Systems Volume III : Energy Savings Potential* (2002)
4. V. Vakiloroaya, B. Samali, A. Fakhar, K. Pishghadam, A review of different strategies for HVAC energy saving. Energy Convers. Manag. **77**, 738–754 (2014)
5. N. Gas, *Renewable Energy Annual 2002*," vol. 0603 (2002)
6. J. Wall, Y. Guo, J. Li, S. West, A dynamic machine learning-based technique for automated fault detection in HVAC systems, in *2011 ASHRAE Annual Conference* (2011)
7. T.M. Rossi, J.E. Braun, A statistical, rule-based fault detection and diagnostic method for vapor compression air conditioners. HVAC&R Res. **3**(1), 19–37 (1997)
8. J. Schein, S. Bushby, N. Castro, J. House, A rule-based fault detection method for air handling units. Energy Build. **38**, 1485–1492 (2006)
9. P.P. Angelov, R.A. Buswell, V.I. Hanby, J.A. Wright, A methodology for modeling HVAC components using evolving fuzzy rules, in *2000 26th Annual Conference* of the *IEEE Industrial* Electronics *Society IECON 2000*, vol. 1, no. 1, (2000), pp. 247–252
10. Y. Song, Y. Akashi, J.-J. Yee, A development of easy-to-use tool for fault detection and diagnosis in building air-conditioning systems. Energy Build. **40**(2), 71–82 (2008)
11. B. Yu, D.H.C. Van Paassen, S. Riahy, General modeling for model-based FDD on building HVAC system. Simul. Pract. Theory **9**(6–8), 387–397 (2002)
12. J. Liang, R. Du, Model-based fault detection and diagnosis of HVAC systems using support vector machine method. Int. J. Refrig. **30**(6), 1104–1114 (2007)
13. H. Yoshida, S. Kumar, ARX and AFMM model-based on-line real-time data base diagnosis of sudden fault in AHU of VAV system. Energy Convers. Manag. **40**(11), 1191–1206 (1999)
14. D. Dehestani, S. Su, H. Nguyen, Y. Guo, J. Wall, F. Eftekhari, Comprehensive sensitivity analysis of heat ventilating and air conditioning (HVAC) system based on neural network model, in *10th International Conference on Healthy Buildings, Brisbane, Australia*, 8–12 July 2012, pp. 6–11
15. Y. Guo, J. Li, S. West, J. Wall, G. Platt, System and method for detecting and/or diagnosing faults in multi-variable systems, US20120185728 A1 (2012)
16. Y. Guo, J. Wall, J. Li, S. West, A machine learning approach for fault detection in multi-variable systems, in *The Tenth International Conference on Autonomous Agents and Multiagent Systems*, (2011), pp. 23–30
17. Y. Guo, D. Dehestani, J. Li, J. Wall, S. West, S. Su, Intelligent outlier detection for HVAC system fault detection, in *10th International Conference on Healthy Buildings, Brisbane, Australia,* 8–12 July, 2012, no. Vapnic (1995), p. 2
18. M. Yuwono, Y. Guo, J. Wall, J. Li, S. West, G. Platt, S.W. Su, Unsupervised feature selection using swarm intelligence and consensus clustering for automatic fault detection and diagnosis in Heating Ventilation and Air Conditioning systems. Appl. Soft Comput. **34**, 402–425 (2015)

19. Z. Yu, F. Haghighat, B.C.M. Fung, L. Zhou, A novel methodology for knowledge discovery through mining associations between building operational data. Energy Build. **47**, 430–440 (2012)
20. A. Kusiak, M. Li, F. Tang, Modeling and optimization of HVAC energy consumption. Appl. Energy **87**(10), 3092–3102 (2010)
21. N. Gaitani, C. Lehmann, M. Santamouris, G. Mihalakakou, P. Patargias, Using principal component and cluster analysis in the heating evaluation of the school building sector. Appl. Energy **87**(6), 2079–2086 (2010)
22. M. Yuwono, S.W. Sir, B.D. Moulton, Y. Guo, H.T. Nguyen, An algorithm for scalable clustering: ensemble rapid centroid estimation, in *Proceedings of the 2014 IEEE Congress on Evolutionary Computation, CEC 2014*, (2014), pp. 1250–1257
23. M. Yuwono, S.W. Su, B.D. Moulton, H.T. Nguyen, Data clustering using variants of rapid centroid estimation. IEEE Trans. Evol. Comput. **18**(3), 366–377 (2014)
24. M.A. Hearst, S.T. Dumais, E. Osman, J. Platt, B. Scholkopf, Support vector machines. IEEE Intell. Syst. **13**(4), 18–28 (1998)
25. J. Li, Y. Guo, J. Wall, S. West, Fault Detection for HVAC Systems, in *10th International Conference on Healthy Buildings, Brisbane, Australia,* 8–12 July 2012, pp. 12–15
26. D. Dehestani, F. Eftekhari, Y. Guo, S. Ling, S. Su, H. Nguyen, Online support vector machine application for model based fault detection and isolation of HVAC system. Int. J. Mach. Learn. Comput. **1**(1), 66–72 (2011)
27. S.R. West, Y. Guo, X.R. Wang, J. Wall, Automated fault detection and diagnosis of HVAC subsystems using statistical machine learning, in *12th International Conference of the International Building Performance Simulation Association* (2011)
28. S. Katipamula, M.R. Brambley, Methods for fault detection, diagnostics, and prognostics for building systems—A review, Part I. HVAC&R Res. **11**(1), 3–26 (2005)
29. EIA, International Energy Outlook 2009 (2009)

High Sensitivity Optical Structures for Relative Humidity Sensing

Joaquin Ascorbe, Jesus Corres, Francisco J. Arregui, Ignacio R. Matias and Subhas Chandra Mukhopadhyay

Abstract This chapter is focused in the different optical structures and materials that have been used for the development of optical fiber humidity sensors. First, we will start with a short introduction of what relative humidity is, and why it has been extensively investigated. We will make also a brief summary of the different options that have been developed by now, showing the evolution of this research field. Then we will look more closely at the most used structures, the most common materials and the devices having greater sensitivity and resolution.

1 Introduction

Humidity constitutes one of the most commonly required physical parameters to be measured. Humidity sensing and control is really important in several application fields, such as semiconductor and electronic manufacturing, food, textile, wood or paper industries, conservation and storage, chemical, biological and pharmacological industry among others.

Different terms related to humidity measurement can be found in the literature and they are commented here before starting. While moisture refers to the water in liquid form that may be present in solid materials, humidity is a measure of water in gaseous state present in the environment and it can be measured as absolute humidity (kg of water vapour per kg of dry air) or as relative humidity. The relative humidity of an air mass is the ratio of water vapour contained and the maximum steam content that it would have if it were completely saturated. For higher temperatures the air has more capacity of containing water so for a given absolute humidity at certain temperature, the relative humidity will decrease if the temper-

J. Ascorbe · J. Corres (✉) · F.J. Arregui · I.R. Matias · S.C. Mukhopadhyay
Institute of Smart Cities, Public University of Navarra, Campus Arrosadia, 31006 Pamplona, Spain
e-mail: jmcorres@unavarra.es

S.C. Mukhopadhyay
Macquarie University, 2109 Sydney, NSW, Australia

S. Mukhopadhyay et al. (eds.), *Sensors for Everyday Life*, Smart Sensors, Measurement and Instrumentation 23, DOI 10.1007/978-3-319-47322-2_4

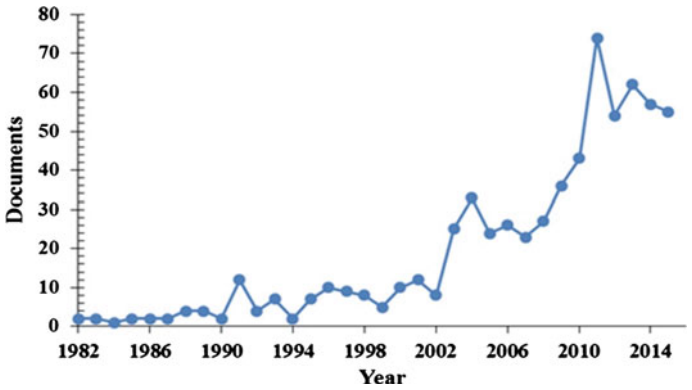

Fig. 1 Evolution of the optical fiber humidity sensors contributions (*Source* Scopus)

ature is increased [1]. In this chapter we will always refer to relative humidity although sometimes it will be mentioned only as humidity.

In Fig. 1, it is shown the evolution of the contributions found in Scopus, related to optical fiber humidity sensors, from 1982 to 2015. As it can be seen, the number of contributions has increased continuously since 1999 keeping today a number worthy of consideration.

This increasing interest in optical fiber humidity sensors is due to the intrinsic advantages of using optical fibers as the sensing structure. These advantages include: small size, lightness, the possibility of working on flammable environments, the ability of working on greater pressure and temperature ranges and, the most important, their electromagnetic immunity.

2 Materials

Several materials have been used for the development of optical fiber humidity sensors, from polymers to metal oxides, from hydrophilic to hydrophobic materials. Hydrophobic materials, which are composed of non-polar molecules, present greater contact angles than the hydrophilic ones. Both of them have been used for the development of humidity sensors [2, 3].

However, for the development of optical fiber sensors, there are other behaviors which provide better performance from an optical point of view. These behaviors are called swelling and adsorption. Swelling is a process whereby a material increases in size when subjected to increasing humidity. This increased thickness provokes that the light traveling through the core of an optical fiber found a greater effective refractive index, which will affect at the transmitted light. The other physical phenomena, adsorption, is defined by the IUPAC as an increase in the concentration of a dissolved substance at the interface of a condensed and a liquid phase due to the operation of surface forces. Adsorption can also occur at the interface of a condensed and a gaseous phase [4]. For humidity measurements, the

result of adsorption is the generation of a thin film of water over the surface of the material. Swelling is common for some polymers while adsorption is the predominant effect in metal oxides.

It does not mean that the previously commented physical phenomenon are the only ones that can be used for measuring relative humidity by an optical set-up. There are other phenomenon used for humidity sensing as it can be fluorescence [5], but in this chapter we will focus on evanescent wave sensors, fiber gratings, sensors based on Lossy Mode Resonances and Fabry-Pèrot interferometers, with coatings based on adsorption and swelling.

3 Conventional Methods

There are conventional methods for measuring the relative humidity and we will make a brief overview of those methods. Different physical phenomena have been used for this methods and they can be classified on these categories:

- Wet and dry bulb psychrometer
- Mechanical
- Electrical
- Infrared (IR) optical absorption hygrometer

The wet and dry bulb psychrometer consists of two thermometers, one of which is covered with a damp wick (wet bulb). The difference between the measured temperatures is due to water evaporation and latent heat transfer [1, 6] and the relative humidity can be calculated with the psychrometric diagram.

Mechanical humidity sensors are based on the expansion/contraction of certain materials. A well-known humidity sensor based on mechanical behavior is the mechanical hygrometer. Common materials used include synthetic fibres and human hair. The first mechanical hygrometers were formed by linking the material with a weak tension by a spring, and a mechanical linkage operates a needle. Other mechanical hygrometers were formed by linking the material to strain gauges or other devices to measure the displacement caused by the change in humidity [6].

Resistive and capacitive-type humidity sensors are included into the electrical category. Resistive-type humidity sensors are based on changes on the electrical resistivity of some materials as conductive polymers, semiconductors or composites. This behavior has been explained in [7–9] by the water adsorbed on the oxide surface in the molecular and hydroxyl forms. Furthermore, Boyle and Jones [7] established that water demonstrates donor properties at adsorption in the molecular form while it shows acceptor properties in the hydroxyl form [10]. In the same way capacitive-type sensors are based on the dielectric changes of a thin film. Common materials used for capacitive sensors are ceramics like alumina [11] and polymers [12]. The capacitive- and resistive-based humidity sensors are the most commonly used, with capacitive-based sensors dominating and making up nearly 75 % of the commercial humidity sensor market [13].

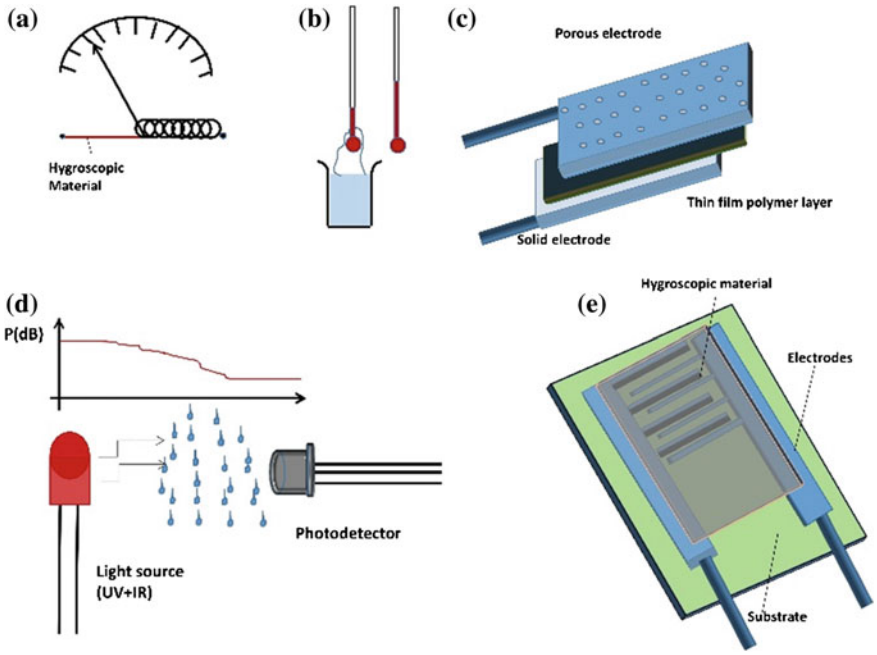

Fig. 2 **a** Mechanical humidity sensor, **b** wet and dry bulb psychrometer, **c** capacitive humidity sensor, **d** IR optical absorption method and **e** resistive humidity sensor

Finally, the infrared (IR) optical absorption hygrometer is based on the optical absorption of the water vapor. It works by emitting light at two different wavelengths. One of them has negligible absorption and it is used as reference. The transmission ratio between those two wavelengths provides a direct measurement of water absorption, making this technique insensitive to contaminants [6] (Fig. 2).

4 Optical Fiber Humidity Sensors

There are many ways of measuring the relative humidity by means of optical set-ups, one of them has been mentioned before. Here, we are going to explain in detail those based on optical fibers and most specifically, those involving coatings onto an optical fiber. Among those devices we will focus on Fabry-Pèrot interferometers and Lossy Mode Resonances based devices although some other structures will be mentioned to have a sight of the differences between them and the evolution that optical fiber humidity sensors have suffered. Optical fiber humidity sensors (OFHS) can be classified by the physical phenomena they used as:

- Evanescent wave sensors

  - Optical absorption
  - Change on the refractive index
  - Lossy mode resonances (LMRs)
- Fluorescence sensors
- Interferometric sensors
- Fiber gratings

4.1 Evanescent Wave Sensors

First of all, we are going to introduce the earlier optical fiber humidity sensors, classified as evanescent wave (EW) sensors. The evanescent field is created as a result of the standing wave generated by the interference between the incident and the reflected signals at the core/cladding interface, inside an optical fiber, due to the Total Internal Reflection (TIR) phenomena [6]. The amplitude of the evanescent field decays exponentially with the distance away from the core/cladding interface and it can be calculated as:

$$E(z) = E_0 \exp(z/d_p) \tag{1}$$

where the penetration depth (dp) is defined as the depth at which the amplitude of the evanescent field, E, has decayed to 1/e of the initial value E0 at the core/cladding interface and this is given by

$$d_p = \frac{\lambda}{2\pi n_{core}\left[\left(\sin^2\theta - \left(n_{clad}/n_{core}\right)^2\right]^{1/2}\right.} \tag{2}$$

where λ is the wavelength of the propagating signal in the optical fiber, θ is the angle of incidence normal at the interface, ncore and nclad are the refractive indices of the fiber core and cladding, respectively.

There are two different approaches: the first one based on changes on the optical absorption and the second one based on changes of the refractive index. The main difference between these two methods is that optical absorption causes changes at a certain wavelength or in a wavelength range and when changing the refractive index there are changes at all wavelengths. Earlier optical fiber humidity sensors were developed by the first method since 1985 using, for example, cobalt chloride [14] or other chemical reagents immobilized in a polymeric matrix, and cladding removed optical fibers. The problem with these sensors is that the evanescent tail has only a small fraction of power, and a long portion of fiber must be coated to have a detectable change at the output end [15]. For that reason some other structures have been developed to increase the amplitude of the evanescent field and consequently the sensitivity of the device. For example U-bent fibers [15] or porous

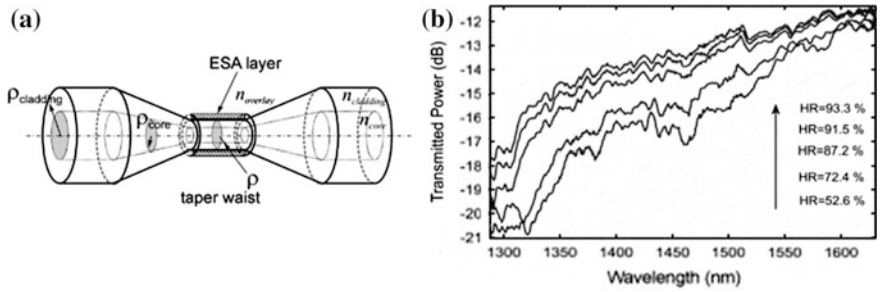

Fig. 3 **a** Humidity sensor structure. Taper profile with ESA overlay and **b** Optical output spectrum dependence with respect to the relative humidity with 23 bilayers deposited. Tapered fiber waist diameter: 20 μm. Taper length: 2.2 mm. Nanofilm: [PDDA+/Poly-R−]. Reprinted from Sens. Actuators B, vol. 122, no 2, Corres, J.M., Arregui, F.J., and Matías, I.R., Sensitivity optimization of tapered optical fiber humidity sensors by means of tuning the thickness of nanostructured sensitive coatings, pp. 442–449, (2007), with permission from Elsevier

fibers [16] have been used to develop more sensitive OFHS based on optical absorption.

Several different approaches have been followed to develop evanescent wave sensors by changing the refractive index of the coating. Removed plastic cladding optical fibers [17], tapered single mode [18, 19] optical fibers or D-shape optical fibers can be used for this kind of devices. Common materials used for these OFHS are hydrogels as poly-hydroxyethyl methacrylate, poly-acrylamide, poly-N-vinyl pyrrolidinone and agarose [17, 18]. As it can be seen in Fig. 3, extracted from [19] changes are produced at all wavelengths with this method.

4.2 Lossy Mode Resonances

Optical fiber sensors based on Lossy Mode Resonances are a special case of evanescent wave sensors and, more specifically, a special case of EW sensors based on changes of the refractive index. Here, the material chosen for coating the optical fiber has to meet two conditions: to be sensitive to the physical parameter for what the sensor is developed and to meet the requirements to generate LMRs. This method, which is included in the wavelength based techniques, overcome the limitations of the previous EW methods, such as external noises or power fluctuations [20].

Lossy Mode Resonances are a physical phenomenon which consists on the absorption of the light at certain wavelength. It is important to remark that this absorbed light is not related to the absorbed light mentioned before. For EW sensors based on optical absorption, the absorption of the light is produced when the coating is subjected to the physical parameter to be measured. However, once the LMR has been generated, the optical absorption occurs without need of an external

parameter. The LMR will be located at different wavelengths depending on the refractive index of the surrounding medium. This is due to coupling between a waveguide mode and a particular lossy mode of the coating, which depends on two conditions: there is a considerable overlap between the mode fields, and the phase-matching condition (i.e. the equality of real parts of propagation constants) is sufficiently satisfied [21–23]. LMR occurs when the real part of the thin-film permittivity is positive and higher in magnitude than both its own imaginary part and permittivity of the material surrounding the thin-film [23].

The wavelength where this absorption occurs depends on the refractive index of the material, the thickness of the coating and the refractive index of the surrounding medium. Several materials have been proved as LMR generators as ITO [23], In_2O_3 [24], SnO_2 [25], PAH/PAA [26], TiO_2/PSS [27, 28] …

It exists other kind of resonances called Surface Plasmon Resonances (SPRs) which are generated by a few materials, generally metallic materials like silver and gold, and they occur when the real part of the thin-film permittivity is negative and higher in magnitude than both its own imaginary part and the permittivity of the material surrounding the thin-film [22]. As contrast to LMRs, in SPRs the collective coherent oscillations of free electrons in the conduction band of a metal is excited by the interactive electromagnetic field at a metal/dielectric interface [29, 30]. There is also a third type of resonances known as Long Surface Plasmon Resonances (LSPRs). The spectral location of the LSPR is sensitive to the shape, size, and composition of the nanostructure, as well as on the optical properties of the surrounding dielectric [31]. Main differences between LMRs and SPRs are resumed in Table 1 and a schema of how and when LMRs are generated is shown in Fig. 4.

4.2.1 Plastic Cladding Removed Multimode Optical Fiber

As it has been mentioned before, metallic oxides are good candidates for the generation of LMRs and they are also a good choice for humidity sensing because of their absorption capability. Most of the research done for LMRs has been developed coating a 200/225 μm core/cladding plastic cladding optical fiber. This optical fiber allows to transmit light in the range 400–2200 nm and the cladding can be removed by simple chemical methods. First LMR devices were developed by coating an optical fiber with ITO and they were characterized as humidity sensors [32] and also as refractometers [33]. Then a typical transmission set-up, Fig. 5, was used while the optical fiber was subjected to changes on the relative humidity and

Table 1 Comparison between lossy mode resonances and surface plasmon resonances

	LMRs	SPRs
Number of absorption peaks	>1	1
Wavelength	Tunable	Fixed
Number of available materials	Many	Few
Visible for both TE and TM polarized light	Yes	No

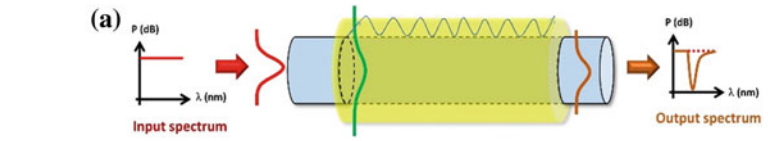

(b)

TYPE OF RESONANCE	$\hat{\varepsilon}$ CONDITIONS	n,k CONDITIONS $\forall\, n>0, k>0$
LRSEP Long Range Surface Exciton-Polariton	$\varepsilon_2' \approx 0$ $\varepsilon_2'' \gg 0$	$n_2 \approx k_2$ $n_2, k_2 \gg 0$
SPR Surface Plasmon Resonance	$\varepsilon_2' < 0$ $\lvert\varepsilon_2'\rvert > \lvert\varepsilon_2''\rvert$ $\lvert\varepsilon_2'\rvert > \lvert\varepsilon_3'\rvert$	$k_2 > (\sqrt{2}+1)n_2$ $k_2^2 - n_2^2 > 1.45^2$
LMR Lossy Mode Resonance	$\varepsilon_2' > 0$ $\lvert\varepsilon_2'\rvert > \lvert\varepsilon_2''\rvert$ $\lvert\varepsilon_2'\rvert > \lvert\varepsilon_3'\rvert$	$k_2 < (\sqrt{2}-1)n_2$ $n_2^2 - k_2^2 > 1.45^2$

(c)

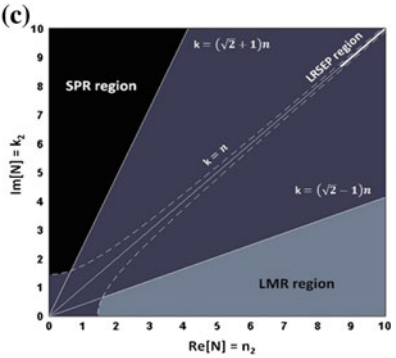

Fig. 4 **a** Scheme of lossy mode resonances generation, **b** dielectric and refractive index conditions for LRSEP, SPR and LMR generation and **c** graphic representation of previously mentioned conditions

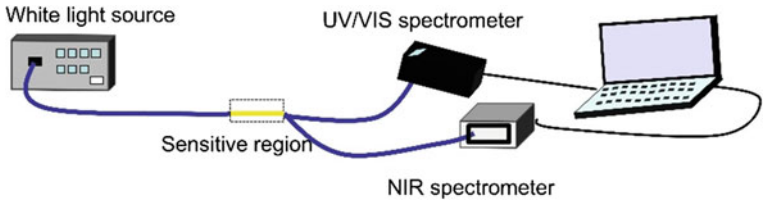

Fig. 5 Optical fiber transmission setup

the wavelength shift of the LMR was observed. A SEM image of the coating can be seen in Fig. 6.

The wavelength shift of the LMR is caused by changes on the refractive index (RI) of the coating. Due to the absorbed water on the ITO surface the effective refractive index increases, and as the LMR wavelength depends on that, its wavelength position shifts to greater wavelengths. It seems to be a general trend that for an increase of the refractive index there is a redshift of the LMR, although there might be exceptions. Main contribution for these OFHS is due to changes on the RI of the coating, although it may be considered that the RI of the surrounding medium is also altered, it is negligible by comparison. Figure 7 shows the dynamic behaviour of these kind of devices.

The previous situation uses the dependence of LMRs on the RI of the coating. But OFHS can be also developed taking advantage of the dependence of LMRs on

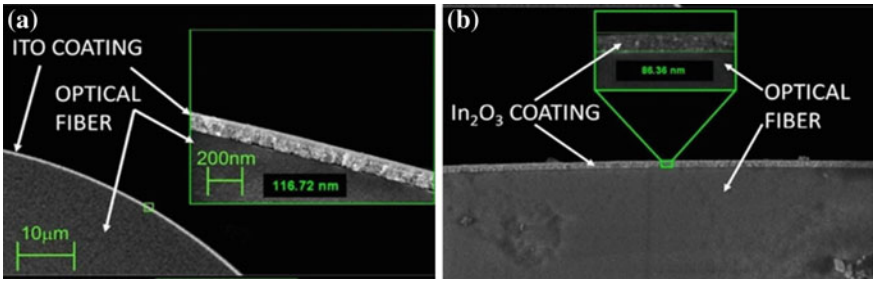

Fig. 6 SEM image of **a** ITO coating and **b** In_2O_3 coating deposited onto the optical fiber core. Reprinted from Lossy mode resonances toward the fabrication of optical fiber humidity sensors, P. Sanchez et al., 2012, Meas. Sci. Technol. 23 014002 doi:10.1088/0957-0233/23/1/014002 with permission from IOP Publishing

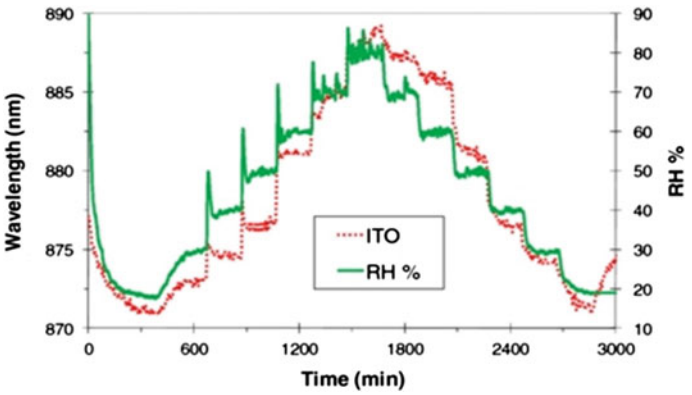

Fig. 7 Dynamical response of ITO sensors from 20 to 80 % of RH. Reprinted from Lossy mode resonances toward the fabrication of optical fiber humidity sensors, P. Sanchez et al., 2012, Meas. Sci. Technol. 23 014002 doi:10.1088/0957-0233/23/1/014002 with permission from IOP Publishing

the RI of the surrounding medium. For that purpose, some devices have been developed using ITO for the generation of LMRs and using other materials like PAH/PAA as the sensitive layer [20, 28]. These devices combine the high sensitivity of LMRs to changes on the external RI with the greater changes on the RI of PAH/PAA when subjected to high humidity, improving the sensitivity of the device to changes on the relative humidity. This combination of two different layers allows to have the LMR located at greater wavelengths, which also enhances the sensitivity of the device. Figure 8 shows the absorption spectrum for this device at two different relative humidity values and its dynamic response.

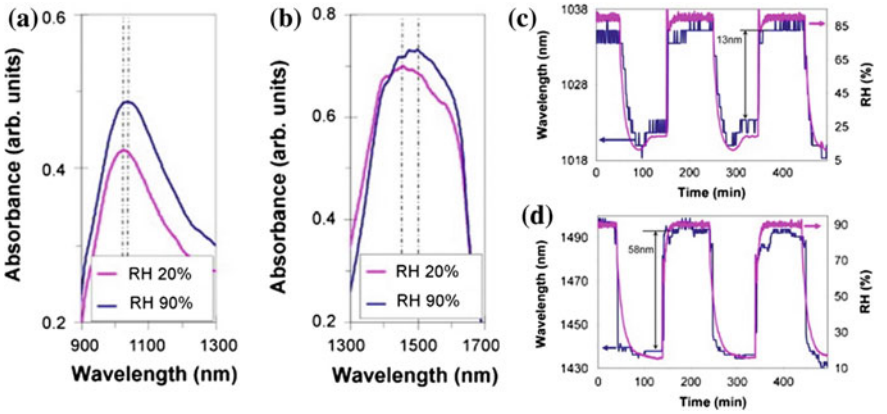

Fig. 8 Spectral response of the **a** non-tuned and **b** tuned sensors for 20 and 90 % RH and dynamical response of the sensors to changes in the RH of the external medium **c** non-tuned sensor (20 PAH/PAA bilayers) and **d** tuned sensor (100 PAH/PAA bilayers). Reprinted from Sens. Actuators B, vol. 146, no 1, Zamarreño, C.R., Hernaez, M., Del Villar, I., Matias, I.R., and Arregui, F.J., Tunable humidity sensor based on ITO-coated optical fiber, pp. 414–417, (2010), with permission from Elsevier and IOP Publishing

4.2.2 Single Mode Optical Fiber

Standard SMFs has some advantages respect plastic cladding multimode optical fiber, and one of them is its price. On the other hand it is more difficult to make a SMF sensitive to external parameters because its cladding it is made of silica instead of plastic. But there are some methods to obtain access to the evanescent field of a SMF. One of these methods consists on tapering the SMF by applying heat and stretching. The heat can be applied by means of a flame or by an electric arc [34–36]. When a single-mode fiber (SMF) is tapered, the core/cladding interface is redefined in such way that the SMF in the tapered region acts as a multimode fiber, sustaining several LP0 m modes. In this case, the light propagation in the waist of the taper extends to the whole fiber, which plays the role of the new core, and the new cladding is the external medium; this fact eases the interaction of the evanescent field with the outer medium so that small changes of the outer medium influence the transmitted optical power. Some OFHSs have been developed using this structure [19, 34–36], most of them based on optical power measurements [19, 35] and others based on resonances [36]. As it can be seen in Fig. 9 from [36], a tapered SMF can be sensitive to external parameters if coated with the appropriate material, indium tin oxide for this case.

There are other ways to gain access to the evanescent field of a SMF as using a D-shape optical fiber [27], but here we are going to focus on another structure that has been recently used [37], which consists of a cladding etched single mode optical fiber (CE-SMF) coated with a semiconductor oxide thin-film. As contrast to tapered SMF, that keeps the ratio core/cladding, in the CE-SMF the core is not narrowed,

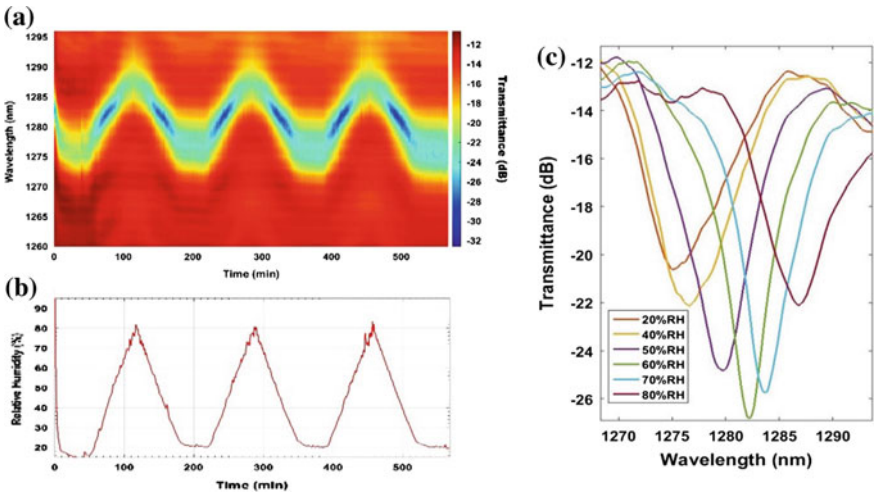

Fig. 9 **a** Evolution of the transmitted optical spectrum of a tapered SMF coated with ITO for **b** some cycles of 20–90 % RH and **c** optical spectra for some values of RH [36]

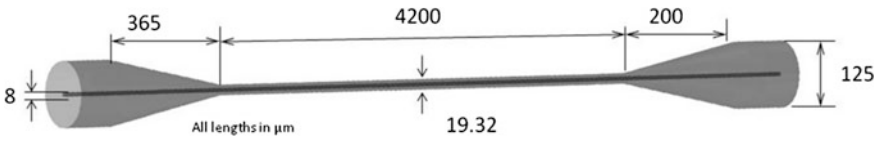

Fig. 10 Cladding-etched single mode optical fiber. Reprinted from Sens. Actuators B, vol. 233, Ascorbe, J., Corres, J.M., Matias, I.R., and Arregui, F.J., High sensitivity humidity sensor based on cladding-etched optical fiber and lossy mode resonances, pp. 7–16, (2016), with permission from Elsevier

only the cladding is partially removed by chemical methods. A common method to remove the cladding is the use of hydrofluoric acid (HF) [38, 39] (Fig. 10).

But the sensitivity of the naked CE-SMF to external parameters is quite small and it transmission spectra has not any absorption peak whose wavelength shift could be measured. Changes of the transmitted optical power lower than 1 dBm are achieved when immersing it in water. That is the reason why it is necessary to coat the CE-SMF with a thin-film which provides a wavelength phenomenon that can be tracked and which is sensitive to the external parameter to be measured at the same time. The material chosen for this purpose has been indium oxide (In_2O_3) which meets the requirements for LMR generation [25]. Indium oxide has been coated onto a CE-SMF by means of Pulsed DC Sputtering System, a physical vapor deposition method, which allows to coat metals and some semiconductor oxides, providing homogeneous coatings and high control of the thickness deposited. In Fig. 11 it is shown how the LMR is generated as the thickness of the coating increases.

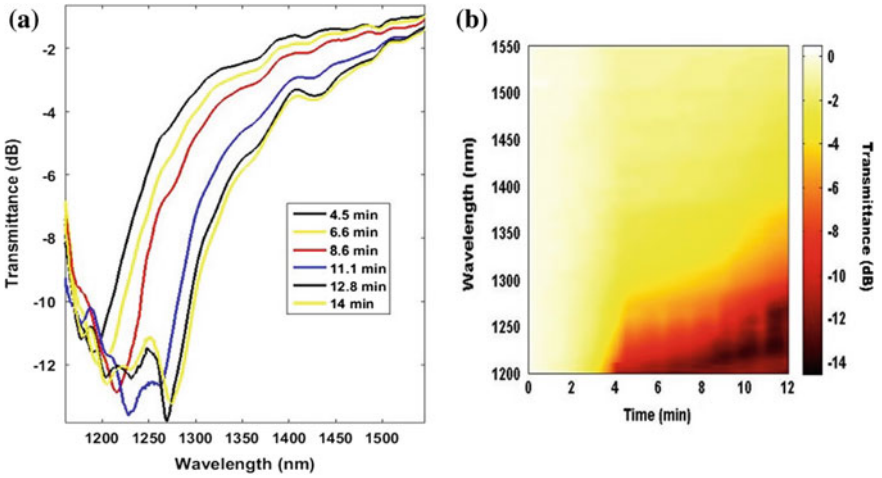

Fig. 11 **a** Some transmitted optical spectra for different thicknesses of In_2O_3 nano film coated onto a cladding etched single mode optical fiber and **b** changes on the transmitted optical spectrum for increasing thickness of In_2O_3 nano film

This coated CE-SMF was then connected to the light source and to an optical spectrum analyzer (OSA). The light source was a super-luminescent emitting diode (SLED) HP-83437A white light source which has four LEDs at 1200, 1310, 1430 and 1550 nm and the OSA was the HP-86142A, which has a wavelength range between 600 and 1700 nm, although 1200–1600 nm range was used. The optical fiber was introduced in a climatic chamber (Angelantoni ACS CH 250), as it can be seen in Fig. 12.

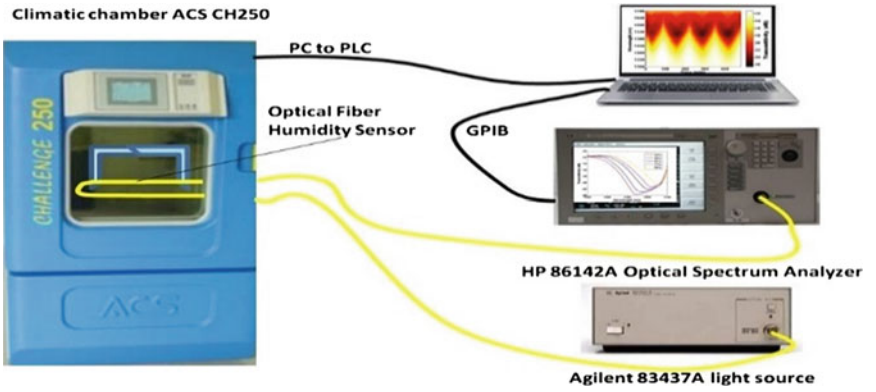

Fig. 12 Experimental set-up for measuring changes on the transmitted optical spectrum while relative humidity changes. Reprinted from Sens. Actuators B, vol. 233, Ascorbe, J., Corres, J.M., Matias, I.R., and Arregui, F.J., High sensitivity humidity sensor based on cladding-etched optical fiber and lossy mode resonances, pp. 7–16, (2016), with permission from Elsevier

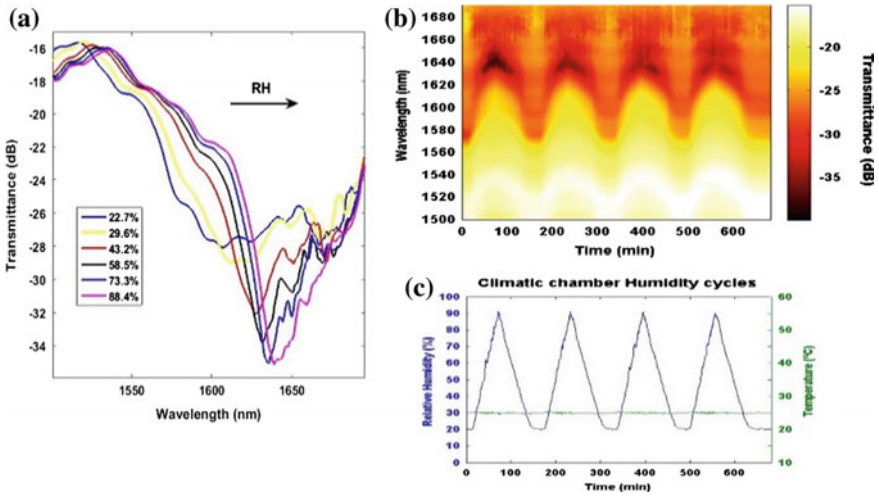

Fig. 13 **a** Optical spectra for some values of RH, **b** evolution of the transmitted optical spectrum of a CE-SMF coated with ITO for **c** some cycles of 20–90 % RH

There, the relative humidity has been increased from 20 to 90 % at a constant temperature of 25 °C. Due to previously commented phenomenon of absorption, the effective refractive index of the coating increases. The LMR shifts to greater wavelengths as the relative humidity increases. Figure 13, shows the spectra for different values of relative humidity and its evolution for some cycles 20–90 % RH.

The optical spectrum varies in several aspects: first of all, the attenuation of the LMR increases, besides the LMR narrows, and finally there is a wavelength shift in the wavelength of the resonance. By locating the wavelength of the resonance point with a higher attenuation it could be possible to measure relative humidity by registering the wavelength as a function of the relative humidity. This has been done by means of MATLAB® software. By applying a simple algorithm, it has been approached the spectrum to a parabola and then its vortex was calculated. Plotting the wavelength position of the LMR and the relative humidity, obtained by an electronic humidity sensor inside the climatic chamber we have obtained the next graph. Changes greater than 30 nm have been obtained for RH varying from 20 to 90 %. High linearity and low hysteresis are some of the characteristics of this device (Fig. 14).

The same structure has been proved with tin oxide as the LMR generator and as the sensitive material in [40]. Tin oxide has greater refractive index than indium oxide and it has also a great adsorption capability. It has proved good performance as humidity sensor based on LMRs. Figure 15 shows different optical spectra for different values of relative humidity. For this material wavelength shifts greater than 130 nm have been obtained, achieving a sensitivity of 1.9 nm/%RH. This increase in sensitivity is due, in part, to the higher refractive index of tin oxide with respect to indium oxide and it might be due also to differences in their adsorption capability.

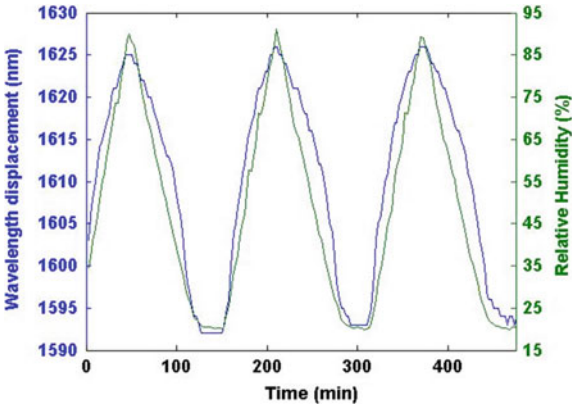

Fig. 14 Wavelength position of the LMR and relative humidity plotted simultaneously as a function of time for previous device

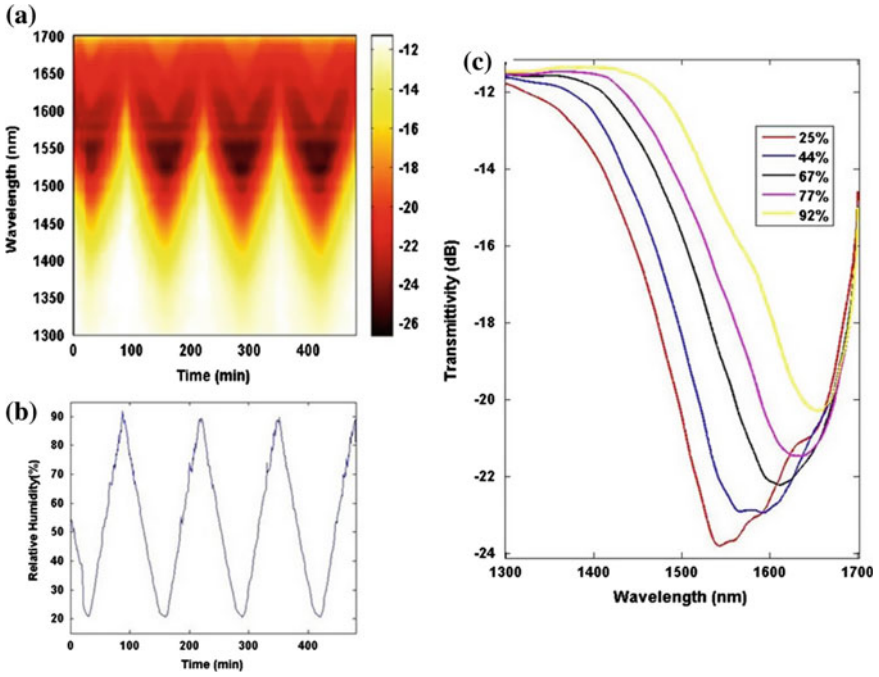

Fig. 15 **a** Optical spectra for four cycles of 20–90 % RH, **b** relative humidity cycles inside the climatic chamber and **c** optical spectra for some values of RH. Reprinted from Sens. Actuators B, vol. 233, Ascorbe, J., Corres, J.M., Matias, I.R., and Arregui, F.J., High sensitivity humidity sensor based on cladding-etched optical fiber and lossy mode resonances, pp. 7–16, (2016), with permission from Elsevier

4.3 Interferometric Sensors

In this section of the chapter we are going to focus on optical fiber humidity sensors based on Fabry-Pèrot interferometers (FPI). There are a lot of different ways to generate interferometry. One of the most known interferometers is the Mach-Zehnder interferometer, which measures the phase difference between light propagating through two arms of different length [41]. These kind of interferometers can be obtained by splitting the optical waveguide and recombining it later, by splicing different kind of fibers [42] or by tapered optical fibers [43]. This interferometers [42, 43] are based on modal interferometry, which is generated between core modes and cladding modes. But there is another kind of optical fiber interferometers which are called Fabry-Pèrot interferometers (FPIs). FPIs can be classified into extrinsic and intrinsic interferometers. In the intrinsic FPIs (IFPIs) the cavity is contained within the fiber and in the extrinsic FPIs (EFPIs) sensors the cavity is external to the fiber. Both of them are based on the interference caused by multiple reflections of light between two reflecting surfaces. Constructive interference occurs if the transmitted beams are in phase, and this corresponds to a high-transmission peak of the etalon. If the transmitted beams are out-of-phase, destructive interference occurs and this corresponds to a transmission minimum. Whether the multiply reflected beams are in phase or not depends on the wavelength of the light, the angle the light travels through the etalon, the thickness of the etalon and the refractive index of the material between the reflecting surfaces [44] (Fig. 16).

Fabrication methods for EFPIs are inexpensive and simpler than those used for the fabrication of IFPIs. Regarding the fabrication of EFPIs different approaches have been followed to obtain the interferometer. Most used structure consists of an air gap between two optical fibers [45, 46]. Hollow core fiber spliced to a single-mode optical fiber (SMF) and filled with a sensitive material [47] has been also used. But the most robust and reliable method for developing an EFPI is generating a nano-cavity by coating the tip of the SMF [48–50]. Although we are going to focus on a sputtered coating, other methods have been used for the fabrication of Fabry-Pèrot interferometers, as dip-coating [47], e-beam evaporation [51] or electrostatic self-assembly [49].

In an interferometric cavity the mirrors are formed by the refractive index differences between the different optical media at either end. In this case by the refractive index differences between the optical fiber and the SnO_2 coating, and then between the SnO_2 coating and the external medium, which is air for this case. The reflectance of each mirror will be approximately that determined by Fresnel's law for the case of normal incidence,

$$R_1 = \frac{(n_1 - n)^2}{(n_1 + n)^2} \tag{3}$$

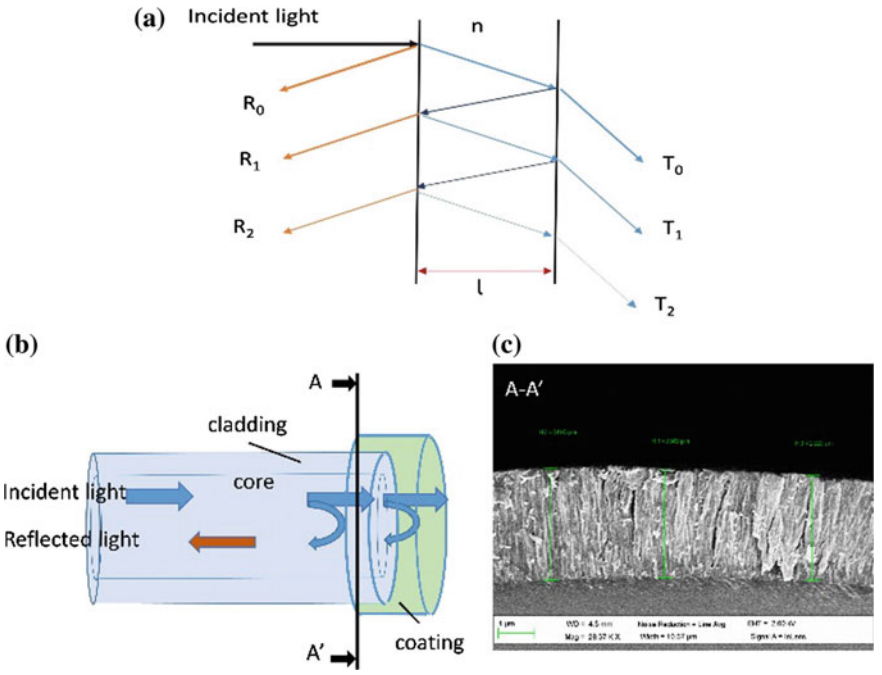

Fig. 16 **a** Schematic representation of interference in an etalon, **b** scheme of an all-fiber Fabry-Pèrot interferometer and **c** SEM image of the coating which will generate the interferometer

$$R_2 = \frac{(n_2 - n)^2}{(n_2 + n)^2} \tag{4}$$

where R_1 is the reflection coefficient of the first interface (optical fiber/SnO_2 coating) and R_2 is the reflection coefficient of the second interface (coating/air). The interferometric cavity functions exactly as an optical fiber Fabry–Perot etalon. The expression of the reflectance for such a Fabry–Perot etalon is:

$$R_{FP} = \frac{R_1 + R_2 + \sqrt{R_1 R_2}cos\theta}{1 + R_1 R_2 + \sqrt{R_1 R_2}cos\theta} \tag{5}$$

and

$$\theta = \frac{4\pi nL}{\lambda} \tag{6}$$

where L is the length of the etalon and λ is the wavelength of the excitation light [48].

4.3.1 Fabry-Pèrot Interferometer as Humidity Sensor

Here we are going to show the behaviour of a FPI obtained by coating the tip of an optical fiber with tin dioxide [52]. Tin dioxide is a good choice for humidity sensing because of its absorption capability and it is also a good choice for the FPI generation because of its high refractive index. First of all, in Fig. 17 it is shown a simulation of how the interferometry is generated and how it changes as the thickness of the etalon increases.

First of all, just one interference peak appears, which shifts to greater wavelengths, then another peak appears which also shifts to greater wavelengths, but it shifts more slowly than the previous one and so and so forth. This difference in the speed of the wavelength displacement makes that, for greater thicknesses there were

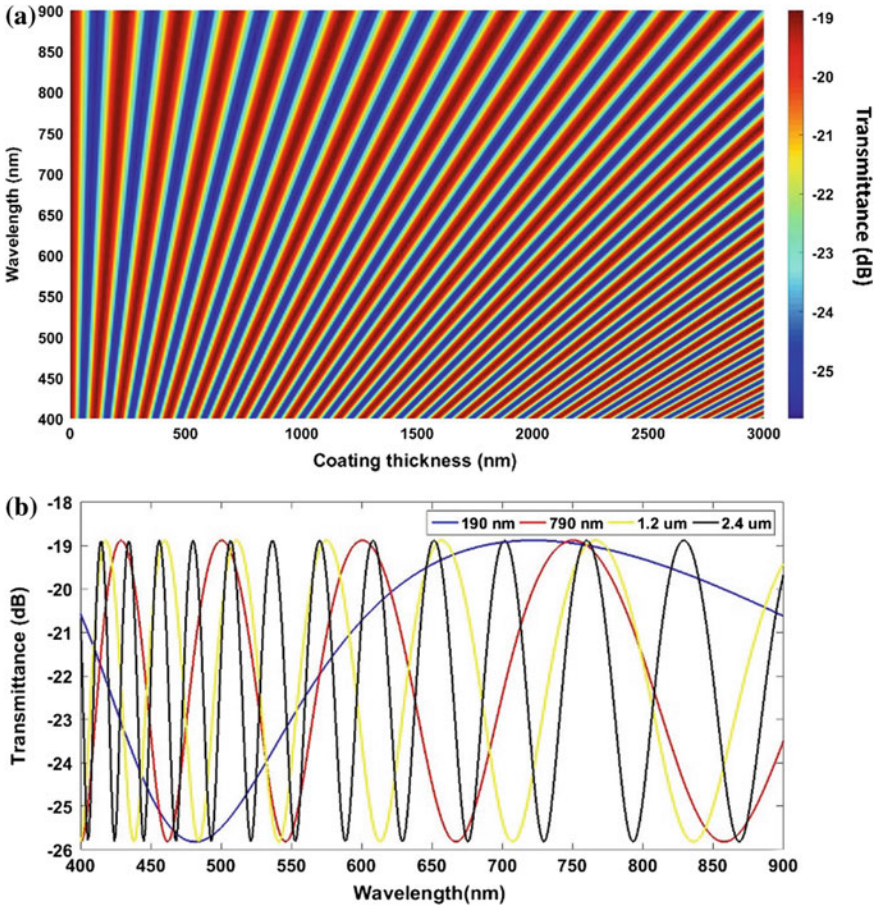

Fig. 17 **a** Evolution of the simulated spectrum as the thickness of the coating increases and **b** simulated optical spectra for different thickness of the coating

more interference peaks, which leads to an increase of the wavelength resolution of the interferometer. The commented behaviour is due to changes on the length of the cavity for a fixed refractive index. Once the length is fixed, it is subjected to changes on the relative humidity using a reflection set-up. Now the optical changes are caused by a change on the refractive index of the cavity.

As it can be seen in Fig. 18, the wavelength where a constructive interference and also where the destructive interference occur shifts to greater wavelengths when the relative humidity is increased. This is due to the adsorbed water onto the tin oxide layer. The effect of the water adsorbed onto the tin oxide layer can be modelled by the following phenomena. Since water is a polar molecule, the negatively charged oxygen of the water molecule is electrostatically attracted to the positively charged cationic side of the metal oxide surface. If the charge density of the cationic side is low, then water remains physically adsorbed at the surface by a weak electrostatic field [53]. When the cationic charge density is high, the electrostatic force is high enough to form a chemical bond between hydrogen and oxygen of a water molecule, which in turn may break the bond between oxygen and one of the hydrogen atoms [54–56]. Mostly, the force is high enough to break the bond in the initially adsorbed water vapour layer. Therefore, the initial monolayer is generally chemisorbed [53]. As relative humidity (RH) increases, an additional layer of water molecules starts to be formed, on the chemisorbed one. Many more physisorbed layers will be joined as humidity gets higher [57]. These layers are easily removed by decreasing the humidity [58, 59]. This layer of water causes an increase of the effective refractive index of the coating, changing the interference conditions.

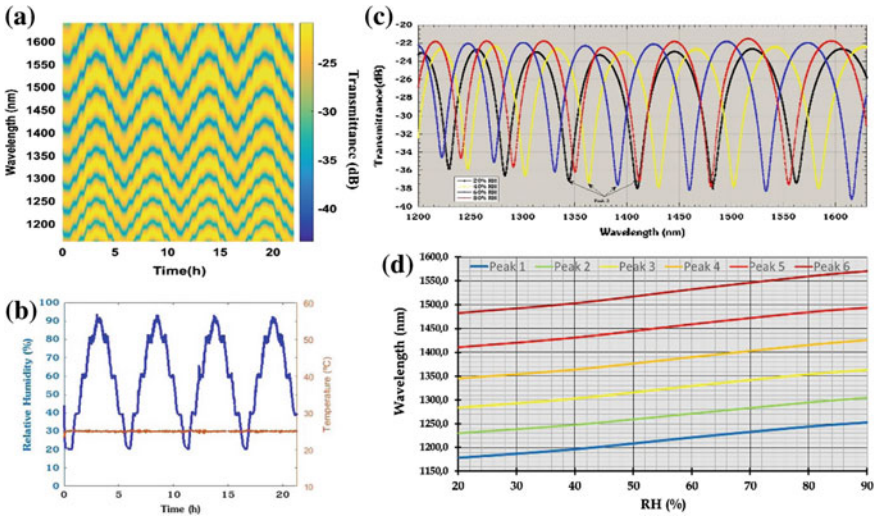

Fig. 18 **a** Evolution of the reflected optical spectrum for **b** four cycles of 20–90 %RH, **c** some optical spectra for different values of RH and **d** wavelength position of the interference peaks as a function of the RH

Wavelength shifts of 100 nm have been achieved for changes on the relative humidity from 20 to 90 %. The wavelength shifts have a dependence on the wavelength, slightly greater displacements are obtained for interference peaks located at greater wavelengths. This kind of devices have low hysteresis, high linearity, good response time and high sensitivity. However, it must be carefully selected the material which is going to be used for the development of this device. It must meet the requirements to be sensitive to RH and to generate a good interferometer. Most semiconductors are sensitive to changes on relative humidity and they will generate a better interferometer as its refractive index is greater.

4.4 Long Period Fiber Gratings

Long period fiber gratings (LPGs) has some desirable characteristics for their use as optical fiber sensors. LPGs structure consists on a periodic modification of the refractive index of the optical fiber. Several approaches have been followed to develop LPGs. Modification of the refractive index of the optical fiber can be obtained by exposing to UV radiation hydrogen-loaded germanosilicate fibers [60, 61], or by methods based on the physical deformation of the fiber [62], diffusion of the core dopants in special nitrogen-doped Ge free fibers [63, 64], or refractive index variation produced by CO_2 lasers [65], CO laser [63, 64], ion implantation [66], or electrical discharges [62, 63, 67, 68] (Fig. 19).

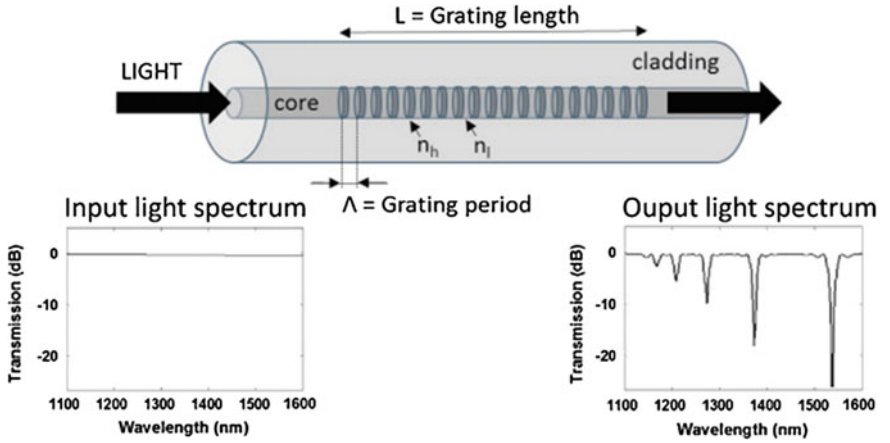

Fig. 19 Scheme of a LPG, indicating their parameters, and its characteristic spectrum when the light goes through the grating. Reprinted from Sens. Actuators B, vol. 227, Urrutia A. et al., Simultaneous measurement of humidity and temperature based on a partially coated optical fiber long period grating, pp. 135–141, (2016), with permission from Elsevier

LPGs have been also studied as humidity sensors [69–74]. Different materials have been checked as the sensitive layer for humidity sensing purposes. In [69], poly(ethylene oxide)/cobalt chloride (PEO/CoCl2) as a hybrid hygrosensitive cladding coating. The material parameters associated with the sensing mechanism may include those of refractive index, absorption, and morphological alterations of the overlaid material. Relative humidity variations in the range from 50 to 95 % have been detected with a resolution better than 0.2 %. The response time constant of the fiber sensor is of the order of a few hundred milliseconds. Maximum wavelength shift of 6 nm have been obtained, but the response of this hybrid coating is nonlinear. In [70] a hydrogel has been used as the sensitive material obtaining a linear wavelength shift of 12 nm for humidity changing from 30 to 100 %. Other approach has been followed in [73] where the LPG has been coated by means of electrostatic self-assembly method with PAH, PAA and silica nanospheres. Wavelength shifts of 14 nm have been obtained for RH varying from 10 to 80 %. Optical spectra for different values of RH are shown in Fig. 20. It has been also checked the influence of temperature on the sensitivity, which has not noticeable effect.

Finally, in [74] a simultaneous measurement of temperature and RH has been accomplished by a half-coated LPG. When half of the LPG coating was chemically removed the main attenuation band was split into two different contributions, one of them due to the grating and the other due to the coating. When this semi-coated LPG was also exposed to RH and temperature tests, the new two attenuation bands presented different behaviors for humidity and temperature. This novel dual-wavelength based sensing method enables the simultaneous measurement of RH and temperature using only one LPG (Fig. 21).

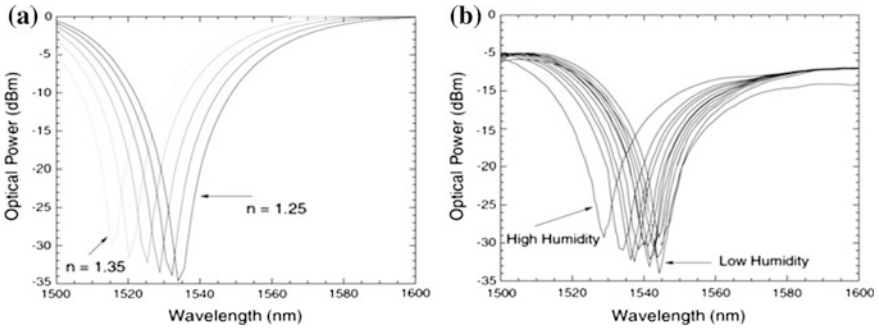

Fig. 20 LPG spectra: **a** theoretical simulation for different refractive index values of the overlay; **b** experimental results for different relative humidity levels. Reprinted from A fibre optic humidity sensor based on a long-period fibre grating coated with a thin film of SiO_2 nanospheres, Viegas, D. et al., 2012, Meas. Sci. Technol. 20 034002, doi:10.1088/0957-0233/20/3/034002 with permission from IOP Publishing

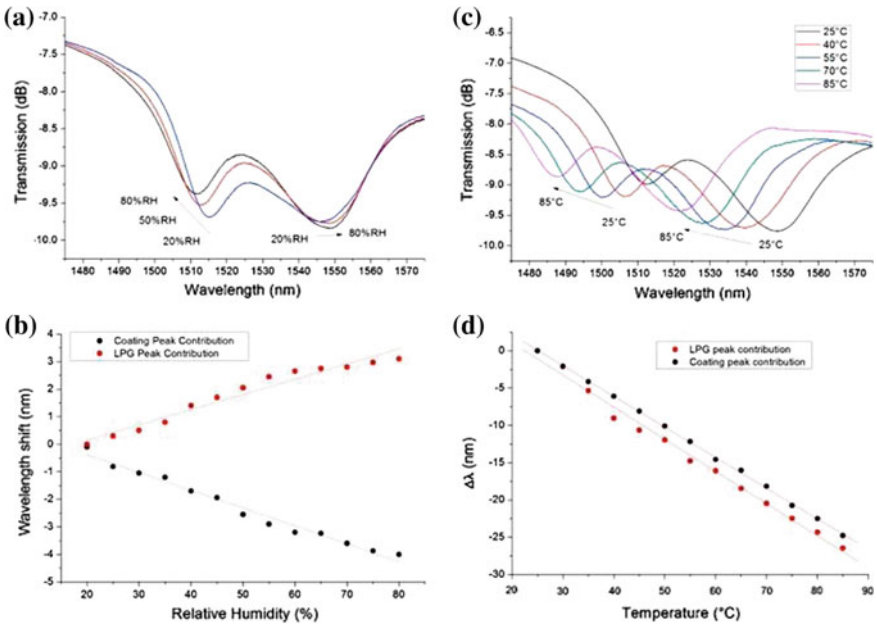

Fig. 21 **a** Transmission spectra evolution of the partially-coated LPG as the RH is changed. **b** Wavelength shift of both attenuation bands during the RH variation, **c** Transmission spectra evolution of the partially-coated LPG as the temperature is changed. **d** Wavelength shift of both attenuation bands with the temperature variations. Reprinted from Sens. Actuators B, vol. 227, Urrutia A. et al., Simultaneous measurement of humidity and temperature based on a partially coated optical fiber long period grating, pp. 135–141, (2016), with permission from Elsevier

5 Conclusions

There are several ways to measure relative humidity by optical set-ups and by optical fiber humidity sensors. Here, we have delved into lossy mode resonances and Fabry-Pèrot interferometers, and LPGs have been briefly commented. These structures have been chosen for this review because each of them presents an optimal feature to function as an optical fiber sensor. Although there are more structures that have not been analysed, some interesting conclusions can be extracted from those that have been explained here.

First of all, polymeric coatings and inorganic salts usually present nonlinear behaviour, especially at high relative humidity values where they have their greatest sensitivity. Metal oxides and semiconductors oxides are a good choice for obtaining linear responses and good sensitivities in the 20–90 % RH range. Their response times are usually smaller than those of hygroscopic materials.

With regard to optical structures, there should be an agreement between the wanted spectral width of the attenuation band and its displacement. LPFGs need a fabrication process to obtain the grating which requires a specific machine. They are

not sensitive to external parameters by themselves and they need an external coating besides the grating. For lossy mode resonances generation, it is also need some process for getting access to the evanescent field. This process is simpler than that used for the development of a LPFG and usually consists on a chemical method to remove partially or completely the cladding. LMRs are a physical phenomenon which allows to generate the absorption peak with the same material that will act as the sensitive layer simplifying the process to obtain an optical fiber humidity sensor. Finally, Fabry-Pèrot interferometers, developed by coating the tip of an optical fiber, seems to be a good choice to obtain optical fiber humidity sensors because of their good performance and their relatively easy method to obtain them. They are also the less invasive way to measure with optical fibers.

References

1. P.R. Wiederhold, Water vapor measurement: methods and instrumentation, vol 1 (CRC Press, 1997)
2. A. Urrutia, P.J. Rivero, J. Goicoechea, F.J. Arregui, I.R. Matías, Humidity sensor based on a long-period fiber grating coated with a hydrophobic thin film, in *(EWOFS'10) Fourth European Workshop on Optical Fibre Sensors* (International Society for Optics and Photonics, 2010), pp. 765320–765320
3. C. Bariain, I.R. Matías, F.J. Arregui, M. Lopez-Amo, Optical fiber humidity sensor based on a tapered fiber coated with agarose gel. Sens. Actuators B: Chem. **69**(1), 127–131 (2000)
4. Glossary of atmospheric chemistry terms (Recommendations 1990), Pure Appl. Chem. **62,** 2167 (1990). doi:10.1351/goldbook.A00155. ISBN 0-9678550-9-8
5. M.M. Choi, O.L. Tse, Humidity-sensitive optode membrane based on a fluorescent dye immobilized in gelatin film. Anal. Chim. Acta **378**(1), 127–134 (1999)
6. T.L. Yeo, T. Sun, K.T.V. Grattan, Fibre-optic sensor technologies for humidity and moisture measurement. Sens. Actuators, A **144**(2), 280–295 (2008)
7. J.F. Boyle, K.A. Jones, The effects of CO, water vapor and surface temperature on the conductivity of a SnO2 gas sensor. J. Electron. Mater. **6**(6), 717–733 (1977)
8. C. Pijolat, R. Lalauze, Influence of adsorbed hydroxyl species on the electrical conductance of SnO 2. Sens. Actuators **14**(1), 27–33 (1988)
9. E.W. Thornton, P.G. Harrison, Tin oxide surfaces. Part 1.—surface hydroxyl groups and the chemisorption of carbon dioxide and carbon monoxide on tin (IV) oxide. J. Chem. Soc. Faraday Trans. 1: Phys. Chem. Condens. Phases **71**, 461–472 (1975)
10. G. Korotchenkov, V. Brynzari, S. Dmitriev, Electrical behavior of SnO_2 thin films in humid atmosphere. Sens. Actuators B: Chem. **54**(3), 197–201 (1999)
11. Y. Kim, B. Jung, H. Lee, H. Kim, K. Lee, H. Park, Capacitive humidity sensor design based on anodic aluminum oxide. Sens. Actuators B: Chem. **141**(2), 441–446 (2009)
12. Y. Sakai, Y. Sadaoka, M. Matsuguchi, Humidity sensors based on polymer thin films. Sens. Actuators B: Chem. **35**(1), 85–90 (1996)
13. K.T.V. Grattan, T. Sun, Fiber optic sensor technology: an overview. Sens. Actuators, A **82**(1), 40–61 (2000)
14. A.P. Russell, K.S. Fletcher, Optical sensor for determination of moisture. Anal. Chim. Acta **170**, 209–216 (1985)
15. S.K. Khijwania, K.L. Srinivasan, J.P. Singh, Performance optimized optical fiber sensor for humidity measurement. Opt. Eng. **44**(3), 034401–034401 (2005)
16. B.D. MacCraith, Enhanced evanescent sensors based on sol-gel derived porous glass coating. Sens. Actuators, B **11**, 29–33 (1993)

17. F.J. Arregui, Z. Ciaurriz, M. Oneca, I.R. Matias, An experimental study about hydrogels for the fabrication of optical fiber humidity sensors. Sens. Actuators B (2003)
18. C. Barian, I.R. Matis, F.J. Arregui, M. Lopez-Amo, Optical fiber humidity sensor based on a tapered coated with agarose gel. Sens. Actuators, B **69**, 127–131 (2000)
19. J.M. Corres, F.J. Arregui, I.R. Matías, Sensitivity optimization of tapered optical fiber humidity sensors by means of tuning the thickness of nanostructured sensitive coatings. Sens. Actuators B: Chem. **122**(2), 442–449 (2007)
20. M. Hernaez, C.R. Zamarreño, C. Fernandez-Valdivielso, I. Del Villar, F.J. Arregui, I.R. Matias, Agarose optical fibre humidity sensor based on electromagnetic resonance in the infra-red region. Phys. Status Solidi (C) **7**(12), 2767–2769 (2010)
21. M. Marciniak, J. Grzegorzewski, M. Szustakowski, Analysis of lossy mode cut-off conditions in planar waveguides with semiconductor guiding layer. IEE Proc. J (Optoelectronics) **140**(4), 247–252 (1993)
22. F. Yang, J.R. Sambles, Determination of the optical permittivity and thickness of absorbing films using long range modes. J. Mod. Opt. **44**(6), 1155–1163 (1997)
23. I. Del Villar, C.R. Zamarreño, P. Sanchez, M. Hernaez, C.F. Valdivielso, F.J. Arregui, I.R. Matias, Generation of lossy mode resonances by deposition of high-refractive-index coatings on uncladded multimode optical fibers. J. Opt. **12**(9), 095503 (2010)
24. C.R. Zamarreño, I. Del Villar, P. Sanchez, M. Hernaez, C. Fernandez, I.R. Matias, F. J. Arregui, Lossy-mode resonance-based refractometers by means of indium oxide coatings fabricated onto optical fibers, in (EWOFS'10) *Fourth European Workshop on Optical Fibre Sensors* (International Society for Optics and Photonics, 2010), pp. 76531 W–76531 W
25. P. Sanchez, C.R. Zamarreño, M. Hernaez, I. del Villar, I.R. Matias, F.J. Arregui, Humidity sensor fabricated by deposition of SnO2 layers onto optical fibers, in *Fifth European Workshop on Optical Fibre Sensors* (International Society for Optics and Photonics, 2013), pp. 87940C–87940C
26. A.B. Socorro, I. Del Villar, J.M. Corres, F.J. Arregui, Lossy mode resonance-based pH sensor using a tapered single mode optical fiber coated with a polymeric nanostructure, in *Sensors, IEEE 2011* (IEEE, 2011), pp. 238–241
27. C. Ruiz Zamarreño, P. Zubiate, M. Sagües, I.R. Matias, F.J. Arregui, Experimental demonstration of lossy mode resonance generation for transverse-magnetic and transverse-electric polarizations. Opt. Lett. **38**(14), 2481–2483 (2013)
28. M. Hernáez, I. Del Villar, C.R. Zamarreño, F.J. Arregui, I.R. Matias, Optical fiber refractometers based on lossy mode resonances supported by TiO 2 coatings. Appl. Opt. **49** (20), 3980–3985 (2010)
29. H.P. Ho, W.W. Lam, Application of differential phase measurement technique to surface plasmon resonance sensors. Sens. Actuators B: Chem. **96**(3), 554–559 (2003)
30. S. Zeng, D. Baillargeat, H.P. Ho, K.T. Yong, Nanomaterials enhanced surface plasmon resonance for biological and chemical sensing applications. Chem. Soc. Rev. **43**(10), 3426–3452 (2014)
31. J.B. González-Díaz, A. García-Martín, J.M. García-Martín, A. Cebollada, G. Armelles, B. Sepúlveda, Y. Alaverdyan, M. Käll, Plasmonic Au/Co/Au nanosandwiches with enhanced magneto-optical activity. Small **4**(2), 202–205 (2008)
32. P. Sanchez, C.R. Zamarreño, M. Hernaez, I. Del Villar, C. Fernandez-Valdivielso, I.R. Matias, F.J. Arregui, Lossy mode resonances toward the fabrication of optical fiber humidity sensors. Meas. Sci. Technol. **23**(1), 014002 (2012)
33. P. Zubiate, C.R. Zamarreño, I. Del Villar, I.R. Matias, F.J. Arregui, High sensitive refractometers based on lossy mode resonances (LMRs) supported by ITO coated D-shaped optical fibers. Opt. Express **23**(6), 8045–8050 (2015)
34. J.M. Corres, F.J. Arregui, I.R. Matias, Design of humidity sensors based on tapered optical fibers. J. Lightwave Technol. **24**(11), 4329–4336 (2006)
35. C. Bariain, I.R. Matías, F.J. Arregui, M. Lopez-Amo, Optical fiber humidity sensor based on a tapered fiber coated with agarose gel. Sens. Actuators B: Chem. **69**(1), 127–131 (2000)

36. J. Ascorbe, J.M. Corres, F.J. Arregui, I.R. Matias, Optical fiber humidity sensor based on a tapered fiber asymmetrically coated with indium tin oxide, in *Sensors*, *2014 IEEE* (IEEE, 2014), pp. 1916–1919
37. J. Ascorbe, J.M. Corres, I.R. Mat, F.J. Arregui, Humidity sensor based on lossy mode resonances on an etched single mode fiber, in *2015 9th International Conference on Sensing Technology (ICST)* (IEEE, 2015), pp. 365–368
38. H.S. Haddock, P.M. Shankar, R. Mutharasan, Fabrication of biconical tapered optical fibers using hydrofluoric acid. Mater. Sci. Eng., B **97**(1), 87–93 (2003)
39. H.J. Kbashi, Fabrication of submicron-diameter and taper fibers using chemical etching. J. Mater. Sci. Technol. **28**(4), 308–312 (2012)
40. S$AB
41. R.A. Becker, Traveling-wave electro-optic modulator with maximum bandwidth-length product. Appl. Phys. Lett. **45**(11), 1168–1170 (1984)
42. N. Liu, M. Hu, H. Sun, T. Gang, Z. Yang, Q. Rong, X. Qiao, A fiber-optic refractometer for humidity measurements using an in-fiber Mach-Zehnder interferometer. Opt. Commun. **367**, 1–5 (2016)
43. Q. Wang, W. Wei, M. Guo, Y. Zhao, Optimization of cascaded fiber tapered Mach-Zehnder interferometer and refractive index sensing technology. Sens. Actuators B: Chem. **222**, 159–165 (2016)
44. G. Hernández, *Fabry-Pèrot Interferometers*, vol 3 (Cambridge University Press, 1988)
45. X. Chen, F. Shen, Z. Wang, Z. Huang, A. Wang, Micro-air-gap based intrinsic Fabry-Pèrot interferometric fiber-optic sensor. Appl. Opt. **45**(30), 7760–7766 (2006)
46. J. Wang, B. Dong, E. Lally, J. Gong, M. Han, A. Wang, Multiplexed high temperature sensing with sapphire fiber air gap-based extrinsic Fabry-Pèrot interferometers. Opt. Lett. **35** (5), 619–621 (2010)
47. L.H. Chen, T. Li, C.C. Chan, R. Menon, P. Balamurali, M. Shaillender, B. Neu, X.M. Ang, P. Zu, W.C. Wong, K.C. Leong, Chitosan based fiber-optic Fabry-Pèrot humidity sensor. Sens. Actuators B: Chem. **169**, 167–172 (2012)
48. J. Goicoechea, C.R. Zamarreño, I.R. Matias, F.J. Arregui, Utilization of white light interferometry in pH sensing applications by mean of the fabrication of nanostructured cavities. Sens. Actuators B: Chem. **138**(2), 613–618 (2009)
49. J. Goicoechea, C.R. Zamarreño, I.R. Matías, F.J. Arregui, Study on white light optical fiber interferometry for pH sensor applications, in *Sensors*, *2007 IEEE* (IEEE, 2007), pp. 399–402
50. F.J. Arregui, Y. Liu, I.R. Matias, R.O. Claus, Optical fiber humidity sensor using a nano Fabry-Pèrot cavity formed by the ionic self-assembly method. Sens. Actuators B: Chem. **59** (1), 54–59 (1999)
51. W. Xie, M. Yang, Y. Cheng, D. Li, Y. Zhang, Z. Zhuang, Optical fiber relative-humidity sensor with evaporated dielectric coatings on fiber end-face. Opt. Fiber Technol. **20**(4), 314–319 (2014)
52. J. Ascorbe, C. Sanz, J.M. Corres, F.J. Arregui, I.R. Mat, S.C. Mukhopadhyay, High sensitivity extrinsic Fabry-Pèrot interferometer for humidity sensing, in *2015 9th International Conference on Sensing Technology (ICST)* (IEEE, 2015), pp. 143–146
53. B.C. Yadav, N.K. Pandey, A.K. Srivastava, P. Sharma, Optical humidity sensors based on titania films fabricated by sol–gel and thermal evaporation methods. Meas. Sci. Technol. **18** (1), 260 (2006)
54. G.W. Bundrett, *Criteria of Moisture Control* (London, Butterworths, 1990), p 19
55. T. Morimoto, M. Nagao, F. Tokuda, The relation between the amounts of chemisorbed and physisorbed water on metal oxides. J. Phys. Chem. **73**, 243–248 (1969)
56. T. King, *Water, Miracle of Nature* (Macmillan, New York, 1953)
57. W.M. Sears, The effect of oxygen stoichiometry on the humidity sensing characteristics of bismuth iron molybdate. Sens. Actuators B: Chem. **67**(1), 161–172 (2000)
58. P.M. Faia, C.S. Furtado, Effect of composition on electrical response to humidity of TiO 2: ZnO sensors investigated by impedance spectroscopy. Sens. Actuators B: Chem. **181**, 720–729 (2013)

59. N. Barsan, R. Grigorovici, R. Ionescu, M. Motronea, A. Vancu, Mechanism of gas detection in polycrystalline thick film SnO 2 sensors. Thin Solid Films **171**(1), 53–63 (1989)
60. J. Lemaire, R.M. Atkins, V. Mizrahi, K.L. Walker, K.S. Kranz, W.A. Reed, High pressure H2 loading as a technique for achieving ultrahigh UV photosensitivity and thermal sensitivity in GeO2 doped optical fibers. Electron. Lett. **29**, 1191–1193 (1993)
61. T. Erdogan, Cladding-mode resonances in short-and long-period fiber grating filters. JOSA A **14**(8), 1760–1773 (1997)
62. N. Godbout, X. Daxhelet, A. Maurier, S. Lacroix, Long-period fiber grating by electrical discharge, in *Proceedings of ECOC'98*, pp. 397–398
63. V.I. Karpov, M.V. Grekov, E.M. Dianov, K.M. Golant, S.A. Vasiliev, O.I. Medvedkov, R.R. Khrapko, Mode-field converters and long-period gratings fabricated by thermo-diffusion in nitrogen-doped silica-core fibers, in *Optical Fiber Communication Conference and Exhibit, 1998. OFC'98.*, *Technical Digest* (IEEE, 1988), pp. 279–280
64. E.M. Dianov, V.I. Karpov, M.V. Grekov, K.M. Golant, R.R. Khrapko, Ultra-thermostable long-period gratings induced in nitrogen-doped silica fiber, in *ECOC'97 Technical Digest*, pp. 2–56
65. D.D. Davis, T.K. Gaylord, E.N. Glytsis, S.G. Kosinski, S.C. Mettler, A.M. Vengsarkar, Long-period fibre grating fabrication with focused CO2 laser pulses. Electron. Lett. **34**(3), 302–303 (1998)
66. M. Fujimaki, Y. Ohki, J.L. Brebner, S. Roorda, Fabrication of long-period optical fiber gratings by use of ion implantation. Opt. Lett. **25**, 88–89 (2000)
67. S.G. Kosinski, A.M. Vengsarkar, Splice- based long-period fiber gratings, in *OFC'98 Technical Digest, paper ThG3*, pp. 278–279
68. G. Rego, O. Okhotnikov, E. Dianov, V. Sulimov, High-temperature stability of long-period fiber gratings produced using an electric arc. J.Lightwave Technol. **19**(10), 1574–1579 (2001)
69. M. Konstantaki, S. Pissadakis, S. Pispas, N. Madamopoulos, N.A. Vainos, Optical fiber long-period grating humidity sensor with poly (ethylene oxide)/cobalt chloride coating. Appl. Opt. **45**(19), 4567–4571 (2006)
70. Y. Liu, L. Wang, M. Zhang, D. Tu, X. Mao, Y. Liao, Long-period grating relative humidity sensor with hydrogel coating. IEEE Photon. Technol. Lett. **19**(12), 880–882 (2007)
71. T. Venugopalan, T.L. Yeo, T. Sun, K.T. Grattan, LPG-based PVA coated sensor for relative humidity measurement. Sens. J., IEEE **8**(7), 1093–1098 (2008)
72. S. Korposh, S.W. James, S.W. Lee, S. Topliss, S.C. Cheung, W.J. Batty, R.P. Tatam, Fiber optic long period grating sensors with a nanoassembled mesoporous film of SiO 2 nanoparticles. Opt. Express **18**(12), 13227–13238 (2010)
73. D. Viegas, J. Goicoechea, J.M. Corres, J.L. Santos, L.A. Ferreira, F.M. Araújo, I.R. Matias, A fibre optic humidity sensor based on a long-period fibre grating coated with a thin film of SiO2 nanospheres. Meas. Sci. Technol. **20**(3), 034002 (2009)
74. A. Urrutia, J. Goicoechea, A.L. Ricchiuti, D. Barrera, S. Sales, F.J. Arregui, Simultaneous measurement of humidity and temperature based on a partially coated optical fiber long period grating. Sens. Actuators B: Chem. **227**, 135–141 (2016)

Oxygen Gas Sensing Technologies Application: A Comprehensive Review

P. Shuk

Abstract Different oxygen gas sensing technologies, i.e., potentiometric, amperometric, paramagnetic and tunable diode laser spectroscopy (TDLS) are reviewed in details. Special attention is given to the theoretical aspects and operation basics of the technologies, application limits and analyzers or system requirements. A comprehensive technologies review is supported with the latest developments trends especially on the potentiometric zirconia and tunable diode laser analyzers.

1 Introduction

Oxygen is the third most abundant chemical element in the universe, after hydrogen and helium, and is one of the most important elements required to sustain the life [1]. Oxygen is vitally important not only to the existence of the human and animal life with ~3 million tons daily of oxygen consumption just for the respiration [2] but also very critical for any combustion process at power generation, chemicals production, heating, process control, safety, and quality. A major oxygen gas sensing application is for the combustion process optimization. The air required for the oxidation of hydrocarbons (fossil or bio fuels) is optimized to ensure the fuel complete combustion with the highest possible efficiency [3, 4]. Oxygen excess in the combustion in normally measured in the flue gas not far away from the fire ball or box and the fuel/air ratio supplied to the burner is controlled to the ideal minimum of oxygen or air excess (Fig. 1). The oxygen is also measured to minimize runaway combustion sometimes leading to the explosion and to control the product formation and quality. Some oxygen sensors work at ambient conditions where oxygen is either dissolved in liquid or solid or oxygen measurements have to be

P. Shuk (✉)
Rosemount Liquid and Combustion Analysis, Emerson Process Management, Emerson Electric Corp. 2400 Barranca Pkwy, Irvine, CA 92606, USA
e-mail: Pavel.Shuk@Emerson.com

S. Mukhopadhyay et al. (eds.), *Sensors for Everyday Life*, Smart Sensors, Measurement and Instrumentation 23, DOI 10.1007/978-3-319-47322-2_5

made under ambient conditions. Mostly these sensors are applied in medical, food processing and waste management industries. The oxygen sensors used under ambient conditions include Clark type cells [5], paramagnetic [6] and optical sensors [7, 8].

The high temperature oxygen sensors can be based on the potentiometric or amperometric electrochemical cells and resistive semiconductors [9, 10]. Potentiometric sensors measure the equilibrium voltage of the cells according to the Nernst equation and would require the reference. The amperometric oxygen sensor with fixed applied voltage and oxygen diffusion barrier is based on electrical current dependence on oxygen concentration and can be only successfully applied to very clean environment and this technology was discussed in many details elsewhere [11, 12].

The resistive oxygen sensor is based on semiconductors with the defect concentrations varying exponentially with the oxygen concentration [13]. The sensitivity of the surface to the particular gas can be as low as parts per billion (ppb) [14–17] and it is highly desirable that metal oxide semiconductor sensors have a large surface area, so as to adsorb as much of the target analyte gas on the surface as possible, giving a stronger and more reliable response especially at low concentrations. The applications of the semiconductors oxygen sensors in severe combustion process would be highly limited because of sensitivity, selectivity and reproducibility issues [10].

Four major oxygen gas sensing technologies are applied in an in situ or extractive mode to the combustion process environment and will be discussed in more details.

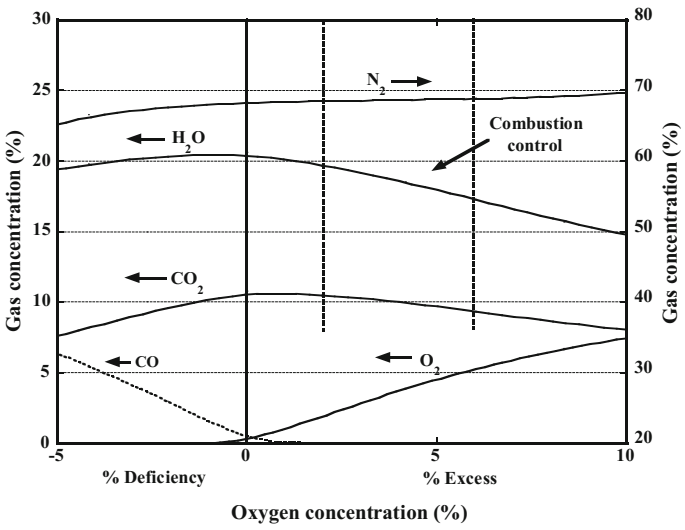

Fig. 1 Combustion flue gas concentration diagram

2 Zirconia Potentiometric Oxygen Gas Sensing Technology

Zirconia potentiometric oxygen gas sensing technology widely used nowadays in O_2 analyzers for different industrial combustion applications and in automotive Lambda sensors was invented in 1961 by Peters and Möbius [18] and Weissbart and Ruka [19] and was rapidly accepted in the power industry traditionally more conservative regarding the new technologies application. The first industrial zirconia oxygen analyser for the process gas application was developed early 70th by Westinghouse Electric Co (Rosemount Analytical Inc.), and was based on the advanced platinum cermet electrode and zirconia solid electrolyte technologies developed initially for the application in solid oxide fuel cells.

All industrial zirconia oxygen sensors are based on an electrochemical cell with solid electrolyte based mostly on yttrium on stabilized zirconia (YSZ) and two platinum based electrodes printed and sintered on the opposite sides of the zirconia ceramic and exposed to the process and reference gases:

$$O_2(p'_{O_2}, \text{Reference}), \text{Pt}|\text{YSZ}|\text{Pt}, O_2(p''_{O_2}, \text{Process}) \quad (1)$$

The oxygen electrochemical reaction in the regular sensor with Pt-electrodes is taking place on the triple phase boundary (TPB: electrode, electrolyte, and gas) where oxygen molecules (O_2), electrons (e^-) and oxygen vacancies ($V_{O}^{\cdot\cdot}$) are available (Fig. 2a) and this electrochemical reaction would be expanding to the all electrode bulk by using Pt-cermet electrode with electronic and oxygen ionic conductivity (Fig. 2b). This reaction includes oxygen molecules absorption, dissociation on the electrolyte/electrode surface, diffusion to the TPB and finally oxygen electrochemical reaction:

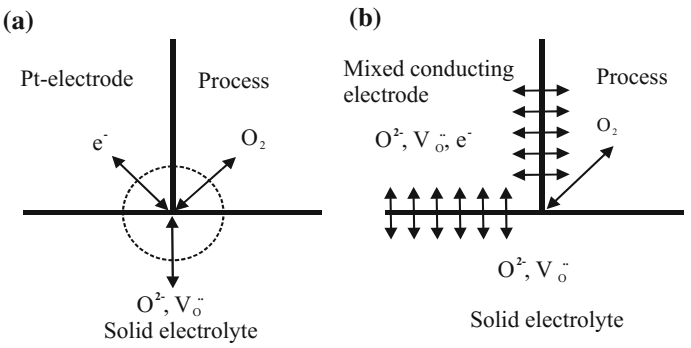

Fig. 2 Oxygen electrochemical reaction on TPB interface [20]

$$
\begin{aligned}
&O_2(\text{gas}) \leftrightarrow O_2(\text{Electrolyte/Electrode})\\
&O_2(\text{Electrolyte/Electrode}) \leftrightarrow 2O(\text{Electrolyte/Electrode})\\
&2O(\text{Electrolyte/Electrode}) \leftrightarrow 2O(\text{Electrolyte/Electrode/Gas})\\
&2O(\text{TPB}) + 4e^{'}(\text{Electrode}) + 2V_O^{\cdot\cdot}(\text{Electrolyte}) \leftrightarrow O_O(\text{Electrolyte})
\end{aligned}
\tag{2}
$$

The process side of the cell is gas tight separated from the reference side with the special high temperature ceramic/metal/glass seals and zirconia ceramic is used in the form of disc (Fig. 3), tube or thimble.

Differential oxygen chemical potentials on the oxygen cell electrodes would develop electromotive force (EMF), E, according to the Nernstian equation:

$$E = \frac{RT}{4F} \ln \frac{p(O_2)^{''}_{\text{Process}}}{p(O_2)^{'}_{\text{Ref}}}, \tag{3}$$

with R universal gas constant, T the process temperature in Kelvin (K) and F the Faraday number.

By using fixed oxygen partial pressure on the reference electrode, e.g., air with 20.9 % O_2 and $p(O_2) = 2.1 * 10^4$ Pa, the sensor signal of the thermally balanced oxygen sensor will be only depending on the sensor temperature (Fig. 4). Oxygen potentiometric gas analysis was established by M bius [21] and is also permitting measurements of not free but chemically bonded oxygen concentration <1 ppm (part per million) or <1 ppb (parts per billion) O_2 released in the reducing conditions in the process and CO/CO_2-ratio (Fig. 5) or H_2/H_2O-ratio (Fig. 6) can be also calculated based on the oxygen sensor signal.

Pt electrode film microstructure is highly depending on the sintering temperature and formation at lower temperatures would create much finer open porosity (Fig. 7) contributing to the better oxygen molecules diffusion to TPB interface but the electrode/electrolyte interface should be well established and lower temperature sintered electrodes might not be reliable in the severe process environment with the

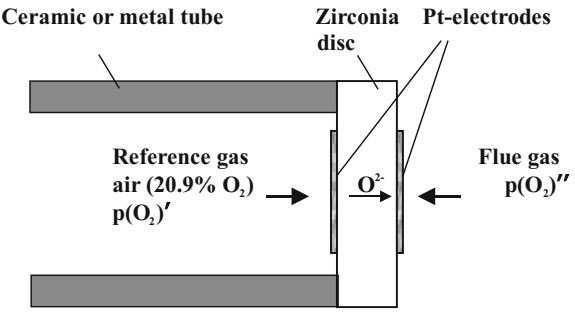

Fig. 3 Zirconia potentiometric oxygen gas sensing cell

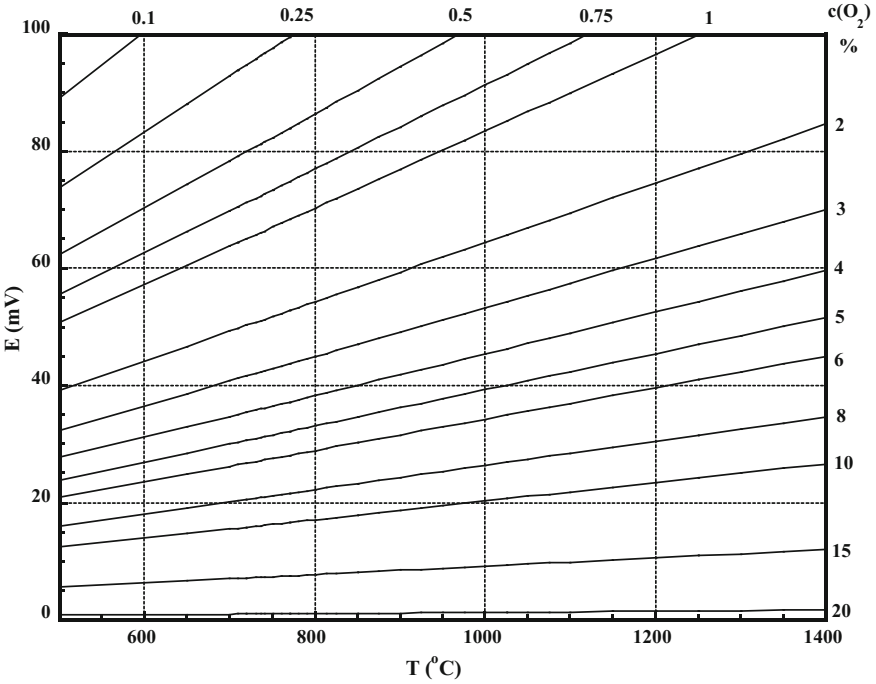

Fig. 4 Potentiometric zirconia oxygen sensor signal-concentration-temperature diagram

significant temperature and pressure variation. A special, highly porous Pt-zirconia cermet electrode formed at higher ~1400 °C temperatures was developed at Rosemount Combustion and Liquid Analysis with the special catalyst treatment to refine and re-open TPB interface for the oxygen diffusion and oxygen electrochemical reaction (Fig. 8) improving zirconia oxygen sensor response and operation life.

Industrial zirconia oxygen sensors are operating at elevated temperatures with oxygen ion migration in zirconia ceramics establishing oxygen equilibrium at the process and reference electrodes and zirconia electrolyte interfaces at >300 °C depending on the electrode composition and microstructure. Over 1400 °C oxygen electrolytic permeability of the zirconia solid electrolyte ceramic might compromise oxygen measurements. Higher application temperature will favour oxygen sensor performance but would be highly limiting the high temperature ceramic/metallic materials variety to be applied in the zirconia oxygen sensor packaging. Most industrial zirconia oxygen sensors are operating at elevated temperatures around 700…800 °C. Disc-shape zirconia ceramics brazed into special metal alloy supporting tube initially developed by Rosemount Analytical Inc. offer an advantage of

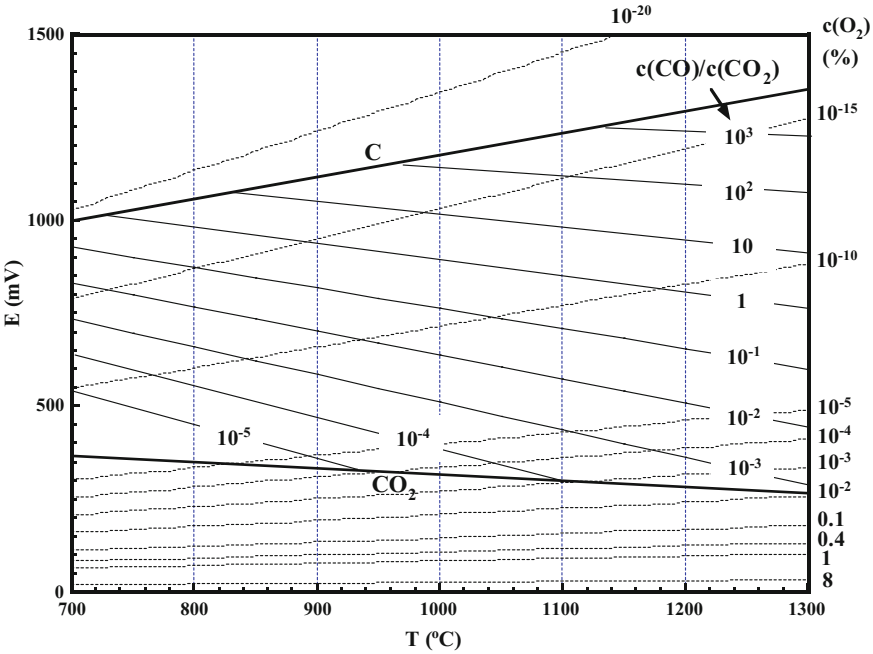

Fig. 5 Potentiometric zirconia oxygen sensor signal dependence on CO/CO_2 ratio

the much less differential temperature profile across the cell on the reference and process sides compared to the tube or thimble ceramic shape and less thermal stress considering a good thermal expansion coefficients (TEC) optimization of all involved in the oxygen sensor packaging metallic and ceramic materials. The small oxygen sensor is gas tight sealed at O_2 analyzer probe end for in situ operation (Fig. 9) or process flue gas can be alternatively delivered to the sensor using special extractive gas guiding tube [22]. The special protective shield, internal calibration line and reference gas line made from the special alloys like Inconel, Hastelloy or stainless steel 316L were implemented in the probe design to resist severe high temperature process environment. With these entire improvements zirconia probe can very precise measure in situ oxygen concentration down to 10 ppm (Fig. 10). A special oxygen cell with improved thermal balance and ceramic or metallic diffuser for the process gas particulate filtration was designed to improve O_2 analyzer [20] delivering an excellent stability (<0.1 % O_2) and reproducibility (±0.01 % O_2) in 2…5 % oxygen combustion concentration range (see Figs. 11 and 12).

Typical installation points of Zirconia O_2-probe in a coal fired boiler as it can be seeing from Fig. 13, would be located before or after heater exchanger

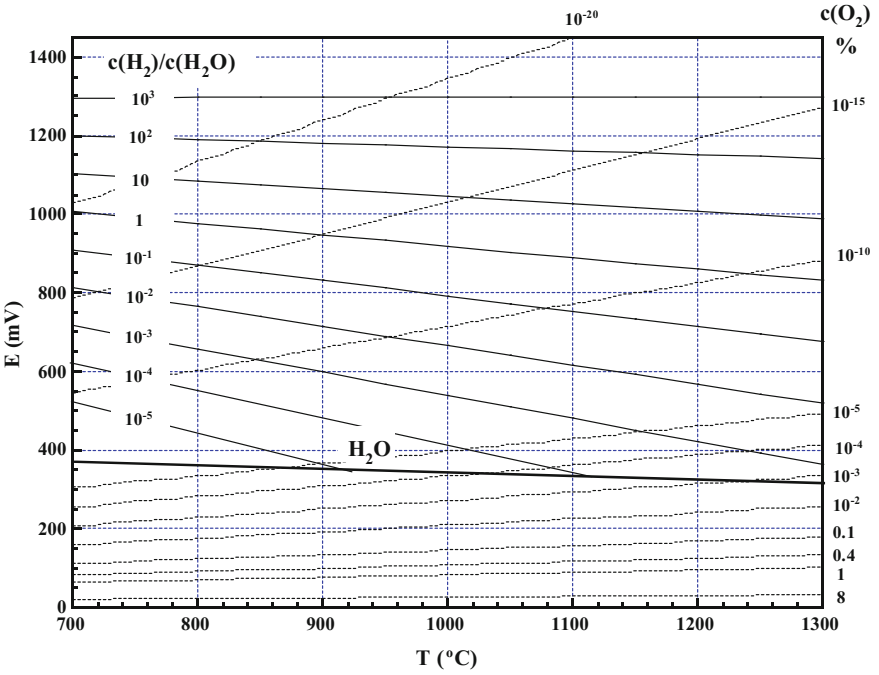

Fig. 6 Zirconia oxygen sensor signal dependence on H_2/H_2O ratio

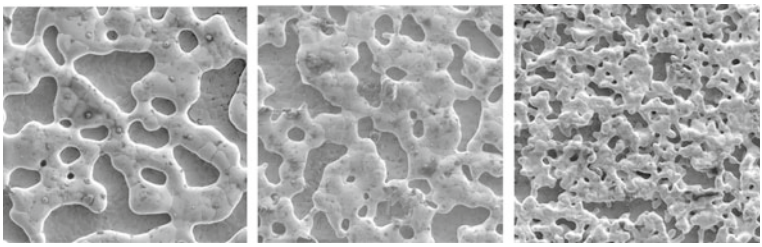

Fig. 7 Pt electrode microstructure dependence on the temperature

(economizer). For the combustion control and higher efficiency single or multiple probe systems might be used depending on the duct size and economizer outlet.

Additional probes may be mounted downstream monitoring the air entrance to ensure efficient operation of fans and dampers. In the combustion process due to

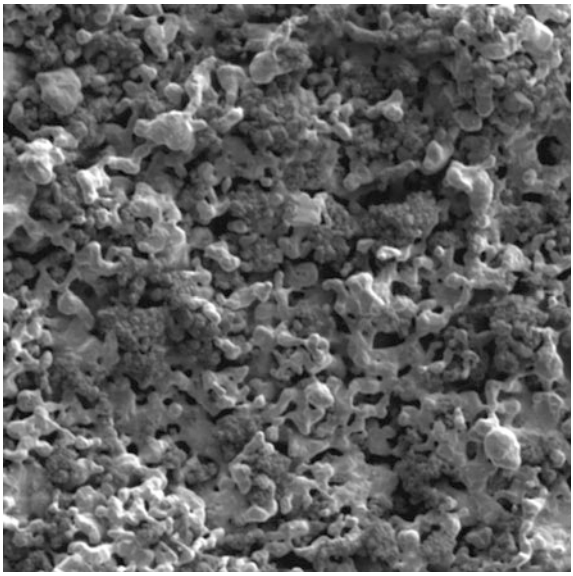

Fig. 8 SEM image of Pt-cermet process electrode [20]

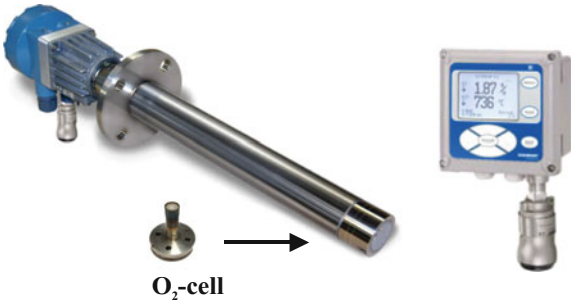

Fig. 9 In-situ O_2 analyzer (Rosemount Liquid and Combustion Analysis)

centrifugal forces, fly ash is concentrated towards the duct outer wall following bends in the duct and the installation of Zirconia O_2 analyzers in these locations should be avoid to reduce the probe body erosion in the high velocity and high concentration abrasive fly ash environment. There is a good Zirconia O_2-probe installation practice (Fig. 14) reducing very fine fly ash accumulation inside the oxygen sensor on the process electrode and on the protection filter on the probe end. In the oil and gas fired applications these problems are not present.

Zirconia O_2 analyzer was applied with very good success in the combustion control of power generation boilers, hot stoves for steelmaking, heating and combustion exhaust gas control of coke ovens for steelmaking, lime and cement kilns

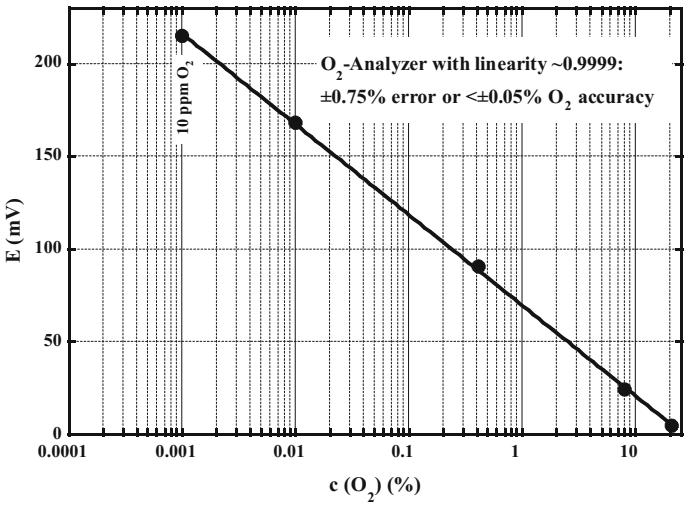

Fig. 10 Zirconia O_2 analyzer linearity

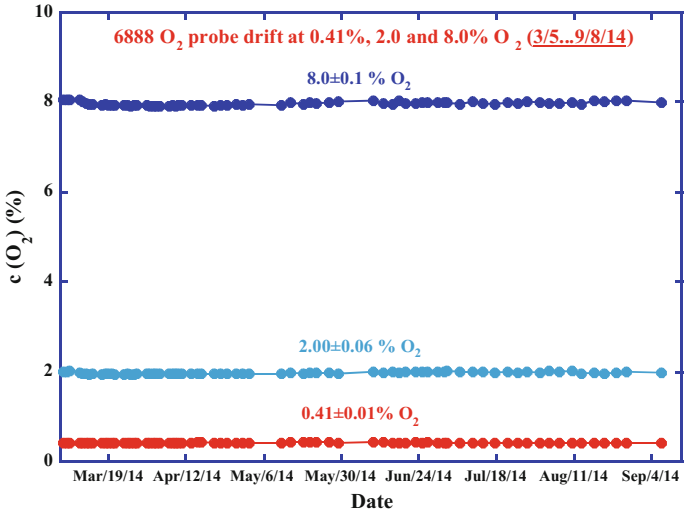

Fig. 11 Zirconia O_2-analyzer stability

combustion control, incinerator combustion control, combustion control of heating furnaces for oil refinery and petrochemical industry and many other applications. After 45 years zirconia potentiometric oxygen gas sensing technology is still

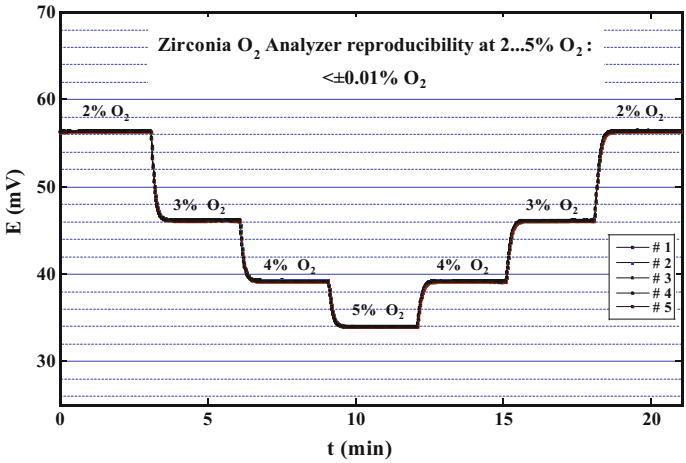

Fig. 12 Zirconia O_2-analyzer reproducibility

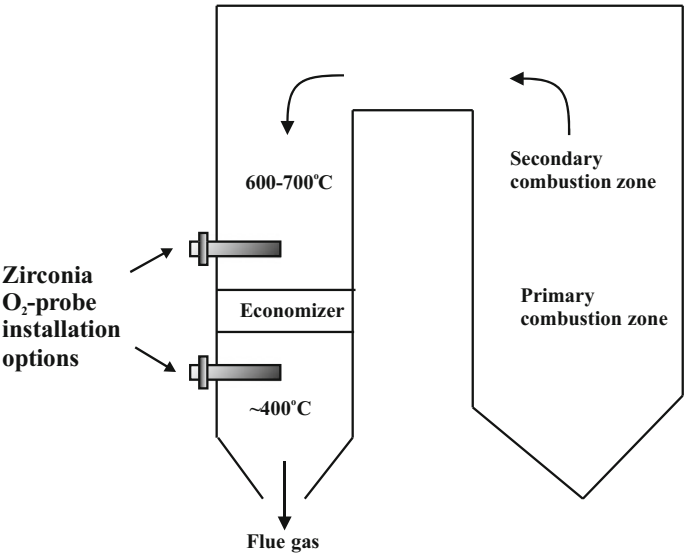

Fig. 13 Zirconia O_2-probe installation locations in coal fired boiler

dominating the combustion market because of the high reliability, accuracy in the most of applications and relative low price. Ametek, Rosemount Liquid and Combustion Analysis, Yokogawa and ABB are the major players on the in situ

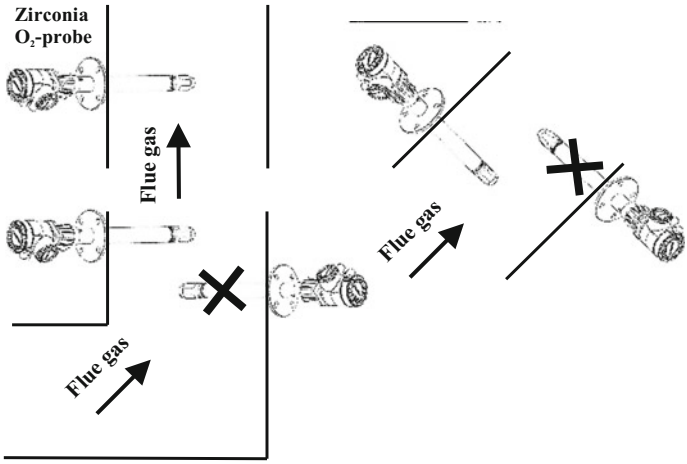

Fig. 14 Zirconia O_2-probe recommended installation options in flue gas

Fig. 15 In-situ Zirconia O_2-analyzers on the market

oxygen measurements market (Fig. 15). The performance of Zirconia O_2-Analyzers on the market is summarized in Table 1.

There have been numerous attempts to miniaturize oxygen sensor with innovative reference like sealed chamber and oxygen pump [23] or glass sealed metal/metal oxide references electrode [24–26] but the evaluation couldn't confirm these designs reliability in traditionally difficult stack gas or waste combustion gas analysis.

Table 1 Standard zirconia in situ O_2-analyzers performance and materials

Company	In situ O_2-probe	Accuracy	Operation temperature (°C)	O_2-sensor temperature (°C)	Materials
Rosemount (USA)	6888 O_2	±0.75 % or ± 0.05 % O_2	704 or 825	736	316L SS E-Brite
Yokogawa (Japan)	ZR202G	±1.0 % error	up to 700	750	316 SS Hastelloy
ABB (Swiss)	Endura Z20	±0.75 % or ± 0.05 % O_2	up to 800	700	316L SS
Ametek (USA)	WDG In situ flue	±1.0 % or ± 0.05 % O_2	up to 677…800	615	310 SS
Enotec (Germany)	Oxitec 5000	±0.2 % of MV*	up to 800 1400 (with cooling tube)	840	316 SS
Fuji (Japan)	ZKF8	±0.5 % of FS**	up to 800	800	316 SS 304 SS
GE-Panametric (USA)	FGA311	±3 % or ± 0.1 % O_2	up to 650 up to 1050 (HT)	700	316 SS Inconel
Energy Support (Japan)	TF-10	±1.0 % of FS**	up to 300	~800	305 SS 308 SS
LamTec (Germany)	LS2	±2.0 % or ± 0.2 % O_2	up to 300	~800	305 SS 308 SS
Zirox (Germany)	SS28	±5.0 %	up to 800	700…800	1.4841 (314 SS)
ETC (UK)	ETC 2800	±1 % of MV*	up to 540	~800	305 SS 308 SS
Ceramic Oxide Fabricators (Australia)	JS probe	±0.1 % O_2	up to 600	70	316 SS
Novatech (Australia)	1231	±1.0 %	up to 800	800	316 SS

* MV—Measured Value, ** FS—Full Scale

3 Tunable Diode Laser Spectroscopy (TDLS)

Tunable diode laser spectroscopy (TDLS) is an innovative optical measurement technique utilizing semiconductor lasers to detect a variety of gases (Fig. 16), including oxygen in the near infrared (IR) range to deliver part per millions (ppm) level measurements [27–30].

Over the last ~45 years, tunable diode laser (TDL) absorption sensing has become an established method for non-intrusive measurements of gas properties in

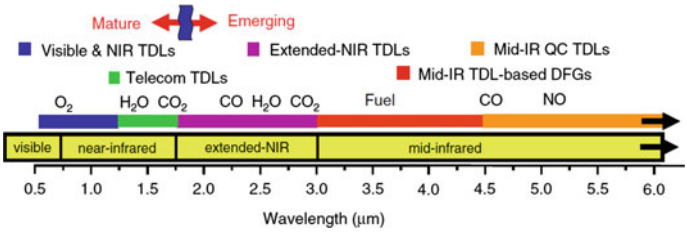

Fig. 16 Diode laser types and combustion gases versus wavelength [30]

combustion environment due to the robust, compact, low-cost TDL sources, and the convenient overlap of TDL wavelengths with absorption bands of O_2. CO, NO_x, H_2O, CO_2 combustion gases. TDLS with the ability to interface directly with the process gas and eliminating the need for the very high cost and high maintenance sample handling systems would be ideal for the real time dynamic measurement of the process conditions. With the federal, state and private companies multi billions investments TDL analyzers have now comprehensively established themselves as a core measurement technology within the portfolio of the gas analysis techniques available on the market [29, 31–33].

The infrared absorption spectrum of the flue gases is like a fingerprint, providing oxygen identification at ~760 nm (Fig. 17) and measurements in a wide concentration range down to ~80…100 ppm as a detection limit.

With the longer optical path length a higher absorption and better sensitivity will be achieved. Laser wavelength can be changed over a wide range by changing the laser operation temperature and over a narrow range by changing the applied current to the laser. Tunable lasers enabling the miniaturization of transmission and receiving units, provide highly sensitive, quantitative measurements with the fast response time without the need for the frequent calibration. TDL analyzers have been shown to be capable of the effective, accurate measurement even loosing up to

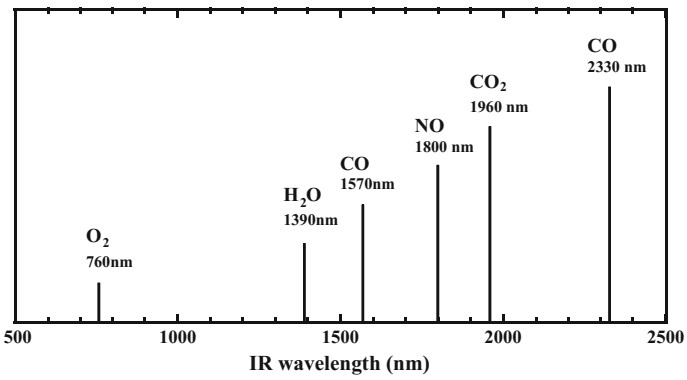

Fig. 17 Combustion gases near IR absorption lines used in TDLS detection

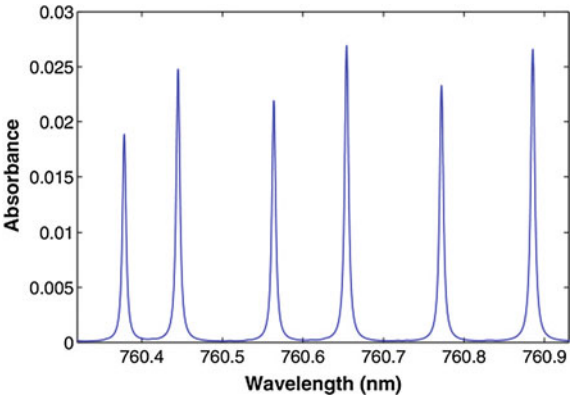

Fig. 18 Partial spectrum of oxygen at 760 nm [34]

90-95 % of the original signal in the dusty environment. TDL spectroscopy is highly distinguishing from the conventional process photometry by the laser ability to be scanned across the narrow oxygen absorption peaks (Fig. 18) many times per second by trimming the current through the laser. Thus the baseline and peak are continuously measured allowing recalculation of the background. While conventional optical filter bandwidth is >5 nm, a laser scan (0.2…0.3 nm typical range) would provide much better resolution and selectivity [35].

Wavelength-modulation spectroscopy (WMS) as a derivative form of absorption spectroscopy has been increasingly applied to these measurements improving sensitivity and selectivity over the direct absorption and would be especially favourable in the harsh and noisy combustion environment [36–38]. Many of the calibration-free WMS methods could be very useful for certain cases with known and stable environmental conditions but would be difficult to employ in some practical environments with the most of the environmental conditions unknown and laser intensity rapidly varying due to the vibration, window-fouling, beam-steering and some interfering species, elevated pressures and temperatures broadening the absorption peaks [38]. The single gas adsorption line selection was found to be very critical with some absorption lines changing less with the temperature and pressure variation. To eliminate moisture (H_2O) interference at high temperature for O_2/CO measurements a spectral survey was done to determine optimum adsorption lines and baseline treatment algorithms were developed to minimize effects of the overlaps. Balanced detector circuit developed by IBM (Hobbs) with a reference detector to reduce or eliminate common mode laser noise was implemented after TDL analyzer testing in the real process environment [32].

The use of the digital signal processing and increasingly sophisticated methodologies continue to improve TDLS sensitivity and selectivity. Initially 0.70…1.70 μm wavelengths laser diodes were developed for telecommunications helping to cover the most gases presented in the combustion environment (see Fig. 1). At near IR wavelengths, molecular absorption band strengths are significantly weaker than in the fundamental absorption region and high sensitivity

detection techniques such as Frequency Modulation Spectroscopy (FMS) and Wavelength Modulation Spectroscopy (WMS) were employed to improve sensitivity and selectivity. Higher sensitivity can be also achieved by using specific microstructures such as Hollow-Core Photonic Bandgap Fibres (HC-PBFs) or high Q cavities that provide longer absorption path lengths for the gases. In micro-sphere based optical cavities, light can be confined by total internal reflection in a so-called Whispering Gallery Mode (WGM) [39]. As the light is guided along the spherical surface of the glass-gas interface, a significant part of the evanescent optical field exists outside the micro-sphere and can be used to interact with gas and to measure the optical absorption. Q factors in glass micro-spheres can be as high as 10 million giving a huge increase in the effective path length and hence absorption sensitivity.

TDL O_2 analyzer would provide near real time measurements with no cross interference to other gases in the combustion environment with an advantage of non-contacting procedure suitable for many aggressive applications.

Considering initially the alignment across the gas stream (Fig. 19) as a major issue in the reliability of oxygen measurements there were some attempts to spread the laser beam to keep the alignment but this would significantly reduce the signal intensity and signal-to-noise ratio, making the measurement sometimes more erratic. Another approach with flexible bellows improving the alignment reliability in the vibration environment was implemented by Yokogawa (Fig. 20).

Highly promoted by Mettler-Toledo Process Analytics an in situ TDL O_2-probe (Fig. 21) with the deflector on the probe end would eliminate misalignment problem but this in situ probe will be exposed to the severe process environment and deflection mirror or prism would be limiting factor for the probe's operation temperature. TDL O_2-probe would provide single point measurement like Zirconia in situ O_2-probe but at much higher cost.

Even TDL O_2 analyzer is promoted to provide the most accurate average O_2-reading in the process, considering the flue gas stratification in the duct, with ~1…5 % oxygen concentration variation, a laser beam ~5…20 cm in diameter shooting

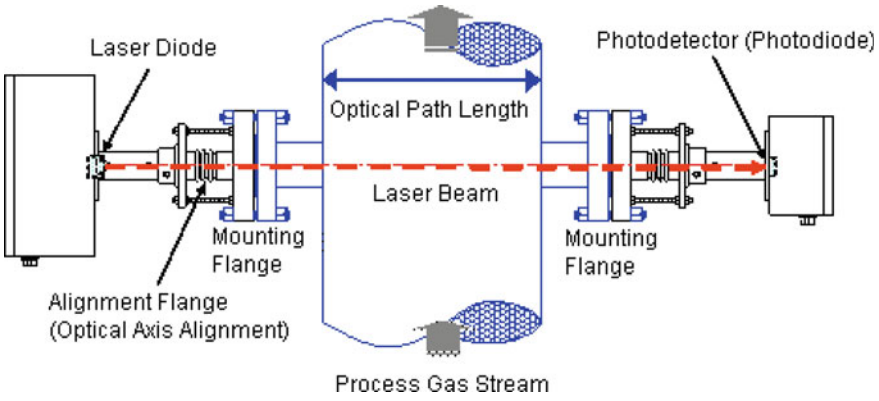

Fig. 19 A typical installation of TDL O_2-analyzer across the combustion duct [40]

Fig. 20 Alignment improvement with flexible bellows without affecting the process seal [41]

Fig. 21 An in situ TDL O_2-analyzer for the clean (top) and dusty applications [42]

across the duct, would be unlikely much more representative than zirconia O_2-analyzer single point measurement. With the increasing temperature oxygen absorption intensity would be reduced [43] and this might bring some challenge in the interpretation of weaker intensity at higher temperature and temperature variation compensation affecting oxygen concentration calculation and contributing to signal to noise ratio reduction. Temperature and pressure variation in the process even claimed to be compensated might bring an additional error in the oxygen measurements. Calibration and validation of TDL O_2 analyzer on line is still waiting for a conclusive answer. Implemented in some TDL instrumentation a reference cell has a different temperature compared to the process and is very short to provide very reliable in situ validation. Alignment across the stack and IR light reflection at high temperature combined with the process windows fouling and wide background radiation from the fire ball or box would bring many challenges in the application and might reduce service life of the TDL O_2-analyzer. Fiber coupled

Fig. 22 TDL O_2 analyzers on the market

laser solution increases the optical noise by a factor of 5–7 compared to the free air lasers [43] and would reduce the sensitivity with detection limit ~500 ppm. The major players on TDL analyzers market are Neo Monitors (Norway), Yokogawa (Japan), Focused Photonics Inc. (China) and Siemens (Germany) (Fig. 22).

One significant difference between traditional Zirconia O_2-sensor single point measurements and TDL O_2 analyzer path average measurements is that the path measurement does not provide spatial information [33]. Zirconia O_2 probes are providing a measurement at a particular point in the process with very useful information identifying variations in O_2 concentration levels caused by burner to burner (unbalanced burners) and this information can be successfully used for the burner diagnostics.

More details on TDLS theoretical background and application can be found in the latest reviews [29, 30, 44–47]. Performance and application option of some of TDL O_2 analyzers on the market is summarized in Table 2.

With wide applicability, TDL O_2 analyzers are enjoying great popularity but being ~4−5 times more expensive compared to the zirconia O_2 analyzers and additional, very expensive and sophisticated up to 4 months installation [32, 33] are generally covering right now special chemicals production and very high temperature (>1400 °C) applications where zirconia O_2-analyzers would be rejected by severe temperature environment or the probe might contaminate the chemicals in the production. An extractive zirconia O_2 analyzer might be considered as an alternative less expensive option for these applications. Majority of the combustion systems is still using zirconia oxygen O_2 analyzers.

Table 2 Tdl O_2 analyzers performance and application options

Company	Product	Detection limit	Accuracy	Application
Yokogawa (Japan)	TDLS8000	Application dependent	±1.0 % or ± 0.01 % O_2	Across the duct, Installation over the fire ball
Siemens (Germany)	SITRANS SL	0.02 % O_2	±1.0 %	Across the duct
ABB (Swiss)	LS4000	0.05 % O_2	±0.2 %	Across the duct No nitrogen purging required
Ametek (USA)	**TDLAS 5100**	0.01 % O_2	±1.0 % or ±0.03 % O_2	Extractive
Servomex (UK)	SERVOTOUGH MiniLaser Oxy	0.01 % O_2	±1.0 % or ±0.01 % O_2	Across the duct
Sick Maihak (Germany)	TRANSIC151LP O_2	0.01 % O_2,	±0.2 % O_2	In situ probe (<80 °C)
Mettler-Toledo (USA-Swiss)	TDLS GPro 500	0.01 % O_2	±2.0 % or ±0.01 % O_2	In situ probe (250 °C or 600 °C with thermal barrier)
Fuji Electric (Japan)	ZSS6 O_2/CO Analyzer	N/A (0.01 % O_2?)	±2.0 % of FS	Across the duct, Dual measurement
NEO Monitors (Norway)	LaserGas III SP	0.01 % O_2	±1 %	Across the duct
Focused Photonics Inc. (China)	LGA-4100 (in situ) LGA-4500 (extractive)	0.01 % O_2	±1 %	Across the duct & extractive
TDL Sensors Ltd (UK)	LGM-CD	0.05 % 20 ppm O_2	N/A	Across the duct
Zolo Technologies (USA)	ZoloBoss 4-channel unit (O_2, CO, CO_2, H_2O)	0.01 % O_2	±0.5 %	Across the duct
Oxigraf Inc. (USA)	O2iL, O2iC, O2E, O2E2, O2C, O2D, O2L	0.01 % O_2	±0.2 %	Extractive

4 Paramagnetic Oxygen Gas Sensing Technology

Oxygen with two unpaired electrons is well known paramagnetic gas and would be attracted into a strong magnetic field. These paramagnetic properties enable relatively selective oxygen measurements method used by industries over fifty years and applied in three different methodologies: magnetodynamic, thermomagnetic or magnetic wind and non-contact Quinke method [48]. The magnetodynamic oxygen

sensors are dumbbell or of the magnetic pressure type. In the dumbbell type O_2-sensor incorporates two nitrogen-filled glass spheres mounted on the rotating suspension (Fig. 23). This assembly is in a strong magnetic field and with the gas sample containing oxygen introduced into the magnetic field, the oxygen molecules will tend to approach the strongest part of the magnetic field pushing the dumbbell aside and causing the suspending wire to be twisted. This twist is detected as the movement of the light from the reflective mirror located at the suspending wire centre (Figs. 23 and 24). The output from the photo-sensor would be fed back to a coil around the suspension assembly restoring torque to the original "zero" position. The current would be directly proportional to the magnetic susceptibility of the sample oxygen gas and oxygen partial pressure. The applied current will be proportional to the oxygen concentration in the gas mixture and would be used for the precise oxygen calculation. This method with the high linearity and good response is however highly sensitive to the different mechanical shocks, like vibration. In the magnetic pressure type O_2-sensor a small amount of reference gas like pure nitrogen or air is externally supplied through a small hole made on one of the magnetic poles. When the sample gas is introduced into uneven magnetic field, paramagnetic oxygen gas would be attracted toward the strongest part of the magnetic field, in which the magnetic poles have come closer to each other. The increase in pressure resulting from the attraction of oxygen can be detected with a capacitor microphone type detector or a mass flow sensor. In order to ensure the stable signals detection, the two magnetic poles are alternately excited to amplify the alternating current. The selectivity of this method is pretty high but a reference gas would be required for these measurements. Thermomagnetic O_2-sensor (magnetic wind method) has two chambers with heating wire element located at the centre. A magnetic field would be provided only on the measurement chamber.

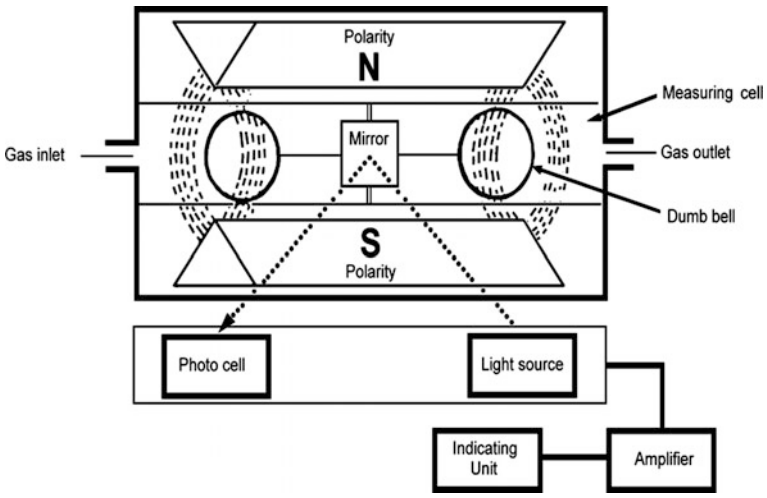

Fig. 23 Paramagnetic O_2-sensor schematically [49]

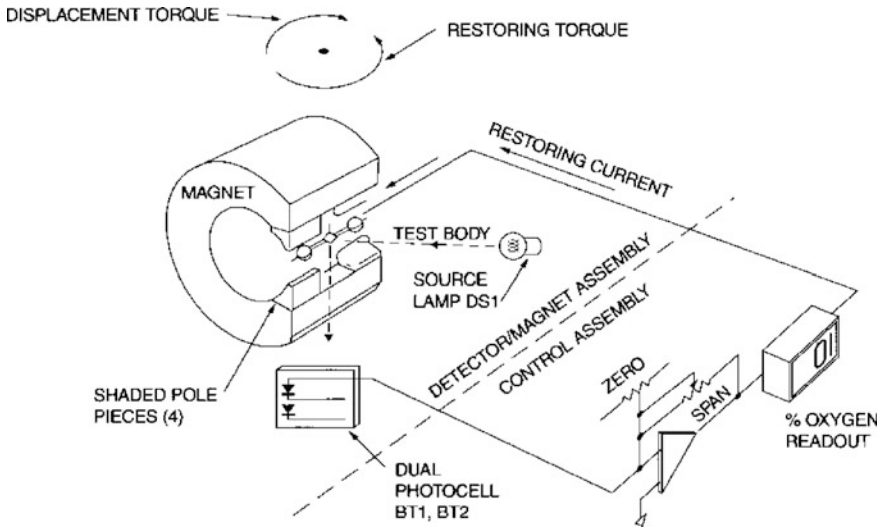

Fig. 24 Paramagnetic O_2-sensor operation [50]

After the analysing oxygen gas is entering the measurement chamber, oxygen would be attracted by the magnetic field and then heated using the heating wire element. The magnetic oxygen flow would be cooling the heating wire element as its intensity varies proportional to the oxygen concentration. The resistance changes during this process would be picked up as unbalanced voltage at the Wheatstone bridge to measure the oxygen concentration. The magnetic wind type analyzer has no movable parts and is more stable in the vibration environment. Carbon dioxide with the some positive interference for oxygen by the small variation in the concentration can be compensated.

Quincke O_2-detector utilizes a pneumatic Wheatstone bridge for the measurements using a differential pressure or flow to determine the oxygen concentration. Reference gas is used so the sample does not come in contact with the sensor. The reference gas is divided into two flow paths recombining at the reference gas outlet, where the sample gas is also introduced. A magnetic field is in one arm of the reference gas outlet creating a back pressure related to the presence of the oxygen in the gas sample.

Measurement range for the paramagnetic O_2-sensor is typically between 0.05 % and 100 % O_2 and sensor can be very precise under certain conditions [48] but would require quite expensive gas sample conditioning system to stabilize the process gas flow, pressure and temperature and to remove hazardous gases and dust. The major disadvantages of the paramagnetic oxygen sensors are the price, low stability in the vibration environment and relative low accuracy ($\pm$ 0.10… 0.25 % O_2). Paramagnetic analyzers have been historically limited to the extractive application with general use (Fig. 25) or intrinsically safe instrumentation version (Fig. 26) and maximum external operation temperature up to 120−145 °C.

Fig. 25 Paramagnetic O_2 analyzer [51]

Fig. 26 Intrinsically safe paramagnetic O_2 analyzer [52]

Paramagnetic O_2-sensor can be also implemented in Multicomponent gas analyser like X-STREAM (Fig. 27) often used in a combination with gas conditioning system (GCS) in Continuous Emission Monitoring System (CEMS).

With some good success paramagnetic O_2-analyzers were used for the process control and monitoring in the chemical and petrochemical industries, combustion efficiency control, ceramic and cement industry, inert gas blanketing and industrial safety in food and beverage industries. With gas handling design paramagnetic oxygen analyzer will be well suiting for the precise ($\pm$0.2 ppm) atmospheric oxygen measurements [54], can be miniaturized using MEMS [55] but can't overcome the technology weaknesses related to the not the strongest magnetic

Fig. 27 Paramagnetic O_2-sensor implemented in X-STREAM analyzer [53]

nature of the oxygen limiting the detection to >100 ppm O_2 and moving parts in the design highly limiting applications especially in high temperature and humid vibration environment. Paramagnetic analyzers are lately often expelled by the new advanced Tunable Diode Laser (TDL) analyzers (see Sect. 3 of this review) providing more expensive but likely more reliable and more precise measurements according to TDLS publications.

Paramagnetic oxygen analyzers are applied to the measurement of trace oxygen concentration in various manufacturing processes, city gas quality control, safety control at various plants, oxygen concentration control of flammable gas containing mixtures and coke dry quenching (CDQ) plants for the steelmaking.

5 Amperometric Oxygen Gas Sensing Technology with Liquid Electrole (Clark Cell)

The electrochemical O_2-sensors with liquid electrolyte date back to the 50th and were used for the environmental oxygen monitoring providing warning of abnormal conditions in industrial safety environments, i.e., mines, oil production facilities and chemical plants. Oxygen measuring instruments containing electrochemical sensors based on consumable lead anodes have been available for over 30 years [56]. These type electrochemical oxygen sensors are metal-air battery type with the diffusion limited barrier [56, 57] and oxygen sensor generates a current proportional to the oxygen diffusion to the cathode limited by the diffusion film or capillary barrier (Fig. 28). Such barriers are typically made of thin, low-porosity Teflon membranes. Besides offering a mechanical protection to the sensor, the membrane performs the additional function as a filter. Selecting the correct pore size of the membrane and capillary is necessary to transfer the proper amount of gas molecules. The pore size should be optimized to allow enough gas molecules to reach the sensing electrode but be small enough to prevent liquid electrolyte from leaking out or drying too quickly.

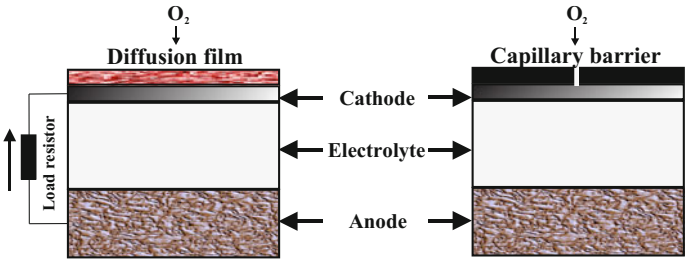

Fig. 28 Electrochemical O_2-sensor with liquid electrolyte

Oxygen in contact with the cathode is reduced to hydroxyl ions, with a balancing reaction of lead oxidation at the anode:

$$\begin{aligned} &\text{Cathode:} \quad O_2 + 2H_2O + 4e^- \rightarrow 4OH \\ &\text{Anode:} \quad 2Pb + 4OH^- \rightarrow 2PbO + 2H_2O + 4e^- \end{aligned} \tag{4}$$

This electrochemical reaction would be resulting in the lead anode oxidization and with the cell electrochemical properties changes a periodic calibration would be always required. The consumption of the lead anode would also limit the sensor life therefore the major part of the oxygen electrochemical sensor with liquid electrolyte should be constructed from lead anode (Fig. 29) to increase the operation life of the sensor.

The lower would be the oxygen concentration to be measured the longer operation life will be expected and these sensors are designed to last for not more

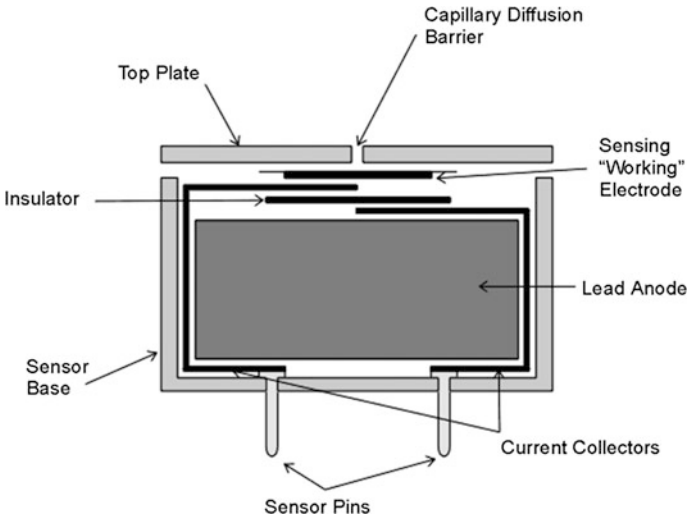

Fig. 29 Oxygen sensor schematic [58]

Fig. 30 Oxygen sensor from City Technology, Honeywell Corp [59]

than one or two years. Some components of the flue gas like carbon dioxide (CO_2) and chlorine (Cl_2) might increase the rate of the oxidation or would react with the lead shortening the life of the sensor. A dust protector is normally installed on the top of the sensor (Fig. 30) to reduce diffuser hole or film pluggage and a scrubber filter is sometimes installed in the front of the sensor to improve the sensor selectivity.

There is a limited selection of the filters with the different efficiency degrees. The most commonly used filter medium is activated charcoal filtering most chemicals except of carbon monoxide (CO) and hydrogen (H_2).

This oxygen electrochemical technology with the liquid electrolyte has been one of the key technologies enabling the availability of the small, compact instrumentation for different applications with the estimated over 50 million sensors sold world-wide since 1980 [56] and this technology is still continuing to dominate industrial safety application. Although lead was recognized as offering an attractive combination of suitable properties some metals like cadmium, bismuth, antimony and copper were identified as potential lead free candidates with only copper being available in a high surface area wire form. With a number of alternative approaches offering longer lifetime for lead-free oxygen sensors a little market penetration was achieved so far. More details on the electrochemical oxygen gas sensing technology with liquid electrolyte latest development can be found in the recent review [56]. These electrochemical oxygen sensors are mostly supplied by City Technology Ltd (UK) and Drägerwerk AG (Germany) and are used primary for the industrial safety or oxygen monitoring at room temperature in portable analyzers and Continuous Emissions Monitoring Systems (CEMS) with the gas conditioning employed.

Acknowledgment The author would like to thank Rosemount Liquid and Combustion Analysis for the research program support.

References

1. J.C.G. Walker, The oxygen cycle, in *The natural environment and the biogeochemical cycles*, ed. by O. Hutzinger (Springer, Berlin, Heidelberg, New York, 1980), pp. 87–104
2. N. Lane, *Oxygen: the molecule that made the world* (Oxford University Press, New York, 2002)
3. N. Docquier, S. Candel, Process control and sensors: a review. Prog. Energy Combust. Sci. **28**, 107–150 (2002)
4. P. Shuk, Process Zirconia oxygen analyzer—state of art. Tech. Mess. **77**, 19–23 (2010)
5. C. Wu, T. Yasukawa, H. Shiku, T. Matsue, Fabrication of miniature Clark oxygen sensor integrated with microstructure. Sens. Actuators **B110**, 342–349 (2005)
6. C. Manning, R.F. Keeling, J.P. Severinghaus, Precise atmospheric oxygen measurements with a paramagnetic oxygen analyzer. Global Biogeochem. Cycles **13**, 1107–1115 (1999)
7. A. Mills, Optical oxygen sensors utilizing the luminescence of platinum metals complexes. Platinum Met. Rev. **41**, 115–127 (1997)
8. S. Chu, Y.L. Lo, T.W. Sung, Review on recent developments of fluorescent oxygen and carbon dioxide optical fiber sensors. Photonic Sens. **1**, 234–250 (2011)
9. W.C. Maskell, B.C.H. Steele, Solid state potentiometric oxygen gas sensors. J. Appl. Electrochem. **16**, 475–489 (1986)
10. R. Ramamoorthy, P.K. Dutta, S.A. Akbar, Oxygen sensors: materials, methods, designs and applications, J. Mater. Sci. 38: 4271–4282
11. W.C. Maskell, Inorganic solid state chemically sensitive devices: electrochemical oxygen gas sensors. J. Phys. E: Sci. Instrum. **20**, 1156–1168 (1987)
12. W. Göpel, G. Reinhardt, M. Rösch, Trends in the development of solid state amperometric and potentiometric high temperature sensors. Solid State Ionics **136–137**, 519–531 (2000)
13. J.W. Fergus, Doping and defect association in oxides for use in oxygen sensors. J. Mater. Sci. **38**, 4259–4270 (2003)
14. N. Barsan, M. Schweizer-Berberich, W. Göpel, Fundamental and practical aspects in the design of nanoscaled SnO_2 gas sensors: a status report. Fresenius J. Anal. Chem. **365**, 287–304 (1999)
15. N. Barsan, D. Koziej, U. Weimar, Metal oxide-based gas sensor research: How to? Sens. Actuators **B121**, 18–35 (2007)
16. A. Oprea, N. Bârsan, U. Weimar, Work function changes in gas sensitive materials: Fundamentals and applications. Sens. Actuators **B142**, 470–493 (2009)
17. H. Wang, L. Chen, J. Wang, Q. Sun, Y. Zhao, A micro oxygen sensor based on a nano sol-gel TiO_2 thin film. Sensors **14**, 16423–16433 (2014)
18. H. Peters, H.H. Möbius, Procedure for the gas analysis at elevated temperatures using galvanic solid electrolyte elements (Germ), DD-Patent 21673 (1961)
19. J. Weissbart, R. Ruka, Oxygen gauge. Rev. Sci. Instrum. **32**, 593–595 (1961)
20. P. Shuk, E. Bailey, U. Guth, Zirconia oxygen sensor for the process application: state of art. Sens. Transducer **90**, 174–184 (2008)
21. H.H. Möbius, Basics of oxygen gas potentiometric analysis (Germ). Z. Phys. Chem. **230**, 396–416 (1965)
22. http://www.fujielectric.com/products/instruments/library/catalog/box/doc/ECNO341b.pdf
23. D.M. Haaland, Internal-reference solid-electrolyte oxygen sensor. Anal. Chem. **49**, 1813–1817 (1977)
24. H. Kaneko, T. Okamura, H. Taimatsu, Y. Matsuki, H. Nishida, Performance of a miniature zirconia oxygen sensor with a Pd-PdO internal reference. Sens. Actuators **B108**, 331–334 (2005)
25. J.V. Spirig, R. Ramamoorthy, S.A. Akbar, J.L. Routbort, D. Singh, P.K. Dutta, High temperature zirconia oxygen sensor with sealed metal/metal oxide internal reference. Sens. Actuators **B124**, 192–201 (2007)

26. K. Dunst, G. Jasinski, P. Jasinski, Potentiometric oxygen sensor with solid state reference electrode. Metrol. Meas. Syst. **21**, 205–216 (2014)
27. E.D. Hinkley, P.L. Kelley, Detection of air pollutants with Tunable Diode Lasers. Science **171**, 635–639 (1971)
28. P. Werle, A review of recent advances in semiconductor laser based gas monitors. Spectrochim. Acta **A54**, 197–236 (1998)
29. P.A. Martin, Near-infrared diode laser spectroscopy in chemical process and environmental air monitoring. Chem. Soc. Rev. **31**, 201–210 (2002)
30. R.K. Hanson, Applications of quantitative sensor laser to kinetics, propulsion and practical energy systems. Proc. Combust. Inst. **33**, 1–40 (2011)
31. S.J. Rye, *TDL: One Size No Longer Fits All, 59th Analysis Division Symposium, ISA*, vol. 503 (Curran Associates Proc, Red Hook, 2014), pp. 1–16
32. J.D. Tate, Development of in situ analysis for the chemical industry. DOE report (DE-FC36-02ID14428) (2006)
33. J.D. Tate, Advanced Combustion Diagnostics and Control for Furnaces, Fired Heaters and Boilers. DOE report (DE-FG36-06GO16093) (2010)
34. Y. Krishna, S. O'Byrne, J.J. Kurtz, Baseline correction for stray light in log-ratio diode laser absorption measurements. Appl. Opt. **53**, 4128–4135 (2014)
35. S. Langridge, On line measurement of oxygen: review and new developments, in *55th Analysis Division Symposium*, ISA, vol. 481. Curran Associates Proc, Red Hook (2010), pp. 113–127
36. H. Li, G.B. Rieker, X. Liu, J.B. Jeffries, R.K. Hanson, Extension of wavelength-modulation spectroscopy to large modulation depth for diode laser absorption measurements in high-pressure gases. Appl. Opt. **45**, 1052–1060 (2006)
37. G.B. Rieker, J.B. Jeffries, R.K. Hanson, Calibration-free wavelength-modulation spectroscopy for measurements of gas temperature and concentration in harsh environments. Appl. Opt. **48**, 5546–5560 (2009)
38. G.B. Rieker, Wavelength-modulation spectroscopy for measurements of gas temperature and concentration in harsh environments, Ph.D. thesis, Stanford University (2009)
39. D. Farnesi, A. Barucci, G.C. Righini, S. Berneschi, S. Soria, G. Nunzi Conti, Optical frequency conversion in silica - whispering-gallery-mode microspherical resonators. Phys. Rev. Lett. **112**, 093901 (2014)
40. http://www.yokogawa.com/an/faq/tdls/spec_1.htm
41. http://www.appliedmc.com/content/images/TDLS200_BU_WEB.pdf
42. http://us.mt.com/dam/MTPRO/Brochures/Leporello_GPro500_en.pdf
43. http://specanalytics.com/index.php?route=information/information&information_id=13
44. R.F. Curl, F.K. Tittel, Tunable infrared laser spectroscopy. Ann. Rep. Prog. Chem **C98**, 219–272 (2002)
45. M. Lackner, Tunable diode laser absorption spectroscopy (TDLAS) in the process industries—a review. Rev. Chem. Eng. **23**, 65–147 (2011)
46. F.K. Tittel, R. Lewicki, R. Lascola, S. McWhorter, Emerging infrared laser absorption spectroscopic techniques for gas analysis, in *Trace Analysis of Specialty and Electronic Gases*, ed. by W.M. Geiger, M.W. Raynor (John Wiley & Sons Inc, New York, 2013), pp. 71–109
47. K. Kohse-H inghaus, R.S. Barlow, M. Alden, J. Wolfrum, Combustion at the Focus: Laser Diagnostics and Control. Proc. Combust. Inst. **30**, 89–123 (2005)
48. R.P. Kovacich, N.A. Martin, M.G. Clift, C. Stocks, I. Gaskin, J. Hobby, Highly accurate measurement of oxygen using a paramagnetic gas sensor. Meas. Sci. Technol. **17**, 1579–1585 (2006)
49. http://www.systechillinois.com/en/paramagnetic-cells_54.html
50. http://www2.emersonprocess.com/siteadmincenter/PM%20Rosemount%20Analytical%20Documents/PGA_Manual_755A_199707.pdf
51. http://www.yokogawa.com/an/download/general/GS11P03A05_01E.pdf
52. http://www.keison.co.uk/products/servomex/Oxy1900.pdf

53. http://www2.emersonprocess.com/siteadmincenter/PM%20Rosemount%20Analytical%20Documents/PGA_PDS_X-STREAM_XEGP.pdf
54. C. Manning, R.F. Keeling, J.P. Severinghaus, Precise atmospheric oxygen measurements with paramagnetic oxygen analyzer. Global Biogeochem. Cycles **13**, 1107–1115 (1999)
55. S. Vonderschmidt, J. Muller (2010) A novel micro paramagnetic oxygen sensor. In: Micro Electro Mechanical Systems (MEMS). 23rd IEEE International Conference, pp. 903–906
56. M. Willett, Oxygen sensing for industrial safety—evolution and new approaches. Sensors **14**, 6084–6103 (2014)
57. K.S. Goto, *Solid state electrochemistry and its applications to sensors and electronic devices* (Elsevier Science Publishers, New York, 2013)
58. http://www.citytech.com/index.html
59. http://www.hsmsearch.com/page_527804.asp

Application of Practical Nitrate Sensor Based on Electrochemical Impedance Spectroscopy

Md Eshrat E. Alahi, Xie Li, Subhas Mukhopadhyay and L. Burkitt

Abstract Nitrate is a naturally occurring ionic compound that is part of nature's nitrogen cycle. Nitrates are readily lost to ground and surface water as a result of intensive agriculture, disposal of human and animal sewage and industrial wastes and the impact of elevated nitrate concentrations on water quality, has been identified as a critical issue facing New Zealand's future. It is therefore, highly desirable to monitor water quality to facilitate regional councils and central governments to understand trends in concentrations and to develop a healthy water management policy. Presently, water quality managers follow the traditional measurement systems that involve physically sampling water from remote sites and laboratory-based testing. These methods are expensive, require trained people to analyze the data and produce a lot of chemical waste. Due to the time and labor required, surface samples are often only collected once per month and these risks missing significant trends in nitrate loss. Therefore, it is of utmost important to develop low-cost, robust embedded sensor nodes to detect the concentration of individual nutrients like nitrate and nitrite in surface and ground water. The interdigital capacitive sensor has been used to measure the different nitrate concentration. The sensor used to measure also the temperature and humidity of the samples. The results have shown that the sensor has high potential in a different application.

1 Introduction

Fresh water is an important part of New Zealand's way of life and economy. The water quality of lakes, rivers, streams, and aquifers in New Zealand is variable and depends mainly on the dominant land use in the catchment. Water quality is good in the areas of indigenous vegetation and less intensive use of land, however, it is poorer where there are pressures from urban and agricultural land use [1]. Rivers in

M.E.E. Alahi · X. Li · S. Mukhopadhyay (✉) · L. Burkitt
Massey University, Palmerston North, New Zealand
e-mail: S.C.Mukhopadhyay@massey.ac.nz

S. Mukhopadhyay et al. (eds.), *Sensors for Everyday Life*, Smart Sensors, Measurement and Instrumentation 23, DOI 10.1007/978-3-319-47322-2_6

New Zealand has reduced water clarity and aquatic life, and higher concentrations of nutrients and Escherichia coli (E.coli) bacteria [1].

The growth of population and increasing agricultural land use have placed increasing pressure on waterways. Between 1990 and 2012, the estimated amount of nitrogen (N) that leached into the soil from agriculture increased 29 % [1]. The reason for this was due to the numbers of livestock (6.4 million dairy cattle and 29.5 million sheep [2]) (and, therefore, urine contains high concentrations of nitrogen (N)) and the use of N fertilizer. Between 1989 and 2013, total N concentrations in rivers increased between 12 to 60 % in the 77 monitored sites around the country which was monitored by NIWA, the National Institute of Water and Atmospheric Research. The physical impact of excessive N concentrations in New Zealand rivers can be nuisance plantopic algae (includes blue green algae), benthic algae (includes periphyton) and macrophytes(rooted plants) growth. This growth reduces oxygen levels in the water, hampers river flows, and smothers the riverbed and plant life, which fish and other aquatic animals depend on for food and habitat. About 49 % of monitored river sites currently have enough N to trigger periphyton growth. High levels of N can also be harmful to fish [1]. A common form of nitrogen is nitrate, nitrite, and ammonium. In the human body, nitrite can react with secondary or tertiary amines forming nitrosamines, which are recognized as carcinogenic agents. When existing in high concentrations in the blood, nitrite can also react with iron(II) in hemoglobin to form methemoglobin, which has no ability to carry oxygen [3–5]. Nitrate can also have the same toxic effects because it can be reduced to nitrite by bacterial colonies that reside within the mouth [6]. Anthropogenic actions, such as agriculture, discharge of industrial and domestic wastewaters and vehicle emissions, have caused the increases in the concentrations of inorganic nitrogenous compounds in aquatic ecosystems [4, 6, 7]. Ingested nitrate from polluted drinking waters can cause methemoglobinemia, particularly in young infants, and also have a potential role in developing cancers of the digestive tract due to the formation of nitrosamines [4]. The regular monitoring of the levels of nitrate in water is, therefore, relevant because of their potentially harmful impact on both the environment and human health.

2 Motivation

New Zealand's lakes, rivers, and groundwater are regularly monitored by regional councils, NIWA, and community interest groups. New Zealand's river network has a total stream length of 199,641 km. Regional councils monitor river water quality to manage environmental impacts. NIWA also monitors water quality at 77 sites on 35 major river systems. Figure 1 indicates the different monitoring sites by NIWA. These sites tend to be in catchments dominated by agricultural land use. Regional councils measure a range of parameters at each of the sites they monitor. The parameters include turbidity, rainfall, different nutrients (nitrate, nitrite, ammonium, and phosphate), pH, Dissolved Oxygen (DO).

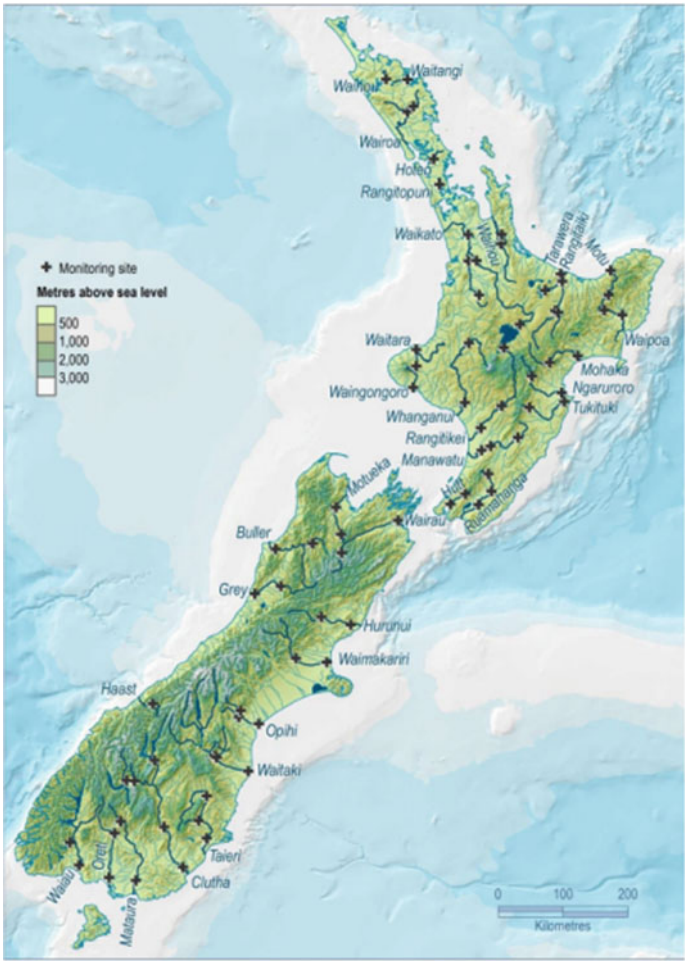

Fig. 1 National River water quality network sites [1]

2.1 Present Status of Water Quality Study

Locally, a water quality monitoring study has been established at Massey University's Agricultural Experiment Station, called Tuapaka, to examine the impact of hill country beef and sheep grazing on stream water quality. This farm is located 15 km from the Massey University campus in Palmerston North and provides the resources for the testing and validation of a water quality sensor for nitrate and nitrate. Currently, water samples are manually collected from Tuapaka every two weeks and analysed for nitrate and ammonium concentrations measured using the colorimeter method using a Technicon Auto-Analyzer in the laboratory.

Weirs (Fig. 2a) have been installed at various locations around Tuapaka (Fig. 2b) to monitor stream flow and water quality. These sites will be used to test and validate the sensors under field conditions. Stream and river water contain sediment and organic material. Under the current manual sampling regime, samples are filtered through a 0.45 μm filter prior to nitrate analysis. It will, therefore, be important to test the sensors performance in the presence of sediments and organic material. The sensors functionality and robustness will also need to be tested under the harsh weather conditions experienced in the remote stream and river locations.

2.2 Current Laboratory Measurement System

Technicon Auto-Analyzer uses continuous flow system (CFS), which samples are taken automatically from the sample tray and pump adds the appropriate reagents. Samples are passed through manifold for mixing, filtering and heating. The colorimeter then measure the absorbance of color in the reaction of sample and is displayed in the recorder [8].

Figure 3 shows the Technicon Auto Analyzer used to determine both of nitrate and ammonium concentration in the laboratory using the current method. The Auto analyzer is set up with a heating bath at 28–29 °C and uses 520 nm filters in the colorimeter. A red azo dye and an indo-phenol prussian blue dye are used to measure nitrate and ammonium respectively. Reagents used for nitrate-N detection include catalyst solution, sodium hydroxide solution, hydrazinum sulphate solution and so on (as shown in Fig. 3b). Reagents are pumped into the system for about 30 min to ensure the system is flushed completely. In the sample tray (Fig. 3a), the prepared nitrate standard and water samples are put in the sample tray. The probe will take each sample in the preset time interval into the system. The samples and reagents are mixed in the system (Fig. 3c) and the measurement is done by a colorimeter (Fig. 3d). The colorimeter analyzes the intensity of the color and the results are displayed on a chart recorder in the computer. This recorder baseline should be set along with the colorimeter baseline control before the measurement starts by standard calibration. This method requires expensive equipment and trained staff to conduct measurements in addition to the limitation on water samples collection, which can only be collected periodically. This approach risks missing key changes in nitrate-N concentration when river-flow rapidly rises or falls. Although high-frequency nitrate sample equipment is available, these cost in the order of $30–50,000.

Typically nutrient and sediment concentrations change with increasing and decreasing stream or river flow rates (Fig. 4). Therefore, a monthly or fortnightly sampling regime may not adequately represent the concentration nutrient profile. This could influence our understanding of the seasonal effects on nutrient loss as well as the total loads of nutrients (i.e. kg of nitrate/ha) estimated to be leaving a catchment. This information is critical for reginal councils to implement policy and management around water quality in their catchments.

Fig. 2 Water sample collection

(a) Paddock down the hill

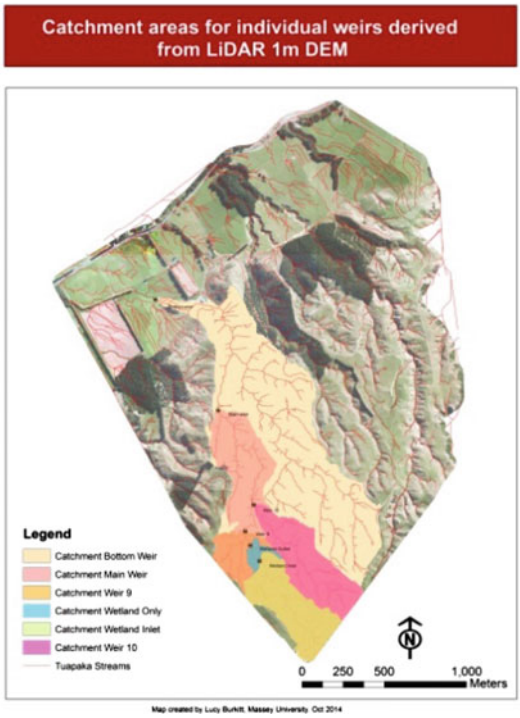

(b) Monitoring sites in Tuapaka

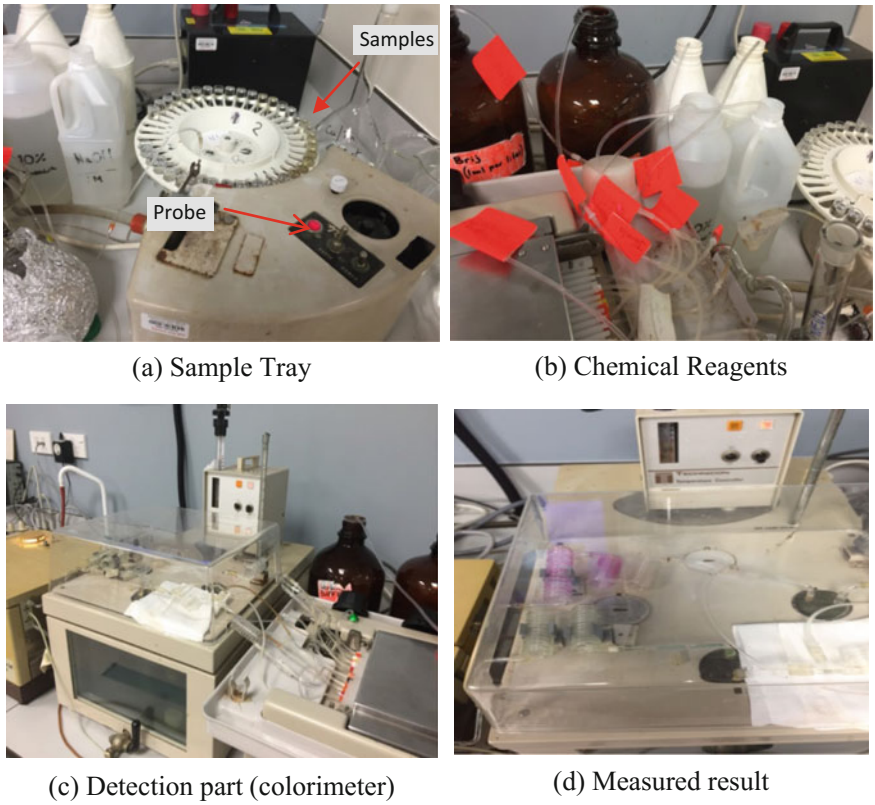

(a) Sample Tray (b) Chemical Reagents

(c) Detection part (colorimeter) (d) Measured result

Fig. 3 Technicon Auto Analyzer currently used in the laboratory

2.3 Laboratory Based Measurement Technique

The maximum permissible levels of nitrate–N and nitrite–N in fresh waters at 10 and 1 mg L−1, respectively [9]. The determination of nitrite and nitrate has been the study object of numerous researchers and a diversity of analytical methods have been developed for this purpose [6]. These include kinetic methods [8], ion chromatography [10, 11], gas chromatography–mass spectrometry [12], capillary electrophoresis [13], electrochemical methods [14–18], luminescence [19] and spectrophotometric methods [5, 20–26]. However, most of these methods have as a disadvantage the employment of large volumes of toxic reagents, the application of time-consuming procedures and complicated systems [27]. Therefore, the development of simple, rapid and reliable methods for the quantification of nitrite and nitrate is opportune.

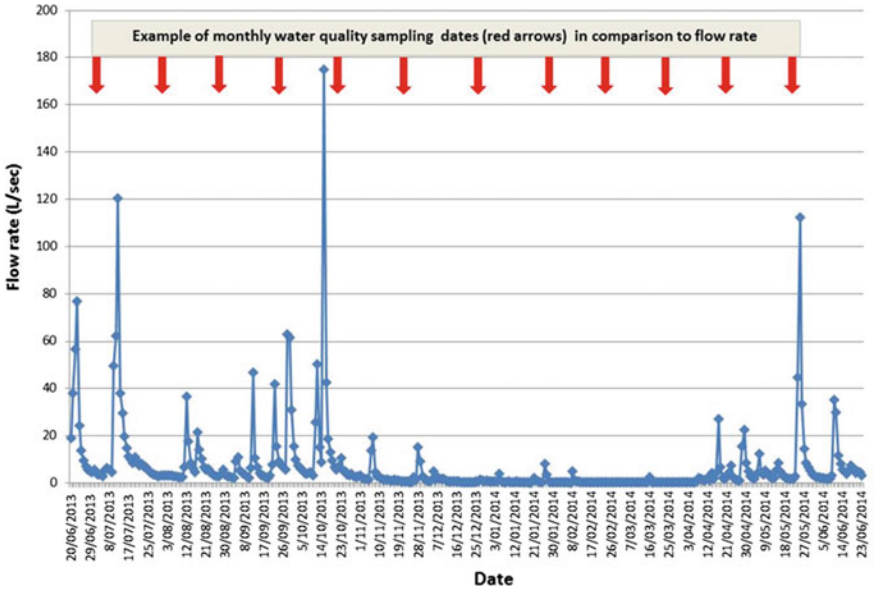

Fig. 4 Sampling date in comparison to flow rate

2.4 Market Research

Hach is well-known as suppliers of an analytical instrument and chemical reagents for the laboratory-based purpose, especially for water quality and other liquid solutions. Take IntelliCal ISENO3181 Nitrate Ion Selective Electrode (ISE) for nitrate detection as an example; it is designed by the solid-state PVC membrane with epoxy, and solid gel ion exchange eliminates the frequency of replacing membrane. The ISE can only be used periodically in the lab or field and is not suited to continual measurement. It can detect the nitrate-nitrogen concentration from 0.1 to 14000 mg/L. It has an integrated temperature sensor which can measure the temperature range from 0–50 °C. The price is at $2100. Hach Nitratax sc tank sensor is being used extensively internationally and in New Zealand. It uses the UV absorption measurement with reagent-free technique. There are three different models with the different detection range: 0.1–100 mg/L by Nitratax plus sc; 1.0–20 mg/L by Nitratax exo sc; and 0.5–20 mg/L by Nitratax clear sc. These models cost around $40 k to 60 k.

"S::can" is Austria-based Company which provides varied product range for water and environmental monitoring. All "s::can" instruments are operated followed by the "plug & measure" principle, so all of them are ready to use with pre-calibrated works. The "spectro::lyser" UV monitors can be used to NO_3-N detection. It is measured based on the UV-Vis spectrometry with the nitrate detection range from 0–20 mg/L. This instrument is also being used extensively

internationally and in New Zealand. However, the whole set of the system is very expensive (around $60–70 k).

Hanna Instruments is focused on developing electro-analytical instrumentation. They provide the products like nitrate portable/benchtop photometer and nitrate ion selective electrode. For example, Hanna HI96728 is a portable checker to detect nitrate in freshwater based on the colorimetric method. A special Tungsten lamp is used as the light source and silicon photocell with narrow band interference filter at the wavelength of 525 nm used to detect the light. It uses the cadmium reduction method to determine the nitrate-nitrogen concentration range from 0.0 to 30.0 mg/L. The price is at around $350 NZD.

Xylem is a world leader in providing compact instruments for water technology. It has a broad range of products under different brands. YSI is one of Xylem brand, which providing the environmental monitoring products. IQ SensorNet 182 is a modular water quality terminal which allowed connecting additional sensors such as 6884 Nitrate ISE sensor and it provides a continuously measurement of water quality parameters like pH, Dissolved oxygen, temperature, conductivity, ammonium, nitrate, potassium, TOC (total organic carbon), COD (chemical oxygen demand), DOC (dissolved organic carbon share of TOC), BOD (biochemical oxygen demand) and SAC (spectral absorption coefficient). It has an easy-to-read digital display and wireless connection via radio transmission with a range of 100 meters. However, when it uses the nitrate sensor such as NitraLyt, the function of real-time monitoring is disabled. Another Xylem brand—WTW, it provides online measurement system—TresCon Analyzer which can monitor Ammonium, Nitrate, and Nitrite continuously. A continuous water sample supply with low solids contents is required for operating this system. For nitrate detection, the UV light is absorbed by the nitrate ions and determines the nitrate concentration at a wavelength of 254 nm.

ABB is a multinational corporation which mainly designs and manufactures power and automation products, including flow measurement, gas and liquid analyzer and environmental monitoring systems. For example, UV Nitrate Monitor AV455 provides a continuous analysis without chemical reagents. It can detect the nitrate concentration at the range of 0–100 mg/L at a wavelength of 220 nm. It requires low-maintenance and simple calibration with auto cleaning for the optical component. It uses de-nitrification as a process to reduce the nitrate concentrations for nitrate monitoring.

ASA Analytics Inc. specializes in the manufacture of the automatic chemical analysis system. ChemScan 6101 Process Analyzer can monitor Ammonia, Phosphate, Nitrate-Nitrite and Phosphate in surface water based on the UV-spectrometric method. The light is absorbed by nitrate ions and into 256 wavelengths of 200–450 nm. The detection range of nitrate is from 0.5–20 mg/L.

Table 1 summarizes the commercially available nitrate detection product/system in the market. Hanna HI 96728 is a portable device, but it still needs to collect the sample and require the reagent for measurement of nitrate. The YSI IQ SensorNet 182 terminal provides the continuous monitoring, but it calls for an additional sensor for nitrate measurement.

Table 1 Summarize of commercially available sensors

Model	Method of detection	Detection range (Nitrate) (mg/L)
IntelliCal ISENO3181	Ion selective electrode	0.1–14000
Nitratax plus sc	UV-photometric	0.1–100
S::can	UV-spectrometric	0–20
Hanna HI96728	Colorimetric	0–30
YSI 6884 Nitrate Sensor	Ion selective electrode	0.0–200.0
TresCon Analyzer	UV-spectrophotometric	0.1–60
UV Nitrate Monitor AV455	Ion exchange	0–100
ChemScan 6101 Process Analyzer	UV-spectrometric	0.5–20

3 Operating Principle of Interdigital Sensors

3.1 Interdigital Sensors

Interdigital sensors are made of comb-like or finger-like periodic pattern of parallel electrodes on a solid phase substrate. These electrodes are used to build up the capacitance which is related to the electric fields that penetrate into the test material and carry useful information about the properties of the material sample [28]. One of the most significant benefits of the planar interdigital sensors is the single-side access to the Material Under Test (MUT). This property helps to penetrate the sample with magnetic, electric, or acoustic fields from only one side. The strength of the output signal can be controlled by changing the area of the sensor, the number of fingers, and the spacing between them. The capability of being used for non-destructive testing is another advantage of these sensors, which makes them more useful for inline trial and process control applications [29].

Planar interdigital sensors follow the operating principle of parallel plate capacitors. Figure 5 [30] shows a gradual transition from the parallel-plate capacitor to a planar, fringing field capacitor, where electrodes open up to provide a single-side access to the MUT.

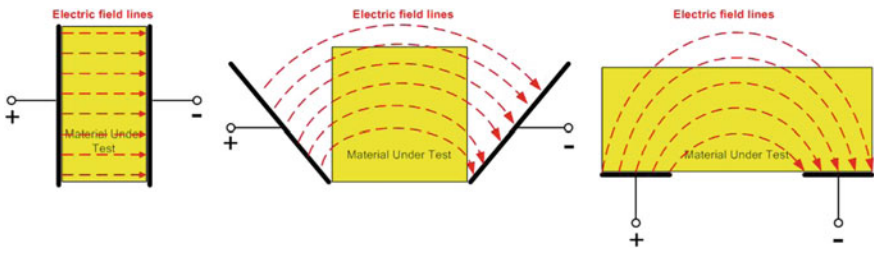

Fig. 5 Gradual transition from the parallel-plate capacitor to a planar capacitor

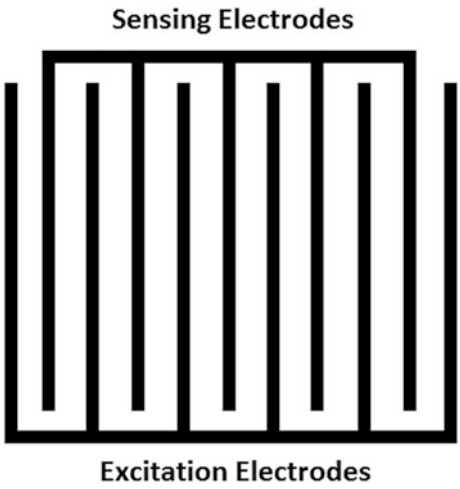

Fig. 6 Geometric structure of conventional planar Interdigital sensor

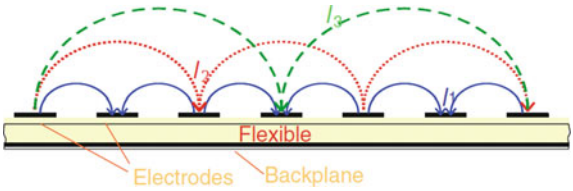

Fig. 7 Electric field formed for different pitch lengths [60]

The electrode pattern of the interdigital sensor can be repeated several times, to get a stronger signal and keep the signal-to-noise ratio in an acceptable range [31]. The configuration of the conventional interdigital sensor is shown in Fig. 6.

When an AC signal is applied as an excitation voltage to the terminals, an electric field is setup from positive to negative terminal. This electric field bulges through the test sample via excitation electrode and is received by the sensing electrode which carries useful information about the properties of MUT such as impedance, density, chemical composition and so on.

Figure 7 shows the electric field formed between positive and negative electrodes for different pitch lengths- the distance between two consecutive electrodes of the same polarity. As it is illustrated in the figure, different pitch length (l_1, l_2 and l_3) shows different penetration depth. The penetration depth improves by increasing the pitch length, at the cost of electric field strength that will get weaker with greater distance between the electrodes at same potential (pitch length).

3.2 Novel Planer Interdigital Sensors

Novel interdigital sensors are designed with number of sensing electrodes as compared to the excitation electrodes, to increase the penetration depth of the

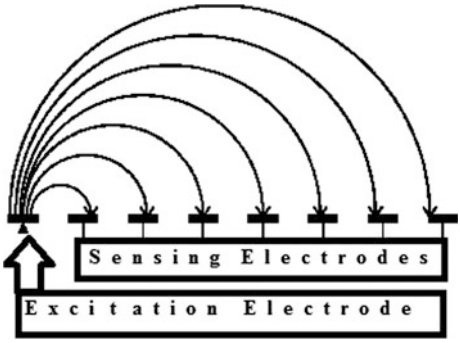

Fig. 8 Schematic excitation patterns for multi-sensing electrode interdigital sensors

Table 2 Geometric design parameters for four types of interdigital sensors

Sensor type	Pitch length (μm)	Number of sensing electrodes	Number of excitation electrodes	Sensing area (mm^2)
1-5-25	25	40	9	6.25
1-5-50	50	30	7	6.25
1-11-25	25	44	5	6.25
1-11-50	50	33	4	6.25

fringing electric field. Different geometries have been studied in research literature [32–34]. Figure 8 shows the excitation pattern for a multi-sensing electrode in interdigital sensor geometry.

The novel interdigital sensors have been fabricated based on different geometric parameters. Table 2 shows geometric parameters of four different interdigital sensors and Fig. 9 shows the schematic of 1-5-25 and 1-11-25 configuration of newly designed planer interdigital sensors [35].

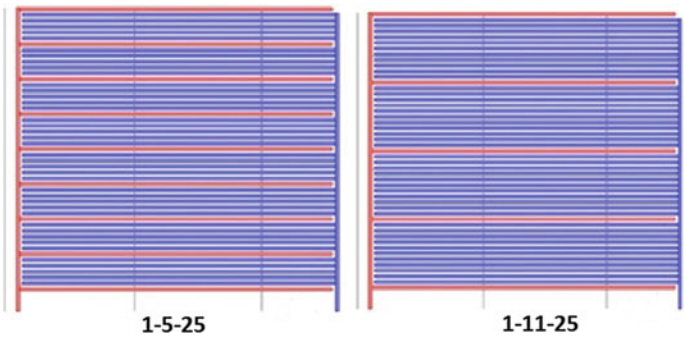

Fig. 9 1-5-25 and 1-11-25 configuration of novel interdigital sensors

A time-dependent sinusoidal electrical perturbation is applied to the excitation electrodes of the interdigital sensor. The switching electric field bulges through the test-sample via excitation electrode and is received by the sensing electrode which carries useful information about the properties of the material under test nearby of the sensing area [28, 29]. These sensors have several applications in manufacturing process [36], environmental monitoring [34, 37–40], humidity and moisture sensing system [41, 42], photosensitive detection [43] and gas sensor [44]. A sensing system was developed based on the interdigital sensor to detect the dangerously contaminated chemical in seafood [32, 40]. Another one was developed based on the electrochemical impedance spectroscopy technique to monitor the presence of phthalates in aqueous solution [37–39].

3.3 Electrochemical Impedance Spectroscopy (EIS)

Electrochemical Impedance Spectroscopy (EIS) is a popular and powerful method to measure the resistive and capacitive properties of materials by applying a small AC signal. EIS method can be applied in non-destructive testing, label-free detection and single-sided access for different chemical analysis. Different application of EIS had been reported such as the detection of fat contents in meat [45], biotoxins in shellfish [32], bacterial endotoxin in food [46], phthalates in water and juices [38], determination of the corrosive behavior of materials [47, 48] and analysis of electrical properties for soymilk coagulation process [49]. EIS has several applications in different research areas such as corrosion mechanisms [50], coating evaluation [51, 52], optimization of batteries [53] and biosensing [30].

Among some methods available for impedance measurements, Frequency Response Analysis (FRA) has become a de facto standard for EIS measurement which is a rapid approach to evaluating the impedance variation in real-time. This technique measures the impedance of the system over a wide frequency range and compares the results with reference data. In order to ensure the system stability, linearity, and repeatability, this method is rendered viable only for a stable and reversible system in equilibrium [54–56].

3.4 Basic Principles of EIS

Electrochemical impedance can be measured by applying a small AC signal and then measuring the phase shift in current signal on the applied potential. Electrochemical impedance is measured using a low excitation signal so that the cell's response is pseudo-linear. In a linear system, this current response to a sinusoidal excitation potential will result in a sinusoidal current at the same frequency but shifted in phase as shown in Fig. 10.

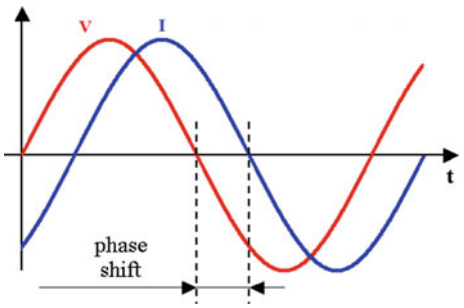

Fig. 10 Phase shift in current signal with reference to the applied voltage

Impedance is defined as the measurement of the ability of a circuit to opposite the flow of electrical current when a voltage is applied. In an AC circuit, impedance is represented as a complex value which involves real part (resistance) and imaginary part (reactance).

According to the basic Ohm's law in Eq. 1, impedance is defined as the ratio of potential, V and current, I;

$$R = \frac{V}{I} \tag{1}$$

The excitation signal can be explained as a function of time;

$$V_t = V_0 \sin \omega t \tag{2}$$

where V_t is the voltage difference at time t, V_0 is the amplitude of the signal, and the angular frequency is ω.It is given by ($\omega = 2\pi f$) expressed in radians/second and frequency, *f,* in hertz [57].

For a linear system, the response signal, I_t, has a phase shift, θ, with amplitude of I_0 which can be explained by

$$I_t = I_0 \sin(\omega t - \theta) \tag{3}$$

Equation 1 (Ohm's Law) can be used to calculate the impedance of the system given by;

$$\begin{aligned} Z &= \frac{V_t}{I_t} = \frac{V_0 \sin \omega t}{I_0 \sin(\omega t - \theta)} \\ &= Z_0 \frac{\sin(\omega t)}{\sin(\omega t - \theta)} \end{aligned} \tag{4}$$

The impedance, Z, now can be expressed in term of a magnitude of Z_0 and a phase shift, θ.

From Eq. 4, it can also be expressed in term of Euler's relationship given by;

$$e^{j\theta} = \cos\theta + \mathrm{j}\sin\theta \tag{5}$$

The impedance, Z, can be expressed in terms of potential, V, and current response, I, given by;

$$V_t = V_0 e^{j\omega t} \tag{6}$$

$$I_t = I_0 e^{j(\omega t - \theta)} \tag{7}$$

Therefore the impedance, Z;

$$Z(\omega) = \frac{V_t}{I_t} = \frac{V_0 e^{j\omega t}}{I_0 e^{j(\omega t - \theta)}} = Z_0 e^{j\theta} \tag{8}$$

$$= Z_0(\cos\theta + j\sin\theta) \tag{9}$$

The impedance now is in the form of real part (Z_0 cosθ) and imaginary part (Z_0 sinθ).

Calculated impedance characteristics can be analysed using Nyquist plot and Bode plot.

3.5 Data Presentation in the Form of Nyquist Plot and Bode Plot

The Nyquist plot is a popular format for evaluating electrochemical impedance data such as electrolytic solution resistance (R_s), electrode polarization resistance (R_p) and double layer capacitance (C_{dl}). These parameters will be discussed in the following sections. Nyquist plot represents imaginary impedance component against real impedance component at each excitation frequency. The Nyquist plot offers several advantages. The effects of solution resistance can be observed easily using this format. One major drawback of the Nyquist plot is that there is no information about the frequency in the Nyquist plot which makes it difficult to calculate the double layer capacitance [55]. The Bode plot represents the absolute impedance and the phase shift versus frequency.

3.6 Randle's Electrochemical Cell Equivalent Circuit Model

Randle's equivalent circuit is the most frequently discussed equivalent circuit [58] used to interpret EIS experimental results in electrical form as shown in Fig. 11. It

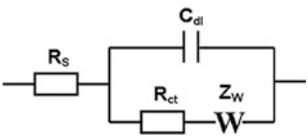

Fig. 11 Randle's equivalent circuit model

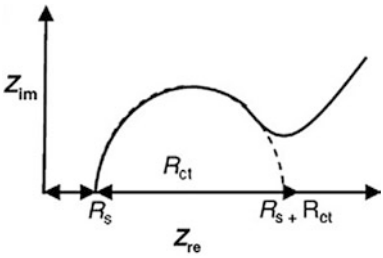

Fig. 12 The Nyquist plot for the Randle's equivalent circuit

consists of solution resistance R_s in series connected to a parallel combination of double layer capacitance C_{dl} to the charge transfer resistance R_{ct} in series with Warburg impedance Z_w [30].

Randle introduced this model in 1947 [59] and it can be used to describe both kinetics and diffusion processes taking place at the electrode-electrolyte interface.

The Nyquist plot from the equivalent circuit consists of a semi-circular region followed by a 45° straight line, as shown in Fig. 12. In this model, the impedance of a faradaic reaction consists of an active charge transfer resistance R_{ct}, and a specific electrochemical element of diffusion which is called Warburg element. The semi-circular region represents a slower charge transfer at higher frequencies whereas the straight line describes a faster mass-transfer at lower frequencies. R_{ct} can be calculated by extrapolating the semicircle to Z_{real} axis. Solution resistance R_s can be calculated by reading the real axis value at the high-frequency intercept which is the intercept near the origin of the Nyquist plot. R_{ct} can be calculated by extrapolating the semicircle to Z_{real} axis as illustrated in Fig. 11. C_{dl} can be obtained from the frequency at the maximum of semicircle portion in the Nyquist plot using $\omega = 1/R_{ct}\, C_{dl}$ [58].

The absolute impedance as a function of frequency is given as;

$$Z(\omega) = R_s + \frac{R_{ct}}{1 + \omega^2 R_{ct}^2 C_{dl}^2} - \frac{j\omega R_{ct}^2 C_{dl}}{1 + \omega^2 R_{ct}^2 C_{dl}^2} \tag{10}$$

where the real part (Z′) is given by;

$$Z'(\omega) = R_s + \frac{R_{ct}}{1 + \omega^2 R_{ct}^2 C_{dl}^2} \tag{11}$$

moreover, the imaginary part (Z″) is given by;

$$Z^{''}(\omega) = -\frac{\omega R_{ct}^2 C_{dl}}{1+\omega^2 R_{ct}^2 C_{dl}^2} \tag{12}$$

The rate of an electrochemical reaction can be strongly influenced by diffusion of reactants towards, or away from the electrode-electrolyte interface. This situation can exist when the electrode is covered with adsorbed solution components or a selective coating. An addition element called Warburg impedance, Z_W, appears in series with resistance R_{ct}. Mathematically Warburg impedance is given by;

$$Z_W = \frac{\sigma w}{\sqrt{j\omega}} \tag{13}$$

where, σ_w is Warburg diffusion coefficient. The diffusion of reactants to the electrode surface is a slow-paced process which can happen at low frequencies only. However, at higher frequencies, the reactants do not have enough time to diffuse. The slope of this line gives Warburg diffusion coefficient.

4 Experimental Setup, Results and Discussion

The interdigital sensor is very sensitive to ambient temperature and humidity. The first experiment was conducted to measure the impedance characterization in a temperature range between 10 to 40 °C and obtain the linear relationship between temperature and impedance. The second experiment was performed to get the relationship between temperature and impedance by varying the humidity in different thermal condition. Then, the sensor was tested to observe the impedance response in prepared diluted water samples from nitrates forms: ammonium nitrates (NH_4NO_3) by commercial equipment-LCR meter.

4.1 Temperature Measurement

The sensor was tested in the Milli-Q water in the temperature range from 10 to 40 °C. The characteristics of the sensor can be extended to accommodate the behavior of it outside the range. The objective of this experiment was to observe the impedance response of the sensor to different temperatures.

4.1.1 Experimental Setup

Figure 13 shows the experimental setup and it involved high precision Hioki 3522-50 LCR meter, Hioki 4-terminal probe 9140, mercury thermometer, SCILOGEX MS 7-H550 Digital Hotplate and computer for data acquisition. The hotplate had the maximum limit from ambient temperature to 550 °C. In order to measure the water sample at a lower temperature (below room temperature), the water sample was stored in the freezer initially to let its temperature fall close to 0 °C and then taken out for testing at room temperature. The mercury thermometer was immersed in the water to obtain a continuous temperature reading. Meanwhile, the sensing surface was also submerged in the water and starts to collect data when the temperature reached to a certain degree. The heating plate was used to heat the water sample to reach the desired temperature. The Parylene coated sensor (1-5-50A) was used for this experiment.

The Hioki 3522-50 was used to obtain the measured parameters for investigating the impedance values in the frequency range between 1 Hz to 100 kHz. The probe 9140 had two sets of terminals connected to the sensor and LCR meter. The H_{CUR} and L_{CUR} were used to measure the current flowing through the sensor and H_{POT} and L_{POT} were used to measure the voltage across the sensor. Table 4.4.1.1 illustrates the technical specifications of the Hioki 3522-50 LCR meter (Hioki 2001).

4.1.2 Results and Discussion

The parylene coated 1-5-50A sensor was immersed into the MilliQ water in varying thermal conditions. The resistance (Rs) and reactance (X) part of the impedance

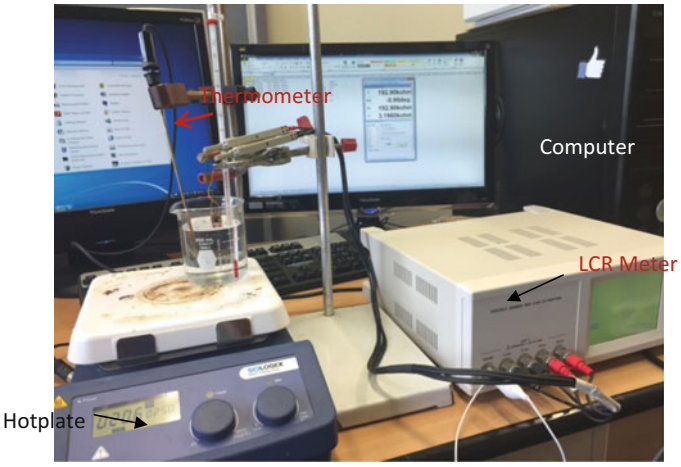

Fig. 13 Lab setup for sensor response at different temperature

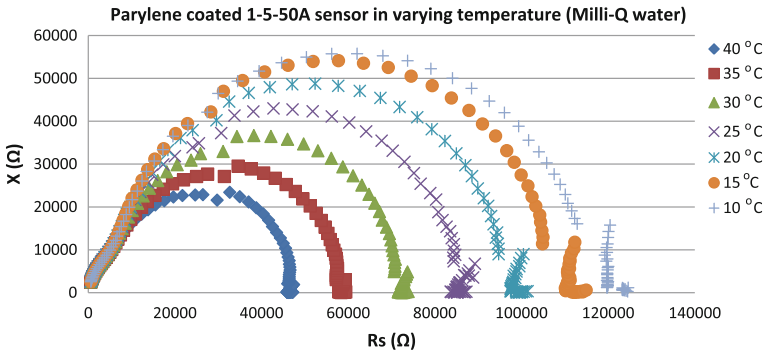

Fig. 14 Nyquist plot for testing MilliQ at various temperatures

were evaluated and plotted in Fig. 14. The X-axis shows resistance part of impedance in Ω and the Y-axis shows the reactance part of the impedance in Ω. With the increase in temperature, the total impedance is decreased. Each data point on the plot indicates the impedance at a specific frequency.

Figure 15 shows the relationship between the resistance of impedance and the frequency. The resistance is decreased with the increasing in temperature and the sensitive range is significant till 400 Hz.

Figure 16 shows the reactance (X) of MilliQ to changing temperature plotted against frequency. This parameter is used to measure the dielectric properties of the MilliQ in different temperature.

The experiment was repeated at different times to observe impedance behavior and to take average results for the measurement of temperature for Parylene coated sensor. Table 3 shows the average measurement results for resistance (Rs) and

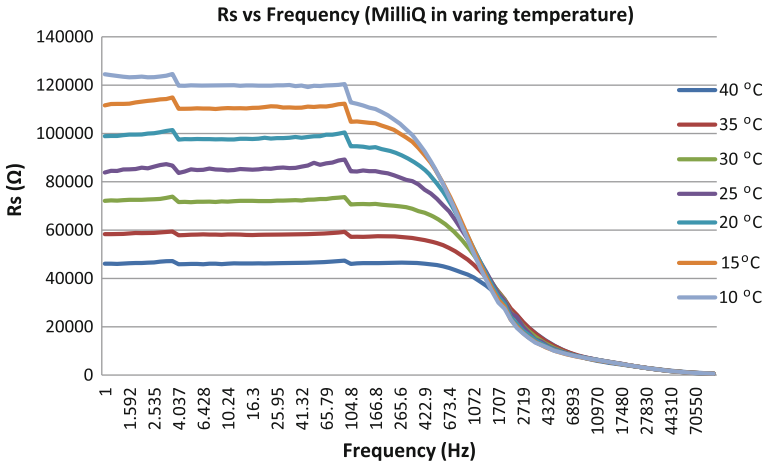

Fig. 15 Real part of impedance versus frequency in varying temperature

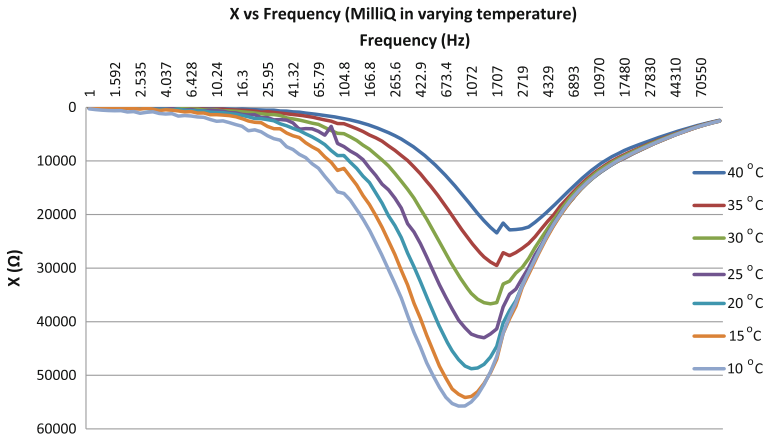

Fig. 16 Imaginary part of impedance versus frequency in various temperature

Table 3 Temperature measurement

Sensor type	Pitch length (μm)	Number of sensing electrodes	Number of excitation electrodes	Sensing area (mm^2)
10	118037.7617	9.55	47125.9455	9.74
15	104281.2167	15.01	41141.9445	14.54
20	91693.88783	20.00	34318.99883	20.00
25	77142.05667	25.77	26339.72167	26.39
30	64181.38833	30.91	19565.99883	31.81
35	52901.83333	35.84	14054.88283	36.23
40	42392.83333	39.55	9658.2	39.75

reactance (X) at a different temperatures. As the linear relationship between the impedance and temperature, the slope can be calculated by the Eq. 14:

$$Slope = \frac{\Delta R}{\Delta T} = \frac{R_{40} - R_{10}}{T_{40} - T_{10}} \quad \text{(Equ. 4.3.2.1)} \tag{14}$$

where:

- R_{40}: Resistance value measured at 40 °C
- R_{10}: Resistance value measured at 10 °C
- T_{40}: Temperature at 40 °C
- T_{10}: Temperature at 10 °C

Therefore, the slope for resistance part is (42392.83–118037.76)/(40–10) = –2521.498. Similarly, replacing the ΔX with ΔR, the slope for reactance part is (9658.2–47125.95)/(40–10) = –1248.92. Figure 17 shows the relationship between the temperature and Rs. The resistance of impedance drops nearly linearly with the increase in temperature.

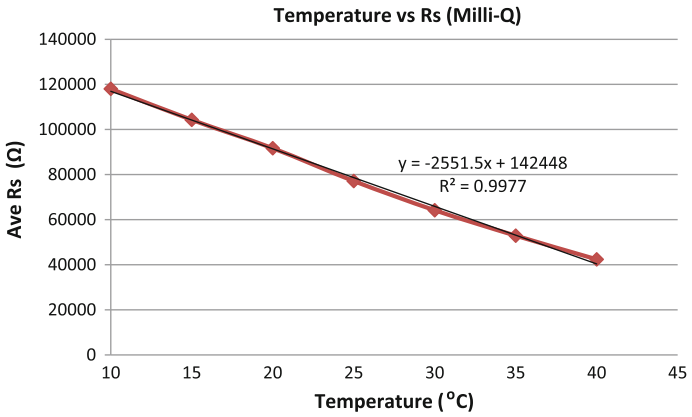

Fig. 17 Relationship between the temperature and resistance part of impedance Therefore, the temperature can be measured by Eq. 4.3.2.2

$$T(^{o}C) = \frac{R_T - R_{20}}{slope} + T_{20} \quad \text{(Equ. 4.3.2.2)} \tag{15}$$

where:

- R_T: Measured resistance value
- R_{20}: Resistance value at 20 °C (which is the reference value)
- T_{20}: Reference temperature is at 20 °C

4.2 Humidity Experiment and Result

This experiment observed the impedance characteristics as a function of humidity and temperature. The experiment was tested at a temperature range from 20 to 40 °C with the step of 5 °C and the varied humidity was applied.

Figure 18 shows the experimental setup for obtaining the impedance of sensor in the various temperature and humidity. It used the Thermo Scientific Heratherm Compact Microbiological Incubator, LCR meter, Humidity and temperature portable sensor and computer.

The incubator can control the temperature between 17 to 40 °C but it cannot monitor the humidity. Therefore, to vary the humidity, a small container with the hot water was used to increase the humidity in the incubator.

However, this humidity rate could not be controlled exactly, so the humidity range in this experiment depended on the volume of hot water in the container. The LCR meter was used to obtain the parameters' measurement for investigating

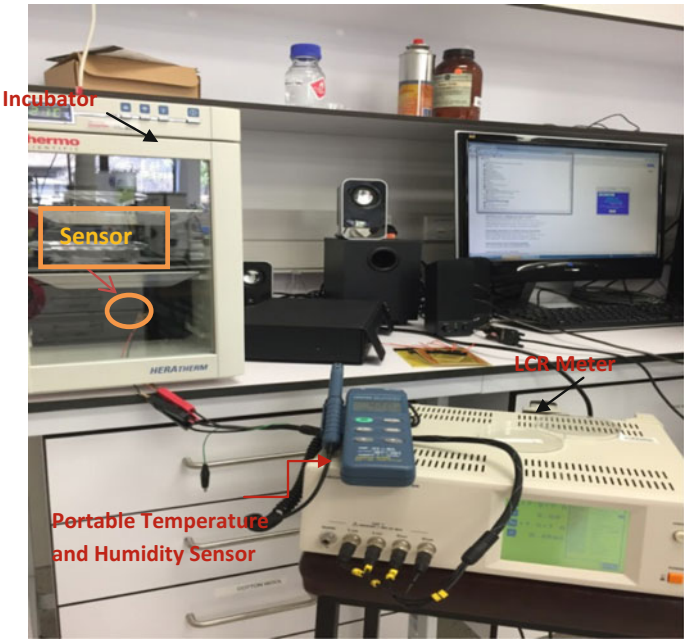

Fig. 18 Experiment setup for temperature and humidity measurement

the impedance value in the frequency range between 1 Hz to 100 kHz, and the computer is used for data acquisition.

Figure 19 shows the Nyquist plot for the Parylene coated sensor test at 25 °C with varying humidity. From the Fig. 19, the total impedance is reduced with the increase in humidity. The relationship between the resistive part of impedance and frequency at different humidity is shown in Fig. 20. The most sensitive area of the sensor is from 1 Hz to 400 Hz.

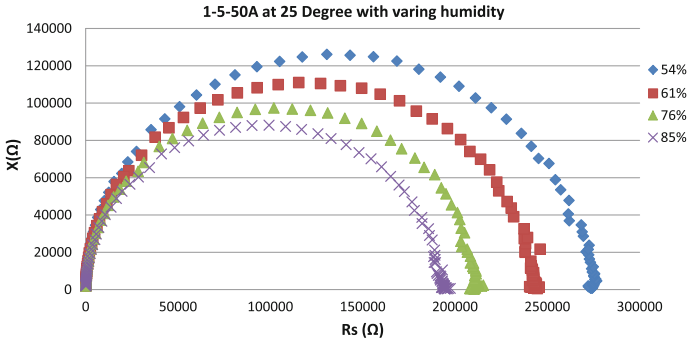

Fig. 19 Nyquist plot for testing varying humidity at 25 °C

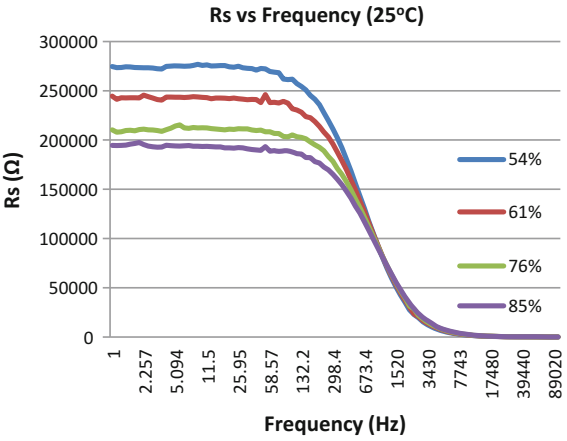

Fig. 20 Resistance part of impedance versus frequency in varying humidity at 25 °C

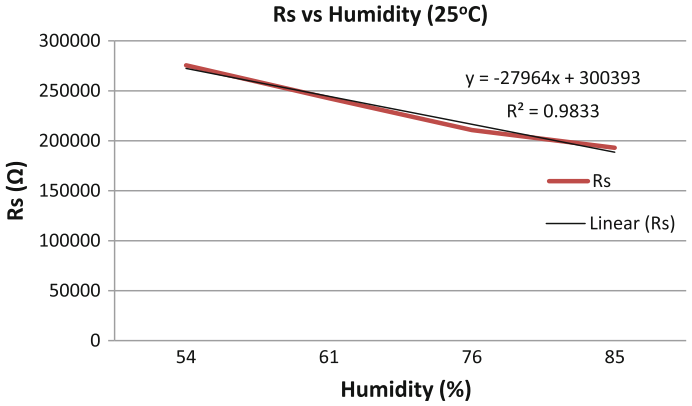

Fig. 21 Resistance of impedance against humidity at 25 °C

Figure 21 illustrates when the increase in humidity, the resistance of impedance reduces and it shows a good correlation with $R^2 = 0.9833$.

4.3 Experimental Setup, Results and Discussion of Nitrate Concentration

The first experiment was to test different concentration of Ammonium Nitrate (NH_4NO_3) between 0.1 and 0.5 mg/L by using commercial measurement equipment: LCR meter. The water samples were prepared using the serial dilution

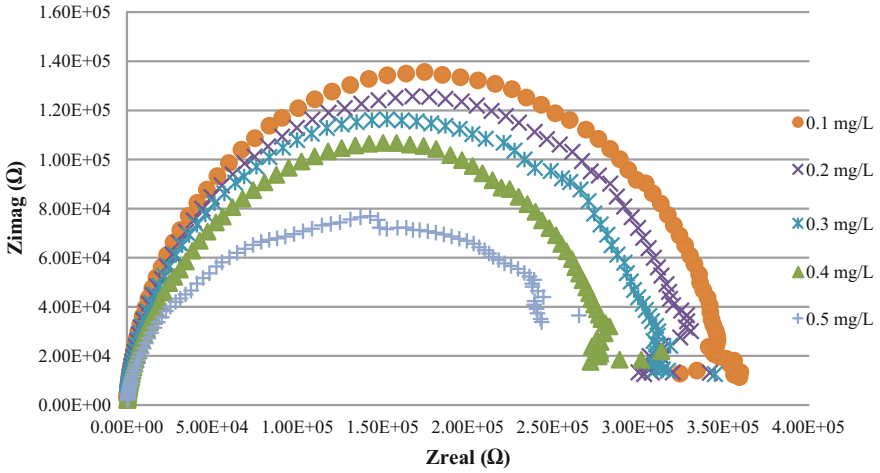

Fig. 22 Nyquist plot for NH_4NO_3 at different concentration

method. Electrochemical impedance spectroscopy [38] was used to perform impedance measurements based on different concentrations as represented by Nyquist plot shown in Fig. 20. The frequency range considered for the experiment was from 1 Hz to 100 kHz (setting from LCR meter). The Nyquist plot illustrates that the impedance of the sensor is inversely related to the concentration of the water samples.

Due to the presence of ionic salts in the solution, there was a significant change in the real part of the impedance compared to the imaginary part. From Fig. 22, it is seen that the real part of the impedance changes with the change in frequency. Different concentrations of solution were considered to determine the sensitive region (from 5 to 150 Hz) of the sensor under consideration (100 Hz is chosen in this case) Fig. 23.

Figure 24 shows the corresponding change in the imaginary part of impedance with the change in frequency. It is seen from the figure that there is not much change in the reactance values for the complete frequency range as compared to the change in the resistive (Real part of Impedance) values as shown in Fig. 24. Equation 7 illustrates the chemical formula for the ionic equilibrium state for ammonium nitrate. As the purpose is the detection of nitrate ions, the real part of the impedance (R) shows a significant change compared to the imaginary part (X), R is chosen as the reference for measurement.

$$NH_4NO_3 \leftrightarrow NH_4^+ + NO_3^- \tag{16}$$

The NH_4NO_3 solution was used as a standard solution to calculate the nitrate concentration in the collected water samples.

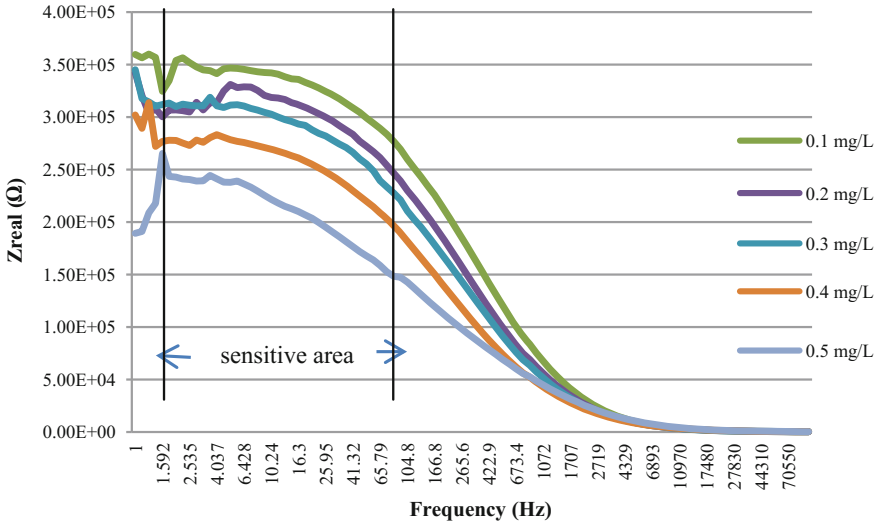

Fig. 23 Real part of impedance versus frequency at low concentration (NH_4NO_3)

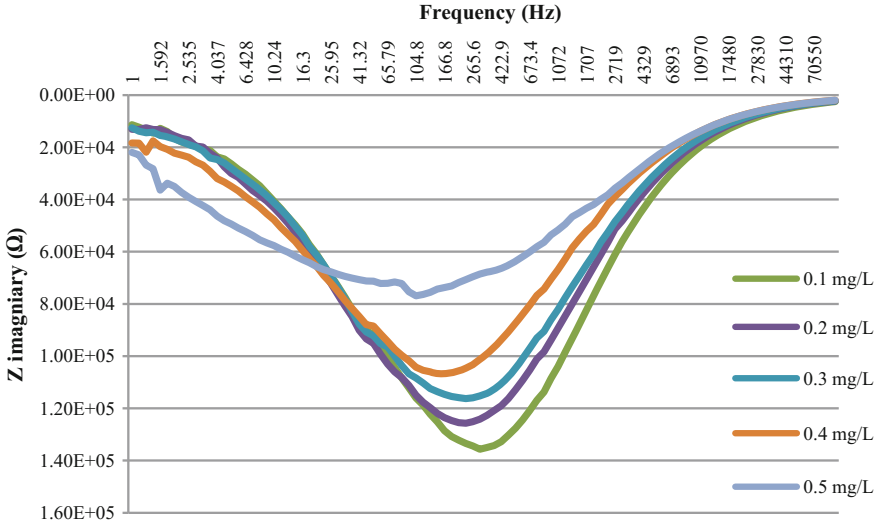

Fig. 24 Imaginary part of impedance versus frequency at different concentration (NH_4NO_3)

$$C = \frac{R - R_{0.3}}{-115543} + C_{0.3} \tag{17}$$

where R is the real impedance of water sample, $R_{0.3}$ is the real part of the impedance at 0.3 mg/L of NH_4NO_3, $C_{0.3}$ represent the concentration of 0.3 mg/L, which

is a reference. Substituting the value of $R_{0.3}$ and $C_{0.3}$ into Eq. (8), the concentration was calculated by:

$$C = \frac{R - 48056.78}{-115543} + 0.3 \tag{18}$$

5 Conclusion

Electrochemical Impedance Spectroscopy was employed to detect and display temperature, humidity and nitrate concentrations by evaluating the impedance change read by the planar interdigital transducer. Calibration curve has also been developed to measure the unknown parameters. The nitrate concentration has been measured without the selectivity. The proper selectivity for the sensor that could capture only the nitrate ions is necessary before an accurate assessment of NO_3-N concentration in the stream water will be explored. However, the interdigital sensor has the potential to be used for testing temperature, humidity and nitrate concentration in real-time applications for a rough estimation. For the in situ purpose, a robust sensor node needs to develop to do the real-time monitoring of the sampling site.

References

1. Fresh Water Environment, http://www.mfe.govt.nz/publications/environmental-reporting/environment-aotearoa-2015-fresh-water/overview. Accessed 17 May 2016
2. Agricultural Production Statistics: June 2015, http://www.stats.govt.nz/browse_for_stats/industry_sectors/agriculture-horticulture-forestry/AgriculturalProduction_HOTPJun15prov.aspx. Accessed 17 May 2016
3. G.C. Brandao, G.D. Matos, R.N. Pereira, S.L. Ferreira, Development of a simple method for the determination of nitrite and nitrate in groundwater by high-resolution continuum source electrothermal molecular absorption spectrometry. Anal. Chim. Acta **806**, 101–106 (2014)
4. J.A. Camargo, Á. Alonso, Ecological and toxicological effects of inorganic nitrogen pollution in aquatic ecosystems: a global assessment. Environ. Int. **32**, 831–849 (2006)
5. A. Ayala, L. Leal, L. Ferrer, V. Cerdà, Multiparametric automated system for sulfate, nitrite and nitrate monitoring in drinking water and wastewater based on sequential injection analysis. Microchem. J. **100**, 55–60 (2012)
6. M.J. Moorcroft, J. Davis, R.G. Compton, Detection and determination of nitrate and nitrite: a review. Talanta **54**, 785–803 (2001)
7. C.L. Pasquali, A. Gallego-Picó, P.F. Hernando, M. Velasco, J.D. Alegría, Two rapid and sensitive automated methods for the determination of nitrite and nitrate in soil samples. Microchem. J. **94**, 79–82 (2010)
8. Z. Moldovan, Kinetic spectrophotometric determination of nitrite with Tropaeolin 00-Bromate System. Anal. Lett. **43**, 1344–1354 (2010)
9. Table of Regulated Drinking Water Contaminants, https://www.epa.gov/your-drinking-water/table-regulated-drinking-water-contaminants. Accessed 17 May 2016

10. D.C. Siu, A. Henshall, Ion chromatographic determination of nitrate and nitrite in meat products. J. Chromatogr. A **804**, 157–160 (1998)
11. P. Niedzielski, I. Kurzyca, J. Siepak, A new tool for inorganic nitrogen speciation study: Simultaneous determination of ammonium ion, nitrite and nitrate by ion chromatography with post-column ammonium derivatization by Nessler reagent and diode-array detection in rain water samples. Anal. Chim. Acta **577**, 220–224 (2006)
12. E. Pagliano, M. Onor, E. Pitzalis, Z. Mester, R. Sturgeon, A. D'Ulivo, Quantification of nitrite and nitrate in seawater by triethyloxonium tetrafluoroborate derivatization—Headspace SPME GC–MS. Talanta **85**, 2511–2516 (2011)
13. N. Öztekin, M.S. Nutku, F.B. Erim, Simultaneous determination of nitrite and nitrate in meat products and vegetables by capillary electrophoresis. Food Chem. **76**, 103–106 (2002)
14. F. Manea, A. Remes, C. Radovan, R. Pode, S. Picken, J. Schoonman, Simultaneous electrochemical determination of nitrate and nitrite in aqueous solution using Ag-doped zeolite-expanded graphite-epoxy electrode. Talanta **83**, 66–71 (2010)
15. A. Serra, S. Jorge, C. Silveira, J. Moura, E. Jubete, E. Ochoteco et al., Cooperative use of cytochrome cd 1 nitrite reductase and its redox partner cytochrome c 552 to improve the selectivity of nitrite biosensing. Anal. Chim. Acta **693**, 41–46 (2011)
16. C. Xia, C. Xiaolan, W. Ning, G. Lin, Hierarchical CuO nanochains: synthesis and their electrocatalytic determination of nitrite. Anal. Chim. Acta **691**, 43–47 (2011)
17. F. Hu, S. Chen, C. Wang, R. Yuan, D. Yuan, C. Wang, Study on the application of reduced graphene oxide and multiwall carbon nanotubes hybrid materials for simultaneous determination of catechol, hydroquinone, p-cresol and nitrite. Anal. Chim. Acta **724**, 40–46 (2012)
18. M. Sohail, R. De Marco, K. Lamb, E. Bakker, Thin layer coulometric determination of nitrate in fresh waters. Anal. Chim. Acta **744**, 39–44 (2012)
19. J. Chen, H. Chen, C. Zhou, J. Xu, F. Yuan, L. Wang, An efficient upconversion luminescence energy transfer system for determination of trace amounts of nitrite based on NaYF 4: Yb 3+, Er 3+ as donor. Anal. Chim. Acta **713**, 111–114 (2012)
20. Z.-T. Jiang, Y.-X. Guo, R. Li, Spectrophotometric determination of trace nitrite with brilliant cresyl blue using β-cyclodextrin as a sensitizer. Food Anal. Methods **3**, 47–53 (2010)
21. M. Pandurangappa, Y. Venkataramanappa, Quantification of nitrite/nitrate in food stuff samples using 2-aminobenzoic acid as a new amine in diazocoupling reaction. Food Anal. Methods **4**, 90–99 (2011)
22. N. Cabaleiro, I. De La Calle, S. Gil, F. Pena, M. Costas, C. Bendicho et al., Simultaneous ultrasound-assisted emulsification–derivatization as a simple and miniaturized sample preparation method for determination of nitrite in cosmetic samples by microvolume UV–vis spectrophotomety. Talanta **83**, 386–390 (2010)
23. H. Filik, D. Giray, B. Ceylan, R. Apak, A novel fiber optic spectrophotometric determination of nitrite using Safranin O and cloud point extraction. Talanta **85**, 1818–1824 (2011)
24. M.D. Patey, E.P. Achterberg, M.J. Rijkenberg, P.J. Statham, M. Mowlem, Interferences in the analysis of nanomolar concentrations of nitrate and phosphate in oceanic waters. Anal. Chim. Acta **673**, 109–116 (2010)
25. S. Senra-Ferreiro, F. Pena-Pereira, I. Lavilla, C. Bendicho, Griess micro-assay for the determination of nitrite by combining fibre optics-based cuvetteless UV–Vis micro-spectrophotometry with liquid-phase microextraction. Anal. Chim. Acta **668**, 195–200 (2010)
26. B.S. Gentle, P.S. Ellis, M.R. Grace, I.D. McKelvie, Flow analysis methods for the direct ultra-violet spectrophotometric measurement of nitrate and total nitrogen in freshwaters. Anal. Chim. Acta **704**, 116–122 (2011)
27. M. Noroozifar, M. Khorasani-Motlagh, A. Taheri, M. Homayoonfard, Application of manganese (IV) dioxide microcolumn for determination and speciation of nitrite and nitrate using a flow injection analysis–flame atomic absorption spectrometry system. Talanta **71**, 359–364 (2007)
28. A.S. Abu-Abed, R.G. Lindquist, Capacitive interdigital sensor with inhomogeneous nematic liquid crystal film. Progress In Electromagnetics Research B **7**, 75–87 (2008)

29. A.V. Mamishev, K. Sundara-Rajan, F. Yang, Y. Du, M. Zahn, Interdigital sensors and transducers. Proc. IEEE **92**, 808–845 (2004)
30. F. Lisdat, D. Schäfer, The use of electrochemical impedance spectroscopy for biosensing. Anal. Bioanal. Chem. **391**, 1555–1567 (2008)
31. Y. Chen, C. Zhu, M. Cao, T. Wang, Photoresponse of SnO2 nanobelts grown in situ on interdigital electrodes. Nanotechnology **18**, 285502 (2007)
32. A.M. Syaifudin, K. Jayasundera, S. Mukhopadhyay, A low cost novel sensing system for detection of dangerous marine biotoxins in seafood. Sens. Actuators B: Chem. **137**, 67–75 (2009)
33. S. Mukhopadhyay, P. Yu, Electromagnetic field computation using COMSOL Multiphysics to evaluate the performance of novel interdigital sensors, in *Applied Electromagnetics Conference (AEMC), 2009*, pp. 1–4
34. M. Yunus, S. Mukhopadhyay, K. Jayasundera, A novel planar interdigital sensor for environmental monitoring, in *Sensors, 2009 IEEE*, 2009, pp. 105–110
35. H. Arwin, Application of ellipsometry techniques to biological materials. Thin Solid Films **519**, 2589–2592 (2011)
36. Y. Yang, G. Chiesura, G. Luyckx, T. Vervust, F. Bossuyt, J. Vanfleteren et al., In situ on-line cure monitoring of composites by embedded interdigital sensor, in *16th European Conference on Composite Materials (ECCM-16)*, 2014
37. A.I. Zia, A.M. Syaifudin, S. Mukhopadhyay, P. Yu, I. Al-Bahadly, C.P. Gooneratne et al., Electrochemical impedance spectroscopy based MEMS sensors for phthalates detection in water and juices, in *Journal of Physics: Conference Series*, 2013, p. 012026
38. A.I. Zia, S.C. Mukhopadhyay, P.-L. Yu, I. Al-Bahadly, C.P. Gooneratne, J. Kosel, Rapid and molecular selective electrochemical sensing of phthalates in aqueous solution. Biosens. Bioelectron. **67**, 342–349 (2015)
39. A. Zia, S. Mukhopadhyay, I. Al-Bahadly, P. Yu, C.P. Gooneratne, J. Kosel, Introducing molecular selectivity in rapid impedimetric sensing of phthalates, in *2014 IEEE International Instrumentation and Measurement Technology Conference (I2MTC) Proceedings*, 2014, pp. 838–843
40. A. Syaifudin, K. Jayasundera, S. Mukhopadhyay, A novel planar interdigital sensor based sensing and instrumentation for detection of dangerous contaminated chemical in seafood, in *Instrumentation and Measurement Technology Conference, 2009. I2MTC'09. IEEE*, 2009, pp. 701–706
41. J. Fischer, H. Dejmkova, J. Barek, Electrochemistry of pesticides and its analytical applications. Curr. Org. Chem. **15**, 2923–2935 (2011)
42. M. Khafaji, S. Shahrokhian, M. Ghalkhani, Electrochemistry of Levo-Thyroxin on Edge-Plane pyrolytic graphite electrode: application to sensitive analytical determinations. Electroanalysis **23**, 1875–1880 (2011)
43. L. Li, F. Yang, J. Yu, X. Wang, L. Zhang, Y. Chen et al., In situ growth of ZnO nanowires on Zn comb-shaped interdigitating electrodes and their photosensitive and gas-sensing characteristics. Mater. Res. Bull. **47**, 3971–3975 (2012)
44. M. Dhull, A. Arora, Design of mems based microheater for enhanced efficiency of gas sensors. J. Therm. Eng. Appl. **2**, 16–21 (2015)
45. S.C. Mukhopadhyay, C.P. Gooneratne, A novel planar-type biosensor for noninvasive meat inspection. Sens. J. IEEE **7**, 1340–1346 (2007)
46. M.S.A. Rahman, S.C. Mukhopadhyay, P.-L. Yu, J. Goicoechea, I.R. Matias, C.P. Gooneratne et al., Detection of bacterial endotoxin in food: new planar interdigital sensors based approach. J. Food Eng. **114**, 346–360 (2013)
47. C. Xhoffer, K. Van den Bergh, H. Dillen, Electrochemistry: a powerful analytical tool in steel research. Electrochim. Acta **49**, 2825–2831 (2004)
48. C.V. Vidal, A.I. Muñoz, Effect of physico-chemical properties of simulated body fluids on the electrochemical behaviour of CoCrMo alloy. Electrochim. Acta **56**, 8239–8248 (2011)
49. X. Li, K. Toyoda, I. Ihara, Coagulation process of soymilk characterized by electrical impedance spectroscopy. J. Food Eng. **105**, 563–568 (2011)

50. C. Liu, Q. Bi, A. Leyland, A. Matthews, An electrochemical impedance spectroscopy study of the corrosion behaviour of PVD coated steels in 0.5 N NaCl aqueous solution: Part II.: EIS interpretation of corrosion behaviour. Corros. Sci. **45**, 1257–1273 (2003)
51. A. Ghasemi, V. Raja, C. Blawert, W. Dietzel, K. Kainer, Study of the structure and corrosion behavior of PEO coatings on AM50 magnesium alloy by electrochemical impedance spectroscopy. Surf. Coat. Technol. **202**, 3513–3518 (2008)
52. R.M. Souto, M.a.M. Laz, R.L. Reis, Degradation characteristics of hydroxyapatite coatings on orthopaedic TiAlV in simulated physiological media investigated by electrochemical impedance spectroscopy. *Biomaterials,* **24**, 4213–4221 (2003)
53. D. Andre, M. Meiler, K. Steiner, C. Wimmer, T. Soczka-Guth, D. Sauer, Characterization of high-power lithium-ion batteries by electrochemical impedance spectroscopy. I. Experimental investigation. J. Power Sources **196**, 5334–5341 (2011)
54. B.-Y. Chang, S.-M. Park, Electrochemical impedance spectroscopy. Ann. Rev. Anal. Chem. **3**, 207–229 (2010)
55. G. Instruments, Basics of electrochemical impedance spectroscopy, *G. Instruments, Complex impedance in Corrosion,* pp. 1–30 (2007)
56. I.I. Suni, Impedance methods for electrochemical sensors using nanomaterials. TrAC Trends Anal. Chem. **27**, 604–611 (2008)
57. A. Zia, Smart Electrochemical Sensing System For the Real time Detection of Endocrine Disrupting Compunds and Hormones
58. J.R. Macdonald, E. Barsoukov, Impedance spectroscopy: theory, experiment, and applications. History **1**, 8 (2005)
59. J.E.B. Randles, Kinetics of rapid electrode reactions. Discuss. Faraday Soc. **1**, 11–19 (1947)
60. M.S.A. Rahman, S.C. Mukhopadhyay, P.-L. Yu, Novel Planar Interdigital Sensors, in *Novel Sensors for Food Inspection: Modelling, Fabrication and Experimentation*, ed: (Springer, 2014), pp. 11–35

Using Wireless Sensor Networks to Determine Pollination Readiness in Palm Oil Plantation

Mohamed Rawidean Mohd Kassim and Ahmad Nizar Harun

Abstract The Wireless Sensors Network (WSN) is nowadays widely used to build decision support systems to solve many real-world problems. One of the most interesting fields having an increasing need of decision support systems is agricultural environment monitoring. Agricultural environment monitoring has become an important field of control and protection, providing real-time system and control communication with the physical world. An intelligent and smart WSN system can collect and process large amount of data from the beginning of the monitoring and manage air quality, soil conditions, to weather situations. Wireless sensors are used in a palm oil plantation to monitor the humidity, temperature and other parameters of a mother palm to find the best time to start a controlled pollination process. Pollination is the process of transferring pollen from the male reproductive organ to the female reproductive organ of a flower. The inaccuracy in determining pollination readiness of the oil palm flower could potentially cause a detrimental effect on the palm oil industry in the long run.

1 Introduction

Agricultural environmental monitoring applications can be broadly categorized into indoor and outdoor monitoring [1]. Indoor monitoring applications typically include buildings and greenhouses monitoring. Outdoor monitoring applications include chemical hazardous detection, habitat monitoring, earthquake detection, volcano eruption, flooding detection and weather forecasting. These applications involve sensing temperature, light, humidity, moisture and air quality. This chapter will explain in detail how a practical, cost-effective and user-friendly pollination readiness of palm oil flower monitoring system was developed based on WSN technology.

M.R.M. Kassim (✉) · A.N. Harun
Product and System Architecture, MIMOS, Ministry of Science, Technology and Innovation, Kuala Lumpur, Malaysia
e-mail: dean@mimos.my

S. Mukhopadhyay et al. (eds.), *Sensors for Everyday Life*, Smart Sensors, Measurement and Instrumentation 23, DOI 10.1007/978-3-319-47322-2_7

Palm oil has become increasingly popular as it provides rich sources of α and β-carotene and vitamin E, which play important roles in blood coagulation, suppression of cholesterol production and cancer inhibition. Besides its nutritional value, it is a well-known raw material for oleo chemical industry and bio-fuel for automobiles. Around 85 % of the palm oil production is concentrated in Indonesia and Malaysia, but its use is rapidly spreading in whole world as China and India are the main importing countries, next to the EU.

At present, Malaysia accounts for an overwhelming contribution to world's palm oil production and export which is 39 % and 44 %, respectively. A massive 17.73 million tons of palm oil and 2.13 tons of palm kernel oil have been produced from about 4.49 million hectares of land. Malaysia has a vital role to play in achieving the rising global need for oils and fats, as Malaysia is one of the major producer and exporter countries of palm oil and palm oil products.

Pollination is an important process in oil palm breeding as correct method increases yield and quality of palm oil production. During pollination process the conditions need to be monitored thoroughly within a time frame to ensure genetic purity that will increase yield. Currently, this monitoring process of pollination is very manual and labour intensive job. Workers need to climb an average height of 3 stories building only to check the conditions of the pollination. Climbing is dangerous as risk of falling down can cause disability and deaths.

Advances in sensor and wireless radio frequency (RF) technologies and their convergence with the Internet of Things (IoT) offer vast opportunities for application of sensor systems for agriculture industry. Emerging wireless technologies with low power needs and low data rate capabilities have been developed which suit precision agriculture [1–5]. The WSNs have become the most suitable technology to monitor and control the agricultural environment.

Wireless Sensor Network (WSN) is the ideal candidate to provide effective and economically viable solutions for a large variety of applications ranging from health monitoring, agriculture, environmental monitoring to military operations. WSN is a very important component in IoT and integrates the knowledge of sensors, automation control, digital network transmission, information storage and information processing. WSN market is forecast to rise from $0.45 billion in 2012 to $2 billion in 2022 [6, 7].

Current pollination processes for oil palm pollination relies heavily on human dependence. It involves manual checking of trees for pollination readiness and is more of a guessing game rather than an exact science. For the process of oil palm pollination to be efficient and cost-effective, a logical solution would be to automate the process and reduce dependence on human tacit knowledge by transferring it into a system. Therefore, a remote monitoring system for pollination readiness using WSN is introduced to help the field workers reduce the dangerous task load besides improving the quality and productivity of yield. Figure 1 shows an oil palm plantation in Malaysia.

Fig. 1 An oil palm tree can reach up to 20 m

2 Agricultural Environmental Monitoring

Environmental monitoring applications can be broadly categorized into indoor and outdoor monitoring [8]. Indoor monitoring applications typically include buildings and greenhouses monitoring. These applications involve sensing temperature, light, humidity, and air quality. Outdoor monitoring applications include chemical hazardous detection, habitat monitoring, traffic monitoring, earthquake detection, volcano eruption, flooding detection and weather forecasting. Sensor nodes also have found their applicability in agriculture. Soil moisture and temperature monitoring is one of the most important application of WSNs in agriculture. When monitoring the environment, it is not sufficient to have only technological knowledge about WSN and their protocols. It is also necessary the knowledge about the ecosystem.

Environmental Monitoring: WSNs have become an important tool in environmental monitoring. The relatively low cost of the devices allows the installation of a dense population of nodes that can adequately represent the variability present in the environment. They can provide risk assessment information for example

alerting farmers at the onset of frost damage and providing better microclimate awareness.

Pierce and Elliot developed a regional and on-farm sensor network that provides remote, real-time monitoring and control of farming operations in two agricultural applications, a weather monitoring network and an on-farm frost monitoring network [9].

Precision Agriculture: The development of WSN applications in precision agriculture makes it possible to increase efficiencies, productivity and profitability in many agricultural production systems, while minimizing unintended impacts on wildlife and the environment. The real time information obtained from the fields can provide a solid base for farmers to adjust strategies at any time. Instead of making decisions based in some hypothetical average condition, a precision agriculture approach recognizes differences and adjusts management actions accordingly.

Greenhouse: Greenhouse plants and crops can benefit a lot from the use of WSNs, because inside the greenhouse the crop conditions such as climate and soil do not depend on external factors and the implementations are thus easier than in outdoor applications. The first application of WSN in a greenhouse was reported in the year 2003. It was a monitoring and control system developed using Bluetooth protocol. Since then, several applications have been developed, most of them making use of IEEE 802.15.4/ZigBee protocol. Gonda and Cugnasca presented a proposal of a distributed greenhouse control and monitoring system using ZigBee [10]. Lea-Cox et al. developed a WSN in a greenhouse, that integrates a number of sensors which can measure substrate water, temperature, electrical conductivity, daily photosynthetic radiation and leaf wetness in real-time [11].

3 Environmental Monitoring System Applications

Habitat Monitoring: Habitat monitoring (HM) is one of the essential components in environmental monitoring. HM is important to make sure there is no any ecological disturbance for animals and plants. Pollution can cause a lot of negative impacts to the eco system. A web-based system was developed to alert and manage the data of pollution efficiently [12].

Greenhouse Monitoring: The greenhouse effect occurs when solar radiation is trapped by the gases in the earth's atmosphere and reflected back from the earth. Greenhouse Monitoring system normally used to measure and monitor environmental parameters such as temperature, pH, humidity, moisture etc. When the temperature and humidity drops below threshold value the host system will trigger misting, turn on fans etc. Figure 2 shows a greenhouse environment for growing *Capsicum Annum.*

Climate Monitoring: Climate change have brought many effects such as breaking of sea ice, heat waves, glazier melting and lake temperature warming. Thus, there is a need to control and monitor the climate change. Flood prediction is

Fig. 2 A greenhouse environment for growing *Capsicum Annum*

another example of climate monitoring, where wireless sensors can be used to detect rainfall and water levels to trigger an alarm system.

Forest Monitoring: Forests are important sources for biodiversity and ecological balance. Currently, the forest has been interrupted by unethical activities such as illegal logging and development activities. Therefore, it is very important to implement an effective forest monitoring system. The forest monitoring system also includes fire monitoring and detection in forests.

4 Important Parameters in Agricultural Environment

Agricultural environment are complex systems where changes in one environmental factors could have an adverse effect on another factor. Environment factors can affect the growth of plants especially sprouting, pollination and fruit development. Furthermore, these factors can also be used to indicate the risk of plant diseases and future forecasting. Therefore, it is very important to monitor these environment factors. Temperature, humidity, light intensity, rainfall level, air pressure, moisture, electrical conductivity (EC) and pH are some of the important factors.

pH is a very important parameter for plants and crops growth. In general, measurement of soil pH will indicate the soil acidity and soil alkalinity. The growth of different types of plants and crops depends on soil pH. Some plants and crops need acidic soil and some need alkaline soil. The pH also affect the availability of nutrients in the soil, therefore the farmers need to know the pH level so that they can use fertilizers at the right time.

Soil moisture is the water that is held in the spaces between soil particles. Soil moisture data will be used to determine when to irrigate and amount of water for each irrigation. Based on observation, most of the time, the fields are over irrigated. Over irrigation prevents the nitrogen to be used by roots, and lack of oxygen in the root area. Different crops need different level of moisture to maximize the productivity.

Temperature is another important parameter in agriculture field. Low temperatures will slow down the photosynthesis process, thus growth is slowed and this results lower yields. Different plants and crops grow best at different temperature. Humidity is one of the very important parameter in agriculture field. Relative humidity (RH) is the ratio of actual water vapour content to the saturated water vapour content at a given temperature and pressure in percentage. RH indirectly affects leaf growth, photosynthesis, pollination and generate pests and various types of plant diseases.

Temperature and humidity are closely linked in a greenhouse environment. The decrease of the relative humidity is a sign of increased air temperature because cold air has a lower moisture-holding capability than warmer air. Humidity control is very important to prevent plant diseases. The range of healthy RH for plants is from 50 to 70 % [13]. If humidity is below 50 % for longer duration, the plant growth will be affected due to loss of water from leaves might be faster.

Electrical conductivity will determine the suitability of an environment for the plants and crops. EC estimates the amount of total salts or ions in the soil. In general, EC shows the level of ability of the soil water to carry an electrical current. In other words, EC level is an indication of the amount of nutrients available for plants and crops to absorb.

Figure 3 shows one of the wireless sensors developed by MIMOS that can be used to measure the above environment parameters.

Fig. 3 Wireless Sensor for environment monitoring

5 Challenges in Palm Oil Industry

Malaysia's position as the world's leading palm oil country has allowed the industry to flourish in the way it has never been before. The results in the churning out of a wide variety of products as a result of continuous R&D efforts. With the escalation in the volume of palm oil products and the fruit itself, it becomes necessary to produce high quality seedlings from high yield trees by automating and transforming the current process of pollination to meet growing demands.

The current methods of pollination involve tacit knowledge of checking whether a palm is suitable for pollination and manual labour being deployed in fields of vast sizes spanning over thousands of hectares in the nation itself. The drawbacks of such a system is late bagging during the pollination process that ultimately impacts overall yield and the process, being labour dependent, relies on a sizeable number of foreign manpower to work the fields. The current gaps are:

- Human dependence to monitor trees for within the plantation and determine if they are ready for pollination.
- Inaccurate human-based decision making based on the determining of the pollination window.
- Vast plantation areas to be monitored to catch the pollination window to maximise yield.

6 Oil Palm Flower Pollination Process

Controlled pollination consists of transferring pollen from one plant to the receptive female reproductive organs of another plant while excluding all other pollen. Controlled pollination plays an important role in the commercial crops production, especially in oil palm production, as it facilitates producing progeny with favorable genetic trait inherited from the parent plants.

Controlled pollination also contributes to offspring generation with more genetic uniformity compared to the naturally pollinated plants. The success of the pollination process depends greatly on the ability to determine the period at which the flower or floral organs is receptive towards the pollens, namely the pollination period. The introduction of pollens out of the pollination period, either too early or too late, will result in the abortion of the unfertilized flowers or the development of pathernocarpic fruits and thus resulted in a poorly pollinated bunch. Thus, the pollination stage must be accurately determined for the pollination process to take place. The ability to correctly determine the pollination readiness of an oil palm flower provides a significant advancement in the oil palm industry.

Research has shown that the average receptive period of a female flower lasts from 3 to 10 days, depending on the species of the flower. When a female flower is found to be in its receptive period, pollination is usually repeated on three

successive days. Conventional methods done in the agricultural industry to determine pollination readiness include examining the structure of the flower to determine its developmental state and its pollination readiness. The main limitation of this method is the dependence on inspection by eye and the subjective nature of this inspection. Observations alone may differ widely between different individuals, and other factors such as quality of light, time of day, or experience of each individual plays a role in influencing the accuracy of these inspections.

Amongst the many species of flowers, the oil palm flower is known for having a shorter receptive period than average. Its receptive period lasts only for about 36–48 h, with flowering starting at the base of the inflorescence and progressing to the top. The shorter time frame of the receptive period of the oil palm flower increases the complexity of being able to accurately determine the pollination readiness of the flower, and performing pollination even a day too early or too late would result in an unsuccessful pollination of the oil palm flower. The inaccuracy in determining pollination readiness of the oil palm flower could potentially cause a detrimental effect on the palm oil industry in the long run.

Therefore, the challenge to overcome the current conventional method to provide a system and method to determine pollination readiness of a flower in an accurate and time-efficient manner is vital in sustaining a successful production of commercial crop. In this system, sensor node will send humidity value inside a pollination bag every 1 h to server. Another sensor node will send humidity value of an empty pollination bag as a reference. The difference between the two sensor reading will be calculated to determine the best pollination time to start the pollination process.

7 Wireless Technologies and WSN

Many wireless technologies were developed over the last few decades to solve many real-world problems. Wireless technologies and sensor networks have become the most suitable technologies to monitor and control the agricultural environment. These technologies are capable of providing greater level of flexibility, mobility at an affordable cost and low power consumption. There are more than 10 wireless technologies available for industrial applications however the most exploited wireless technologies are Wi-Fi, ZigBee and Bluetooth. The selection of these technologies dependents on the nature of the applications.

Bluetooth: Bluetooth is a short range wireless communication intended to replace portable or fixed device. Bluetooth operates at 2.4 GHz ISM band. Bluetooth has the capability to simultaneously handle data and voice transmissions and used in applications such as hands-free handsets for voice calls.

Wi-Fi: Wi-Fi requires high frequency radio waves, usually 2.4 or 5 GHz for data transmissions and supports several hundred meters between two places. Wi-Fi was initially used in mobile computing devices in LANs but now diversified to more applications such as Internet and consumer electronics. There are few generations of Wi-Fi standards available and carter for different applications.

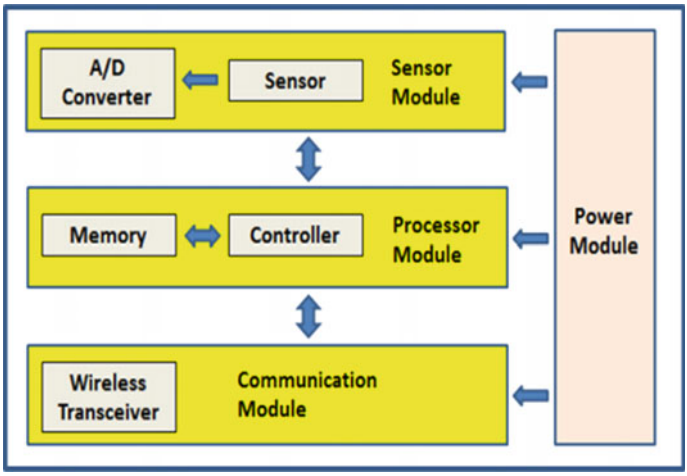

Fig. 4 WSN Node architecture [23]

ZigBee: ZigBee is used for short range wireless communications. ZigBee is targeted for cost sensitive applications such as home and building automation. ZigBee supports data transmission up to 100 meters and consumes less power and most suitable for portable and low power consumption applications.

Figure 4 shows a general WSN node architecture. Each sensor network node consists of a sensor module, processor module, communication module and power module using battery. The rapid evolution of the Micro-Electro-Mechanical Systems (MEMS) has contributed to the development of small and smart sensors. These sensors have become increasingly very small in terms of size, more intelligent and less expensive. WSN is a network of small sensing devices known as sensor nodes or motes, arranged in a distributed manner, which collaborate with each other to gather, process and communicate over wireless channel about some physical phenomena.

The selection of wireless technologies depends on their applications. For example, ZigBee technology cannot be applied to high data transmission applications because of their high bandwidth requirements. Bluetooth and Wi-Fi are not suitable for battery powered applications because of their high power consumption.

8 Platform Architecture

MIMOS PA solution comprise of three platforms; MIMOS Wireless Sensor network called as MSCAN, Precision Agriculture Management System (PAMS) which has MBPS parser engine and raw database, and Application Database (DB) and Web-based Application Services.

Figure 5a shows general MSCAN architecture which consists of sensor node, router and gateway. Sensor node has two main parts; tip and mote. Gateway also has two main parts; collector and main microcontroller unit (MCU). Currently MSCAN platform is using ZigBee as the wireless communication technology. At application layer, MSCAN architecture use proprietary protocol named as MBPS for application data communication.

MSCAN make use ZigBee technology to provide mesh network, self-organised and self-healing network features. By making used of application specific profile, MSCAN platform is allowed to implement application for MIMOS PA solution. Products that had been developed for MSCAN Platform are Sensor Node, Router and Gateway.

MSCAN Sensor Node: Fig. 5b shows MSCAN sensor node product. There are two types of tip, sensor tip and actuator tip. Tip will has unique identification number and version identification. Version identification will determine number of difference sensors or actuators on the tip. Each sensor or actuator has a type ID to identify type on sensor or actuator on the tip.

Mote is a wireless end device that has battery which also supply power to the tip attached to the mote. Mote has unique MAC address and will be assigned a network address when it joins the network. Mote has two push-button and two led for the user interface. Mote implements power management that able to save battery for long operation and longer life. Mote controls tip operation by controlling power and using MBPS protocol for communication between mote and tip.

MSCAN Router: MSCAN Router provides hopping feature that allows Sensor Node to be placed longer distance from the Gateway [14]. MSCAN architecture has been configured to support maximum of 5 depth of hopping from Gateway to the last Sensor Node in a network. Gateway and Router both can support maximum of 5 Routers child. Using multiple routers in a network will allow wide coverage of

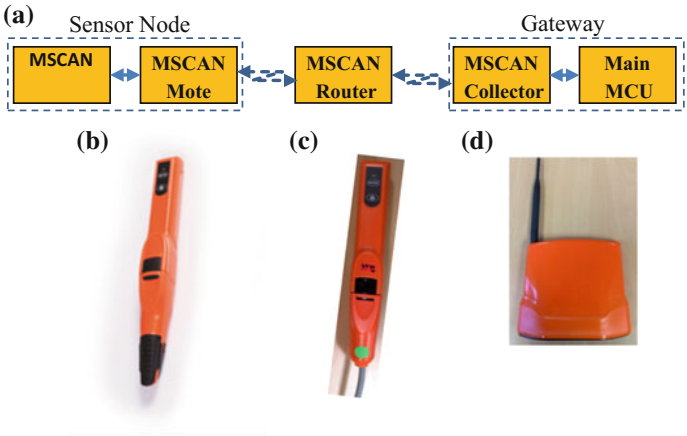

Fig. 5 MSCAN platform architecture

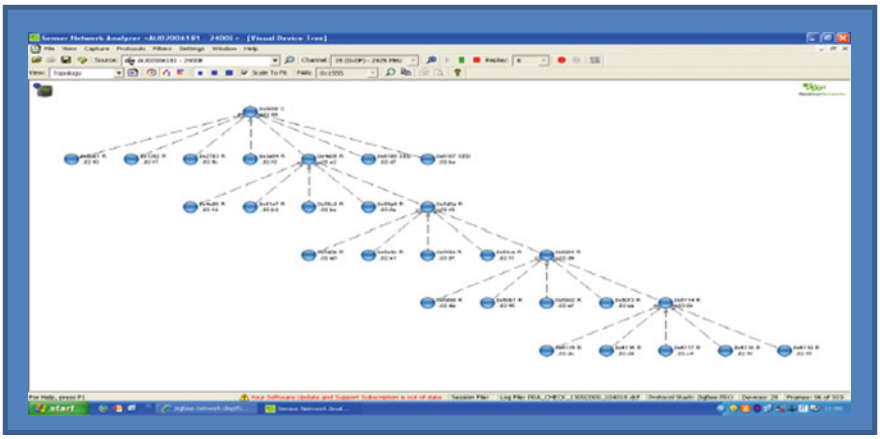

Fig. 6 Maximum of 5 depth of hoping by routers

network with mesh network capability [15]. Router has to be powered up to ensure network is always available for the sensor node to send sensor data to the Gateway [16]. Router use external battery that has enough capacity to provide power longer life. Figure 5c shows MSCAN router product that has cable to connect to the external battery [17] Fig. 6.

MSCAN Gateway: MSCAN Gateway has two main module; Collector and Main MCU board. Collector is a ZigBee coordinator that control router and Sensor Node in the wireless sensor network. Collector interfaces to the main CPU using serial interface. Main CPU board has GPS module, GSM module and other control circuit for the gateway.

Collector forwards sensor data in MBPS packet format to the Gateway main CPU which sends the packet to LSMS server using GPRS or SMS over GSM network. Gateway is located in the field, powered by battery and solar panel. Figure 5d shows MSCAN gateway product.

9 System Architecture

The system architecture of the Pollination Monitoring System consists of three layers as shown in Fig. 7. The Physical Layer represents the physical sensors, actuators and CCTV cameras. The Middle Layer represents the WSN interface, CCTV interface, sensor and image manager, database, App server and Web server. Finally, the Application Layer represents the Graphical User Interface (GUI), monitoring services (sensor and image monitoring), alerting services and decision making services.

The applications developed using this architecture can measure and analyse external weather conditions such as temperature, humidity, rain fall, wind direction,

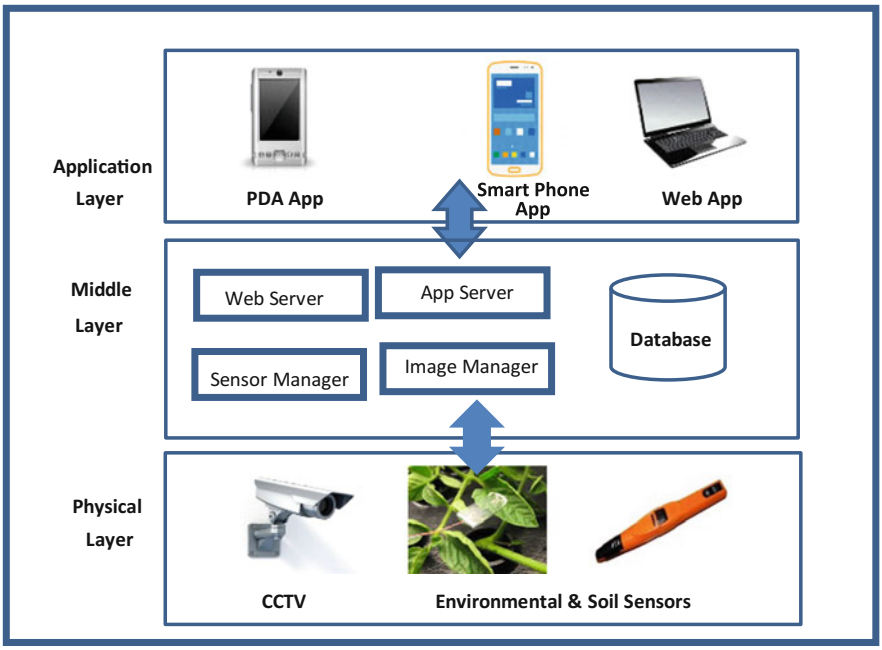

Fig. 7 System architecture

wind speed and also internal weather conditions in a greenhouse such as temperature, pH, relative humidity, moisture, CO_2, EC, and the intensity of light. The information collected in real-time is then converted and stored into a database through a web server, which provides critical information to users.

Physical Layer: The physical layer consists of wireless environmental, soil sensors (temperature, humidity, moisture, EC, pH and CO_2), actuators and CCTV cameras. These sensors will collect environmental and soil information from indoor (e.g. greenhouses) and outdoor environment periodically and sent the data to sensor manager.

The measurement data include temperature, humidity, soil and water pH, soil moisture, rainfall quantity, EC, wind speed and direction, water level, water consumption, etc. The data is further analyzed and converted into appropriate formats and finally sent to Middle Layer for storing in databases.

Middle Layer: The middle layer (ML) supports communication between physical layer and application layer. Currently this architecture is using *ZigBee* as the wireless communication technology. The ML converts the data received from the physical layer and store it in a database. The ML will also support the data request from the application layer. The Web server and App server allows users to monitor data processed by the components through a Web browser, PDA or smart phone at any time.

The sensor manager converts and analyses this data and store it in a database. The web server will fetch the sensing data stored in the database at a fixed interval and send it to the GUI. The users can view the sensor data through the GUI in the Application Layer. The GUI will also display and send emails and SMS if there is any alerts and warnings. The CCTV cameras will collect real-time image information (real-time streaming) on the indoors and outdoors and send it to image manager. The image manager will store it in the database. The user can access the image data at anytime and anywhere through the GUI using PDAs or Smart Phones.

The web server used to host sites and deliver web pages content to clients who can access them through the Internet. Another use of web server is to connect any component of the physical layer to browse any monitoring or actuating device in real time.

Application Layer: The application layer consists of various GUIs to provide suitable information and support user requests. The users can access environmental information and status through various platforms such as smart phone, web and PDA. This layer also consists of monitoring support, actuating support, alerting support and decision making support.

10 Pollination Readiness Monitoring Process

A review of pollination studies conducted on palms by Henderson showed that mainly insects are responsible for transferring pollen from anthers to stigma [18]. Henderson concluded that three major pollination syndromes exist in palms: beetle pollination (*cantharophily*), bee pollination (*mellitophily*) and fly pollination (*myophily*).

More particularly, in palm trees bearing inflorescences which will develop into fruit bunches upon fertilization, specific procedure is adopted in the controlled pollination system. Prior to the anticipated pollination occurrence, the inflorescence is required to be covered with a tight bag fitted with a transparent window (refer Fig. 11), so that unwanted pollens will not reach the inflorescences during the receptive period of the inflorescence.

The transparent window is necessary to enable visual inspection on color and structural developments of the inflorescence, according to the conventional way of detecting pollination. Upon visual detection of pollination, controlled pollination is carried out by applying pollens of a desired progeny directly onto the female inflorescence using a hand puffer. Santos et al. [19] reported that the inflorescence should be inspected daily or every alternate day, starting from the day of bagging, to verify the onset of pollination of the inflorescence.

The pollination readiness monitoring process developed in this project starts with identifying the female inflorescences which are going to be pollinated. The complete process is described below and Fig. 3 represent the overview system for determining pollination readiness.

(a) The female inflorescences which are going to be pollinated are identified. The female inflorescences which are anticipated to undergo pollination within certain number of days are covered with a bag attached with a main humidity sensor on the interior surface of the bag.
(b) A reference humidity sensor is installed inside another bag similar to the bag covering the main humidity sensor. The bag containing the reference humidity sensor is placed in a position similar to the bag containing the main humidity sensor in terms of the height of the surrounding trees.
(c) The humidity value is taken by the main humidity sensor and the reference humidity sensor at certain times of the day. Each reading of the humidity detected will be compiled into a database in a matrix form, wherein the humidity readings will be arranged in one row in the matrix. For each day, a new row is added to the humidity matrixes of the main humidity [H_m] and the reference humidity [H_r]. The humidity profiles are compared regularly to determine whether pollination has occurred.
(d) A general formula for determining pollination is shown below, where pollination is deemed to have occurred when:

$$[\alpha] \cdot [H_m] - [\beta] \cdot [H_r] > [H_R]$$

In which [α] and [β] are the coefficient matrixes and [H_R] is the triggering matrix. The meaning of the above equation is that if a predefined combination of the humidity of the main bag is greater than a predefined combination of the humidity of the reference bag by the triggering (threshold) value, then pollination is deemed to have occurred. The threshold humidity values are based on pre-existing information of humidity values emitted from flowers ready for pollination that were collected over the years using sensors in different plantations.
(e) Once pollination is determined to have occurred, the system will notify the user regarding the event on the GUI (Web) and also by sending a message to the user's mobile phone. Upon receiving the notification, the user will introduce the male pollen to the female inflorescence.
(f) The bag covering the inflorescence is opened and the pollens of the desired progeny are transferred to the inflorescence. This can be carried out, for example, by applying the pollens onto the inflorescence by using a hand puffer. In a preferred embodiment, the pollination has to be performed on the same day or the subsequent day of the receipt of the notification. This will complete the controlled pollination process Fig. 8.

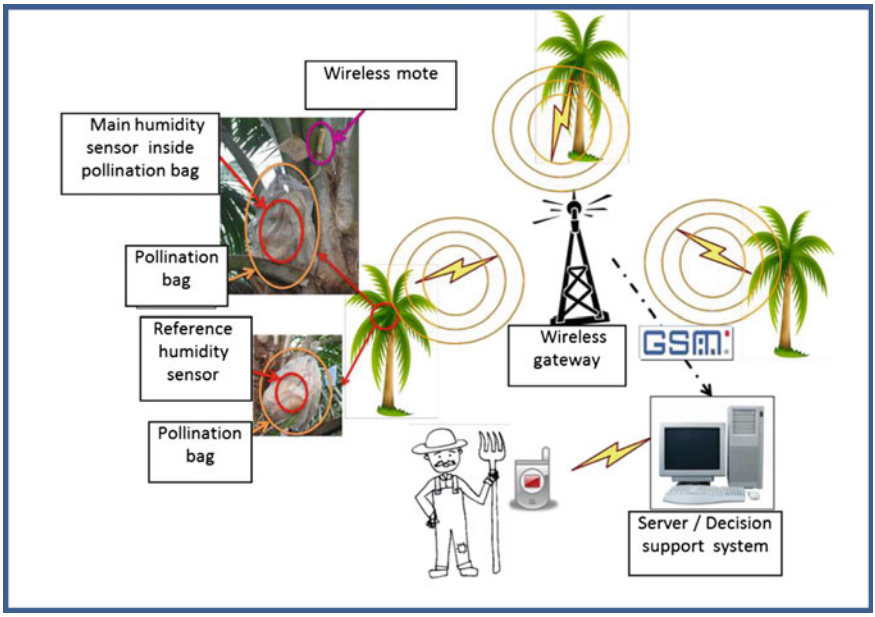

Fig. 8 Overview system for determining pollination readiness

Fig. 9 GUI of pollination monitoring system

(a) Gateway installation - fixed pole and powered by car battery & solar.

(b) Router installation use portable pole.

Fig. 10 Router and gateway installation at site

11 Pollination Monitoring Systems (PMS)

The above mentioned architecture in Fig. 7 has been deployed to monitor the humidity of a mother palm to find the best time to start a pollination process. Sensor Node will send humidity value inside pollination bag at a predefine interval and forward by Gateway to PMS using SMS/GPRS over GSM.

The GUI of PMS present important information such as list of data from sensor node, sensor status, pollination alert list and sensor battery level. Figure 9 shows the GUI for PMS. Each of the node in the GUI represent a sensor node installed at

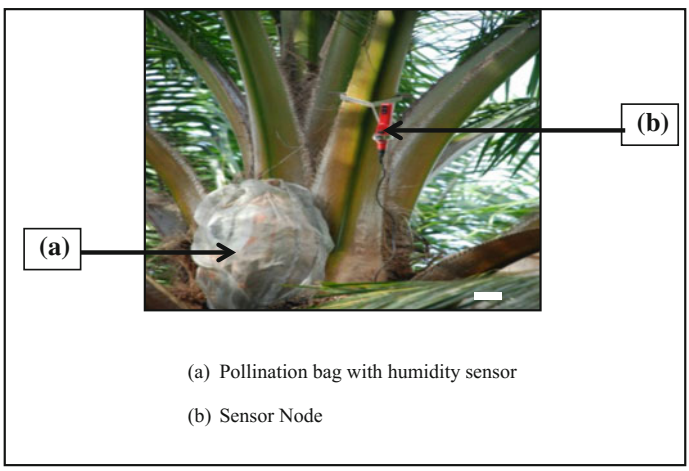

Fig. 11 Sensor node installed at palm oil frond

palm oil frond. The colour of each node represent the pollination status of each palm tree. The trees which are ready for pollination is represented in blue colour.

Figure 10 shows the router and gateway installed at the palm oil plantation. Figure 11 shows the sensor node and pollination bag with main humidity sensor.

12 Results and Discussion

In Phase 1 of this project, 200 palm oil trees are deployed with wireless sensors. Each palm oil tree will be tagged for identification purposes. The initial threshold value for pollination readiness are based on values obtained from manual observation. In Phase 2, another 300 palm oil trees are deployed. The improved threshold value from Phase 1 was used in this phase. The final results show that the threshold value from Phase 1 is very consistent throughout this project.

The data collection after the certain days of bagging will be carefully monitored to see whether any pollination readiness has taken place. Figure 12 shows a set of data (humidity from a pollination bag) collected on the nth day after bagging.

Figure 13 shows the graph of humidity difference between the humidity value from main sensor and reference sensor. This graph will help us to determine whether pollination has taken place or not.

Once pollination have occurred, the system will notify the user regarding the event on the GUI (Web) and also by sending a message to the user's mobile phone. Upon receiving the notification, the user will introduce the male pollen to the female inflorescence on the same day of receipt of the notification to complete the controlled pollination process.

In an oil palm plantation, 69 palm oil trees were selected randomly to install with sensors. The purpose is to test pollination readiness (CP) success rate. In this test, PMS manage to detect a total number of 64 trees means these oil palm trees are ready for pollination. We can conclude that the IPMS success rate in detecting pollination readiness is 93 %.

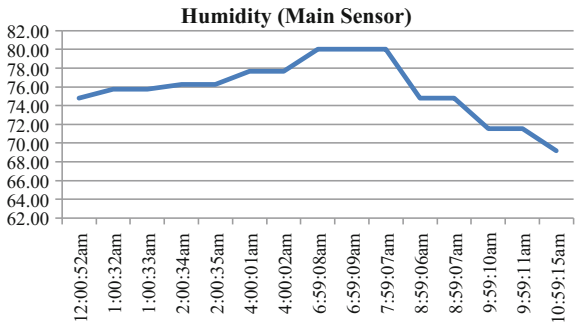

Fig. 12 Humidity form main sensor node

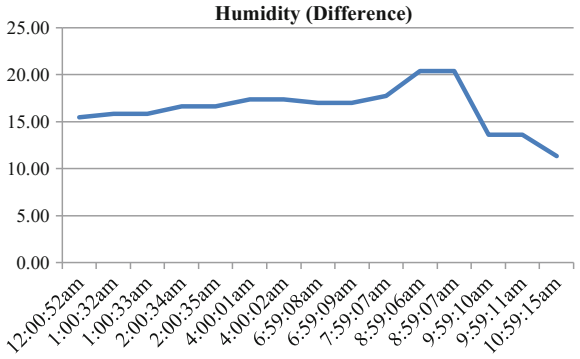

Fig. 13 Humidity (Main)—Humidity (Reference)

13 Conclusions

Using the key elements of information, technology, and management, PMS can be used to increase production efficiency, improve product quality, conserve energy and protect the environment. Moreover, PMS with minor customization can also be applied to other agricultural environmental applications.

Some of the benefits of using smart agriculture system for oil palm pollination are as follows:

- To be able to trigger pollination period within certain days.
- To increase yield.
- To increase productivity.
- Possible reduction of labour dependency.
- To be able to directly communicate with the sensor nodes to get real time data using WSN.

WSN ecosystem can be deployed in various sectors provided that the end-to-end devices and solutions are properly configured. WSN is the key for deployment of IoT as it provides large pool of sensors to be configured to the end devices. Among the critical issues in palm oil pollination readiness monitoring is the RF range due to the coverage of palm leaves and also terrain of the plantation area [20, 21]. The second issue is on the power management for the sensor node which uses battery to operate. However, in this project we only target sensor node battery life up to 2 years due to battery life time limitation [22]. We can conclude that the PMS success rate in detecting pollination readiness is more than 90 %. The network data security and power management with efficient algorithms will also be given higher priority in our future work.

References

1. M.S. Chaudhari, R. Jaiswal, C. Birhade, V. Bhapkar, Wireless sensor network as a tool for supporting agriculture in the precision irrigation. Int. J. Adv. Res. Comput. Commun. Eng. **4** (2), 311–314 (2015)
2. N. Wang, N. Zhang, M. Wang, Wireless sensors in agriculture and food industry—recent development and future perspective, review. Comput. Electron. Agric. **50**, 1–14 (2006)
3. M. Sherine, A. El-Kader, B.M. Mohammad El-Basioni, Precision farming solution in Egypt using the wireless sensor network technology. Egyptian Inform. J. **14**(3), 183–250
4. Sagar Lachure, Amol Bhagat, Jaykumar Lachure, Review on precision agriculture using wireless sensor network. Int. J. Appl. Eng. Res. **10**(20), 16560–16565 (2015)
5. S.R. Nandurkar, V.R. Thool, R.C. Thool, Design and development of precision agriculture system using wireless sensor network, in *2014 First International Conference on Automation, Control, Energy and Systems (ACES)*, 2014, pp. 1–6
6. P. Harrop, R. Das, Wireless sensor networks 2012–2022. IDTechEx (2012)
7. P. Harrop, Wireless sensor networks and the new Internet of things. Energy Harvest J. (2012)
8. T. Arampatzis et al., A survey of applications of wireless sensors and wireless sensor networks, in *Proceedings of 13th Mediterranean Conference on Control Automation*, Turkey, 2005, pp. 719–724
9. F.J. Pierce, T.V. Elliott, Regional and on-farm wireless sensor networks for agricultural systems in Eastern Washington. Comput. Electron. Agric. **61**, 32–43 (2008)
10. L. Gonda, C.E. Cugnasca, A proposal of greenhouse control using wireless sensor networks, in *Proceedings of Computers in Agriculture and Natural Resources, 4th World Congress Conference*, Orlando, FL, USA, 24–26 July 2006
11. J.D. Lea-Cox, G. Kantor, J. Anhalt, A. Ristvey, D.S. Ross, A wireless sensor network for the nursery and greenhouse industry, in *Proceedings of Southern Nursery Association Research Conference*, Atlanta, GA, USA, 8–9 August 2007
12. S. Roy, D. Anurag, S. Bandyopadhyay, Testbed implementation of a pollution monitoring system using wireless sensor network for the protection of public spaces. Recent Advances in Broadband Integrated Network Operations and Services Management, pp. 263–276 (2011)
13. T. Ahonen, R. Virrankoski, M. Elmusrati, Greenhouse monitoring with wireless sensor network. Department of Computer Science, University of Vaasa (2003)
14. M. Beldjehem, Toward a multi-hop, multi-path fault-tolerant and load balancing hierarchical routing protocol for wireless sensor network. School of Information Technology and Engineering, University of Ottawa, Ottawa, Canada (2013)
15. I. Stojmenovic, Ad hoc and sensor wireless networks **1** (2005)
16. S.K. Singh, M.P. Singh, D.K. Singh, Routing protocols in wireless sensor networks: a survey. Int. J. Comput. Sci. Eng. Surv. (IJCSES) **1**(2) (2010). doi:10.5121/ijcses.2010.120663
17. A. Kellner, O. Alfandi, D. Hogrefe, A survey on measures for secure routing in wireless sensor networks. Ashdin Publ. Int. J. Sens. Netw. Data Commun. **1** (2012)
18. A. Henderson, A review of pollination studies in the Palmae. Bot. Rev. **52**, 221–259 (1986)
19. G.A. Santos, P.A. Batugal, A. Othman, L. Baudouin, J.P. Labouisse (eds.), *Manual on standardized research techniques in coconut breeding* (IPGRI, Rome, Italy, 1996)
20. M.R.H. Khan, R. Passerone, D. Macii, RF-level power consumption measurement (RF-PM) for zigbee wireless sensor network-towards cross layer optimization. University of Trento, Via Sommarive, I-38100 Povo, Italy
21. J. Tyzzer, Easing the challenge of RF. Nordic Semiconductor White Paper (2010)
22. I.M. Yusoff, A.N. Harun, S.S. Ramli, RF and battery performance study for WSN in palm oil plantation applications. IEEE Conf. Wirel. Sens. (ICWiSE) **2014**, 85–89 (2014)
23. C. Alippi, R. Camplani, C. Galperti, M. Roveri, A robust, adaptive, solar-powered WSN framework for aquatic environmental monitoring. IEEE Sens. J. **11**(1), 45–55 (2011)

Time Domain Reflectometer for Measuring Liquid Waste Levels in a Septic System

Shreya Reddy Mamidi, Kaushik Bukka, Michael Haji-Sheikh, Martin Kocanda, Donald Zinger and Mansour Taherinezahdi

Abstract The objective of this study was to determine the level of water in a septic tank by inserting a waveguide at the top of the tank. A TDR (i.e. waveguide) probe is immersed in the water tank, through which a pulse signal is launched. The impedance mismatch occurs at the air-water interface and the bottom of the tank, which results in the reflection of the signal. This reflected signal is algebraically added to the incident signal. From the time difference between the incident and reflected signal, the distance between the TDR and the surface of water is calculated. The distance is generally twice the time traveled by the wave. Thus, the calculated distance helps in finding out the length of water in the tank. Additionally, the TDR was compared with a Doppler radar system to determine if the Doppler system would be a feasible non-contact measurement system as compared to the TDR.

1 Introduction

A Time Domain Reflectometer (TDR) level measurement device capable of generating and receiving electromagnetic waves for the measurement of waste water is demonstrated. Waste water in a septic system is a mixture of solids and liquids along with various levels of acidic compounds of urea. Disinfectants and other additive chemicals also effect the melange that are in the human waste-water systems. Typical measurement systems for these type storage containers often are float based and or they use ultrasonic transceivers. Septic systems that could use this type of measurement system are, but not limited to, transportation systems. These transportation systems are buses, planes, and trains. If the system cost is low enough, the application space can be expanded to recreational vehicles. These vehicles have extremely large storage tanks and a measurement system can help

S.R. Mamidi · K. Bukka · M. Haji-Sheikh (✉) · M. Kocanda · D. Zinger · M. Taherinezahdi
Department of Electrical Engineering, Micro-Electronic Research an Development Center, Northern Illinois University, Dekalb, IL 60115, USA
e-mail: mhsheikh@niu.edu

S. Mukhopadhyay et al. (eds.), *Sensors for Everyday Life*, Smart Sensors, Measurement and Instrumentation 23, DOI 10.1007/978-3-319-47322-2_8

prevent accidental spillage and localized environmental damage. The primary objective, though, is to measure the height of waste water in a tank and design an efficient measuring device. The TDR is based on the reflection mechanism, in which the time delay between the transmitted and reflected signals helps to determine the distance from the source to the surface of water, which is later used to calculate the height of water in the tank. The TDR is built using a 74AC14 IC, which is capable of producing pulse signals with very low rising and falling times that provide greater accuracy. Thus, the generated pulse signals are transmitted into the probe inserted in a tank. The total time taken by the pulse to travel the path to and from is calculated, which in return helps in calculating the height of the liquid in the tank. The functioning of the proposed TDR circuit and the bi-axial probe is also tested in the laboratory.

Level estimation is used to determine the linear vertical separation between a reference point and the surface of the liquid or top of a pile of divided solids [1]. The water level in a tank such as underground septic tank or overhead water tank or airplane septic tank has to be estimated. If the sewage overflows a groundwater tank it could cause a shutdown of drinking water systems. If it reads full in an aircraft the regulators force an unplanned landing not to mention that the passengers will have to deal with unpleasentness. It is necessary to know the level of water in the tank to avoid problems, like overflow and leakage. There are many ways to estimate the water level in tanks, such as sight glasses, hydrostatic devices, capacitive level sensors and microwave sensors. Sight glasses are susceptible to leakage and also conceal visible level of water due to the sediment buildup on it. Hydrostatic devices such as displacers, bubblers and differential pressure transmitters have reduced measurement accuracy, due to the shift in the liquid's gravity based on change in temperature. In case of capacitive sensors, long conductive cables suffer cable breakage due to extreme mechanical tension. Radar systems through-air are affected by divergence problems. In order to estimate the level of water in the tank, engineers have to come up with a technique, which is more efficient than the above mentioned procedures. The trending technology these days is measurement of distance between the source and liquid level by time-based measurement, which replaced mechanical and pressure-based measurement tools. One such method is Time Domain Reflectometry where the probe provides the focused path [2]. The TDR system does require contact to the liquid which may be an issue in some applications. Unlike, ultrasonic measurement systems which may be fooled by floating debris that absorbs ultrasonic energy (materials such as water logged paper), the TDR is immune to those effects.

Time Domain Reflectometer (TDR) is fundamentally a radar in which a voltage pulse is launched along a co-axial cable. Whenever distortion (or defect) occurs along the cable, a reflection of the transmitted wave happens. The location of the cable defect is determined by the reflection travel time, and the reflection magnitude is proportional to the magnitude of the defect. In case of water level measurement, a hollow co-axial cable can be installed in a monitoring tank, and it is observed that the reflection occurs at the air-water interface. This strong reflection makes it possible to monitor changes in water level. A common component in sewage is the

presence of toilet tissue. Some of this material breaks down readily and some of the material floats. Since this material is saturated with water is should not significantly affect the reflection from the air water interface.

The TDR technique was introduced in the early 1980s. Since its introduction, it has gained interest by many fields of science for various applications [3]. TDR has wide variety of applications and is very efficient compared to other measurement techniques. TDR is also used for measuring impedance of the transmission lines, dielectric constant of the medium of transmission, electrical conductivity and types and position of faults in the transmission lines. A brief mention of some of the previous work performed in the area. Tomi Engdahl designed a simple TDR using 74AC14 IC, which was primarily used to detect faults along the cable. He also analyzed the outputs and classified them into different types of distortions [4]. Jim Bartling worked on a "Low cost, high resolution Time Domain Reflectometer" which was designed using a 16-bit microcontroller and a Charge Time Measurement Unit (CTMU) peripheral on-chip that is used to measure time with a high degree precision and resolution. The main goal of his work was to find out transmission-line length, location of faults due to opens and location of faults due to shorts [5]. Jim Bartling also developed a "Time Domain Reflectometer for liquid level measurement". He has designed a TDR using PIC microcontroller and used it with a probe to measure the level of liquid. Time measurement is again accomplished using CTMU. It provides information of the fluid composition as well [6]. Brian Kenner and John Wettroth designed a TDR using Intel 87C51 microcontroller to measure length and termination impedance of co-axial cables commonly used in computer networks, like Ethernet, Arcnet etc. A high-speed comparator is enabled to measure the length. The software consists of approximately 3 K of 8051 assembly language [7]. James R. Andrews analyzed "Time Domain Reflectometry and Timer Domain Transmission Measurement fundamentals" in 2004. The main aim of his study was to identify the nature of the Device Under Test (DUT) [8]. Scott B. Jones, Jon M. Wraith and Dani Or discussed "*Time domain reflectometry measurement principles and applications*" in 2002. Their main motive was to determine the porous media water content based on dielectric properties and electrical conductivity of the medium [3]. Kevin M O'Conner and Charles H. Dowding worked on "*Real-Time monitoring of infrastructure using TDR technology*". His study reveals the summary of principles involved in various applications of TDR. This work was primarily intended to provide background on the principles involved in geotechnical and infrastructure applications of TDR [9]. Xinbao Yu and Xiong Yu studied on "*Measurement of simulated scour by Time domain reflectometry*" in 2006. "TDR instrument and analyses framework can be potentially refined into a useful tool for bridge scour surveillance". Their study shows the determination of dielectric constant, electrical conductivity, the depth of the scour and properties of the soil sediments (porosity, density) [10]. A. Thomsen, B. Hansen and K. Schelde proposed a TDR technique for measuring water level in tanks collecting surface water runoff and soil moisture in their paper "*Application of TDR to water level measurement*" in 2000. They designed a two-wire closed loop TDR probe with balun transformer for transforming impedance from 50 to 200 Ω. The water level calibration depended on

time-based measurements [11]. D. Moret, M. V. Lopez, J. L. Arrue worked on water level measurement and volumetric water content of the soil in Mariotte reservoir using TDR method. Their work was published as "*TDR application for automated water level measurement from Mariotte Reservoirs in tension disc infiltrometers*". A three-rod TDR probe was designed that was used for simultaneous measurements of both water flow and volumetric water content of soil below the infiltrometer disc, placed at the bottom of the reservoir. The measurement was done considering the summation of pulse travel times [12]. W.F. Kane studied "*Embankment monitoring with time domain reflectometry*", where the slope movement and peizometric levels were determined. The work proposed the use of coaxial cable which was embedded in the vertical hole to locate shear failure in the embankment, rate of ground movement and water levels. It was the first application of TDR in civil engineering in 1998 [13].

2 Scope of Work

The objective of this study is to determine the level of water in a septic tank by placing a waveguide at the top of the tank. A TDR (i.e. waveguide) probe is immersed in the water tank, through which a pulse signal is launched. The impedance mismatch occurs at the air-water interface and the bottom of the tank, which results in the reflection of the signal. This reflected signal is algebraically added to the incident signal. From the time difference between the incident and reflected signal, the distance between the TDR and the surface of water is calculated. The distance is generally twice the time traveled by the wave. Thus, the calculated distance helps in finding out the length of water in the tank. Additionally, the TDR was compared with a Doppler radar system to determine if the Doppler system would be a feasible non-contact measurement system as compared to the TDR.

2.1 TDR Measurement System

TDR was basically developed to check for faults in cables. That where it got its name as 'cable tester' [3]. TDR is also called guided-wave RADAR, i.e. the positive pulse generated by TDR, travels along the cable or a metal rod under test. The signal waveform is seen on the Oscilloscope, which is connected at the source and DUT connection. This explains the basic TDR setup. It generates a step signal or an impulse with fast rising and falling edges. The rise and fall time of the pulse matters, the steeper the slope the greater the resolution [10].

Once the incident pulse is fed into the DUT, the waveform displayed by the Oscilloscope is monitored. If the load impedance matches the characteristic impedance of the line, no reflection is seen. Since the whole signal transmitted is absorbed at the load. The only thing seen on the Oscilloscope screen is the incident pulse. But, if the load impedance does not match the characteristic impedance of the

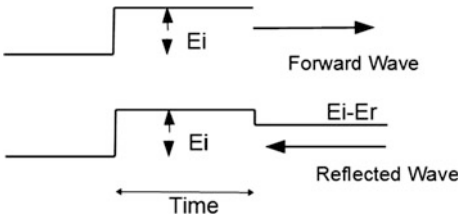

Fig. 1 (*Top*) Oscilloscope display when load impedance matches characteristic impedance. (*Bottom*) Oscilloscope display when load impedance mismatches characteristic impedance [14]

line, part of the incident pulse is reflected back to the source, which is recorded by the Oscilloscope as in the Fig. 1. This reflected pulse can be easily noticed as there is a time difference between incident and reflected pulses [14].

For cable testing, a cable of known length with velocity of propagation, Vp, is taken, and reflections from discontinuities are observed on the Oscilloscope screen. The time difference and the voltage difference between the incident and the reflected peaks are noted, from which the distance of the discontinuity from the source can be calibrated. The time difference is the time taken by the wave to travel the round trip (i.e. two times the length, L) between source and discontinuity. Therefore the time difference is:

$$t = \frac{2\mathrm{L}}{v} \tag{1}$$

where, L is the length of the discontinuity from the source, t is the time difference (total time taken from source to discontinuity and again back to source) and v is the velocity of light in the medium. TDR is also used to measure the properties of the materials surrounded by the probe. Typical properties are impedance, dielectric constant, its conductivity and velocity of propagation.

2.2 Advantages and Disadvantages of TDR

TDR has many advantages compared to other measurement techniques.

1. It has the ability to measure reliably even in temperature and pressure fluctuations, dust and noise, condensation and steam generation.
2. TDR can be used to measure the level of any kind of liquid. It is immune to different properties of liquids like dielectric constant.
3. Multiple discontinuities can be measured at same time unlike other techniques.
4. It is a non-destructive method of testing.
5. It has the ability to provide thorough time series measurements at multiple locations.

6. It provides simultaneous measurement recording. The TDR probe is resistant to corrosion and also immune to mechanical shock, TDR parts do not wear out, circuitry is simple and operates at low voltage and better resolution compared to other techniques.

There are also few limitations and disadvantages in TDR.

1. Discontinuities that are either small or closely spaced are mathematically smoothed into single irregularity. This effect does not show up all the discontinuities and also leads to inaccurate impedance readings. If the distance between the two neighboring discontinuities is less than half the rise time of TDR, then the discontinuities are merged into one signal [14].
2. TDR system's resolution can be affected by rise time, settling time and pulse aberrations.
3. By the time the incident pulse reaches the end of the cable, the rise time and settling time might be degraded, which affects the resolution and accuracy of the system.
4. Internal reflections from the mismatches and random noise induce error.
5. The electrical interface from coaxial cable to probe might cause localized disturbance.

But the advantages of TDR technique outweigh the disadvantages when using with wastewater.

2.3 Proposed Circuit

In the previous section, TDR basics and transmission line basics were discussed. Their functions and various applications have been analyzed. In this chapter the proposed circuit and the experimental setup for measuring the water level in the tank will be studied.

The TDR circuit discussed starts Wolke's [15] TDR circuit. This simple circuit comprises of a Schmitt trigger for generation of a square wave which acts as the source of incident voltage pulse.

The Fig. 2 shows the block diagram of the experimental setup. The setup is divided into three main parts. The signal generation, TDR probe and Oscilloscope. The signal generation is carried out by the simple TDR circuit built in the laboratory. The Oscilloscope is used to check the waveforms and also to extract the data in the digital form. The probe used here is a bi-axial probe built using two brass rods. All these three parts are inter-connected using a BNC Tee-connector.

In the sections below, all the parts will be discussed. The Oscilloscope used here is Agilent Technologies Digital Storage Oscilloscope DSO1102B. It is a 2-channel, 100 MHz Input bandwidth oscilloscopes with a sample rate of 500 MSa/s–1 GSa/s [16]. Signal generation is done by a simple TDR circuit, built using 74AC14 IC as shown in the Fig. 3. It generates a square wave with fast rising and falling edges,

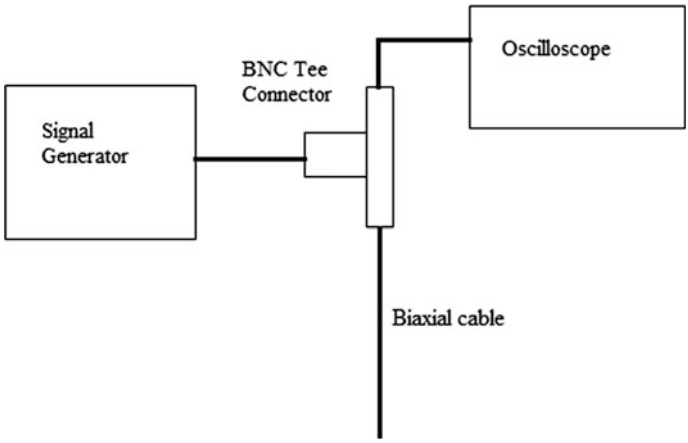

Fig. 2 Block diagram of the TDR system used in this study

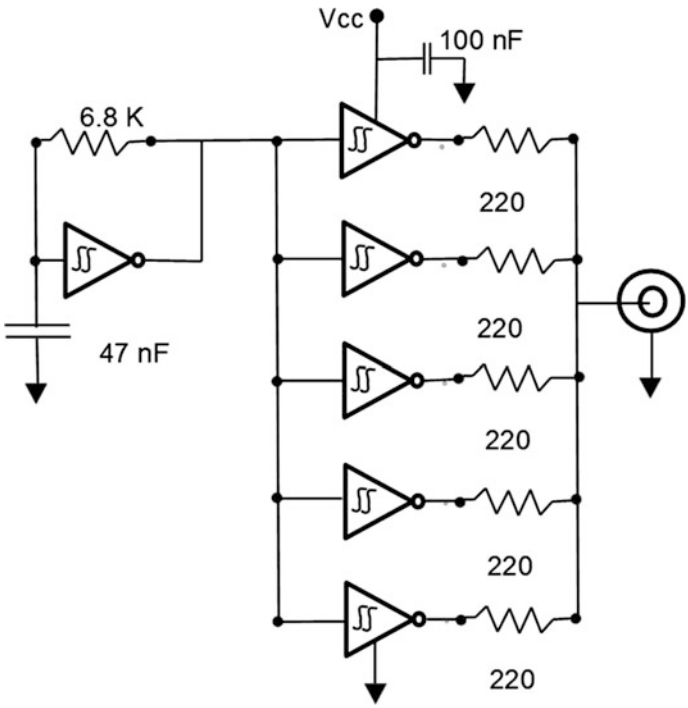

Fig. 3 Schematic of TDR circuit [15]. Signal generation is done by a simple TDR circuit, built using 74AC14 IC

which is transmitted to the biaxial cable that is immersed in the water tank. This TDR circuit has the Schmitt trigger in the circuit which yields the square wave.

The TDR probe used here is a bi-axial probe (i.e. 2-wire transmission line). It is made out of two 3/32 brass rods which are 36 inches long and have 2.38 mm diameter. These two brass rods which have to be immersed in water and are connected to a coaxial cable at one end. First, the outer conductor of the coaxial cable is unbraided and connected to one of the brass rods, and the inner conductor is connected to the other rod using crimp connectors. The main stretch of the bi-axial cable in targeted to be at 50 Ω in air to minimize the reflections when the tank has no water in it. The connections to the bi-axial cable create a static reflection node which does not change.

3 Experimental Procedure

The TDR circuit and probe built are now used to calibrate the level of water in the tank. Firstly, the TDR launches the voltage pulse into the probe. This incident pulse reflects at the bottom of the tank and the air-water interface, due to change in impedance. As the probe is open at the end, reflection happens at the end of the probe. At air-water interface, due to large difference in the dielectric constants of air and water (i.e. 1 and 80.4 respectively) impedance mismatch occurs. The incident and reflected signals are captured on the Oscilloscope screen. The time difference between the two peaks (i.e. the incident and reflected peaks) is found out, which in return helps to find out the height of water in the tank.

The Fig. 4 shows the setup in the water tank. The propagation velocity of the probe inserted in the medium must be known to find out the height of water. The wave propagates through coaxial cable, air and water mediums. The velocity of propagation is different in each section. The total time will be the summation of travel times in all the phases (coaxial cable, air and water). Then from the measured travel time, it will be easy to find out the level of water in the tank [12].

The coaxial cable used here has a solid polyethylene dielectric with dielectric constant 2.23, and characteristic impedance 50 Ω. The velocity factor of coaxial cable is 67 %, i.e. the velocity of propagation of wave in coaxial cable is 0.67 times the velocity of propagation in air (3×10^8 m/s). Therefore, the velocity of propagation of wave in coaxial cable is 2×10^8 m/s.

The relative dielectric constant of water is 80.4. The speed of EM wave propagating through a dielectric medium is given by:

$$V = c / (\varepsilon_r^{1/2}), \tag{2}$$

where, V is the velocity of wave in medium, c is the velocity of wave in vacuum = 3×10^8 m/s, ε_r is the relative permittivity.

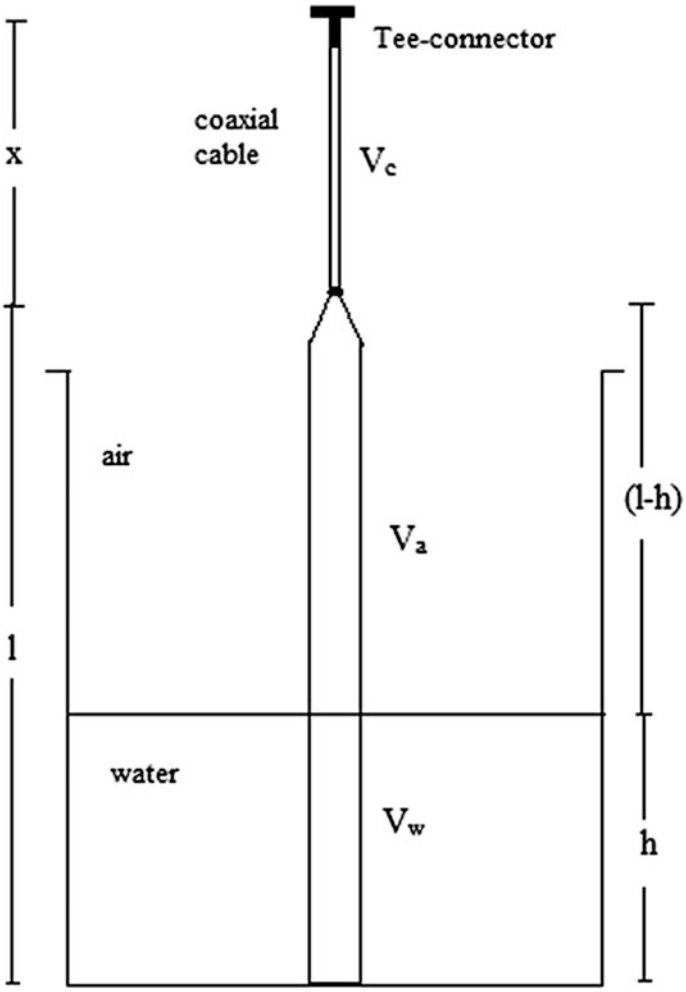

Fig. 4 Probe setup in the tank describing the various reflection points

$$V_w = 3 \times 10^8 \text{ m/s} / 80.4^{1/2} = 3.33 \times 10^7 \text{ m/s} \quad (3)$$

where, V_w is the velocity of wave in water. The velocity of propagation of a wave in water column is equal to 0.33 $\times$ 10^8 m/s. The velocity of the TDR pulse in water to air is in the ratio of 1:9 [11]. The sum of all the travel times in different media will be equal to the total measured time. The wave travels the total length twice, i.e., to and from the discontinuity.

$$time = \frac{2*Length}{velocity} \tag{4}$$

$$t = 2\left(\frac{x}{V_c} + \frac{(l-h)}{V_a} + \frac{h}{V_w}\right) \tag{5}$$

where, t is the total time taken to travel the probe

h is the height of the water in the tank
x is the length of coaxial cable
l is the length of the bi-axial cable
V_c is the velocity of wave in coaxial cable = 2×10^8 m/s
V_a is velocity of wave in air = 3×10^8 m/s
V_w is velocity of wave in water = 0.33×10^8 m/s

For a given tank, by substituting all the known values and constants into the above equation, the relation between time and height can be derived. In this way the height of water can be found out.

4 Results and Discussion

The experiment was carried out under laboratory conditions to simplify the experimental environment. Below is the Fig. 5, which shows experimental setup and TDR circuit. During initial testing of the TDR circuit, a square wave which did not have clean edges was obtained. There was little bit ringing on the edges, which will be used to identify the location of the reflected signal in order to calculate the distance between the source and surface of water. The square wave generated by the TDR circuit has amplitude of about 5.2 V and frequency 2.84 kHz.

The waveform, in Fig. 6, is the screen-shot of the Oscilloscope. Here, the x-axis represents time and y-axis represents voltage. The first peak here is the incident peak, whereas the second peak is the sum of incident and reflected peaks. The other peaks are the ringing at the edge of the square wave. Later, water is added into the tank, and the readings are noted at regular intervals (for every 100 ml addition of water). The time difference between the incident and reflected peaks is observed. The height of the water in the tank is also noted manually by measuring it with a scale, which will later be used for verification. Table 1 shows the data from the experiment. These results are taken directly from the oscilloscope output. This is because, as the water height increases, the signal travels through more water than before. Therefore, the time taken to travel the complete path also increases. The bottom of the tank, i.e. the probe termination and air-water interface are both considered as discontinuities. But due to the close proximity of the discontinuities placed at close proximity to each other the reflection was smoothed into a single discontinuity. As the water level increases, the distance between the discontinuities

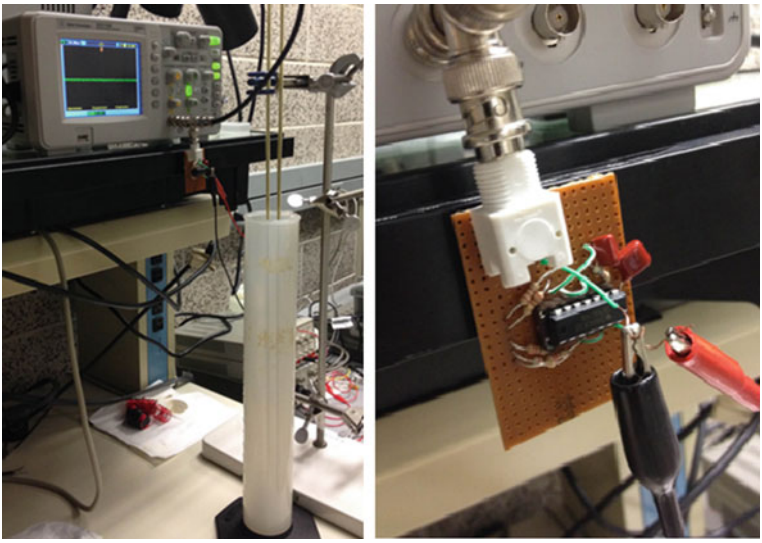

Fig. 5 Experimental setup for the TDR experiment. The image on the *right* is the pulse generator. The graduated cylinder allows for testing against multiple contaminated water types

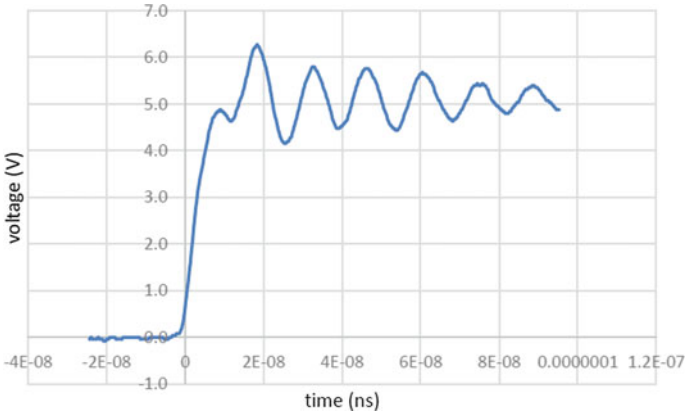

Fig. 6 Output due to reflection from probe termination

also increases and therefore there are two reflections which are observed. For an example, many points can be made out from Fig. 7. The red line represents the x-y plot at 100 ml and blue line at 200 ml. The second peak reflects from the bottom of

Table 1 Readings of TDR experiment

No.	Height (cms)	Time difference (ns)	Voltage difference (mV)	Volume (ml)
1	3.6	13.79	1360	100
2	7.1	14.4	1120	200
3	10.2	17	800	300
4	13.7	19	520	400
5	17.3	28	640	500
6	20.3	29.5	640	600
7	23.9	31	680	700
8	27.4	33	720	800
9	30.5	33.7	560	900
10	34	34	520	1000

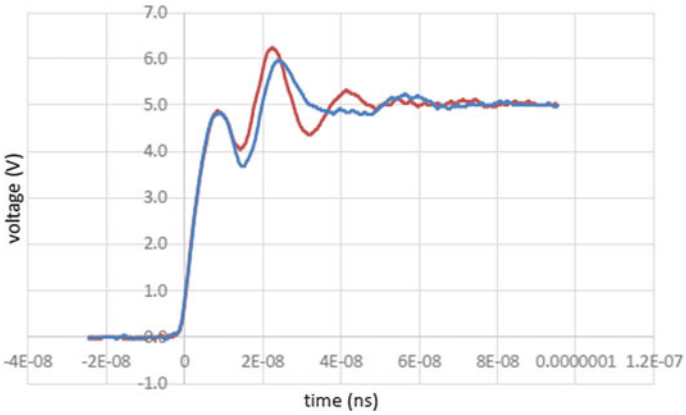

Fig. 7 Waveforms at 100 ml (*red line*) and 200 ml (*blue line*) water

the tank. We can see that as the height of the water increases, the reflected signal shifts toward right. Figure 8 is the waveform at 800 ml water, i.e. 27.4 cm height and Fig. 9 is the data for the pulse edge of the 34 cm height (1000 ml).

Table 2 shows the data obtained during the measurement of the water height and Fig. 10 shows a plot of the actual water column height versus the calculated height. For many application this amount of accuracy is sufficient. Many wastewater storage tank systems for the transportation industry only need to know when the tank is full or when the tank is empty. The wave-guides used in this experiment were covered in a thin Teflon® tubing. This tubing allowed the wave-guides to be placed in both acidic and basic solutions with no change in the signal.

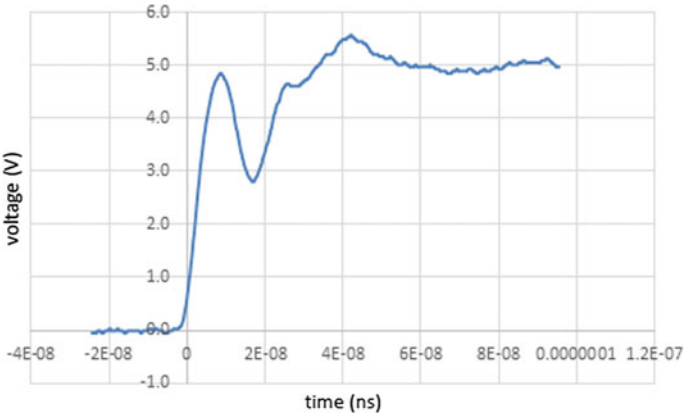

Fig. 8 x-y plot at 800 ml water (27.4 cms)

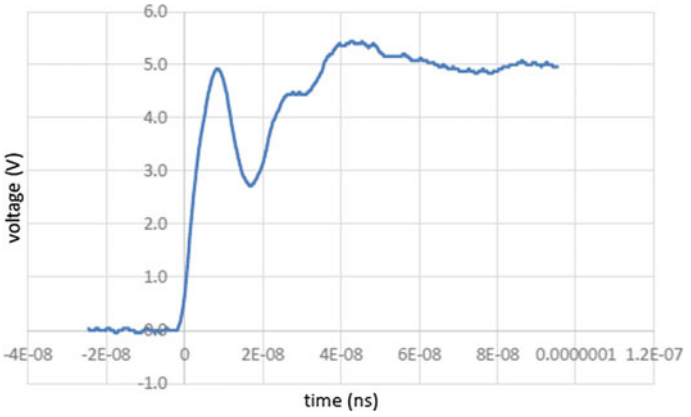

Fig. 9 x-y plot at 1000 ml water (34 cms)

Table 2 Error between empirical and actual heights

S.No.	Time difference (ns)	Empirical height, h_e (cms)	Actual height, h_a (cms)	Error (hc-ha) (cms)	Normalized error
1	13.79	3.97	3.6	0.37	10.27
2	14.4	5.09	7.1	−2.01	−28.3
3	17	9.9	10.2	−0.3	−2.94
4	19	13.7	13.7	0	0
5	28	30.5	17.3	13.2	76.3
6	29.5	33.5	20.3	13.2	65.0
7	31	36.17	23.4	12.8	54.7
8	33	39.92	27.4	12.5	45.6
9	33.7	41.4	30.5	10.9	35.73
10	34	41.8	34	7.8	22.94

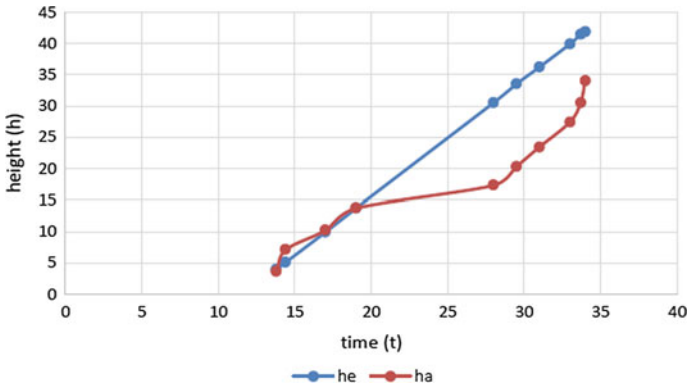

Fig. 10 **a** Empirical height versus time difference, **b** actual height versus time difference

5 Alternative Sensing Method—Low Cost Doppler Radar

An alternative measurement scheme was considered which employed Doppler sensing. The Doppler method was first considered to be the primary sensing methodology but was subsequently chosen to be secondary to corroborate the TDR measurements or to also serve as a backup in the event of TDR was not as sensitive as necessary [17–20]. Water level measurements are mostly used by water managers and hydrographers to compute water flow and volumes. Here we are dealing with measurement of water level in a septic tank. A radar sensor can measure the level of water by propagating electromagnetic waves with the help of an antenna. The reason is, radar energy (being an electromagnetic wave) is reflected and scattered similar to that of light. Objects in the path of propagation reflect the microwave energy back to an antenna. The time it took for the energy to return to the radar is determined and the resulting time of flight is used to determine the distance of the object from the emission of energy (due to a predictable speed of light). The advantages of radar as a level estimation procedure are clear. Radar is a non-contact sensor that is essentially unaffected by changes in target temperature, pressure of the gas and the vapor structure inside of a vessel. The estimation precision is also unaffected by changes in density, conductivity and dielectric constant of the target being measured or any turbulence in the air. Doppler systems are primarily employed as speed and range sensing where the time-domain measurements correspond to propagation of a reflected signal from a moving object. Both the velocity and position can be determined when the reflected pulses are compared to the initial transmitted signal pulse. This difference is commonly known as phase delay. In this application, the liquid waste would only contain lateral motion, typically the sloshing, or waves and vibration when the tank is in a

non-resting position relative to the ground. Figure 11 shows an concept of how a Doppler system would be deployed in a large tank. Hence, only a reflected signal whose amplitude would decrease following the inverse-square law should be used to determine the relative height of the liquid waste column. A change in liquid level could be determined, however, if additional liquid were added rapidly to the column.

To enhance the signal a pyramidal horn antenna was needed for the measurement. Early experiments with out the antenna confirmed this need. The Doppler equation for a pulsed electromagnetic wave is:

$$F_D = \frac{2 \cdot V_r \cdot f_{tx}}{c_0} \tag{6}$$

where F_D is the Doppler frequency, v_r is the radial velocity of the target, f_{tx} is the transmitter frequency and c_0 is the propagation velocity of the signal. For most instances, c_0 is given as 2.99×10^8 m/s.

Rearranging the equation to determine the radial velocity of the target

$$v_r = \frac{F_p \cdot c_0}{2 \cdot f_{tx}}. \tag{7}$$

The module used in this experiment is the MACOM MA 7801-M Mono-Doppler transceiver which has a minimum operating frequency of 24.1 GHz (Fig. 12). It contains three pins input, output and ground. It is a pulse radar transmitter and transmits pulses inside term of nano-seconds and performs gathering operation too in the meantime. The signal received by the mono-Doppler transceiver is measured using an oscilloscope.

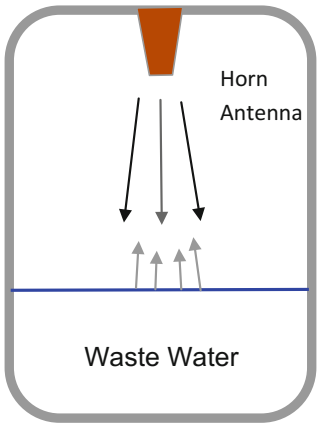

Fig. 11 Schematic of a Doppler radar measurement technique for a liquid measurement system

Fig. 12 MACOM MA 7801-M Mono-Doppler transceiver used in this experiment. Operating frequency is 24.1 GHz

5.1 Antenna Design

To improve the gain and directivity during signal transmission and reception, an antenna needed to be designed to match the transceiver. To keep the cost down, the materials used for the horn antenna had to be readily available. The material for the horn antenna consists of circuit board sheet and copper sheet. The design of the horn antenna was performed using Antenna Magus software. The results of the simulation of the horn antenna is shown in Fig. 12. The antenna had a gain of 12 dB in the design and a center frequency of 23 GHz. This missed the target by a GHz but was sufficient for this experiment. The S11 (or reflection coefficient) at 24 GHz was still −22 dB.

An antenna not only helps with gain but more important it improves directivity. Directivity is the ability to radiate maximum possible amount of microwave energy into a particular direction i.e., to the direction where we are measuring the solid or liquid level. It is almost impossible to design an ideal antenna because no matter how well the antenna may be designed a considerable amount of energy will still be radiated into all directions. The goal is to design an efficient antenna. The output of the modeling software is shown in Figs. 13 and 14 demonstrating the resulting gain and directionality along with the reflection coefficient. Figure 15 shows the final antenna construction. The antenna was machined in segments and assembled by

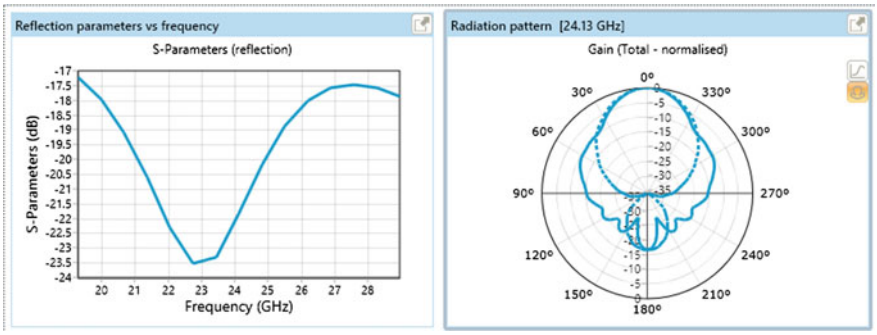

Fig. 13 Output of the Antenna Magus software for the horn antenna used in the test. This design has good directionality

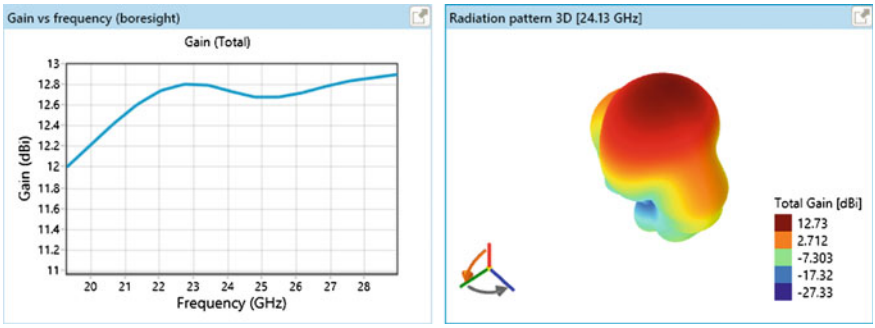

Fig. 14 Gain and radiation pattern for the Horn Antenna

soldering the segments together using copper strips. A copper flange was also machined and then the horn was soldered to the flange.

The observed signal in an oscilloscope was below the resolution of the oscilloscope. This required an operational amplifier circuit LM 741 to increase the output voltage range of the Doppler unit to allow for better matching to the oscilloscope.

5.2 Test and Measurement

To get the distance to the top of the septic wastewater it will be necessary to manipulate the Doppler equations to get the range i.e. the distance to the top of the liquid to the opening of the horn antenna. The equations can be further manipulated to provide this distance or range to the target

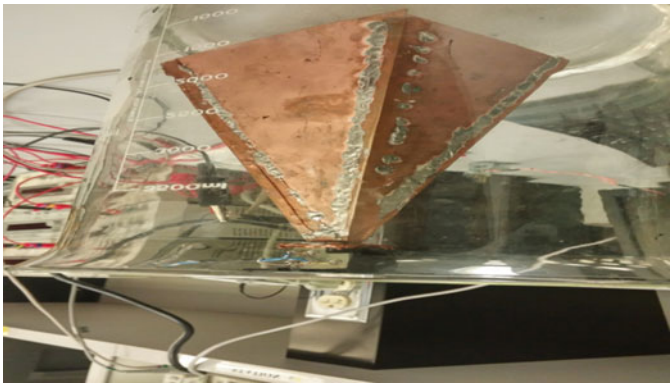

Fig. 15 Pyramidal horn antenna used to improve signal to noise ratio. This is a fairly large antenna

$$r = \frac{c_{0 \cdot t_r}}{2}, \tag{8}$$

where t_r is the phase delay of the returning pulse and is typically calculated and displayed using microcontroller technology. This measurement assumes, however, that the signals emanating from the Doppler transceiver are transmitted and received perpendicular to the target. Otherwise, an angular correction must be employed to account for increased distance and increased phase delay. The Doppler system consisted of a Ma/Com MACS-007801 transceiver. A +18 dBi horn antenna was fabricated using copper shim stock to focus the signal toward the liquid column. The horn antenna and mounting over the water tank used in these initial tests is shown along with the instrumentation. Subsequent Doppler signal amplitude measurements were made, as shown in Fig. 13 and it was determined that for the given range of liquid column heights the change in intensity was negligible and would not be included in the instrument package.

This measurement assumes, however, that the signals emanating from the Doppler transceiver are transmitted and received perpendicular to the target. Otherwise, an angular correction must be employed to account for increased distance and increased phase delay. The Doppler system consisted of a Ma/Com MACS-007801 transceiver. A +18 dBi horn antenna was fabricated using copper shim stock to focus the signal toward the liquid column. The horn antenna used in these initial tests is shown in Figs. 11 and 12 shows that antenna in the test fixture. Subsequent Doppler signal amplitude measurements were made, as shown in Fig. 13 and it was determined that for the given range of liquid column heights the change in intensity was negligible and would not be included in the instrument package (Figs. 16, 17).

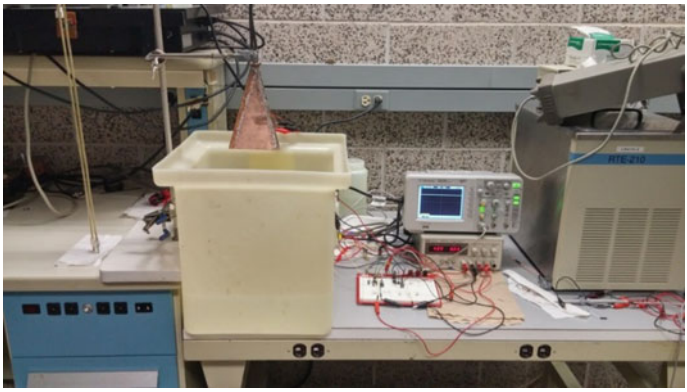

Fig. 16 Measurement setup for radar system. Horn antenna is over the ¼ full water tank

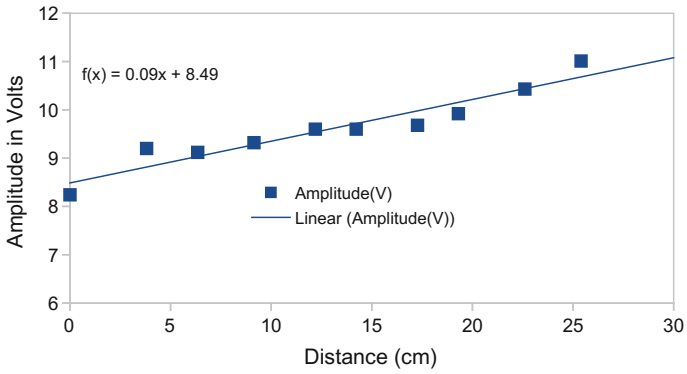

Fig. 17 Results of the Doppler experiments showing the amplified signal versus the distance. This signal was usable but have some issues with large outliers

6 Conclusions

The TDR technique has been developed for calibration of liquid level in the tank. It important to remember that the material in a septic system is non-ideal. The TDR probe used in this thesis is a bi-axial cable which is designed using two brass rods encased in a Teflon® sheath. They were assembled in such a way that the characteristic impedance was close enough to 50 Ω, which matches with the source impedance. The transmission of the wave through the probe and its parameters were studied. The TDR circuit was built with 74AC14 IC for signal generation. The generated signal was transmitted through the bi-axial probe, where part of the incident signal was reflected back to the source when the signal was incident to a discontinuity. This TDR technique was tested in the laboratory, in a plastic graduated cylinder from which a few conclusions were drawn. The TDR technique is

simple and accurate for measurement of liquid level, and it is a technique that can be used in situations that regular float-type or pressure based systems cannot. To verify whether or not this was the most effective type of radar system, the results were compared with a Doppler based radar. This comparison shows that the TDR has significantly higher sensitivity than the Doppler. The installation and the use of a TDR twin-axial probe also is much simpler than the antenna since it conceptually could use a port on the side of the tank. Other types of probes could be constructed an implemented allowing for a probe that had a lower chance of catching solids. This probe was a first pass design and with some problems with impedance matching though the entire system were observed. Future work will be on optimizing the concept. Additional work will be on designing a measurement technique that will reduce the need to use an oscilloscope to measure the time-based signal. Modern high speed oscilloscope on a chip devices could also be used but most of the devices that can be used to collect information like this are still quite expensive.

References

1. W. Thompson, On the electro-dynamic qualities of metal: effects of magnetization on the electric conductivity of Nickel and of Iron. Royal Soc. Phys. (1897), http://encyclopedia2.thefreedictionary.com/level+measurement
2. http://www.sensorsmag.com/sensors/leak-level/a-dozen-ways-measure-fluid-level-and-how-they-work-1067
3. S.B. Jones, J.M. Wraith, D. Or, Time domain reflectometry measurement principles and applications, http://www.usu.edu/soilphysics/wintdr/pdfs/TDRMeasurment_Prncple_App.pdf
4. T. Engdahl, Time domain reflectometer (TDR), http://www.epanorama.net/circuits/tdr.html
5. J. Bartling, Low-cost, high resolution time-measurement application, http://www.ecnmag.com/articles/2009/07/low-cost-high-resolution-timemeasurement-application
6. J. Bartling, Use time-domain reflectometer for low cost liquid level measurement, http://www.edn.com/design/sensors/4433411/Use-Time-Domain-Reflectometry–TDR–for-low-cost-liquid-level-measurement–Part-III
7. B. Kenner, J. Wettroth, The design of a time domain reflectometer
8. J.R. Andrews, Time domain reflectometry (TDR) and time domain transmission (TDT) measurement fundamentals, in *Symposium and Workshop on Time Domain Reflectometry in Environmental, Infrastructure, and Mining Applications held at Northwestern University, Evanston, Illinois*, September 17–19, 1994 (Washington, DC: U.S. Bureau of Mines, 1994), pp. 4–13 (USBM special publication SP 19-94)
9. K.M. O'Connor, C.H. Dowding, Real time monitoring of infrastructure using TDR technology: principles, http://www.iti.northwestern.edu/tdr/publications/Dowding_and_OConnor-2000-Real_Time_Monitoring_of_Infrastructure_Using_TDR_Technology _Principles.pdf
10. Time domain reflectometer, http://en.wikipedia.org/wiki/Time-domain_reflectometer
11. X. Yu, X. Yu, Measurement of simulated scour by time domain reflectometry, https://engineering.purdue.edu/TDR/Papers/5_Paper.pdf
12. A. Thomsen, B. Hansen, K. Schelde, Application of TDR to water level measurement, http://www.elsevier.com/locate/jhydrol
13. D. Moret, M.V. Lopez, J.L. Arrue, TDR application for automated water level measurement from Mariotte reservoirs in tension disc infiltrometers, http://www.researchgate.net/

publication/222533231_TDR_application_for_automated_water_level_measurement_from_Mariotte_reservoirs_in_tension_disc_infiltrometers
14. W.F. Kane, Embankment monitoring with time domain reflectometry, http://www.iti.northwestern.edu/tdr/ publications/emwtdr.pdf
15. Time Domain Reflectometry. Hewlett hp Packard Application note 62, http://www.hpmemoryproject.org/an/pdf/an_62.pdf
16. R.M. Heitsenrenther, Using microwave radar for long term remote sensing of ocean surface dynamics (2009). Accessed 30 May 2015
17. A. Wolke, #88: Cheap and simple TDR using an oscilloscope and 74AC14 Schmitt Trigger Inverter, https://www.youtube.com/watch?v=9cP6w2odGUc
18. P. Devine, Radar level measurement (Vega controls, West sussex, 2000). Accessed 30 May 2015
19. J. Fehrenbach, K. Griessbaum, Patent No. US 6,987,481 B2, United States of America (2006). Accessed 29 May 2015
20. J.M. Fulford, L.W. Ester, J.W. Heaton, Accuracy of Radar Water Level Measurements (2006), http://www.waterlog.com/media/pdfs/USGS-Study.pdf. Accessed 30 May 2015, from Waterlog

Nanowire (S3) Device for the Quality Control of Drinking Water

Estefanía Núñez Carmona, Matteo Soprani and Veronica Sberveglieri

Abstract The control and sanitation of water it's a worldwide concerning problem. In particular is in developing countries where the need is more evident due to the lack of sources and appropriate structures to cope with the outbreaks of waterborne diseases. In most of cases, the cause of these significant epidemiological events have microbial origin. Despite of it the situation of water supplies and sanitation has improve all over the world in the last decades. Nanowire technology has already shown their ability to perform very effective and fast monitoring microbiological spoilage and quality control. The aim of this study was to test the ability of a novel S3 (Small Sensor System) nanowire device for the detection of complex mixtures of bacteria in potable water in order to approach into a real condition, in cooperation with GC-MS- SPME technique. The achieved results notably advocate the use of EN as a very easy to use, fast and accurate tool in water quality control.

1 Introduction

Water is one of the most basic chemical compounds, on Earth, it occupies the 71 % of the total surface area. Even though it provides no calories or organic nutrients is essential to humans and any kind of life. The amount of fresh water on earth is limited and its quality is under constant threat. Preserving the quality of fresh water is important for the drinking-water supply and food production (Table 1).

Nowadays in the developed continents such as Europe and North America access to drinking water is easy, directly from aquifers, and at a low cost. This leads to a great waste of this resource, to which there is no longer the proper social and

E. Núñez Carmona (✉)
University of Brescia, Brescia, Italy
e-mail: e.nunezcarmona@unibs.it

E. Núñez Carmona · V. Sberveglieri
CNR-INO Sensor Lab, Brescia, Italy

M. Soprani
University of Modena and Reggio Emilia, Reggio Emilia, Italy

S. Mukhopadhyay et al. (eds.), *Sensors for Everyday Life*, Smart Sensors, Measurement and Instrumentation 23, DOI 10.1007/978-3-319-47322-2_9

Table 1 The world's water resources

Water source	Water volume (km^3)	% Fresh water	% Total water
Oceans, seas, and bays	1,338,000,000	–	96.54
Ice caps, glaciers, and permanent snow	24,064,000	68.7	1.74
Groundwater	23,400,000	–	1.69
Fresh	10,530,000	30.1	0.76
Saline	12,870,000	–	0.93
Soil moisture	16,5	0.05	0.001
Ground ice and permafrost	300	0.86	0.022
Lakes	176,4	–	0.013
Fresh	91	0.26	0.007
Saline	85,4	–	0.006
Atmosphere	12,9	0.04	0.001
Swamp water	11,47	0.03	0.0008
Rivers	2,12	0.006	0.0002
Biological water	1,12	0.003	0.0001

environmental value. In particular, in a developed country as Italy were this research has being carried out, the 60 % of the piped drinking water is loosed in leaks every year.

Conversely in the world's poorest areas the drinking water is rare, expensive and inadequate compared to the necessary requirements. The major part of the population in these regions is compelled to use natural sources of water such as: river, ponds and rivulets to meet their drinking water needs. These resources are generally polluted because of the human activities. When consumed, this water leads to malnutrition and poor hygiene of the population living in these areas.

The data published by UNIDO (United Nations Industrial Development Organization) (2013) recall that: 1.4 million children die from water-borne diseases caused by the lack of adequate sanitation every year, in average one child each 20 s.

The World Health Organisation's (WHO) report "Progress on Drinking Water and Sanitation" upgraded to 2014 [1] recalls that access to safe drinking water is essential to human health, food production and urban development. The United Nations General Assembly (UN) recognized the human right to water and sanitation on 28 July 2010, through Resolution 64/292.

The biggest differences in the availability of drinking water and sanitation are between urban and rural areas, the rich and the poor and marginalized. The vast majority of those without sanitation are poorer people living in rural areas.

The drinking water availability is strictly linked with the sanitation conditions in which people live. Since 1990, 2 billion people gained access to improved source of drinking water and other 2 billion people gained access to improved sanitation. Currently almost 4 billion people, enjoy the highest level of water access: a piped water connection at their homes.

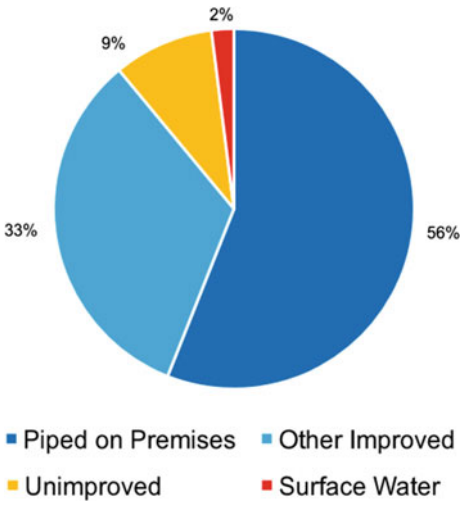

Fig. 1 Global drinking water coverage 2014

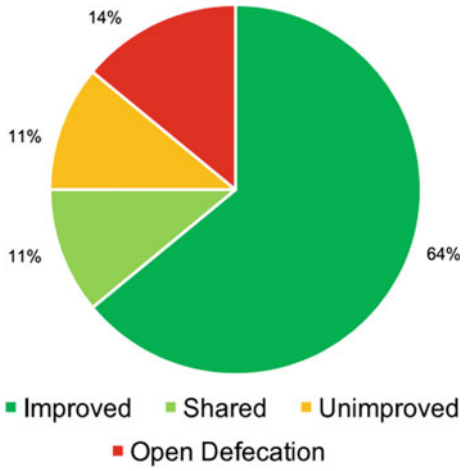

Fig. 2 Global sanitation coverage 2014

Conversely 700 million people still lack a ready access to improved sources of drinking water and some 2.5 billion people do not use an improved sanitation facility (Figs. 1 and 2).

2 Increasing the Amount of Drinking Water in the World

About 2.6 billion people—half the developing world—lack even a simple 'improved' latrine and 1.1 billion people has no access to any type of improved drinking source of water. As a direct consequence [2]:

- 1.6 million people die every year from diarrhoeal diseases (including cholera) attributable to lack of access to safe drinking water and basic sanitation and 90 % of these are children under 5, mostly in developing countries;
- 160 million people are infected with schistosomiasis causing tens of thousands of deaths yearly; 500 million people are at risk of trachoma from which 146 million are threatened by blindness and 6 million are visually impaired;
- intestinal helminths (ascariasis, trichuriasis and hookworm infection) are plaguing the developing world due to inadequate drinking water, sanitation and hygiene with 133 million suffering from high intensity intestinal helminths infections; there are around 1.5 million cases of clinical hepatitis every year.

Between 1990 and 2014 the drinking water coverage is growing up from 76 to 89 % (Figs. 3 and 4).

Regarding all continents' situation for the drinking water coverage is possible to remark in particular:

- Europe. In Europe the drinking water coverage is optimal; the range is from 91 to 100 %;
- North America, South America, Asia and Oceania. The North America, South America, Asia and Oceania situation is similar to the Europe one; the range is from 91 to 100 %;
- Sub-Saharan Africa. In a further 35 countries, 26 of which are in sub-Saharan Africa, coverage of improved drinking water supply was between 50 and 75 %.

Access to drinking water from an improved source is significantly higher in urban than in rural areas. In rural areas, in virtually the entire developing world, drinking water coverage from an improved source remains unacceptably low.

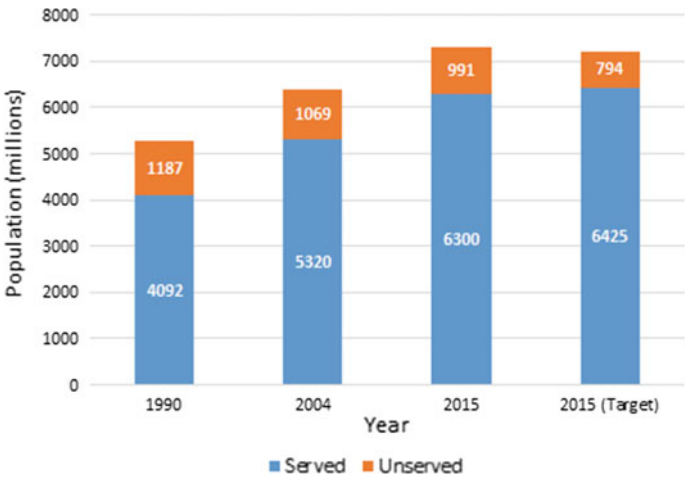

Fig. 3 World population with and without access to an improved drinking water source in 1990, 2004 and 2015

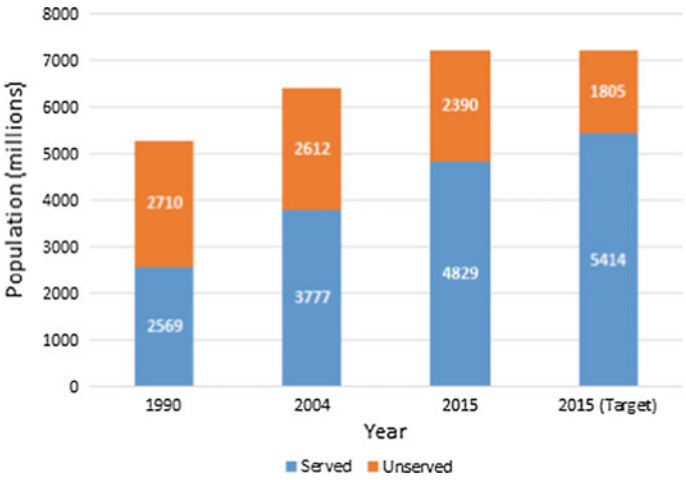

Fig. 4 World population with and without access to improved sanitation in 1990, 2004 and 2015

Urban drinking water coverage remained the same from 1990 to 2004 at 95 %, whereas in rural areas coverage increased to 73 % in 2004 from 64 % in 1990. In 27 developing countries, less than 50 % of the rural population have access to improved drinking water.

3 Sensors Background

One of the types of sensors most frequently used is the metal oxide (MOX or MOS). The working principle of this technology is that in the presence of a variation in gas concentration ΔC_{gas} produce a change of electrical conductivity $\Delta\sigma$, and, therefore, a change of resistance ΔR, for which the measured parameter in this case is the sensor resistance, R. In other words the principle on which is based the MOS consists in a variation of the conductivity of the metal oxide in the presence of volatile compounds compared to the value assumed by the same conductivity in reference conditions.

The characteristics that should possess an ideal sensor are the following:

- High sensitivity to chemicals;
- High selectivity (low noise) and stability;
- Low sensitivity to humidity and temperature;
- High reproducibility and reliability;
- Reaction time and return short;
- Strength, durability, ease of calibration;
- Small size.

Conductometric gas sensors based on semiconducting metal oxides are among the most promising solid state gas sensors thanks to their high sensitivity to a broad range of chemicals, reduced size and weight, low power consumption, compatibility with silicon technology, possibility to produce these devices by means of cheap techniques compatible with industrial scaling up such as sputtering or evaporation and condensation methods.

Conductometric gas sensors, also named chemiresistors, transduce the presence in the atmosphere of a given chemical compound through a variation of their electrical resistance. They are based on semiconducting metal oxides, whose electrical properties are modulated by red-ox interactions with adsorbing gaseous molecules.

In particular, active species, such as O–, O_2–, O_2–, OH–, have been identified as the active centers responsible for the above red-ox reactions [3]. Such species cover the oxide surface with their relative population depending on the oxide temperature and atmospheric composition [4]. In the typical temperature range of metal oxide chemiresistors (200–500 °C), O_2– ions are the most abundant at low temperature (below 300–350 °C), while a higher temperature favors the dissociation of molecular oxygen leading to atomic oxygen ions O–. From an electrical point of view, when a semiconducting oxide is exposed to air, the adsorption of water and/or oxygen from the atmosphere modifies the band structure of the material at the surface with respect to the bulk. Chemisorption, involving the transfer of electrons between the conduction of the semiconductor and the adsorbed atom/molecule, is that particular form of adsorption responsible for building up the population of active ions at the oxide surface and the consequent band bending [5].

The further interaction of gaseous molecules with the aforementioned active ions modulates their population over the semiconductor surface and thus the electrical properties of the material. According to this mechanism, reducing gases, such as CO and hydrocarbons, get oxidized reacting with oxygen ions and their population over the oxide surface decreases, thus increasing the material conductance (for n-type semiconductors). Oxidizing gases, such as NO_2 and O_3, are reduced by the interaction with the oxide surface and, as a consequence, the population of oxygen ions increases as does the material resistance (for n-type semiconductors).

Through the data acquisition system signals are collected from the n sensors installed in the measurement chamber of the electronic nose, converted into analog signals, then acquire, and process through a computer.

During the processing stage, the digital signal of the sensor is managed by software and is subdivided into a pre-treatment, where they are extracted the so-called main features of the responses, and in a final treatment for the classification and recognition of the smell.

Each element in the sensors array produces an electrical signal in response to the gaseous mixture. This signal is dependent on a multitude of factors such as:

- The exposure technique and the type of carrier gas used;
- The chemical nature and the concentration of the odorant;
- The kinetics of diffusion and reaction between the smell and the active material;
- The physical and chemical properties of the materials constituting the sensor;
- The environmental conditions such as temperature and relative humidity.

4 Nanowire Sensors

Metal oxides in the form of nanowires are interesting for their peculiar morphology and their exceptional crystalline features, the first assuring a high surface to volume ratio necessary to maximize surface related properties such as the ones governing chemical sensing transduction principles, while the latter guarantees stable crystallinity and therefore electrical properties over long-term operation, i.e., a required quality for an industrial application of any kind of sensor in real environments.

Different experimental techniques that may lead to the formation of these quasi one-dimensional structures. First of all there are two main groups that can be distinguished: top down and bottom up technologies. The first starts from bulk structures, reducing them to nanometric dimensions usually with lithographic techniques, while the latter involve a direct assembly in the desired morphology that can be obtained from vapor or liquid phase.

At the beginning the research was focused on the vapour phase methods that were producing, with cheap instrumentation, high quality nanostructures in terms of crystallinity and stoichiometry. We have thoroughly studied the deposition using evaporation and condensation from powder in controlled environments using a different experimental set up.

Tin oxide was preferred over other oxides thanks to its well known chemical sensing properties and the easy preparation conditions, but indium and zinc oxide were also studied [6–11].

The experimental procedure consists in the evaporation of the powder (metal or metal oxide) at high temperatures in a controlled atmosphere at pressures lower than hundreds of millibar and the following mass transport of the vapour towards the substrates kept at lower temperatures with respect to the source evaporation region.

Argon, an inert gas, is used for the mass transport in order to avoid unwanted reactions with the oxide vapour. Critical variables are the distance between the source and the substrates and the temperature gradient that are controlling the supersaturation conditions in the vapour phase causing the condensation in the desired morphology (Fig. 5).

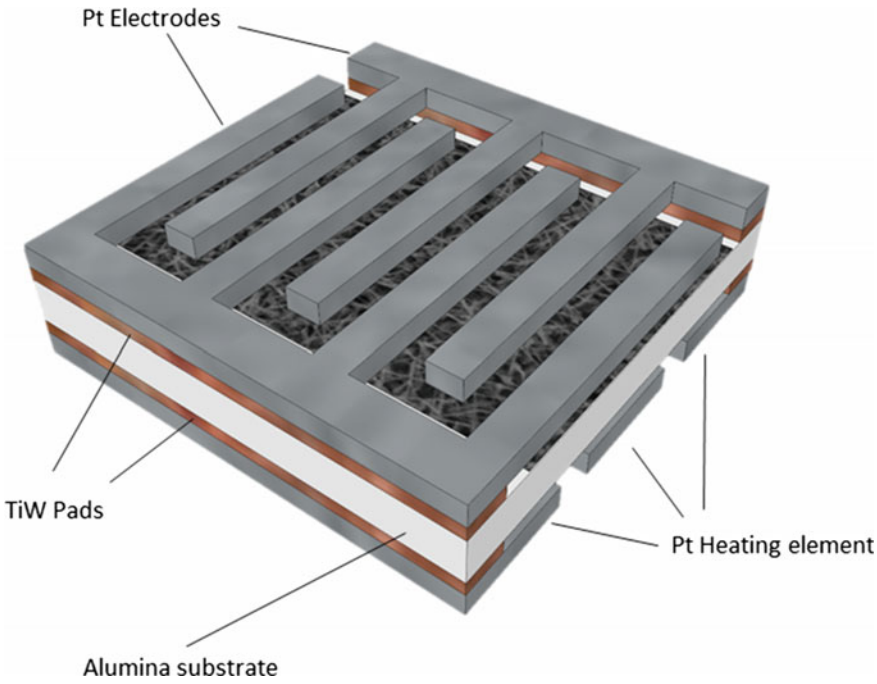

Fig. 5 Scheme of a Nanowire sensor, from the *top* to the *bottom*: Pt electrodes (*grey colour*), TiW Pads (*brown colour*), ZnO Nanowires, Alumina substrate (*white colour*), Pt heating element (*grey colour*)

5 Device Design

The S3 (Gas Sensor System srl—Spin-Off University of Brescia, Italy) used during the experimental analysis is constituted of: Auto-sampler headspace system HT280T (HTA srl, Brescia, Italy). The auto-sampler supports a 40 loading sites carousel and a shaking oven, to provide the equilibrium of the samples head space. The sensor's chamber is a thermally controlled chamber with 9 loading sensors places (Fig. 6).

The sensor array installed in the used instrument is described in Table 2. The study has been carried out using an hybrid array composed by 3 Nanowires and 3 RGTO.

The advantage of having an hybrids array enhance the performance of the instrument, that possess the capacity to detect a widest range of volatile chemical compounds.

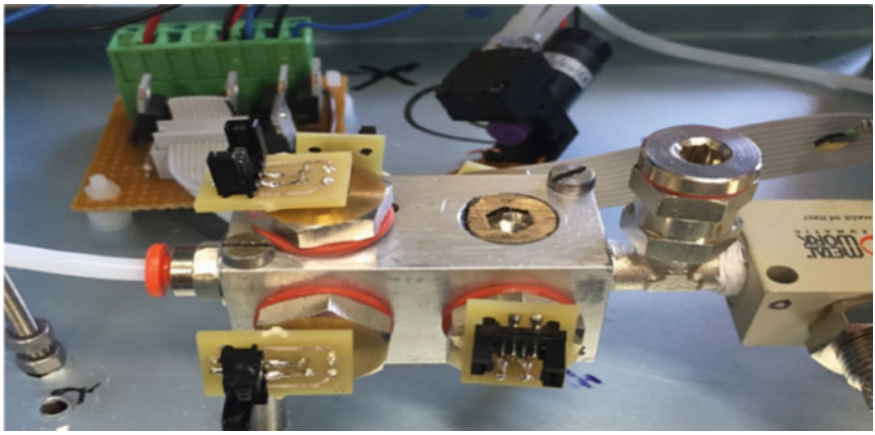

Fig. 6 Sensors' chamber inside the S3

Table 2 Sensor array details

Sensor	Operating temperature (°C)	Composition	Description
1	245	SnO_2–MoO_2	RGTO sensor made of a blend of Tin and Molybdenum oxides
2	280	ZnO	Nanowire sensor made of Zinc oxide
3	375	SnO_2	Nanowire sensor made of Tin oxide
4	400	SnO_2//Ag	RGTO sensor made of Tin oxide catalyzed with silver
5	500	ZnO	Nanowire sensor made of Zinc oxide
6	500	SnO_2–WO_3	RGTO sensor made of a blend of Tin and Tungsten oxides

6 Aim

The study and introduction of innovative technologies, that make possible the access to drinking water and sanitation, are fundamental for the poor countries' growth and for the welfare maintenance in the developed countries. The wastewater purification process in the developing countries is the only possible way to make contaminated water drinkable and, at the same time, it allows to save water in the aquifers and to increase the availability of drinking water and also to improve the sanitation conditions.

The improvement of the water quality control systems in both developing and developed countries is one of the better approaches to reach this objective. This improvement will not have just an impact in the enhancement of the water sources for agriculture and industry (incomes and outcomes), but the most important will have a big impact on the final consumer.

Currently used methods require high tech lab equipment, high level trained lab staff, a big investment of money and which is more important requires time. The aim of this work was to establish a new, rapid and economic fouling, based on the cooperation between the use of the new S3 device, nanowire tech, and chemical analytical techniques to detect the presence of complex microbial contaminant sets in water.

This is possible by using the innovative e-sensing device: Small Sensors System (S3. S3 device equipped with nanowire tech is based in the analysis of the head space. The Nanowires are gas sensors based on semiconducting metal oxide are a promising technology thanks to their high sensitivity to a broad range of chemicals, reduces size, weight, and low power consumption. These entire characteristic makes S3 device equipped with nanowire sensor an optimum portable device for the attainment of on field test. The optimization of the beginning wastewater purification process and the management of potable water is obtained through the identification of volatile metabolites (VMs) and volatile organic compounds (VOCs) released from the microorganisms' metabolism, that typically contaminate water [12–21].

7 Materials and Methods

Samples of tap water were sterilized and inoculated with varying rates of the reference microorganisms, to verify the threshold of the instrument to detect the presence of bacteria in an environment as close as possible to the real one. The samples were subjected to conventional microbiological methods aimed at assessing the magnitude of microbial growth, such as measurement of pH, turbidity and seeding on selective media. The results obtained were then compared with those resulting from the analysis conducted by means of electronic nose. This comparison enabled to investigate the ability of the instrument to perceive precociously the presence of volatile organic compounds resulting from the development of the bacterial load of the substrate to different microbial loads of departure. These tests were conducted at first individually considering the different bacteria under study; later were analyzed bacterial mixtures simulating a real case of multiple contaminations. Finally, the samples associated with better outcomes have been subjected to analysis by GC-MS-SPME technique in order to determine the chemical nature of the organic compounds most frequently detected from the microbial mixtures examined.

7.1 Single Microorganisms Water Tests

7.1.1 Sample Preparation

E. coli, S. Typhymurium, L. monocytogenes and *P. fluorescens* cultures were develop in 7 ml Brain Heart Infusion (BHI) (OXOID) liquid media tubes [22]. Once inoculated the tubes were incubated at 30 °C during 48 h. Once the cultures were grow, were centrifuged at 3000 rpm during 10 min. The supernatant was discarded and the cells were re-suspended in 1.5 ml of sterilized tap water.

A total volume of 400 ml of sterilized tap water was inoculated with the suspension of cells prepared before until it reaches the same turbidity as the third standard of the McFarland series. These standards are used as a reference to adjust the turbidity of bacterial suspensions in order to have a number of bacteria within a given range. Number 3 of McFarland standard corresponds with a bacterial concentration of 9×10^8 CFU/ml. It were prepared as well other 2 dilutions, 400 ml of sterilized tap water inoculated with 9×10^5 CFU/ml and 400 ml of sterilized tap water inoculated with 9×10^2 CFU/ml.

A volume of 2 ml was placed separately for every dilution in a sterilized chromatographic vials (20 ml). Once inoculated all the vials were cover with an aluminum crimp, a coated PTFE/silicon septum and crimped. This operation was repeated during the 5 days of analysis (from T0 to T4).

7.1.2 Electronic Nose

The vials were placed in a randomized mode into the HT280T carousel. Each vial was incubated at 40 °C for 10 min into the HT280T oven, by shaking it during all the incubation in order to reach the equilibrium of the headspace. The sample headspace (2 ml) was then extracted from the vial in static headspace path and injected into the carrier flow (speed 4 ml/min) through a properly modified gas chromatography injector (kept at 40 °C to prevent any condensation). Using synthetic chromatographic air with a continuous flow rate of 10 ml/min performed the sensor baseline and the recovery time was 28 min [23]. The sensor baseline was performed by using synthetic chromatographic air with a continuous flow rate of 10 ml/min and the recovery time was 28 min. In every carousel 4 of the 40 loading positions were dedicated to vials containing 500 µl of butanol. This compound act as the internal standard of the instrument.

7.1.3 pH

A control of the pH was done for all the three dilutions. The pH was measured each hour during the first 24 h of analysis. Whereas During their grow the *E. coli* produce organic acids that will acidify the pH of the water.

7.1.4 Photometer

To survey the development of the microorganisms in water it was measured the Optical Density (OD) at 600 nm for all three dilutions. The OD data were taken each hour during the first 24 h of analysis.

7.2 Microbial Blends Water Tests

7.2.1 Samples Preparation

The used microorganisms in this work are *Escherichia coli, Salmonella Typhymurium, Listeria monocytogenes*. Cultures were developed in 7 ml of Brain Heart Infusion (BHI) (OXOID) liquid media [22]. The cultures were incubated at 30 °C during 48 h. Subsequently the cultures were centrifuged at 3000 rpm during 5 min, the supernatant was discarded and the cells were re-suspended in 3 ml of physiological solution. A second step of centrifugation at the same conditions was performed in order to clean any trace of media from the suspension. At the end of the process the supernatant was discarded and the pellet was suspended in 4 ml of sterilized tap water. The sterilization process was carried out at 121 °C during 15 min at one over pressure atmosphere in order to eliminate all the microorganisms present in the tape water.

Once culture had been cleaned, the turbidity has been adjusted adding sterilized tape water until it reached the same turbidity as the third standard of the McFarland series. These standards are used as a reference to adjust the turbidity of bacterial suspensions in order to have a number of bacteria within a given range. Number 3 of McFarland standard corresponds with a bacterial concentration of 9×10^8 CFU/ml. These microbial solutions were subsequently used to prepare the bacterial combinations as it's indicated in Table 3 to inoculate the samples with a total concentration of 9×10^2 CFU/ml.

A total volume of 400 ml of sterilized tap water for each mix of bacteria was inoculated with the suspension of cells prepared before until it reaches 9×10^2 CFU/ml. Once prepared all three dilutions were incubated in the dark at 30 °C during the 4 days of analysis (T0, T2, T3 and T7).

Table 3 Microbial species combination for each kind of prepared sample

CODE	Microorganisms
EC + LM	*E. coli, L. monocytogenes*
EC + ST	*E. coli, S. Typhymurium*
LM + ST	*L. monocytogenes, S. Typhymurium,*
EC + LM + ST	*E. coli, S. Typhymurium, L. monocytogenes*

A control sample was also performed using sterilized tap water. In addition, in this case the parameters of incubation were the same followed by the inoculated samples.

7.2.2 Electronic Nose

The same procedure as the epigraph 7.1.2 was used for the analysis of samples and data.

7.2.3 GC-MS-SPME Analysis

GC-MS analysis was performed using a Shimadzu Gas Chromatograph GC2010 PLUS (Kyoto, KYT, Japan) equipped with a Shimadzu single quadrupole Mass Spectrometer MS-QP2010 (Kyoto, KYT, Japan) ultra and a HT280T auto sampler (HTA srl, Brescia, Italy) that allowed SPME analysis.

The vials were incubated in an oven thermostatically regulated at 50 °C for 15 min due to create the headspace equilibrium. In order to extract the volatile compounds of the samples was used a DVB/carboxen/PDMS stable flex (50/30 μm) (Supelco Co. Bellefonte, PA, USA) SPME fiber. To provide the adsorption of volatile compounds the SPME fiber was exposed to the headspace of the vials for 15 min at 50 °C. For desorption of the compounds the fiber was placed in the injector of the heated GC for 6 min at 200 °C.

Volatile organic compounds were separated using and analytical capillary column (DB-WAX capillary column, 30 m × 0.25 mm × 0.25 μm, Agilent Technologies, Santa Clara, CA, USA) and the carrier gas was ultrapure helium (99.99 %) at a constant flow rate of 1.3 mL/min. The temperature program for the GC was performed in the following way: from 50 °C follow of a linear gradient 10 °C/min to 150 °C and held for 5 min, followed by a rise from 150 to 250 °C at 5 °C/min, temperature held 2 min.

8 Results and Discussion

8.1 Single Microorganisms Water Tests

8.1.1 pH and OD

Regarding the OD obtained results, it is possible to observe a typical microbial curve of growth in all the three dilutions. The Lag phase goes from 0 to 8 h, then the inoculated cells start to divide and the OD increase until it reach the stationary phase at 20 h. A proportional but inverse response came out observing the pH data.

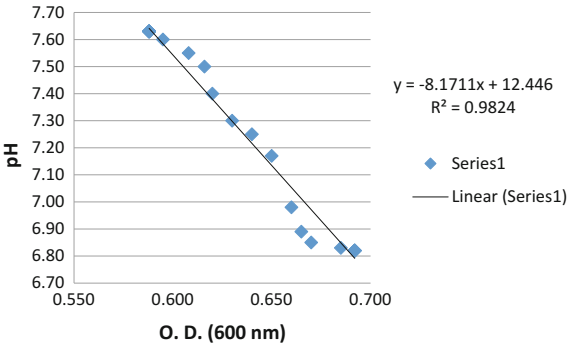

Fig. 7 Linear correlation and R^2 value for the pH and OD data of the 9×10^3 CFU/ml of *E. coli*

As the microorganisms develop inside the water, the OD increases because the turbidity increases as well. The metabolic activities carried out by the microorganisms during their grow causes the production of a big amount of organic acids that subsequently decrease the pH values. These two variables are inversely related so a test of correlation between pH and OD was performed for the 3 dilutions. In the three cases, the negative correlation between the 2 variables were confirmed obtaining a $R^2 > 0.98$ (Fig. 7).

8.1.2 Electronic Nose

In the two following score plot (Figs. 8 and 9) the control samples are compared, separately, with samples contaminated with *E. coli* and *P. fluorescens* in the days T0 and T3. All the concentrations studied were considered in the statistical analysis.

For both PCA is possible to observe three clusters of dots clearly separated from each other, the first of which (at the top left—black) regarding the samples inoculated with the microbial species of reference, the second covering not contaminated samples (blue) and the third (right, upper extremity—green) relative to the internal standard (pure butanol, 500 μL).

In particular in the second chart (Fig. 9) can be observed a progressive trend line of the statistical objects included in the cluster of *E. coli* against the cluster of analytical blank. This result is in agreement with the nature of the samples subject to analysis, which are referable to all microbial concentrations studied. In fact the tail observed is due to samples with a lower microbial load, which will be associated with a lower odorous intensity, arranging itself in proximity of the non-inoculated samples. The experimental investigations were prolonged in order to determine whether the olfactory system was able to distinguish different microbial agents of contamination, different microbial loads and/or the different days of experimentation. In general the instrument has proved to be able to carry out, at fixed concentration, a proper distinction of individual species concerned over the several days of analysis, remarkable results were obtained for *E. coli* at very low concentrations (Fig. 10).

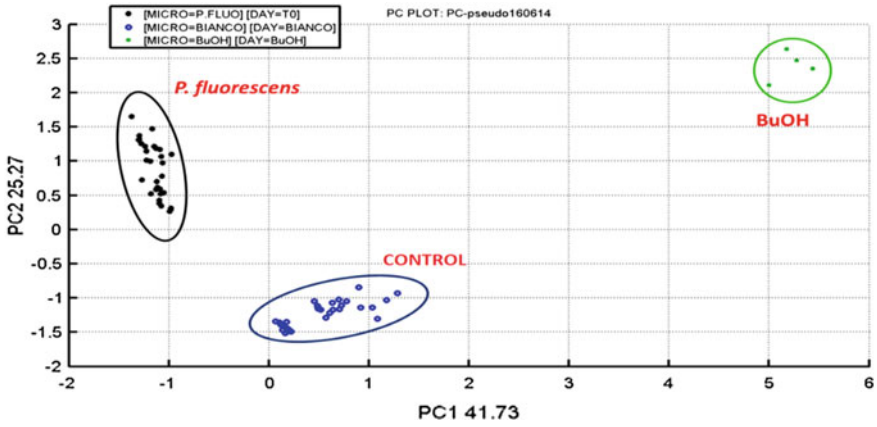

Fig. 8 Score plot PCA samples of water contaminated with *P. fluorescens* (all concentrations, T0) compared with samples not contaminated and those of BuOH (internal standard)

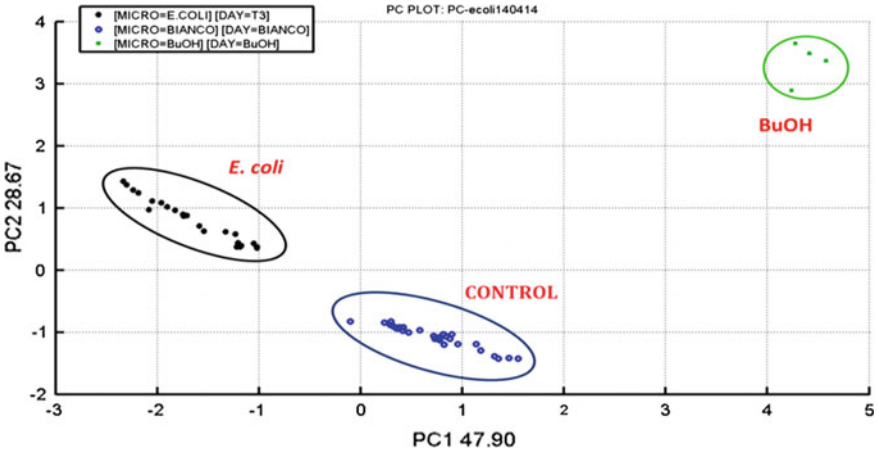

Fig. 9 Score plot PCA samples of water contaminated with *E. coli* (all concentrations, T3) compared with samples not contaminated and those of BuOH (internal standard)

From the chart above (Fig. 10) its possible to observe three homogeneous groups of statistical objects, among them adequately separated along the first principal component (PC1), associated with *E. coli* at a concentration of 9×10^2 CFU/ml. The PCA demonstrates the ability of the instrument to properly discriminate the microbial presence in water for the days of experimentation T0, T1 and T3. The change in the flavor profile detected in the course of time by the electronic nose could be due to a gradual accumulation of volatile secondary metabolites. It is possible to relate that response to a release in the surrounding medium of odorous compounds, which in turn can be associated with phenomena

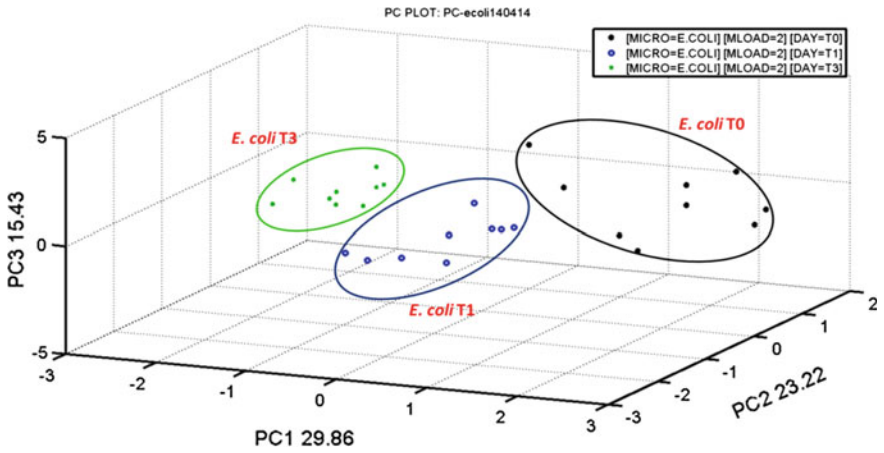

Fig. 10 PCA Score plot: comparison of water samples contaminated with *E. coli* set up at the time T0, T1 and T3

of cell lysis, frequently observed in advanced stages rather than in the more precocious. In the following graph (Fig. 11) are compared the results obtained *E. coli* and *S. Typhymurium* (T0 and T4).

The concentration considered is 9×10^8 CFU/ml. The graph shows some distinction of the cluster relative to *E. coli* from those of *S. Typhymurium* most central with respect to the first, which on the contrary undergo a clear separation along the first principal component as a function of the different days of experimentation, T0 and T4. The identification of four separate groups demonstrates the potential of the instrument to discriminate between different microorganisms and

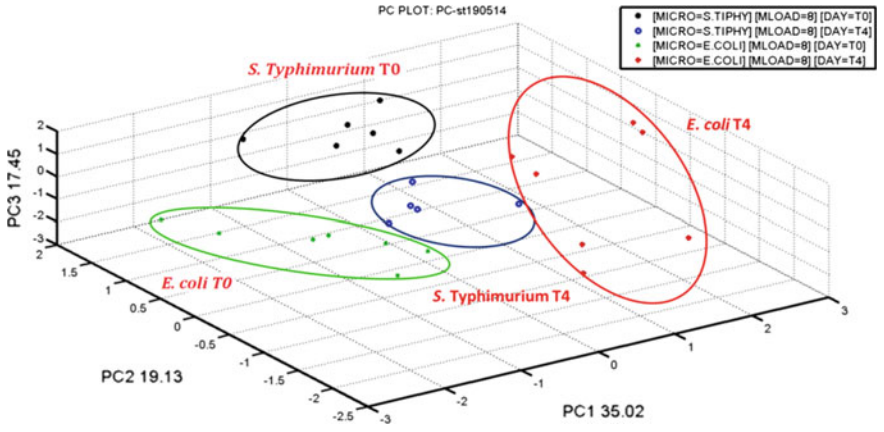

Fig. 11 PCA Score plot of comparison of water samples contaminated with *E. coli* and samples contaminated with *S. Typhymurium*. Days considered: T0 and T4; concentration: 9×10^8 CFU/ml

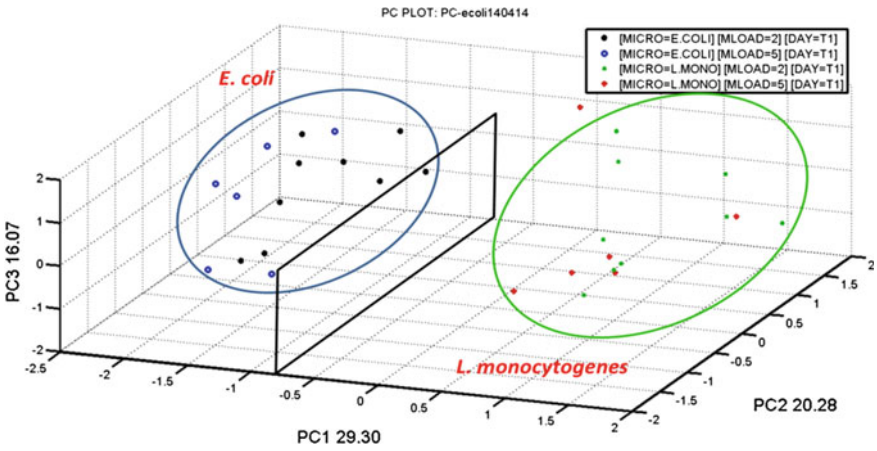

Fig. 12 PCA Score plot of a comparison of water samples contaminated with *E. coli* and samples contaminated with *L. monocytogenes*. Concentrations considered: 9×10^2 CFU/ml and 9×10^5 CFU/ml; day: T1

for the same microorganism, among the different days of analysis considered. The greater separation of the clusters may indicate a greater metabolic reactivity of *E. coli* than *S. Typhymurium* as well as a greater ability to adapt and proliferation within the medium water, generally poor in nutrients. In the next figure is showed (Fig. 12) the scores for the water samples inoculated with *E. coli* and *L. monocytogenes* at the time T1 compared with the different concentrations 10^2 CFU/ml and 10^5 CFU/ml.

Although in the figure is not possible to make a proper distinction between the different microbial loads is still evident discrimination of the various species considered in two clusters clearly separated along the first principal component (PC1).

In general the lower concentrations have proved to be those associated to the best instrumental performance in terms of the distinction of the microbial kind than the different days of analysis. This could be due to the by saturating effect of the sensor with the higher microbial loads, in absolute terms, greater emissions of volatile compounds could lead to a reduction in the resolving power of the instrument exceeding a certain concentration threshold value.

8.1.3 Electronic Nose

In the case of the mixed microorganisms contamination, was demonstrated the ability of the S3 device to detect the different between contaminated and uncontaminated samples.

Below is shown the evidence of the above relating to the mix EC + LM + ST, well explained previously in the Table 3 (Fig. 13).

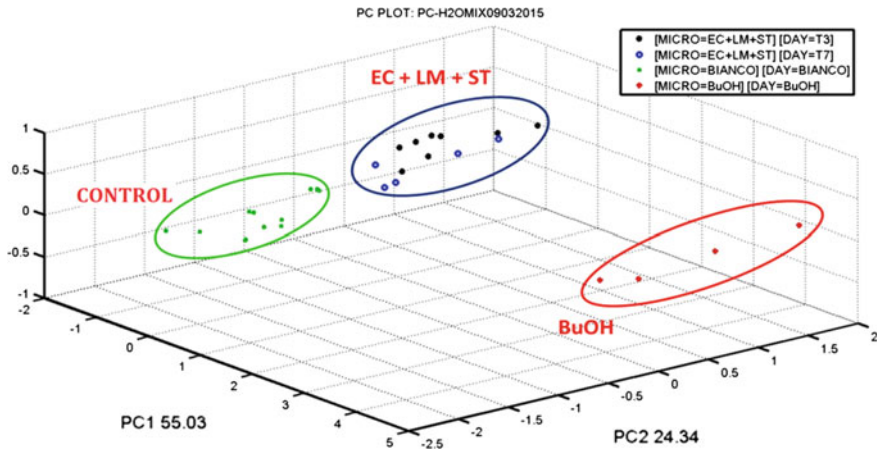

Fig. 13 PCA score plot of water samples contaminated with *E. coli*, *L. monocytogenes* e *S. Typhymurium*—EC + LM + ST (T3/T7) compared with control samples and BuOH

It is possible to identify three distinct clusters, one of which, relative to the internal standard, distinctly detached along the PC1 respect to the other two cluster. The remaining clusters correspond, respectively, to samples not contaminated and bacterial mixtures with two or three components. The experimental determinations carried out on bacterial mixtures allowed to test the electronic nose in relation to a more complex environment, simulating a real case of multiple contaminations. It was possible to confirm their ability to correctly discriminate, for a given mix, the

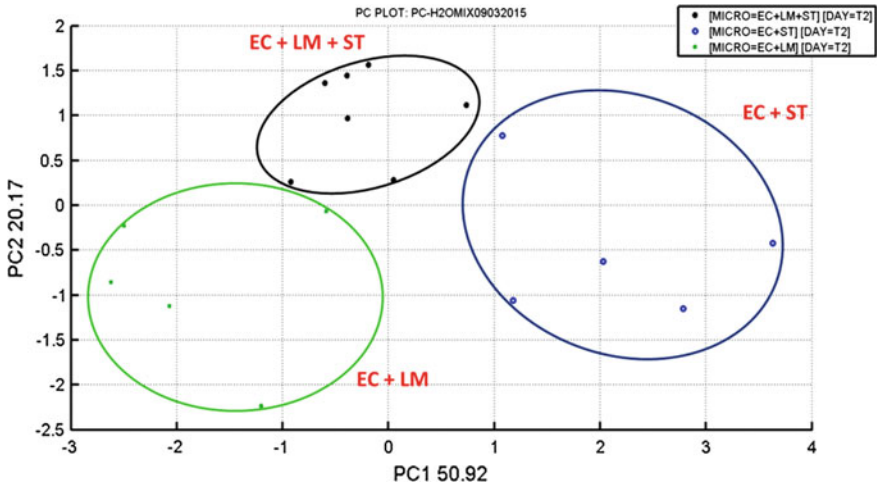

Fig. 14 PCA score plot, comparison of water samples on 3 different microbial mixtures: EC + LM + ST, EC + LM, EC + ST. Day: T2

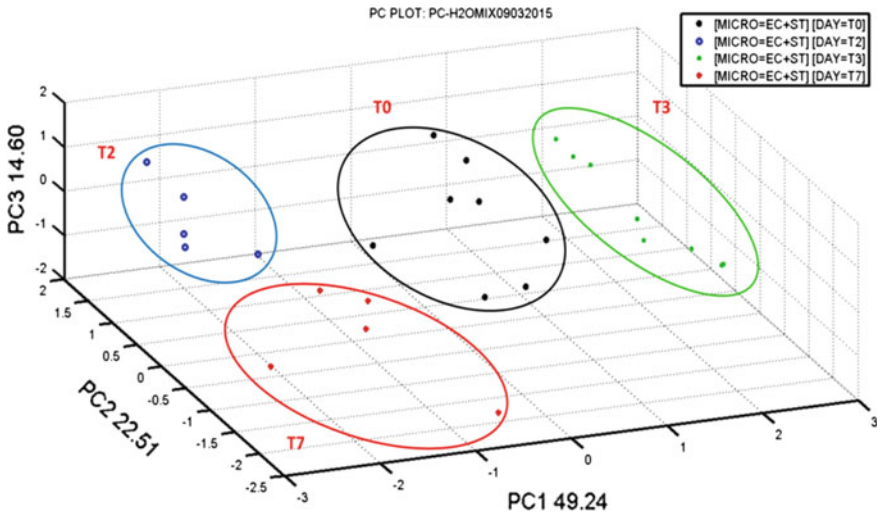

Fig. 15 PCA score plot showing T0, T2, T3, T7 for the microbial mix EC + ST

samples obtained on different days (T0, T2, T3, T7). The best results were obtained for the mixture of *E. coli* and *S. Typhymurium* (EC + ST) (Fig. 14).

In the chart below (Fig. 15) is shown the distribution of clusters for the microbial mixture EC + ST within the information space identified by the principal components PC1, PC2 and PC3 for everyday trials of analysis considered.

From the graph con be observed the correct distinction of the samples prepared in the days of analysis as demonstrated by the identification of four separate clusters.

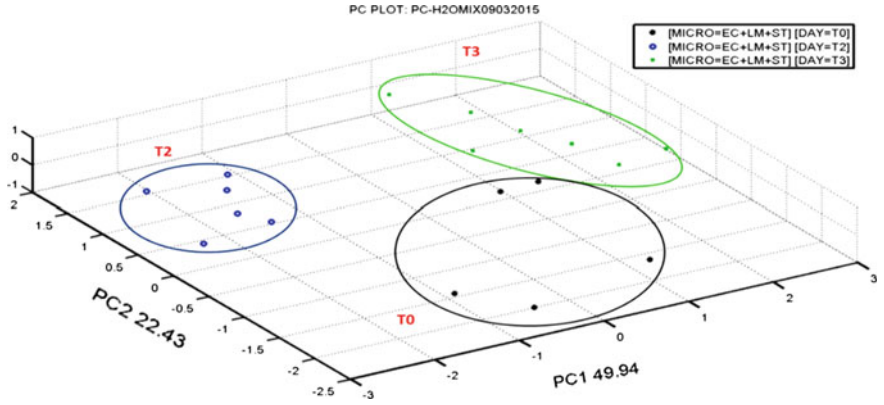

Fig. 16 PCA score plot comparison between the samples of T0, T2, T3 for the microbial mix EC + LM + ST

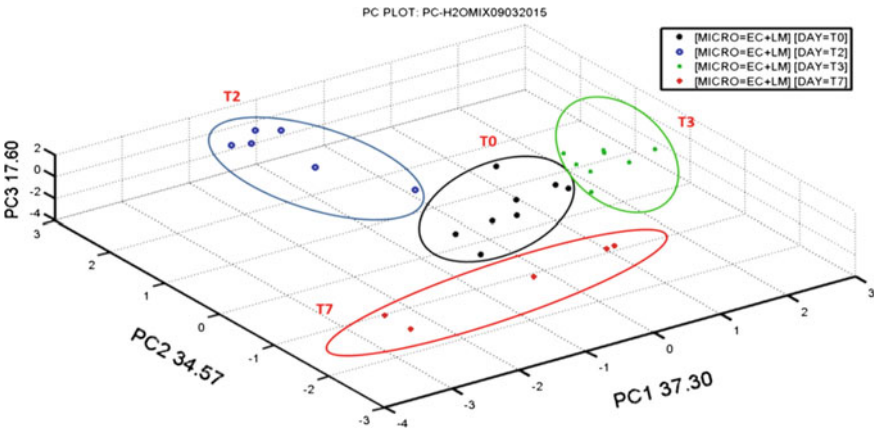

Fig. 17 Score plot of PCA: Comparison between the samples during the analysis time of T0, T2, T3, T7 for the microbial mix EC + LM

Parallel results to that just described above have also been obtained for mixtures microbial.

EC + LM + ST of which are reported the relative score plot (Figs. 16 and 17).

8.1.4 GC-MS-SPME Analysis

The experimental determinations carried out by GC-MS had as a purpose, the identification of the main volatile organic compounds synthesized by the bacteria under investigation, when combined in mixture. Thank to the analysis of the results it was possible to select the odorous substances associated with higher rates of detection. In the next table (Table 4) are shown, for each mixture, the volatile compounds of greater importance identified in the course of several days of experimentation.

Among the VOCs isolated from the mixtures it is possible to observe a prevalence of alcohols with a carbon chain of variable length from a minimum of 4 to a maximum of 15 carbon atoms, especially in the mix EC + LM and EC + LM + ST. The alcohols with a number of C atoms greater than 10 (dodecenol, dodecanol, tetradecanol and pentadecanol) are synthesized and secreted by-products typical of the degradation of fatty acids. It can be synthetized by several different bacterial species (including *E. coli*) mainly in aerobic growth conditions [23]. The biochemical pathways of this catabolic metabolism are highly conserved in a wide range of different microorganisms.

A second major class of compounds isolated from the bacterial mixtures subjected to analysis is aldehydes. Among these, the most frequently reported are benzaldehyde, heptanal, nonanal and decanal.

Table 4 Main VOCs detected by each microbial mixture by GC-MS; Days: T0, T2, T3, T4

Microbial blends	VOCs
EC + LM + ST	Indole, 1-pentanolo, 1-nonantiol, Nonanal, 1-dodecen-3-ol, 1-dodecanol, 3-metilbutanol, n-pentadecanol
EC + ST	Indole, Benzaldeide, 3-metilbutanol, Nonanal, Decanal, Benzoic acid, Butirric acid, 2-etilesanol, n-amilisovalerate, Acetilmetilcarbinol, 1-pentanol, 1-dodecanol, 1-tetradecanol
EC + LM	Indole, Benzaldeide, Butanoic acid, Decanal, 1-pentanol, 1-ottantiol, Nonanale, 3-metilbutanol
LM + ST	Benzaldeide, Eptanal, 1-tridecen, n-tridecanol, 3-metilbutanol, 3-metilbutilformiate

The compound ever more frequently isolated from mixtures containing *E. coli* is indole. Indole is a heterocyclic compound of empirical formula C_8H_7N. At room temperature is presented as a white solid colorless with characteristic aroma. It is in fact one of the compounds that give the typical smell of the fecal matter along with several other indole-derivatives such as skatole. It can be found in low percentages in combination with other substances such as aromatic component of many foods such as Camembert, Swiss cheese, coconut, black and green tea, rum and toasted hazelnuts [24]. Various microorganisms (over 85 different species among Gram-positive and Gram-negative) secrete the indole as a by-product of protein degradation. It constitutes one of the characteristic metabolites of *E. coli*, as such frequently used as a marker for the identification/detection of the bacterium in different culture media (indole test).

In the following histogram (Fig. 18) is shown the trend of indole emission for each one of the mixtures studied. The maximum abundance of indole is recorded, for all mixtures, at T0 and then gradually fell down. This phenomenon is

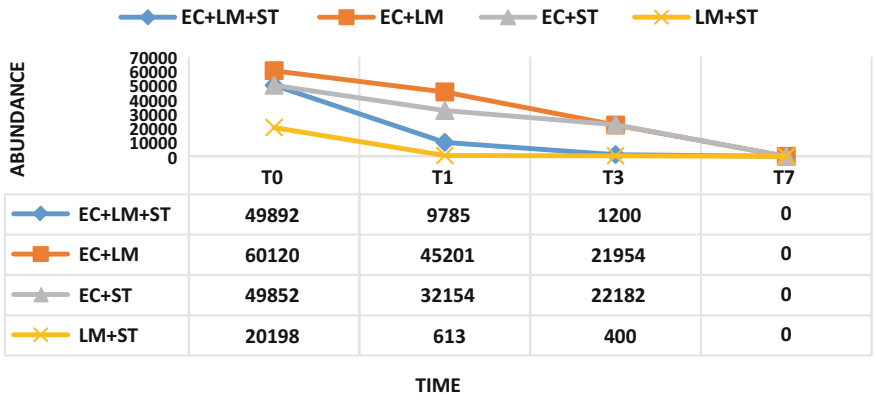

Fig. 18 Yield of indole emission for each of the microbial mixtures studied throughout the week of testing

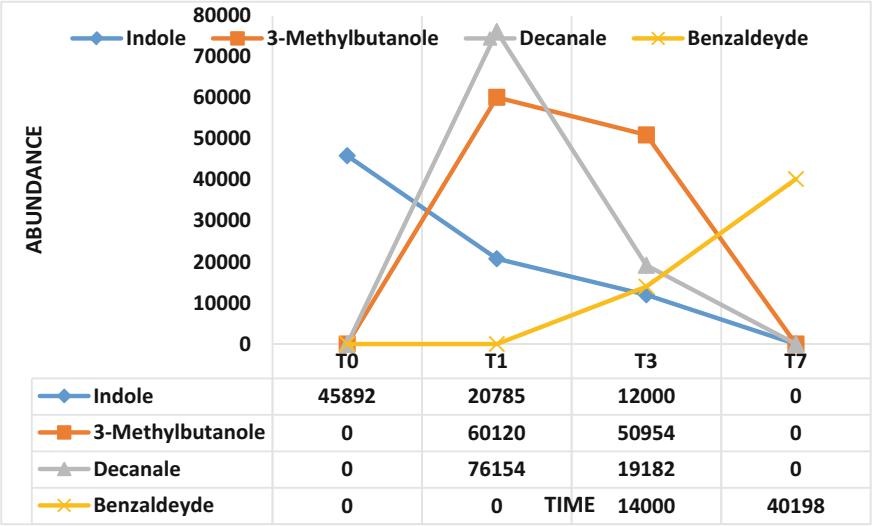

	T0	T1	T3	T7
Indole	45892	20785	12000	0
3-Methylbutanole	0	60120	50954	0
Decanale	0	76154	19182	0
Benzaldeyde	0	0	14000	40198

Fig. 19 Yield of the emission of indole, 3-methyl butanol, decanal and benzaldehyde throughout the week of testing. Mixtures of microbial reference: EC + ST (indole and 3-metilbutanol), EC + LM (decanal) and LM + ST (benzaldehyde)

attributable to the microbial transfer from a rich culture media (BHI) to the water a poorer growth medium (water) and therefore less able to support the cell metabolism. It is conceivable that the biosynthetic capacity of the bacteria decreases as a function of permanence within the system in response to a gradual decreasing of nutrients with the consequent increase of the cell mortality. The data collected from the mix EC + ST and EC + LM are examples of the above explanation.

The following graph (Fig. 19) shows the abundance trend versus time of indole and three other selected VOCs, 3-metilbutanol, decanal and benzaldehyde, considered of major importance for the various mixtures considered.

In Fig. 19 can be observed 3-metilbutanol and decanal with a similar trend to indole with a progressive reduction in the synthesis up to complete absence in last day of analysis.

Whatever distinguishes these compounds from indole is the absence of production in the first day of experimentation that might suggest a late synthesis in the course of bacterial growth. It is possibly facilitated by phenomena of synergy or competition among different microbial species once these are arranged in the same medium of growth. An opposite trend with respect to that described above is recorded for the benzaldehyde whose synthesis is until the time T2 to increase and become maximum at the time T7.

9 Conclusions

During this investigation was possible to confirm the potential application of the S3 device to perform earliest and on-situ analysis of the water microbiological quality.

The results achieved demonstrate a capacity to discriminate reliably between contaminated samples with samples of sterile water, so much as regards the individual microorganisms as for mixtures microbial.

The most significant performance was obtained distinguishing different days of testing (associated at different stages of microbial growth). The artificial olfactory system (S3) has shown a remarkable versatility in finely distinguish the samples of lower bacterial concentrations (10^2 CFU/ml) from samples of sterile water.

In general, the most promising responses were observed in the analysis of the microbial samples with a concentration of 10^2 CFU/ml. This is due to a possible saturation effect exerted on the sensors from bacterial higher concentrations, such as those associated with a higher emission of volatile compounds.

Predictably mixing the bacteria under study was accompanied by a general reduction in the ability of the device to distinguish easily the samples that share the same microorganism. However, it was possible to correctly discriminate and reconfirm for a given mixture, the different stages of the culture development.

It is necessary to pursue a process of continuous technological improvement through the design and implementation of sensors, more sensitive and possibly specific to selected VOCs they appropriate for use as a marker of contamination.

Extending the investigations for the identification and quantification of the organic substances of microbial origin in contexts gradually more and more complex would allow increasing the knowledge regarding any synergy/antagonism between microorganisms colonizing the same ecological niche.

The future perspective will be to realize a device, possibly portable, that will be able to provide, with high degree of sensitivity, a reliable answer in real time about the hygienic status of drinking water by the simple analysis of odor. The artificial olfactory system may be used as a screening tool for the distinction of water samples subject to risk contamination and then proceed accordingly to microbiological investigation.

This kind of approach will offer a considerable savings in terms of time and money. It will allow sustained control of water sources indicating in situations of real risk when will be important to perform traditional microbiology and chemical investigation (longer and more expensive) [24, 25].

References

1. “Progress on sanitation and drinking-water—2014” update. WHO Library Cataloguing-in-Publication Data. World Health Organization. II. UNICEF (2014). ISBN: 978 92 4 150724 0

2. Meeting the MDG drinking water and sanitation target: the urban and rural challenge of the decade. I. WHO/UNICEF Joint Monitoring Programme for Water Supply and Sanitation, WHO Library Cataloguing-in-Publication Data. World Health Organization, UNICEF (2015). ISBN: 92 4 156325 7
3. N. Barsan, U. Weimar, Conduction model of metal oxide gas sensors. J. Electroceram. **7**, 143–167 (2001)
4. P.T. Moseley, J.O.W. Norris, D.E. Williams, *Techniques and Mechanism in Gas Sensing* (Adam Hilger, Bristol, UK, 1991)
5. S.R. Morrison, *The Chemical Physics of Surfaces*, 2nd edn. (Plenum Press, New York, NY, USA, 1977)
6. S. Bianchi, E. Comini, M. Ferroni, G. Faglia, A. Vomiero, G. Sberveglieri, Indium oxide quasi-monodimensional low temperature gas sensor. Sensors Actuators B Chem. **118**, 204–207 (2006)
7. G. Sberveglieri, C. Baratto, E. Comini, G. Faglia, M. Ferroni, A. Ponzoni, A. Vomiero, Synthesis and characterization of semiconducting nanowires for gas sensing. Sensors Actuators B Chem. **121**, 208–213 (2007)
8. E. Comini, G. Faglia, M. Ferroni, G. Sberveglieri, Gas sensing properties of zinc oxide nanostructures prepared by thermal evaporation. Appl. Phys. Mater. Sci. Process **88**, 45–48 (2007)
9. E. Comini, S. Bianchi, G. Faglia, M. Ferroni, A. Vomiero, G. Sberveglieri, Functional nanowires of tin oxide. Appl. Phys. Mater. Sci. Process **89**, 73–76 (2007)
10. E. Comini, C. Baratto, G. Faglia, M. Ferroni, G. Sberveglieri, Single crystal ZnO nanowires as optical and conductometric chemical sensor. Appl. Phys. Mater. Sci. Process **40**, 7255–7259 (2007)
11. E. Comini, G. Faglia, M. Ferroni, A. Ponzoni, A. Vomiero, G. Sberveglieri, Metal oxide nanowires: preparation and application in gas sensing. J. Mol. Catal. A Chem. **305**, 170–177 (2009)
12. E. Núñez Carmona, V. Sberveglieri, A. Pulvirenti, Detection of microorganisms in water and different food matrix by electronic nose, in *Proceedings of the 2013 Seventh International Conference on Sensing Technology*, Wellington, NZ, pp. 703–707, Dec 2013
13. V. Sberveglieri, E. Comini, D. Zappa, E. Núñez Carmona, A. Pulvirenti, Electronic nose tor the early detection of different types of indigenous mold contamination in green coffee, in *Proceedings on the Seventh International Conference on Sensing Technology*, Wellington, NZ, pp. 465–469, Dec 2013
14. V. Sberveglieri, E. Núñez Carmona, E. Comini, A. Ponzoni, D. Zappa, O. Pirrotta, A. Pulvirenti, A novel electronic nose as adaptable device to judge microbiological quality and safety in foodstuff. BioMed Res. Int. **2014**, 1–6 (2014)
15. E. Núñez Carmona, V. Sberveglieri, A. Ponzoni, D. Zappa, A. Pulvirenti, Detection of microbial contamination in potable water by Nanowire technology, in *Proceedings of the 8th International Conference on Sensing Technology*, Liverpool, UK, pp. 136–139, Sept 2014
16. V. Sberveglieri, A. Pulvirenti, E. Comini, E. Núñez Carmona, What happens at the aroma of coffee beans after roasting? MOX nanowire technology by Novel Electronic Nose to discover the finger print, in *Proceedings of the 8th International Conference on Sensing Technology*, Liverpool, UK, pp. 136–139, Sept 2014
17. E. Núñez Carmona, V. Sberveglieri, E. Comini, D. Zappa, A. Pulvirenti, Nanowire technology for the detection of microorganism in potable water. Proc. Eng. 1453–1456 (2014). ISSN: 1877-7058
18. V. Sberveglieri, E. Núñez Carmona, D. Zappa, E. Comini, A. Pulvirenti, Classification of different roasting processes by MOX nanowire. Proc. Eng. 572–575 (2014). ISSN: 1877-7058
19. V. Sberveglieri, M. Falasconi, E. Gobbi, E. Núñez Carmona, G. Zambotti, A. Pulvirenti, Candida milleri detected by electronic nose in tomato sauce. Proc. Eng. 584–587 (2014). ISSN: 1877-7058

20. G. Zambotti, V. Sberveglieri, E. Gobbi, M. Falasconi, E. Núñez Carmona, G. Zambotti, A. Pulvirenti, Fast identification of microbiological contamination in vegetable soup by electronic nose. Proc. Eng. 1302–1305 (2014). ISSN: 1877-7058
21. I. Concina, M. Falasconi, V. Sberveglieri, Electronic noses as flexible tools to assess food quality and safety: should we trust them? IEEE Sensors J. **12**(11), 3232−3237 (2012)
22. J.E.L. Corry, G.D.W. Curtis, R.M. Baird, Handbook of culture media for food microbiology progress in industrial microbiology. Brain Heart Infus. (BHI) **37**, 409–411 (2003)
23. W.F. Naccarato, R.A. Gelman, J.C. Kawalek, J.R. Gilbertson, Characterization and metabolism of free fatty alcohols from Escherichia coli. Lipids **7**(5), 275–281 (1972)
24. E. Núñez Carmona, V. Sberveglieri, E. Comini, D. Zappa, A. Pulvirenti, Nanowire technology for the detection of microorganisms in potable water. Proc. Eng. **87**, 1453–1456 (2014)
25. E. Núñez Carmona, V. Sberveglieri, A. Pulvirenti, Small sensor system S3 device to control the microbial contamination in water. Approaching to the real condition, in *Proceedings of the 9th International Conference on Sensing Technology*, Auckland, New Zealand, pp. 258–262, Dec 2015

Milk Quality Monitoring Using Electromagnetic Wave Sensors

Keyur H. Joshi, Alex Mason, Olga Korostynska and Ahmed Al-Shamma'a

Abstract This chapter presents a novel approach to monitor the quality of milk products, based on electromagnetic wave spectroscopy. A comparative analysis is made to demonstrate the effectiveness of using microwave sensors over the other types, existing in the wide field of sensing technology. Three broadly used commercial varieties of milk, namely skimmed, semi-skimmed, and whole milk types are considered for the test measurements. The overall quality parameters of these products obtained from the market are comparatively measured in terms of their composition and spoilage with reference to ageing. The experiments carried out have illustrated that the sensor was able to distinguish one milk type from another. Moreover, it was also able to differentiate between fresh and aged milk samples of a given milk type as the number of days passes. The methodology used here employs Vector Network Analyser to capture spectral signatures in the form of scattering parameters from electromagnetic wave sensors. These data are then analysed to evaluate quality monitoring process achieved by these sensors. This work offers a potential platform for an economical, less complicated, and real-time milk quality control mechanism that can be employed outside of the laboratories at medium or large scale retailers in milk supply chain hierarchy.

1 Introduction

Milk, along with other dairy products, is consumed by over 6 billion people around the world [1]. This shows the importance of milk and milk products, as an integral part in daily life, especially for those who follow a vegetarian diet, inevitably due to their nutritional values. Milk supplies nutrients like good quality proteins, fat, carbohydrates, vitamins and minerals in significant amount than any other single food [2]. Dairy industries, that procure milk from dairy farms to process the raw milk in

K.H. Joshi (✉) · A. Mason · O. Korostynska · A. Al-Shamma'a
BEST Research Institute, Faculty of Engineering and Technology,
Liverpool John Moores University, Liverpool, UK
e-mail: K.H.Joshi@2014.ljmu.ac.uk

S. Mukhopadhyay et al. (eds.), *Sensors for Everyday Life*, Smart Sensors,
Measurement and Instrumentation 23, DOI 10.1007/978-3-319-47322-2_10

order to produce pasteurised milk, cheese, butter, ice-cream etc., also play a very significant part in overall economy of many developing as well as developed countries. The interest in milk products is continuously growing around the globe over the years because of several factors like changing dietary habits, improving nutritional awareness, rising population and overall development in the economy [3]. This growth can be observed from the fact that the milk production, worldwide, has increased by over 50 %, from 482 million tons as in 1982 to 754 million tons as in 2012, in 30 years, which is projected to increase by 175 million tons (23 %) by 2024 with comparison to that of the base years (2012–2014) [4, 5]. Milk processing at industrial level, following milk production at dairy farms, is next important stage in the supply chain of all dairy products [6]. Milk, because of being highly nutritious food, offers a very good environment for the microorganisms called bacterial pathogens to develop, breed and grow, eventually causing spoilage of milk. This phenomenon leads to short shelf-life of milk itself as well as other dairy products made by processing the milk. Besides shortening the overall edible life span, bacteria adulteration of any milk products can also cause consumers to contract various food borne diseases when such affected products are consumed. This can be eliminated to an extent by milk processing which enables its preservation over longer time-period and also helps to avoid the problems pertaining to health deterioration because of the lack in its quality or due to spoilage. Processing of raw milk ensures that its original nutritional value is maintained which also allows its preservation. Milk with improved overall natural quality is more preferred over the milk products that have artificially added nutritious values by processing. The increasing intake of dairy products provides vital health benefits to a large population of the globe especially that of the developing countries, in spite of the fact that millions of people in these nations still cannot afford better quality diets which are expensive [7]. These high costs of production are not only because of the high value raw milk but its subsequent stage of milk processing also adds to overall retail value of the end product.

Various milk quality testing techniques are available in industries and are being developed within research laboratories. The tests focusing on adulteration of milk are predominant in the industries, besides certain general tests applied to check overall quality of milk; like phosphatase test used on pasteurised milk and the acidity development test done on Ultra High Temperature (U.H.T.) processed milk [3]. There is also growing interest in techniques that are specifically aimed at determining the contamination within milk, such as Detergent Residue Testing [8]. Microwave sensors are used for a wide variety of applications including measurement of distance, movement, shape, and particle size, but the largest group of applications is concerned with the measurement of material properties [9]. Novel applications for these types of sensor have been introduced in food and water quality monitoring—for meat products [10], vegetable oils [11], and analysis of water contaminants [12] in the past. The other domain of application for these sensors is health monitoring where various applications have been introduced which includes the real-time indication of neurological impairments during surgeries [13, 14], and in detection of specific biomarkers in human cerebrospinal fluid [15]. The fundamental principle of EM wave sensors that operate at microwave and

radio frequencies (RF) is based on the interaction of these signals with the material under the test. The object under test changes the actual velocity of the electromagnetic wave signal, by either attenuating or reflecting it. The advantage of microwave sensors is that they can be implemented cheaply for a wide range of applications in a non-destructive yet effective manner and are capable of measuring without physical contact over a short distance, with the help of penetrating waves without creating any health hazards [16].

This chapter reports on a novel measuring technique that assesses overall quality of the milk by employing EM wave spectroscopy approach. Bespoke EM sensors that operate at microwave frequencies were developed and tested. The quality assessment is done in terms of classification of the milk type and detection of spoilage or bacterial adulteration developing over the days within the milk samples. The three categories of milk majorly sold in the market; namely whole milk, semi-skimmed milk and skimmed milk were tested. The sensor developed for this purpose was a resonator cavity designed to radiate within microwave range of frequencies between few hundred MHz to few GHz. The full laboratory setup makes the use of Vector Network Analyser (VNA) connected with the EM wave cavity to record the spectral signatures. The results of these test experiments, as explained in the following sections, are quite promising for further design and development of an all-in-one system. This innovative system for quality monitoring of milk products using EM wave spectroscopy is real-time, with less complexity and bearable costs, in comparison with many other existing methods currently in practise. This does not only classify one type of milk from another but also distinguishes between fresh and aged milk samples under test conditions.

2 Milk Production Stages and Need for New Quality Control Techniques

Milk is a perishable product, hence, spoils very quickly. Its nature of having lower acidity and higher nutrients make it the perfect breeding platform for bacterial micro-organisms, including those which are responsible for food poisoning, known as pathogens. Bacteria contaminate the milk, and their destruction is the main reason for milk processing which enables milk preservation. This can be achieved by fermentation, heating, cooling, and removal of water or concentration or separation of various components from milk, to produce foods like butter and cheese [17]. Table 1 lists the nutritional content of milk types used for making test samples.

Milk quality control is the use of approved test methods to ensure standards concerning the milk and milk products are regulated to accepted levels. This takes the account of composition and purity as well as the level of different micro-organisms within milk. It includes testing milk and milk products for quality and monitoring that milk products, processors and marketing agencies adhere to

Table 1 Nutritional content value of the three categories of milk

Typical values (per 100 ml)	Milk type		
	Whole milk	Semi-skimmed milk	Skimmed milk
Energy (kJ)	268 (64 kcal)	209 (50 kcal)	147 (35 kcal)
Fat (g)	3.6	1.8	0.1
Saturates (g)	2.3	1.1	<0.1
Carbohydrate (g)	4.7	4.8	5.0
Sugars (g)	4.7	4.8	5.0
Fibre (g)	0.0	0.0	0.0
Protein (g)	3.2	3.6	3.4
Calcium (mg)	120.0	124.0	124.0

accepted codes of practices [3]. The milk producer expects a fair price in accordance with the quality of milk that they produce. The milk processor pays the producer and assures that the milk received for processing is of normal composition and is suitable for processing into various dairy products. The consumer expects to pay a fair price for milk and various other milk products of acceptable to excellent quality.

To design a methodology and for developing a system that can test the overall quality of milk products, it is required to understand the basics of the milk categories under consideration. Here, the three commercially predominant categories of milk in consumer market—whole milk, skimmed milk and semi-skimmed milk are explained along with their spoilage patterns. The Dairy Council, UK, classifies the three types based on the fat content that they carry. Skimmed milk should not have fat in excess of 0.3 g per 100 ml whereas whole milk is expected to have a minimum of 3.5 g per 100 ml, while, the fat value in semi-skimmed milk ranges between 1.5 and 1.8 g of the 100 ml of product [18]. Several parameters for the spoilage of milk were studied and discussed including bacterial growth for both the milk types, and the observations showed that the bacterial growth patterns in the skimmed milk did not significantly vary from those in the whole milk. In addition to that, it was also confirmed that the milk spoilage bacteria grow at similar rates, in both, skimmed and whole milk types but have different metabolic behaviours within the two of them [19]. This also supports the results achieved in this work and the results of other researchers who observed similar rates of growth in skimmed and whole types [20–22]. These findings lead us to a common conclusion that the different shelf-lives of skimmed and whole milk types are not characterized by different bacterial growth rates within them.

In the past two decades, the evolvement in high-speed instrumental testing techniques to measure milk and dairy product composition provided the required platform for improvement in overall effectiveness and accuracy of classical chemical analysis methods [23]. For example, the development of Gas Chromatography Olfactrometry (GCO), in combination with mass spectrometry is the development of analytical tools that can be correlated with aroma/odour perception of foods. GCO basically detects aroma compounds developed due to degradation of

proteins and amino acids. In improving the milk preservation techniques, spoilage detection plays a vital role.

Milk spoilage can be defined in many ways and its measure could be different each time depending upon the context it is discussed in. For example, the simplest definition of quality product, for a common buyer it would be, a product that tastes good and smells good [24]. Many times we may find that the milk which is expired as per its 'Use By' date, labelled on its packaging, is not actually outdated and sometimes it is the opposite way around. This vagueness troubles both, the consumers as well as the manufacturers. Buyers are mostly reluctant to purchase products close to their dates of expiry. This ultimately imposes a negative financial impact on dairy industry [25]. Therefore, there's a developing need for an accurate milk spoilage detection method as much as there's a growing demand in preventing the wastage of milk and the illnesses occurring due to deteriorated milk consumption.

2.1 Issues Involved in Milk Supply Chain

Shown in the Fig. 1, is the basic block diagram of milk supply chain. To understand where the crucial challenges and problems lie in the system, it is necessary to study this hierarchy including the inherent difficulties involved in it. This ranges from the procurement level of milk taking place in dairy-farms, to the transport and handling of milk, and stretches to the end consumer level. Primary quality concerns rise at various stages of this chain, including the retailers that sell the packaged and processed milk products received from the dairies. For example milk is tested at both, procurement and packaging levels, by the industries for required amount of quality and its assurance, but after each phase of transportation it is most likely that the quality of milk product is altered, especially when the distance is longer and the quantity is large.

Fragmented Milk Production, where milk production takes place in an unorganized sector, is a big challenge and raises concerns when it comes to milk quality

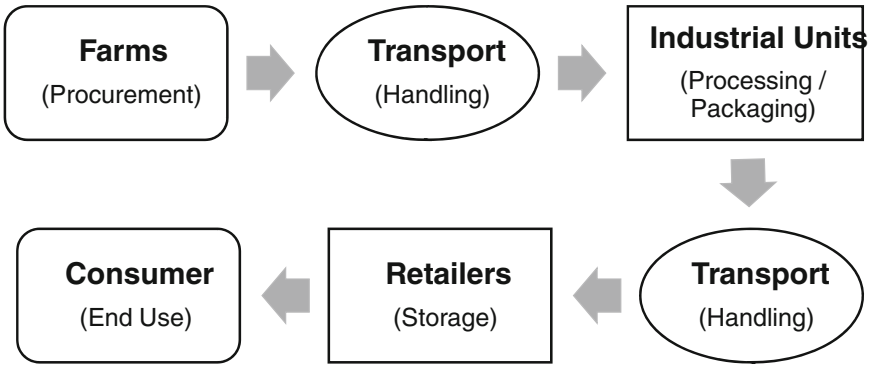

Fig. 1 Basic block diagram of milk supply chain hierarchy

and milk procurement over many economies like India—which is the largest producer as well as consumer of milk, having the largest livestock worldwide [26]. The research report by the team also adds that milk supply chains face difficulties in transporting milk, especially in large quantity, under desired conditions over longer distances (>200 km) while ensuring the quality of milk products.

This research work is motivated by the need to eliminate the above mentioned adversities faced by the dairy industry, milk supply chain and the consumers with regards to the contamination, spoilage and overall quality of milk in terms of constituents present, including milk adulteration. The issues concerning suitable levels of fat, added sugar and flavouring in milk also needs to be addressed [7], where no economical, effective yet easy-to-use method currently exists to achieve these goals [25]. In the past two decades, the evolvement in high-speed instrumental testing techniques to measure milk and dairy product composition provided the required platform for improvement in overall effectiveness and accuracy of classical chemical analysis methods [23].

In October 2015, raw milk produced by a dairy in state of California, USA, was ordered to be immediately recalled and quarantined, by a state veterinarian, whereas consumers were asked to dispose of any products from the given batch of code date Oct 24 [27]. The order was enforced after confirmed detection of *Campylobacter* type bacteria were found in raw whole milk, by the inspectors at routine sample test. Infection caused by these bacteria could show no symptoms at all or it could harm the immune system and be life threatening too. Mainly it includes symptoms like diarrhoea, cramps in stomach, or fever after 2–5 days of being exposed to the bacteria and remains around a week. Less likely yet possible symptoms could be joint pain or swelling. Also, a rare illness known as Guillain-Barré syndrome which brings weakness and paralysis can also occur some weeks after the initial sickness.

This is one of many stories, which surface regularly from around the world, related to milk, its contamination, spoilage or adulteration. Food Safety and Standards Authority of India (FSSAI) defines adulteration in food as, 'An act of intentionally debasing the quality of food offered for sale either by admixture or substitution of inferior substances or by the removal of some valuable ingredient' [28].

Adulteration can be in either form:

- Deliberate, which is done to gain commercial benefits, like addition of water or
- Accidental, that occurs incidentally due to several reasons like inappropriate handling.

Around 68 % of milk in India, which is the largest producer of milk worldwide with 16 % share of global milk production [4], doesn't meet the quality standards as recommended [29].

2.2 Application and Need for Novel Methods of Milk Quality Monitoring

This work seeks to address the issues faced at consumer end of the milk production supply chain hierarchy as at the milk procurement level dairy industries already have the robust quality assessment techniques suitable just within the industries as explained in following Sect. 3 of this chapter.

With this novel sensor application at retailers' end, the sellers can implement random checks for the packaged products from a given batch of packaged milk without having to check every single pack of the same batch. Therefore, it is broadly applied at the link just before the very end consumer filling in the gap that the dairy industry has after long transport phase where milk is most likely to get altered in its quality over longer distances as explained earlier. This can also eliminate the need to send the test samples to laboratories and awaiting their quality test results for a day or two, offering a real-time solution to the problem.

3 Current State of the Art

3.1 Spoilage Detection Techniques

Following is brief review of the current advancements being experimented for spoilage detection in milk.

- **pH indicators**, is one simple yet widely used sensing scheme. It normally sense the pH level, and on the basis of detected pH value they aim to determine the deterioration which leads to inaccurate results. For example, the pH value for milk which is hygienic enough to be consumed is around 6.7, and this is the pH level suitable for many types of bacterial micro-organisms to develop [30]. At lower pH values between 4.0 and 5.0, lactic acid bacteria can grow and produce lactic acid, which is the phenomenon being used for fermentation of milk for making various other dairy products at dairy industries and processing units.
- **Disposable wireless sensors**, are another approach applied for spoilage detection by the means of detecting bacteria. Remote-query sensor, used to measure the bacterial count of *Staphylococcus aureus* ssp. *anaerobius* (*S. aureus*) in milk, is normally a magneto-elastic sensing layer made of ribbon-like thick-film linked with some chemical. It's a stand-alone unit. *S. aureus* are the bacteria that are residing in milk and breed in multiple as milk spoils; *S. aureus* infection can cause human illnesses like toxic shock syndrome, septicaemia or endocarditis [31]. The disposable sensors are generally made up of a magnetoelastic sensor composed by a magnetic strip. This sensor is normally a low-cost design but with magnetoelastic sensors, bacteria detection becomes complex following the reason that speed becomes a problem with the ATP (Adenosine Tri-Phosphate)

bioluminescence method and the PCR (Polymerase Chain Reaction) [25]. Hence, this approach is not so favourable for real-time and rapid testing systems. The sensor reacts in terms of shifts in its resonance frequency depending upon the viscosity changes pertaining to *Staphylococcus aureus* (*S. aureus*) growth. Thereby, it undertakes sensing of the spoiled milk. The sensitivity of the sensor is achieved better in milk than in the culture medium as milk is having higher viscosity than the culture medium. The passive sensors, particularly, don't require internal battery as they receive the power from the query-field. These sensors get deformed mechanically when they are exposed to magnetic field, which launches elastic waves that have the highest value at mechanical resonance frequency, within the sensor [32]. Eventually, the mechanical deformation of the sensor generates specific amount of magnetic flux which is detected remotely by a pickup coil, without any physical connection between sensor and remaining apparatus.

- **Gas sensor arrays**, specifically aim to detect the strains due to the strong volatile compounds, and they require a very bulky and costly setup. These arrays normally involve solid state devices, i.e. Metal Oxide Semiconductor (MOS) and MOS Field Effect Transistor (MOSFET) supported by IR based CO_2 gas-sensor arrays [33]. The growth of three various spoilage bacteria, *Serratia marcescens*, *Serratia proteamaculans* and *Pseudomonas putida*, in milk was investigated by applying a commercial, solid state system of gas-sensor array. It was shown that the gas-sensor signals can be used as early indicators for the beginning of bacterial growth. Start detection for volatile bacterial metabolites was achieved around 7 h after inoculation corresponding to bacterial number of 10^4 (cfu/ml). In summary, the gas-sensor detects bacterial metabolites which are volatile by predicting the strain cultures that a certain compound produces. This operational behaviour of gas-sensors imposes a limitation to the whole mechanism, as for each independent volatile compound produced by different bacteria—it is required to establish a dedicated gas sensor to detect resulting strains. In addition to that, in case of bacteria that generate compounds which are less volatile, the sensitivity of the sensor has to be made significantly high in order to be able to sense the low amount of strains.
- **Infra-Red (IR) spectroscopy** is less famous in industrial platform than the other methods and also requires a costlier laboratory setup. The biochemical changes occurring in milk following pH level reduction occurred due to bacterial growth can be detected by visible and Short Wavelength Near Infra-Red (SW-NIR) diffuse spectroscopy (600–1,100 nm). This distinguishes between good-quality and spoiled milk samples without having to take account of every individual bacterium by monitoring quality loss in pasteurised skimmed milk [34]. The main disadvantage of this method is its high installation cost for experimental setups as the frequency of operation here is in terms of few hundred GHz to few hundred THz.

- **Electrical methods** are traditional and use the changes in current through an amperometric sensor as a measure of determining spoilage. This technique employs a potentiostat and two electrodes which are immersed in milk samples having different concentrations of bacterial inoculums and containing methylene blue [35]. In these types of method spoilage is detected when growing metabolism due to multiplying bacteria leaves a coloured solution into colourless [25]. The microbial metabolism causes the reduction in methylene blue, which eventually results into change of current through the electrodes. The Detection Time (DT) required to sense the detectable change of current gives the measure of present microorganisms at a given time. This is simpler method as compared to the orthodox bacteria plating techniques with the only drawback that it requires continuous supervision.
- **Optical test methods**, which are conventional, are costly approach to determine milk spoilage because of the reason that fresh milk micelles have sizes that require scattering setups to include sources and detectors that operate at wavelengths $\lambda < 300$ nm, which are on the deep Ultraviolet (UV) range, covering the visible (VIS) range [36]. An approach, with low-cost optical capillaries, to test the quality of milk involves an optical sensor configuration along with the fibre optical setup used a simple photonic system with optical capillaries to determine the milk quality by observing under certain heating conditions [37]. It proved that the optical capillary is a suitable medium to analyse liquids that show high scattering of light, e.g. milk. The overall setup used there is still more complex than the proposed technique based on EM wave sensor in this chapter. Also, such instrumentation is relatively costlier, compared to the proposed work here, as that is made up of a light source, fibre optical link, sensing head, and two photo-detection units which are controlled by an intelligent detection-and-control system. It, primarily, focused on the variation in quality resulting from predefined storage conditions. This process requires the heating of milk, as the test takes into account the influence of temperature on the structure of milk, and hence local heating to the capillary is introduced [38], which results in quite a large instrument setup.
- **Protein count** or **fat count** is also one approach to determine the spoilage in milk as by measuring the protein or fat counts [39]. *Pseudomonas aeruginosa* (*P. aeruginosa*) have been correlated to proteolytic activities in all food systems by many other studies as well. It produces a large amount of proteinases and lipases as well as plays an important role in producing by-products by taking part in lipid and protein breakdown along with temperature effects and storage time conditions [40]. So a good amount of technical ability and knowledge is required, which makes this method less favourite amongst end users. The industrial approach for determination of protein levels is known as Dumas method, which is more preferred as it is enhanced version of the standard

Kjeldahl method [41]. Both the methods first need to convert measured nitrogen concentration to a protein concentration, as they don't directly measure the protein, which leads to inaccuracies.

3.2 Composition Analysis Methods

As one report from Food and Agriculture Organization of the United Nations suggests that even after the efforts over past half-century, there still exists the need for an internationally accepted methods with supporting data [42]. In fact, as it further describes, the development of new methods for analysing specific composition elements that yields energy (like protein, fat or carbohydrates) has further increased the complexity and made this need greater than ever before.

Milk sensing technologies, currently being used, still lacks the intelligent approaches in practice [43]. As after the determination of good or poor quality of milk, most of the systems don't offer the automated diversion of poor quality of milk so as to maintain the high standards of their products at manufacturers end. From the above discussion, it is clear that there is scope and also need of improvement in milk quality testing methods. When it is hard to overcome all the limitations in all the characteristics as shown in Table 1, there is still a way to minimize the overall shortcomings of existing approaches.

The use of EM wave sensor can offer good balance among the overall aspects including performance, costs, reliability and less complexity, in comparison with the currently used standards. In this chapter, as described in following section, the attempt is to address these limitations by the design and development of a sensory system that is able to distinguish among given types of milk based on:

- Fat composition (five different samples ranging from 3.6 to 0.1 g per 100 ml) and
- Spoilage detection between fresh and old milk samples

Table 2 summarises these current advancements, as discussed above, for detecting milk quality using various measures, along with the main parameter that they detect to enable the test, its main limitation and primary advantages as further explained in [25]. The techniques are categorised based on whether they are spoilage detection methods or composition tests. This list can be more extensive with increasing amount of interest in the field of food quality assessment, especially with the help of various sensing technologies. This work is an attempt to address the shortcomings that the current technologies have while giving optimum results for determining the milk quality.

Table 2 Summary of current advancements in milk quality testing technique

Type	Techniques	Detection parameter	Advantage	Limitation
Spoilage detection methods	pH Indicators	pH levels due to presence of lactic acid bacteria (*Lactobacillus, Lactococcus, Leuconostoc*)	Instantaneous response	Inaccuracy; pH level fluctuates
	Disposable remote-query sensors	Viscosity changes due to *S. aureus* growth	Low-cost raw material; No external power required	Speed deficiencies
	Gas-sensor arrays	Volatile compounds (produced due to *S. marcescens*, *S. proteamacufans*, *Ps. putida*)	Rapid and accurate determination of shelf-life	Less sensitive towards bacteria producing less volatile compounds
	IR/NIR spectroscopy	Metabolic byproducts (developed due to proteolysis and lipolysis)	High efficiency	High costliness
	Electrical method	Changes in current flowing through an amperometric sensor (due to microbial organisms)	No supervision required	Time redundant
	Optical sensors	Scattered light through fresh and old milk samples in optical capillaries	Suitable for analysis of liquids giving high light scattering	Milk samples in optical capillaries require heating
	Protein/fat count	Changes in milk lipids/proteins due to varying *P. aeruginosa* levels	Fast methods	Extensive sample preparation; Requires acquired skill
Composition analysis methods	Fat analysis (Gerber method; Babcock method)	Milk fat released using centrifugation in butyrometer with sulfuric acid and Isoamyl alcohol	Low-cost methods	Not automatic; Requires high concentration sulfuric acid
	Protein analysis (Kjeldahl method; Dumas method)	Measures nitrogen levels to convert into protein value	Automated and quick-time	High initial costs

4 Electromagnetic Wave Sensing Technology

4.1 Fundamentals of Microwave Sensors

The antennas used for wireless and mobile communication operate on the EM wave transmission and reception. The EM wave based sensors, as used in this work, are the similar devices customized for different type of applications of sensing and detection. Wide range of variety exists within this group of sensors based on the way they are made, type of operation or range of frequency they work upon. EM wave or microwave sensors are mainly categorized into two groups, based on their applications. One group is of the radiometer, topographic and radar sensors for applications related to distance, movement and shape measurement [44]. The second group, which is related to this research work, is of the sensors like resonance cavity, waveguide sensors and transmission or reflection sensors, which are used for measuring material property, especially those of liquids and gases flowing or held through within them [9].

EM wave sensing or microwave sensors operate based upon the fact that the material under test condition, e.g. milk sample in this case, when placed into proximity or in direct contact with a microwave sensor, interacts with the EM waves that can be specifically correlated with the properties of the given material (milk). Particularly, the sensing is based on the interaction of propagating or resonating modes with the liquid under test. Due to this interaction, the permittivity of the material changes and it reflects itself as a frequency change, attenuation of the signal or a phase shift [45].

The material to be tested with this methodology is exposed to the electromagnetic field generated by the sensor fed through a source. For example, the 2-port microwave resonator cavity is designed to hold the test-tube containing milk sample to carry out the quality sensing, as depicted in Fig. 2. The changes captured in the sensor's spectral responses, through a network analyser, then become indication of the differences among samples under consideration [46]. These differences could be based on the composition, i.e. milk types, or could be changes between the adulterated (spoiled) and fresh samples of the same milk product.

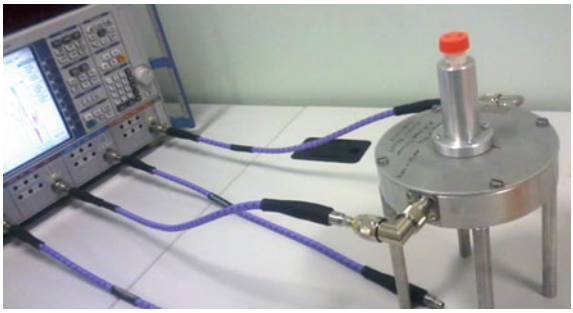

Fig. 2 An EM wave resonator cavity sensor

These types of sensor have following primary advantages over the types that have been discussed in earlier sections:

- Less complexity in installation of experimental/lab setups
- Universal applications (i.e. not specific to each bacteria/lipid/protein type)
- Wide range of variety according to needs of the application
- Better accuracy and less costs

4.2 Dielectric Properties of Milk

For development of a new technology that can evaluate milk quality, it can be important to possess the understanding of dielectric properties of milk. The dielectric constants for both, the raw milk (with 100 % concentration of milk) and the diluted milk (with 70 % milk concentration to deionized water) decreases with increasing frequency, more so at the lower frequency range of 10–4500 MHz, but dielectric constants for raw milk decreased more rapidly than in case of the diluted one, at room temperature of 22 °C [47]. For raw milk it was 97.7, 68.1, and 65.9, whereas 93.3, 70.9 and 69.1 for 70 % milk solution, at 10 MHz, 915 MHz, and 2450 MHz, respectively. The dielectric loss factor can be another potential indicator for prediction of milk concentration as well as freshness. Since, the adulteration of milk with water dilutes the ionic concentration within milk, the loss factor decreases with the increase in water content, which is decrease in the milk concentration.

Another work, concludes, that both, the dielectric constant as well as the loss factor, for cow milk, are affected by the protein content and also the temperature of milk. The frequency of electric field influences these two values, too. The dielectric constant decreased with increase in the frequency within range 10–4500 MHz [48]. The dielectric loss factor increased with increasing temperature below around frequency values of 600 MHz and decreased above frequencies of 1000 MHz. Poor correlation was seen between the dielectric constant and the protein content in the region of 100–600 MHz frequency values which means that this frequency range is insufficient for being used to develop milk protein detector on the basis of dielectric constant values.

5 Methodology and Measurements

This work takes into account the literature studied and uses resonator cavity as an EM wave sensor operating at microwave frequencies to evaluate milk quality. The procedures adopted to carry out the milk sensing and quality tests using this sensor, are explained below.

5.1 Sample Preparation and Measurement Conditions

Three milk types, namely skimmed, semi-skimmed and whole milk were bought from a local chain of stores for the tests. Five samples were made from each of this categories and labelled as shown in Fig. 3. To ensure that we have more accurate results and more no. of points for Fat versus Frequency graphs, another two categories were made by mixing two types of milk respectively. That is 50 % whole milk was mixed with 50 % semi-skimmed milk and 50 % of skimmed milk to the another 50 % of semi-skimmed milk which ultimately gives us 2 more varieties (5 in total) in terms of fat content. Each sample was of 15 ml in size, held in a polypropylene plastic test-tube.

The samples were made at room temperature and the storage conditions were governed in a temperature controlled climate with minimum fluctuations. For the better accuracy of captured spectral data, 5 repetitions were made for each of the 5 samples for all 5 categories of milk giving eventually 125 iterations to be mathematically analysed. The test-tubes as shown in Fig. 3, were labelled as W-1, W-2, …, W-5 for whole milk, SS-1, SS-2, …, SS-5 for semi-skimmed milk and S-1, S-2, …, S-5 for skimmed milk as abbreviated, respectively. Similarly semi-skimmed + skimmed milk solution and semi-skimmed + whole milk solutions were labelled SSS-1, SSS-2, …, SSS-5 and SSW-1, SSW-2, …, SSW-5, respectively. Table 3 lists the test measurement specifications with sample storage condition.

For the measurements with EM wave cavity resonator sensor a slot that can be inserted with the milk samples in 15 ml test-tubes, was used as shown in Fig. 4. The 2-port cavity was calibrated with the VNA, prior to measurement to enable accurate measurements of S_{11} (reflected back signal to input port-1) and S_{21} (transmitted signal from input port-1 to output port-2). The captured raw data of spectral signatures consisted of 60,000 point values each for different frequency within the range given, i.e. 10 MHz–15 GHz. Laser beam thermometer along with the digital probe thermometer were used to ensure stable temperature conditions before, during and after the measurements as can be seen from the illustration.

For the measurements a 2-port EM wave cavity was used as shown in Fig. 4 along with a VNA. Wide frequency sweep (10 MHz–15 GHz) allows more spectral

Fig. 3 Sample preparation for milk quality testing using EM wave spectroscopy

Table 3 Measurement specifications and sample storage conditions

No. of measurements	5 Samples × 5 Repetitions × 5 Categories = 125 Iterations
EM wave resonator cavity	Φ = 130 mm (distance between ports) h = 20 mm (height of cavity)
Size of samples	15 ml (polypropylene test tubes)
Period of supervision	1 week
Temperature	21 ºC ± 1 ºC
Frequency sweep	10 MHz–15 GHz
Channel base power	0 dBm

Fig. 4 EM wave cavity testing milk sample using VNA in temperature controlled climate

data to be captured before sending to further analysis ensuring comparison of more spectral signatures for better results. The distinguishing frequencies were identified for all 3 types of milk to enable their classification. Same goes for the detection of spoilage for a given type of milk and its comparison with previous day measurements to the following days in 1 week period. S_{11} and S_{21} parameters plots were captured with the use of VNA, in one minute, for each sample test.

5.2 HFSS Design and Simulations of the Sensor

The EM wave cavity sensor was modeled and simulated with the help of High Frequency Structure Simulator (HFSS), as shown in Fig. 5, before the development of its fabricated hardware. The resonance frequencies for TE mode and TM mode equations for microwave cavity are given by Eq. (1) and Eq. (2), respectively [49]:

$$f_{mnp} = \frac{1}{2\pi\sqrt{\mu\epsilon}}\sqrt{\left(\frac{X'_{mn}}{R}\right)^2 + \left(\frac{p\pi}{L}\right)^2} \tag{1}$$

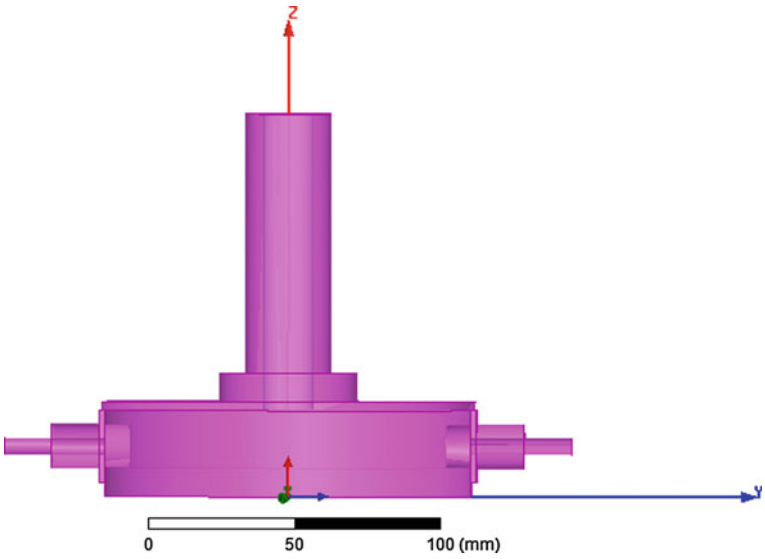

Fig. 5 HFSS model of the resonator cavity

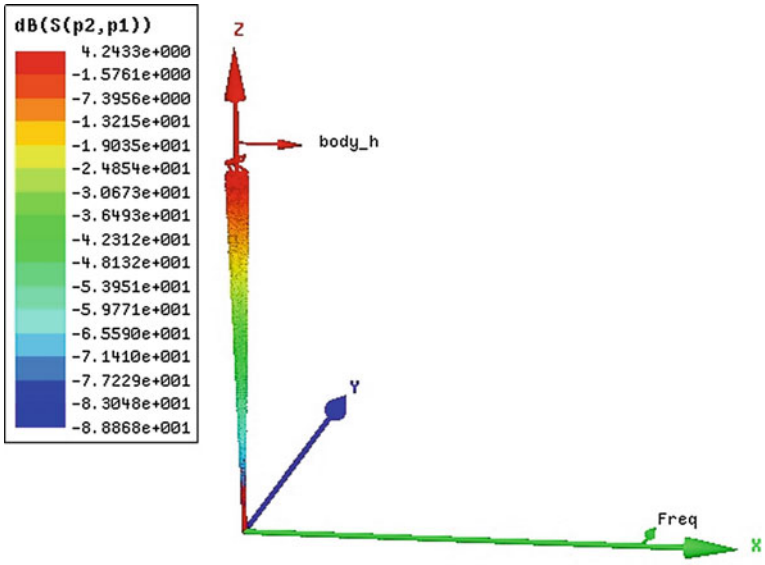

Fig. 6 3-D Polar plot of EM wave cavity for the frequency sweep 10 MHz–15 GHz

$$f_{mnp} = \frac{1}{2\pi\sqrt{\mu\epsilon}}\sqrt{\left(\frac{X_{mn}}{R}\right)^2 + \left(\frac{p\pi}{L}\right)^2} \quad (2)$$

where, R and L are radius and length for a cylindrical cavity, respectively. X_{mn} represents nth zero of mth Bessel function and X'_{mn} represents nth zero of derivative of mth Bessel function. μ and ϵ are permeability and permittivity of the medium, respectively. Here, p is the no. of half waves in the axial direction.

Figure 6 illustrates the field polar plot in 3-dimensions showing how the radiated EM wave energy spreads through the cavity. The primary difference between the microwave sensors and communication antennas is their far-field patterns. As we can see from the plot, in the case of a sensor, radiation is mainly near-field whereas it is opposite in case of an antenna. The reason behind that is, an antenna is supposed to radiate over a distance to enable wireless communication between two points while a sensor is ideally meant to sense the material in its nearest proximity with or without physical connection with the material being sensed.

6 Results Discussion

As shown in Fig. 7 for whole milk, there is a clearly visible distinction between the curves for S_{21} plot of Day-1 and Day-7. Five repetitions for each sample were made. Similarly, Figs. 8 and 9 show the graphs for semi-skimmed and skimmed milk, respectively. These plots are identical with minor shifts for all 3 given types

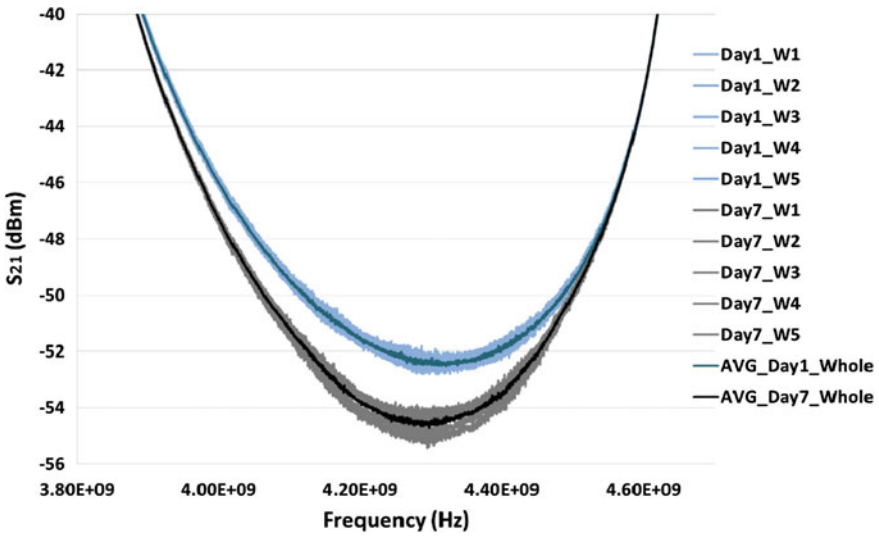

Fig. 7 S_{21} variations between Day-1 (*Blue*) and Day-7 (*Grey*) for whole milk

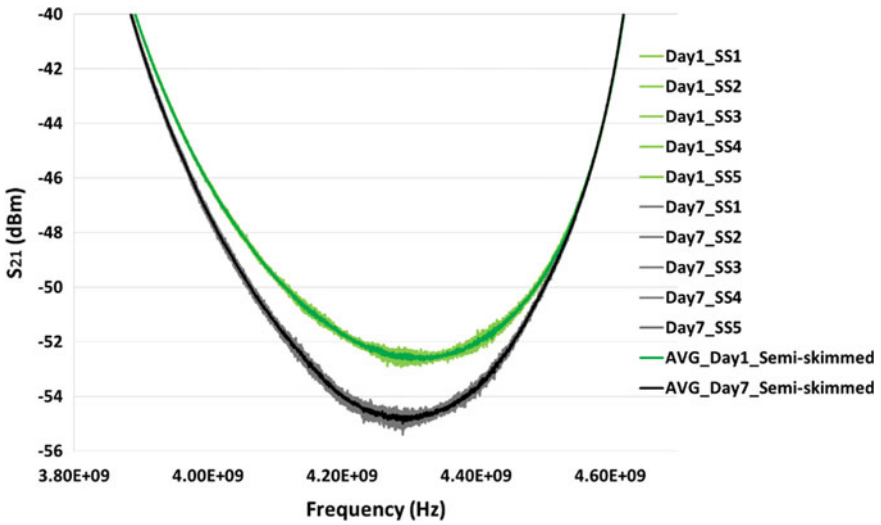

Fig. 8 S_{21} variations between Day-1 (*Green*) and Day-7 (*Grey*) for semi-skimmed milk

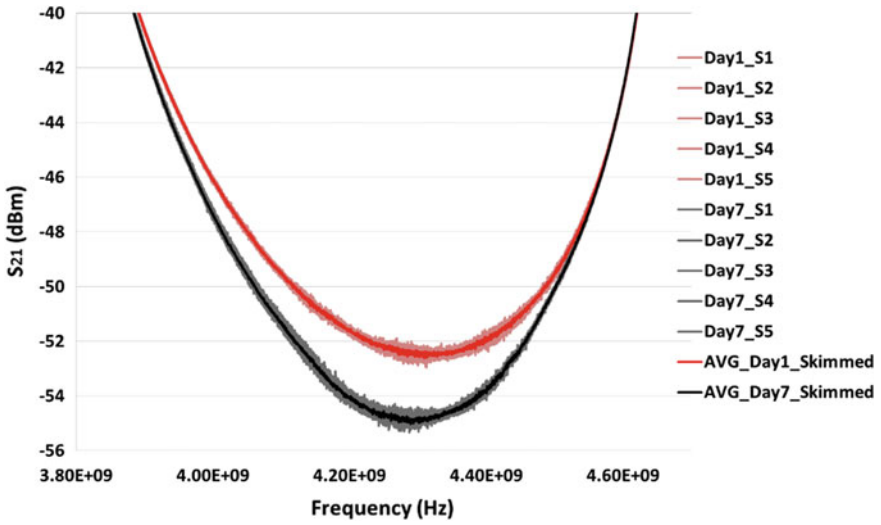

Fig. 9 S_{21} Variations between Day-1 (*Red*) & Day-7 (*Grey*) for skimmed Milk

of milk and shows effective results to distinguish between the aged and fresh milk samples.

Figure 10, on the other hand, distinguishes among the 5 various samples made from 3 categories, based on their fat content, of milk and labelled as S, SSS, SS, SSW and W as explained earlier. The figure shows spectral graph of S_{21} against the fat content of milk. The biggest advantage of this novel technique is, it does not

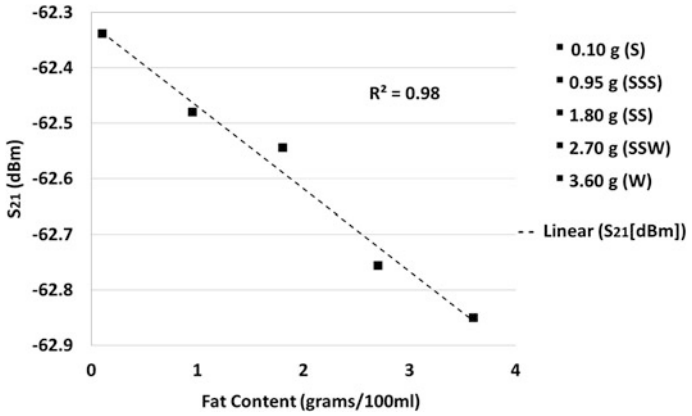

Fig. 10 S_{21} variations with respect to fat contents of 5 types of milk samples (Day-1)

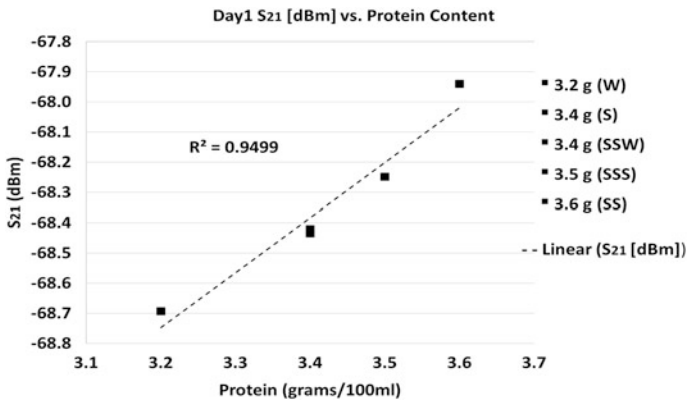

Fig. 11 S_{21} variations with respect to protein contents of 5 types of milk samples (Day-1)

only detect ageing but also distinguishes quite well among the types of milk as can be seen below. These 5 samples are achieved by 3 different milk types; skimmed, semi-skimmed and whole, and another two by adding 50 % of each, Skimmed milk with Semi-skimmed milk, and 50 % of each Semi-skimmed milk with the Whole milk, in order of fat content values.

We see the linear regression with correlation value, $R^2 = 98$ %, at the frequency value of 5.4598 GHz. This technique is less complex, and therefore, quick-time result oriented method than other methodologies previously explained in this article. The results achieved in this preliminary work of the whole project give accurate detection and efficient outcomes.

Figure 11 shows the S_{21} plot versus the protein content graph of the five types of milk. Here, unlike in case of fat content variations, the linear regression gives

R^2 = 94.99 % at 4.989 GHz, which is due to relatively less variations in protein content. These results, in a way, compliment the previous findings by others as discussed in the dielectric properties of milk section of this chapter.

7 Future Work

The future extension of this work contains:

- Design and development of a single EM wave patch (resonator) sensor, instead of a cavity, that can accommodate the following three quality check and control parameters:

  (i) Spoilage/Adulteration
  (ii) Composition and
  (iii) Contamination

Optimization and customization of the final design that integrates all these objectives into a single sensor can further help for real-time, stand-alone operation. With a patch resonator, which is of few centimetres by centimetres sizes, the milk sample can actually pass between the wings of resonating patch sensor using a fluidic pipe system for determination of quality.

Also, it should be noticed that the same category of consumer milk may still have differences in its compositional values, the ultimate design with certain customisation can be targeted to achieve grading among various samples given. To enable real-time operation, and grading of samples, the support of tools like MATLAB or LAB View can be incorporated.

8 Conclusion

The electromagnetic wave cavity is acting as a microwave sensor to detect adulteration and the type of milk. A wideband source applied to the cavity helps locate the values of frequency thereby allowing customization of the design that gives optimum results. Once having located the responding frequency values, dedicated EM wave sensors including microwave patch sensors, like Interdigitated Electrodes (IDE) or hairpin resonator, can be designed to operate on the same corresponding resonant frequencies for an optimized milk quality testing system.

This technique indeed shows a promising future for design and development of a milk quality testing and control system, of milk products, as it has several advantages over the other already existing standard practices. These advantages include less complexity, higher accuracy, time and cost-effectiveness and universal approach to milk types and quality detection. This work presents a very good prototype model for a novel, online EM wave based quality testing system that can

be made standalone and applied to large or medium scale retailers' level of milk supply chain hierarchy to avoid ambiguities and wastage of large quantity of milk as well as prevent any food-borne illness occurring due to spoilage or adulteration of milk.

This, with further optimasation, can help the large-scale or medium-scale retailers, who receive the milk from dairies for selling in packaged form after long stages of transport, to help allow the quality assurance and also to ensure that the customers are getting what they are paying for. This work not only will establish a strong base for the laboratory based research but also must aid towards the problem solving that the dairy industries and end consumers face due to either complexity or costliness of existing standard practices for milk quality control.

References

1. FAO, *Milk and Milk Products* (FAO Publications, 2015). http://www.fao.org/agriculture/dairy-gateway/milk-and-milk-products/en/#.Vc_BJpXH_mQ. Accessed 01 Apr 2016
2. A. Afzal, M.S. Mahmood, I. Hussain, M. Akhtar, Adulteration and microbiological quality of milk (A review). Pakistan J. Nutr. **10**(12), 1195–1202 (2011)
3. FAO: Ministry of Agriculture—Republic of Kenya, "Milk testing and Quality Control," FAO/TCP/KEN/6611 Project, Naivasha (2011)
4. FAO, *Milk Production* (FAO Publications, 2015). http://www.fao.org/agriculture/dairy-gateway/milk-production/en/#.Vc_CHZXH_mQ. Accessed 01 Apr 2016
5. OECD and FAO (eds.), *OECD-FAO Agricultural Outlook 2015-2024* (OECD Publishing, Paris, 2015)
6. FAO, *Milk Processing* (FAO Publications, 2015). http://www.fao.org/agriculture/dairy-gateway/milk-processing/en/#.Vc-_vpXH_mQ. Accessed 01 Apr 2016
7. Food and Agriculture Organization of the United Nations, *Milk and Dairy Products in Human Nutrition* (FAO Publications, Rome, 2013)
8. F.A. Gunther (ed.), The incidence and implications of residues of detergents and sanitizers in dairy products, in *Residue Reviews* (1983)
9. E. Nyfors, Industrial microwave sensors—a review. Subsurf. Sens. Technol. Appl. **1**(1), 23–43 (2000)
10. A. Mason, B. Abdullah, M. Muradov, O. Korostynska, A. Al-Shamma'a, S. Bjarnadottir, K. Lunde, O. Alvseike, Theoretical basis and application for measuring pork loin drip loss using microwave spectroscopy. Sensors **16**(2), 182 (2016)
11. S.B. Osman, O. Korostynka, A. Mason, J.D. Cullen, A.I. Al-Shamma'a, Application of microwave spectroscopy analysis on determining quality of vegetable oil, in *Proceedings of the 8th International Conference on Sensing Technology* (2014), pp. 556–559
12. O. Korostynska, A. Mason, A.I. Al-Shamma'a, Flexible microwave sensors for real-time analysis of water contaminants. J. Electromagn. Waves Appl. **27**(16), 2075–2089 (2013)
13. J.H. Goh, A. Mason, P. Browning, A. Al-Shamma'a, Using a microwave sensor as an online indicator of neurological impairment during surgical procedures. Key Eng. Mater. **543**(7), 368–372 (2013)
14. R.T. Blakey, A. Mason, A.I. Al-Shamma'a, A fluidic cell embedded electromagnetic wave sensor for online indication of neurological impairment during surgical procedures. J. Phys. Conf. Ser. **450**, 012024 (2013)

15. M. Fok, M. Bashir, H. Fraser, N. Strouther, A. Mason, A novel microwave sensor to detect specific biomarkers in human cerebrospinal fluid and their relationship to cellular ischemia during thoracoabdominal aortic aneurysm repair. J. Med. Syst. **39**(4) (2015)
16. S.G. Bjarnadottir, K. Lunde, O. Alvseike, A. Mason, A.I. Al-Shamma'a, Assessing quality parameters in dry-cured ham using microwave spectroscopy. Meat Sci. **108**, 109–114 (2015)
17. P. Fellows, A. Hampton, *Small-Scale Food Processing—A Guide for Appropriate Equipment* (FAO, Intermediate Technology Publications, London, 1992)
18. Milk Factsheet, *The Dairy Council* (The Dairy Council, London, 2016)
19. H.C. Deeth, T. Khusniati, N. Datta, R.B. Wallace, Spoilage patterns of skim and whole milks. J. Dairy Res. **69**(2), 227–241 (2002)
20. J.J. Janzen, J.R. Bishop, aB Bodine, Relationship of protease activity to shelf-life of skim and whole milk. J. Dairy Sci. **65**(12), 2237–2240 (1982)
21. J.V. Brown, H.M.P. Ranjith, G.A. Prentice, Comparative shelf-lives of skimmed, semi-skimmed and whole milks. Int. J. Dairy Technol. **37**(4), 2–5 (1984)
22. R.E. Chandler, S.Y. Ng, R.R. Hull, Bacterial spoilage of specialty pasteurised milk products. CSIRO Food Res. Q. **50**, 11–14 (1990)
23. D.M. Barbano, J.M. Lynch, Major advances in testing of dairy products: milk component and dairy product attribute testing. J. Dairy Sci. **89**(4), 1189–1194 (2006)
24. S.C. Murphy, *Shelf-Life of Milk Products—Microbial Spoilage—The Evaluation of Shelf-Life* (Ithaca, New York, 2009)
25. M. Lu, Y. Shiau, J. Wong, R. Lin, H. Kravis, T. Blackmon, T. Pakzad, T. Jen, A. Cheng, J. Chang, E. Ong, N. Sarfaraz, N.S. Wang, Milk spoilage: methods and practices of detecting milk quality. Food Nutr. Sci. **04**(07), 113–123 (2013)
26. NPCS Team, Market Research Report on Milk Processing & Dairy Products in India (Butter, Yogurt, UHT Milk, Cheese, Ice Cream, Ghee & Other Products). NIIR Project Consultancy Services (2014)
27. News Desk, Raw Milk Recalled in California for Campylobacter Contamination. Food Safety News (2015). http://www.foodsafetynews.com/2015/10/raw-milk-recalled-in-california-for-campylobacter-contamination/#.VnJ4MFduTOs
28. Food Safety and Standards Authority of India, Adulteration in Milk and Milk Products, FSSAI (2014). http://www.fssai.gov.in/Portals/0/Pdf/Adulteration(26.02.14).pdf. Accessed 03 Apr 2016
29. S. Saxena, Is the Milk You're Drinking Safe? 4 Easy Ways to Spot Adulteration, NDTV Food, 18 Mar 2016
30. T.R. Klaenhammer, Bacteriocins of lactic acid bacteria. Biochimie **70**(3), 337–349 (1988)
31. R. Guntupalli, R.S. Lakshmanan, J. Hu, T.S. Huang, J.M. Barbaree, V. Vodyanoy, B.A. Chin, Rapid and sensitive magnetoelastic biosensors for the detection of Salmonella typhimurium in a mixed microbial population. J. Microbiol. Methods **70**(1), 112–118 (2007)
32. C. Ruan, K. Zeng, Ca Grimes, A mass-sensitive pH sensor based on a stimuli-responsive polymer. Anal. Chim. Acta **497**(1-2), 123–131 (2003)
33. J.E. Haugen, K. Rudi, S. Langsrud, S. Bredholt, Application of gas-sensor array technology for detection and monitoring of growth of spoilage bacteria in milk: a model study. Anal. Chim. Acta **565**(1), 10–16 (2006)
34. H.M. Al-Qadiri, M. Lin, Ma. Al-Holy, aG Cavinato, Ba Rasco, Monitoring quality loss of pasteurized skim milk using visible and short wavelength near-infrared spectroscopy and multivariate analysis. J. Dairy Sci. **91**(3), 950–958 (2008)
35. Y.G. Lee, H.Y. Wu, C.L. Hsu, H.J. Liang, C.J. Yuan, H. Der Jang, A rapid and selective method for monitoring the growth of coliforms in milk using the combination of amperometric sensor and reducing of methylene blue. Sensors Actuators B Chem. **141**(2), 575–580 (2009)
36. P. Dress, M. Belz, K.F. Klein, K.T.V. Grattan, H. Franke, Water-core waveguide for pollution measurements in the deep ultraviolet. Appl. Opt. **37**(21), 4991–4997 (1998)
37. M. Borecki, M. Szmidt, M.K. Paw, M. Beb, T. Niemiec, P. Wrzosek, A method for testing the quality of milk using optical capillaries. Photonics Lett. Pol. **1**(1), 37–39 (2009)

38. M. Borecki, M.K. Pawlowski, P. Wrzosek, J. Szmidt, Capillaries as the components of photonic sensor micro-systems. Meas. Sci. Technol. **19**(6), 065202 (2008)
39. S.O. Yagoub, F.A. Bellow, I.E.M. El Zubeir, Effect of temperature and storage period on the constituents of milk inoculated with Pseudomonas aeruginosa. Res. J. Microbiol. **3**(1), 30–34 (2008)
40. K.L. Kohlmann, S.S. Nielsen, L.R. Steenson, M.R. Ladisch, Production of proteases by psychrotrophic microorganisms. J. Dairy Sci. **74**(10), 3275–3283 (1991)
41. E. Chiacchierini, F.D. Ascenzo, D. Restuccia, G. Vinci, Milk soluble whey proteins: fast and precise determination with Dumas method. Anal. Lett. **36**(11), 2473 (2003)
42. WHO/FAO, *Food Energy—Methods of Analysis and Conversion Factors* (Rome, 2002)
43. D.J. Reinemann, J.M. Helgren, *Online Milk Sensing Issues for Automatic Milking*, vol. 0300, no. 04 (2004)
44. S.H.H. Alhajeri, *Online Electromagnetic Wave Monitoring System for Petroleum Industry Applications* (Liverpool John Moores University, 2010)
45. O. Korostynska, M. Ortoneda-Pedrola, A. Mason, A.I. Al-Shamma'a, Flexible electromagnetic wave sensor operating at GHz frequencies for instantaneous concentration measurements of NaCl, KCl, MnCl2 and CuCl solutions. Meas. Sci. Technol. **25**, 6 (2014)
46. A. Mason, S.C. Mukhopadhyay, K.P. Jayasundera, N. Bhattacharyya, Flexible electromagnetic wave sensors, in *Sensing Technology: Current Status and Future Trends I* (Springer, Cham, New York, 2014)
47. W. Guo, X. Zhu, H. Liu, R. Yue, S. Wang, Effects of milk concentration and freshness on microwave dielectric properties. J. Food Eng. **99**(3), 344–350 (2010)
48. X. Zhu, W. Guo, Y. Jia, F. Kang, *Dielectric Properties of Raw Milk as Functions of Protein Content and Temperature* (2015), pp. 670–680
49. T.P. Wangler, RF *Linear Accelerators*, 2nd and Complete Edition (Wiley, 2008)

Grated Parmigiano Reggiano Cheese: Authenticity Determination and Characterization by a Novel Nanowire Device (S3) and GC-MS

Veronica Sberveglieri, Manohar P. Bhandari, Andrea Pulvirenti and Estefania Núñez Carmona

Abstract Parmigiano Reggiano (PR) cheese is produced from the bovine milk in a limited geographic area in northern Italy. It is one of the oldest traditional cheeses manufactured in Europe (XII century) and is still one of the most esteemed Protected Designation of Origin (PDO) cheeses of Italy. The Parmigiano Reggiano Cheese Consortium (CFPR) is the institutional system that covers all the cheese dairy factories and controls the cheese production in terms of cow feeding, cheese manufacture and ripening processes. The aim of this study was to establish a new, rapid, portable, easy-to-use, economic and non-destructive fouling based on nanowire technology device (S3) to control the presence of false grated PR. All the analyzed samples were collected from the Consortium that picked the samples produced in different European countries (three samples from Germany, one from Ireland, one from Latvia and one from Lithuania). The achieved samples were analyzed with the cooperation of multidisciplinary technologies like Colorimeter, pH Meter, GC-MS with SPME and the new nanowire gas sensor device (S3). The applied techniques were able to create a specific database for the S3 device, capable to give results in a few minutes. The use of a Small Sensor System (S3) device to determine the specific volatile organic compounds (VOCs) of the grated PR is a promising approach offering, at the same time, a simpler, faster and easier to handle (no specialized technicians are required) solution with respect to the analytical techniques (GC-MS, HPLC). However, from the commercial point-of-view, low cost and reduced power consumption are the fundamental features that should entail a sensor device. In this study, S3 device was applied and found to be efficient in the discrimination of the different grated PR cheese samples. In particular, the discrimination was checked quali-quantitatively thanks to the analysis performed with the GC-MS-SPME technique. In fact, the achieved results demonstrated the

V. Sberveglieri (✉) · M.P. Bhandari · E.N. Carmona
Sensor Lab, CNR-INO, Brescia, Italy
e-mail: veronica.sberveglieri@ino.it

M.P. Bhandari · E.N. Carmona
Department of Information Engineering, University of Brescia, Brescia, Italy

A. Pulvirenti
Department of Life Sciences, University of Modena and Reggio Emilia, Reggio Emilia, Italy

S. Mukhopadhyay et al. (eds.), *Sensors for Everyday Life*, Smart Sensors, Measurement and Instrumentation 23, DOI 10.1007/978-3-319-47322-2_11

quali-quantitative differences of the VOCs emitted by the samples. S3 device is a promising tool for the quality discrimination of the PR cheese and other foodstuffs. In our future works, specific database of the grated PR will be amplified for the direct use of S3 in the cheese-chain productions.

1 Introduction

Parmigiano Reggiano is a hard cheese, slowly matured, made from the raw semi-skimmed milk from cows whose diet consists mainly of fodder from the original area (Reggio Emilia, Parma, Modena, Bologna and Mantova). The milk may not be subjected to a chemical treatment and is not allowed for the use of additives [1–4].

Through this characteristics a form of cheese is produced called as Parmigiano Reggiano, a Protected Designation of Origin (PDO) product, according to the European EEC Reg. 2081/92 and the recognition of Reg. (EC) No 1107/96 by its disciplinary and as evidenced by the Consortium.

This organization, therefore, has the task to protect the Parmigiano Reggiano from its imitations and many frauds that are being reported around the world. In fact, the designation of origin of the cheese 'Parmigiano Reggiano' extends to the grated type cheese.

In addition, the cheese must have some special characteristics: fat content in dry matter must not be less than 32 %; aging not less than 12 months and within the limits fixed by the production standard.

It must not contain additives; organoleptic characteristics must be consistent with the definitions laid down by the production standard; humidity not less than 25 % and not more than 35 %; aspect: not crumbly, homogeneous, particles of diameter less than 0.5 mm not exceeding 25 %; rind quantity not greater than 18 %; amino acid composition: specific of 'Parmigiano Reggiano' [4, 5].

All these characteristics will be treated deeply in the next epigraphs of the current chapter.

1.1 Production Area and Spinneret

The link between Parmigiano Reggiano and its area of origin is essential. Parmigiano Reggiano comes from the territory and the tradition of man. It is produced today just as nine centuries ago: the same ingredients (milk, salt, rennet), the same care and passion, the same area of origin.

The area of production of Parmigiano Reggiano (Fig. 1) is located in the provinces of Parma, Reggio Emilia, Modena, Bologna to the left of the Reno River and Mantova to the right of the River Po.

Fig. 1 The area of production of Parmigiano Reggiano

This area must be involved either in the milk production or its transformation into the cheese.

1.2 Production Technique

The milk for the production of Parmigiano Reggiano comes from the cattle fed with natural fodder and the production process starts from the raw milk. The actual process is carried out using the same ancient technique but in modern settlements with new machinery.

The raw material is the evening milk, which is allowed to stand in large stainless steel tanks, as shown in the Fig. 2, to bring out the cream, and the whole milk from the morning milking. In the morning, it proceeds with mixing the semi-skimmed milk and the whole milk in copper vats shaped like an inverted bells.

The whey and the calf rennet are added after the milk has been heated to a temperature of 33 °C. After the mongrel coagulation, which takes place in 15 min, and thanks to the spino (Fig. 2), the curd is broken into small fragments having the size of a grain of rice and is cooked up to 55 °C [1].

After these operations, the mass is left to rest for 30 min, then extracted with a linen canvas of 1 m^2 and is placed in the molds, where it undergoes a pressing step.

After a few hours, the wet cloth is changed with a new one and then is removed to insert a matrix for stamping the identification data of the form on the crust: month and year of manufacture, the serial number of the dairy and the dots-label for Parmigiano Reggiano. Salting is carried out by bathing in brine for 25–30 days.

Maturation takes place in appropriate constant temperature and humidity warehouses, where the forms are constantly brushed and turned; to perform a homogenous seasoning and to prevent the overgrowth of surface mold.

Only after a minimum period of 12 months, the forms that will be found correct by the examination of the Consortium Body Control become full Parmigiano Reggiano.

Fig. 2 **a** The addition of rennet, **b** the dowelling, **c** collection in the linen bands, **d** the molding, **e** salting and **f** the curing in a controlled environment

Therefore, it becomes important to find a method to determine the origins of the grated PR cheese based not only on the classical expensive and slow chemical and physical techniques. The possibility of detecting the addition of cheese (with a big range of different seasoned cheeses from different country of origin) to the grated PR cheese has been always studied by means of destructive chemical methods.

Aroma (fingerprint) is one of the most significant parameters of foods from the sensory point of view, and it may offer information about the safety and quality of the food, acting sometimes as an indicator of processing mistakes as well.

The use of a Small Sensor System (S3) device, to determine the specific VOCs of grated PR is a promising approach offering, at the same time, a simpler, faster and easy to handle (no specialized technicians are required) solution with respect to the analytical techniques (GC-MS, HPLC).

However, from the commercial point-of-view, low cost and reduced power consumption devices are the fundamental features.

Gas chemical sensor arrays or Electronic Noses (EN) have been identified in the past few years as the valuable candidates for different applications including food quality control.

1.3 Aim

The aim of this study was to establish a new, rapid, portable, easy-to-use, economic and non-destructive fouling based on the nanowire technology device S3 to control the presence of false grated PR. All the grated cheeses were prepared using the same grinding machine using a predefined mesh dimension (ASTM series, mesh n°35).

The possibility of detecting the addition of cheese (with a big range of different seasoned cheeses from different country of origin) to the grated PR cheese has been always studied by means of the destructive chemical methods.

Thus the application of a novel nanowire device S3 can serve as an effective means to determine the authenticity of a PR cheese and also to characterize its quality parameters at the same time. Six different foreign cheese samples originated from Latvia, Lithuania, Ireland and Germany (Hartkase, Hartkase 1, Hartkase 11) were analyzed.

2 Materials and Methods

2.1 Sample Preparation

The preparation of the samples (Table 1) was carried out as follows: 2 g of grated cheese was placed in a 20 ml chromatographic vial. Subsequently all the vials were covered with the Silicon-PTFE septum and crimped with an aluminium crimp. At

Table 1 Foreign cheese samples and their Aw values

ple List	Aw
Latvia (CMP1)	0.821
Lithuania (CMP6)	0.824
Ireland (CMP4)	0.836
Harkcase1 (CMP2)	0.833
Hartkase11 (CMP3)	0.832
Hartkase (CMP5)	0.823

the same time, the water activity was measured in order to control and assure that this parameter will not influence the sensor response.

2.2 S3 Device Analysis

At SENSOR laboratory, the studies on chemical sensors started in 1988 with the improvement of thin films and then of a new technique for the planning of thin films with an extremely porous structure.

In 2002, quasi-one-dimensional metal oxide nanostructures were achieved with several advantages compared to their thin and thick film counterparts such as large surface-to-volume ratio, lateral dimensions comparable to the surface charge region, and superior stability when in the single crystal structure.

The novel nanowire device S3 is a production of the SENSOR laboratory.

The Small Sensor System (S3) device (Fig. 3) is equipped with a thermally controlled sensor chamber of 20 ml internal volume where there are placed 6 MOX gas sensors.

Three of these sensors were prepared with the RGTO thin film technology [6], and the other three constructed with the nanowire technology [7]. In fact, two of the three nanowires in the array are zinc oxide sensors but with different operating temperatures and the third one is a tin oxide sensor [8].

Fig. 3 Small Sensor System (S3) device

The vials containing different samples were placed in a randomized mode into the HT280T carousel. Each vial was incubated at 40 °C for 10 min into the HT280T oven, by shaking it throughout the incubation.

The sample headspace (4 ml) was then extracted from the vial in the static headspace path and injected into the carried flow (speed 4 ml/min) through a properly modified gas chromatography injector (kept at 40 °C to prevent any condensation).

Using synthetic chromatographic air with a continuous flow rate of 10 ml/min, the sensor baseline was performed and the recovery time was 28 min. The data analysis was run by means of Principal Component Analysis (PCA), operated with the Nose Pattern Editor software (SACMI Imola scarl, Imola, Italy).

The scheme of the sensor device based on an alumina transducers 2×2 mm^2 with the heater on the backside is shown in Fig. 4 together with the SEM images of nanowires. Tin and Zinc oxide nanowires exhibit a remarkable crystalline quality and a very high length-to-width ratio, resulting in an enhanced sensing performance.

The nanowire sensors thus manifesting a very high length-to-width ratio create a 3 dimensional network (Fig. 4). In this way, the adsorption surface is increased in a huge amount enhancing the response of the instrument and decreasing the threshold.

They exhibit a remarkable crystalline quality as well. These characteristics result in an enhanced performance and a long-term stability for the sustained operations.

The data analysis was run by means of Principal Component Analysis (PCA). Data were processed by EDA software, a home written software developed in MATLAB® at SENSOR laboratory [9].

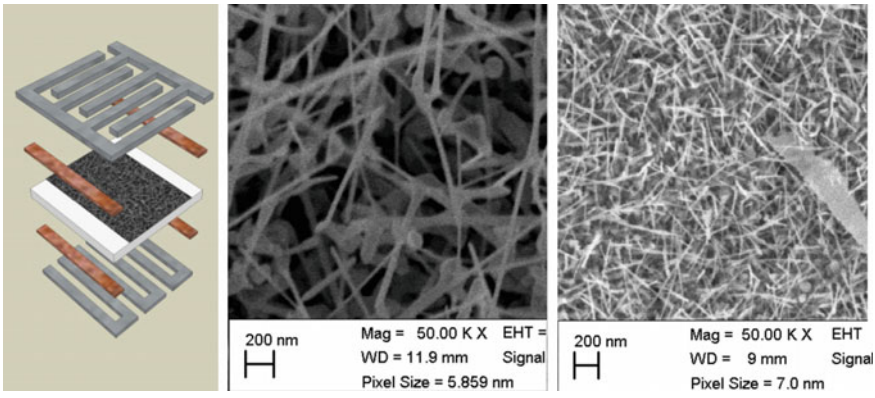

Fig. 4 *Left* Schematic sketch of the conductometric device. Alumina substrate is *white* colored in the *middle*, platinum heater and contacts are in metallic *gray*. SEM images of Tin (*center*) and Zinc (*right*) oxide nanowires

Feature extraction is usually unsupported, the most common example being the Principal Component Analysis. PCA can, by itself, transfer a good visual idea of the interclass split-up; in fact, this is how it is usually applied.

The goal was to obtain a good visual separation of the clusters, not just to have high estimate accuracy. To this end, PCA was systematically used to judge the clusters separation [10, 11].

2.3 GC-MS Analysis

GC-MS analysis was performed using a Shimadzu Gas Chromatograph GC2010 PLUS (Kyoto, KYT, Japan) equipped with a Shimadzu single quadrupole Mass Spectrometer MS-QP2010 (Kyoto, KYT, Japan) ultra and a HT280T autosampler (HTA srl, Brescia, Italy) that allowed SPME analysis.

The vials were incubated in an oven thermostatically regulated at 50 °C for 15 min in order to create the headspace equilibrium. In order to extract the volatile compounds of the samples, a DVB/carboxen/PDMS stable flex (50/30 μm) (Supelco Co. Bellefonte, PA, USA) SPME fiber was used.

To provide the adsorption of the volatile compounds, the SPME fiber was exposed to the headspace of the vials for 15 min at 50 °C. For desorption of the compounds, the fiber was placed in the injector of the heated GC for 6 min at 200 °C.

Volatile organic compounds were separated using an analytical capillary column (DB-WAX capillary column, 30 m × 0.25 mm × 0.25 μm, Agilent Technologies, Santa Clara, CA, USA) and the carrier gas used was ultrapure helium (99.99 %) at a constant flow rate of 1.3 ml/min. The temperature program for the GC was performed in the following way: 40 °C held for 8 min, linear gradient 4 °C/min up to 190 °C and held for 5 min, followed by a rise from 190 to 210 °C at 5 °C/min.

3 Results and Discussion

3.1 S3 Device

The data were processed by the software 'Nose Pattern Editor'. In Fig. 5, PCA score plot can be observed showing the comparison of all the samples for the foreign cheeses. The instrument was able to well differentiate the groups of the samples, here represented by different colors.

The two PC components alone covered over 60 % of the total information. This difference is then explained by the analysis first conducted with the GC-MS in

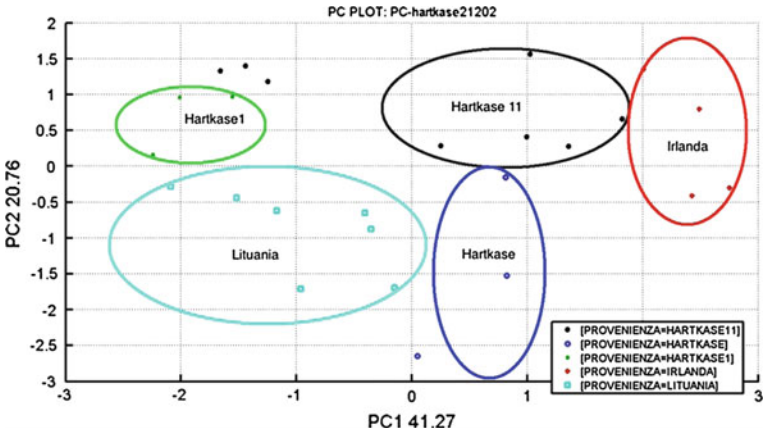

Fig. 5 PCA score plot from the foreign cheeses esters

which several compounds are observed between the different samples and also different amounts of the same compounds (Fig. 5).

The next step was then to compare these foreign samples with the pulp and crust composition of the real Parmigiano again using the PCA analysis. From the obtained PCA (Fig. 6), the clusters of the samples were observed to be quite compact.

From the figure, it is seen that the foreign samples are not confused with the real Parmigiano Reggiano cheese samples, but some similarities in the foreign cheese samples with the crust or the pulp are found. In fact, in the left side the black dots

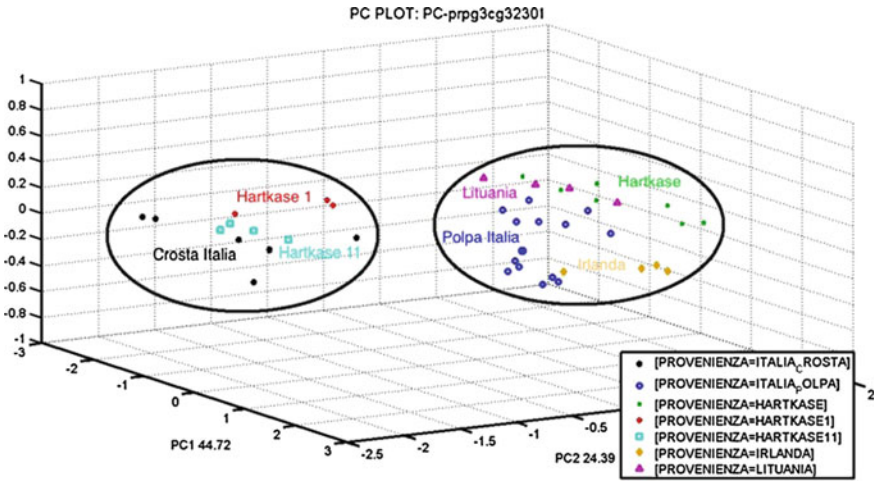

Fig. 6 PCA score of foreign cheeses in comparison with 100 % pulp and 100 % crust of Parmigiano Reggiano

are the detached samples of the crust and near these are all Hartkase1 and Hartkase11 samples.

These samples are more similar to Parmigiano Reggiano crust compared to the pulp or to other foreign samples, confirming the fact that probably these samples have very high percentages of the crust that characterize them.

On the other hand, the PCA score plot includes the pulp cluster of the real Parmigiano close to the clusters of Ireland, Hartkase and Lithuania. Probably these samples show the most similarities to the pulp of Parmigiano Reggiano over the crust.

3.2 Gc-Ms with Spme Analysis

The figures below report the frequency histograms of the compounds present in different samples divided into two parts to allow an easier viewing of the graphs (Figs. 7 and 8).

The samples analyzed are very different from the true Parmigiano: even with a fast sensory analysis many atypical features are observed later confirmed by the gas chromatography, which included the analysis of different true Parmigiano Reggiano cheese samples.

In particular, there are very significant compounds present such as butanoic acid derivatives that characterize especially the Ireland grated sample.

The most abundant compounds in this sample are propanoic acid, butanoic acid and derivatives, tridecyl-3-butyric acid ester, acetic acid phenylmethyl ester.

These compounds are typical for Cheddar cheese, therefore the Irish sample could possess a small percentage of real Parmigiano (in fact possesses some similarities: 1-butanol-2methyl, 2-nonanone, octanoic acid ethyl ester and propanedioic

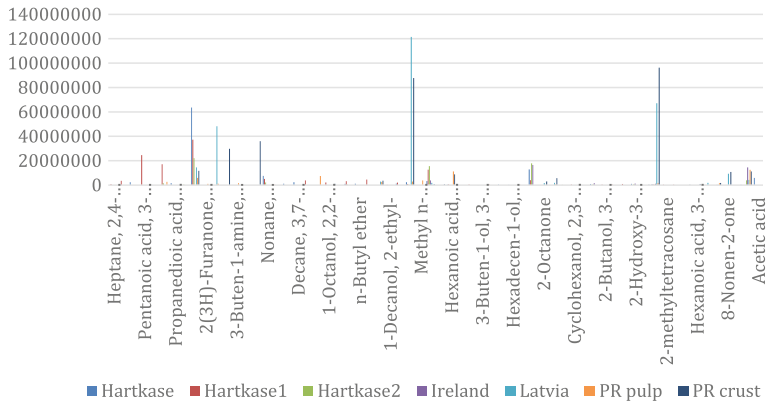

Fig. 7 Frequency histogram of foreign cheeses compounds from 1 to 24.1 min

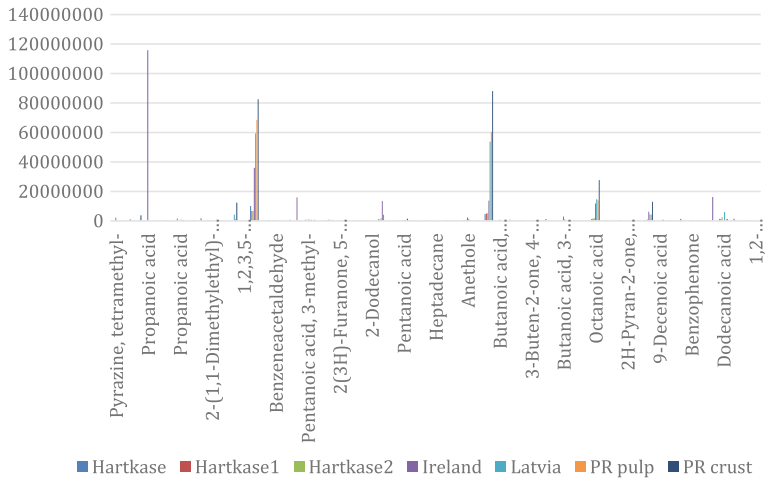

Fig. 8 Frequency histogram of foreign cheeses compounds from 24.1 to 59.5 min

acid) but for the major part it seems to have been mixed with the Cheddar cheese. It is also very different from the other foreign samples.

The German samples have similarities between them and even consist of different compounds. They are very different from the true Parmigiano, small analogies may be found with the crust as confirmed by the PCA provided by the Electronic Nose and could probably contain Emmental or Camembert as confirmed by the comparison with the bibliography.

The Latvian sample is the only one to get closer to the true profile of Parmigiano Reggiano (see for example: 2-heptanone) which presents the typical compounds of Parmigiano both from the pulp and the crust.

However, the analogy is greater for the crust (see the presence of 2-pentanol, 2-heptadecanone, 2-octanone, 2-nonanone, octanoic acid ethyl ester, 2-nonanol, 2-undecanone, heptanoic acid, octanoic acid).

Significant is the presence of dodecanoic acid which denotes a typical aroma of the cheese crust and the presence of 5-methyl-2-hexanol, wood aroma denoted by the real Parmigiano crust during ripening in which the forms remain for months on the wooden planks.

The only foreign presence of phenylmethyl acetic acid ester and anethole in the samples makes us suspect that the foreign samples and imitations are mixed with the small percentages of Parmigiano indicating the commercial fraud.

Here the compounds found in the chromatograms have been classified selecting only those compounds that characterize the different origins of the foreign cheese samples defining the aroma.

- *Latvia*: The compounds that characterize the aroma of the cheese from Latvia were:

- N-tert-Butyl ethylamine: Mainly present in Latvia sample and even small part in the pulp of real Parmigiano. From the published papers, it is found to have a smell of ammonia [12, 13].
- 2-pentanol: Compound present in Latvia in the pulp samples and real Parmigiano crust. More abundant in the crust than the pulp, while it has intermediate values for Latvia sample. Found in many foods: fruit, cheese, drinks and gives fresh aroma [13].
- 2-Decanone: Aroma trace of the crust of Parmigiano Reggiano and present in a lesser amount in the sample of Latvia but absent in all other samples. From bibliography, it is an aroma from various plants [13].
- 2-Nonanol: Compound behaving exactly like the previous one. It is present in oranges, ginger and some wines and cheeses [13].
- Butanoic acid phenylmethyl ester: Aroma trace in Ireland and Latvia samples (more in the latter than the former). It is present in purple, papaya, black tea, vanilla, sweet smell of apricot and pear [13].
- Benzyl alcohol: Constituent of Jasmine scent from bibliography, present in orange juice, tangerine peel oil, pineapple, cinnamon, cloves, mustard, basil and sage [13].
- Heptanoic acid: Found in Latvia sample and the pulp samples of Parmigiano in similar quantities. Absent in other samples. It is found in strawberries, ginger, apples, black tea and grains. It has a rancid odour of fatty acids [13, 14].
- 9-Decenoic acid: This aroma is found in traces in the pulp of Parmigiano, in Latvia and in most of the Parmigiano Reggiano crust samples. It is typical of Parmigiano Reggiano [12].

- *Ireland*: The compounds that characterize the aroma of the cheese from Ireland were:
  - 3-Pentanol: From bibliography, it is a characteristic odor from olive and is also present in cranberry [13].
  - 2-Hydroxy-3-pentanone: It is a part of lavender, ginger, peppermint [13].
  - Tetramethyl-pyrazine: It is present in french fries, bread, sausages, tea, cocoa, coffee, beer, dairy products and soy products [13, 14].
  - Propanoic acid: Aroma present in all the samples in a trace amount but abundant in the Ireland sample. It gives a pungent odor and is a preservative often used in agriculture. It gives a pungent fruity aroma in Cheddar cheese [13, 14].
  - 2-Tridecanone: In literature, it is shown to be isolated from the vegetable oils such as palm oil and coconut, blueberry, raspberry, grapefruit, onion, ginger and cheese [13].
  - 2-methyl-butanoic acid: Abundant in the Irish sample. It is present in bananas, apples, butter, bread, papaya, black cherry and cheese [13].
  - Heptadecane: Compound ubiquitous in all the samples analyzed. Slightly more abundant in Ireland sample. It is present in vegetables such as beans and sunflower [13].

  - Tridecyl-3-butyric acid ester: It is found in apples, bananas, papaya, bread, cheese, butter and coffee [13].

- *Hartkase*: The compounds that characterize the aroma of the cheese from Germany were:
  - Methylene heptane: Present only in Hartkase1 in low quantity. From bibliography, it is a component of some flowers [13].
  - 3-methyl-4-oxo-pentanoic acid: Compound present only in Hartkase1 in a small quantity. It has an aroma of cocoa, Fontina cheese, cooked asparagus, beer and pumpkin [13].
  - Ethanol: Present only in Hartkase1 and Hartkase11 in a small quantity. It has a fermentative aroma [13].
  - 3,7-dimethyl-decane: Present in Hartkase in a very small quantity. It has a fruity and floral aroma [13].
  - 2,2-dimethyl-1-octanol: Compound in trace amount only in Hartkase1. In bibliography, it is described to have a penetrating aroma of different essential oils [13].
  - 4-methyl-undecane: Present only in Hartkase1 in a trace amount. It is an aroma component of chickpeas [13].
  - Styrene: Aromatic compound found in trace amount in Hartkase. It is present in blueberries, grapes, vinegar, parsley, milk and dairy products, coffee, cocoa, roasted hazelnuts and peanuts [13].
  - Acetic acid: Present in Hartkase, provides pungent odor in vinegar.

4 Conclusion

The fight against counterfeiting has been a priority for the protection of PDO products. The globalization of markets not only provides several opportunities but also many risks: the ability to package the product in the world makes the making of documentary controls increasingly difficult.

In this sense, the Parmigiano Reggiano Cheese Consortium is working to change the rules of the production of Parmigiano Reggiano, to make the packaging compulsory in the area and to develop the sophisticated solutions for the traceability of the product.

In parallel, however, the target is to find the technical and organizational solutions that increase the chances of the cheese downstream control that enters into the commercial circulation, in terms of compliance with the same standards imposed by the regulations and the way it is included in the agreements signed between the Consortium and the packers.

In addition to this, several foreign samples and imitation of Parmigiano Reggiano are widely available in the market. The grated suspects were examined and found to be mixed with the PR. Using the SPME-GC-MS and Electronic Nose

techniques, the most significant compounds of the different samples were identified, observing many differences in the chromatogram and in the PCA score plots obtained from the Electronic Nose. In particular, the butanoic acid compounds and derivatives were found to characterize especially the Ireland grated sample.

This sample presented different levels of those compounds in comparison to the other samples. It is more abundant in propanoic acid, butanoic acid and derivatives, tridecyl-3-butyric acid ester and acetic acid phenylmethyl ester.

These compounds are typical for the Cheddar cheese, therefore the Irish sample could have possessed a small percentage of real Parmigiano but for the most part, it seems to have been mixed with the Cheddar. The German samples are very different from the true Parmigiano; little analogies may be found with the crust as confirmed by the PCA provided by the Electronic Nose [15].

They could probably contain Emmental or Camembert cheese as confirmed by the comparison with the published literature. The Latvian sample is the only one to get closer to the true profile. It, in fact, presents the typical compounds of Parmigiano both from the pulp and the crust.

S3 device is a promising tool for the quality discrimination of different cheeses and other foodstuffs. This ability to distinguish cheese quality by an easy-to-use, rapid, economic, portable, non-destructive and low power consumption S3 device is crucial as it can be utilized to validate if a given sample is according to the law and standards in order to assess the fraudulent or imitative production.

The nanowire based S3 Electronic Nose represents a simple, fast, economic and portable tool for the quality control and authenticity evaluation of grated PR cheese.

In our future works, we propose to illustrate an amplified database of the grated PR for the direct application of S3 in the cheese-chain productions and also to perform a data fusion by integrating different results for a deeper analysis.

References

1. Consorzio del Parmigiano-Reggiano. Disciplinare di produzione del formaggio parmigiano reggiano, standard di produzione del formaggio. Consorzio Parmigiano Reggiano (2003)
2. M.T.S.R. Gomes, Electronic nose in diary products, in *Electronic Noses and Tongues in Food Science* (2016), pp. 21–30
3. S. Benedetti, N. Sinelli, S. Buratti, M. Riva, Shelf life of crescenza cheese as measured by electronic nose. J. Dairy Sci. **88**, 3044–3051 (2005)
4. J. Thihaas, L. Vognsen, P.V. Nielsen, Electronic nose: new tool in modelling the riperning of Danish blue cheese. Int. Dairy J. **15**, 679–691 (2005)
5. C. Cevoli, L. Ragni, A. Gori, A. Berardinelli, M.F. Caboni, Quality parameter assessment of grated Parmigiano-Reggiano cheese by waveguide spectroscopy. J. Food Eng. **113**, 20–209 (2012)
6. G. Sberveglieri, G. Faglia, S. Groppelli, P. Nelli, A. Camanzi, A new technique for growing large surface-area SnO_2 thin-film (RGTO technique). Semicond. Sci. Technol. **5**(12), 123–1233 (1990)
7. G. Sberveglieri, I. Concina, E. Comini, M. Falasconi, M. Ferroni, V. Sberveglieri, Synthesis and integration of tin oxide nanowires into an electronic nose. Vacuum **86**(5), 532–535 (2012)

8. V. Sberveglieri, E. Núñez Carmona, A. Pulvirenti, Detection of microorganism in water and different food matrix by electronic nose, in *Sensing Technology: Current Status and Future Trends III* (Springer International Publishing, 2015), pp. 243–258
9. M. Vezzoli, A. Ponzoni, M. Pardo, M. Falasconi, G. Faglia, G. Sberveglieri, Exploratory data analysis for industrial safety application. Sensors Actuators B: Chem. **131**(1), 100–109 (2008)
10. V. Gobbi, M. Falasconi, G. Zambotti, V. Sberveglieri, A. Pulvirenti, G. Sberveglieri, Rapid diagnosis of Enterobacteriaceae in vegetable soups by a metal oxide sensor based. Sensors Actuators B: Chem. **207**, 1104–1113 (2015)
11. V. Sberveglieri, E. Núñez Carmona, A. Pulvirenti, Nanowire sensor array for the rapid quality control on grated Parmigiano Reggiano, in *IEEE Xplore Digital Library, XVIII AISEM Annual Conference* 2015 (in press)
12. E. Meinhart, P. Schreier, Study of flavour compounds from Parmigiano Reggiano cheese. Milchwissenschaft **1**, 689–691 (1986)
13. Group, T. e F. 'Dictionary of food compounds'. CRC Press, II Edition, 2013
14. D.C. Frank, C.M. Owen, J. Patterson, Solid phase microextraction (SPME) combined with gas-chromatography and olfactometry-mass spectrometry for characterization of cheese aroma compounds. Food Sci. Technol. **37**(2), 139–154 (2004)
15. V. Sberveglieri, Validation of Parmigiano Reggiano cheese aroma authenticity, categorized through the use of an array of semiconductors nanowire device (S3). Matherials **9**, 1–81 (2016)

Lard Detection in Edible Oil Using Dielectric Spectroscopy

Masyitah Amat Sairin, Samsuzana Abd Aziz, Nina Naquiah Ahmad Nizar, Nurul Adilah Abdul Latiff, Alyani Ismail, Dzulkifly Mat Hashim and Fakhrul Zaman Rokhani

Abstract Food adulteration is the process of adding or mixing of substance(s) that should not be into food products for financial gain or other motives. Food adulteration is a serious problem worldwide not just because it is a fraud to consumer, but it can also harm the health and causes serious consequences to the well being of people. Among the food products, edible oil has been identified as the top ingredient involved in food fraud. Studies show that adulteration in fats and oils are mainly economically motivated and in some cases intended to enhance food flavor. In general, adulteration of edible oil causes two great concerns to the consumer. First, it concerns consumers that practice vegetarian diet or followers of religions that prohibit from consuming pig, pork or any of its products. Second, it may cause serious health related issues particularly those who have allergies to certain types of substances or consumers who suffer coronary disease. Several conventional techniques have been utilized in order to study food adulteration particularly on fats and oil, such as polymerase chain reaction, differential scanning calorimetry, electronic nose and chromatography. Until recently, dielectric spectroscopy technique that have been widely used to analyze food products, attain research community's attention in the study of adulteration on fats and oil. In this chapter, a review on conventional techniques and dielectric spectroscopy approach for analyzing food products are presented. In particular, a review on dielectric spectroscopy to study adulteration in fats and oils and recent work on lard detection at both low and high frequency range are discussed. Results show that dielectric sensing can be a great technology to detect lard adulterated edible oil and applying data analysis technique can further enhance the detection ability.

M.A. Sairin (✉) · N.N.A. Nizar · A. Ismail · D.M. Hashim · F.Z. Rokhani (✉)
Halal Product Research Institute, Universiti Putra Malaysia, Seri Kembangan, Malaysia
e-mail: masyitahamatsairin@gmail.com

F.Z. Rokhani
e-mail: fzr@upm.edu.my

M.A. Sairin · S.A. Aziz · N.A.A. Latiff · A. Ismail · F.Z. Rokhani
Faculty of Engineering, Universiti Putra Malaysia, Seri Kembangan, Malaysia

S. Mukhopadhyay et al. (eds.), *Sensors for Everyday Life*, Smart Sensors, Measurement and Instrumentation 23, DOI 10.1007/978-3-319-47322-2_12

1 Introduction

Food fraud is a collective term to explain the intentional substitution, addition, tampering or misrepresentation of food, food ingredients, or food packaging [1]. Food fraud can be in the form of adulteration, tampering, over-run, theft, diversion, simulation and counterfeiting. Among the food-related risk, food fraud is highly economically motivated and can cause public fear and possibly lowering the price of product industry-wide [2]. Adulteration is the process of adding or mixing of substances which should not be contained within other substances for legal or other reasons [3]. It can be further breakdown into several types which includes substitution or dilution, unapproved additive, counterfeit, mislabeling, transshipment or origin masking and intentional distribution of potential hazardous materials [2].

Oil is a food product that has been consumed widely throughout the years for baking, frying and in other food preparations like in salad dressing, condiments, flavorings and confectioneries [4, 5]. Edible oil can come from both plant and animal sources. Examples of plant-based edible oils mostly comes from coconut, palm kernel, palm, soya bean, groundnut, cottonseed, linseed, sunflower, rapeseed, olive and sesame [6] while animal-based fats or oils can come from livestock (such as cattle, mutton, pigs), poultry (such as chicken, duck and goose) and fish [7]. Food industries that produce food products like spreads, butter, ghee, margarine, baking fats and shortenings, frying oils and fats, salad oils, mayonnaise, salad cream, salad dressing, chocolate and confectionery, ice cream and dairy products are the major industries that used fat and oil in their food preparation [8]. Examples of the major industries include fast food chains and bakeries that use tons of oil for frying chicken and fast food products and infused oil or fats into shortenings and moistening agents, respectively.

Among food products categories, edible oil has been identified as the top ingredient involved in food fraud adulterated for economic motivated reason as shown in Fig. 1 [2]. Report indicates oils, among other food categories, are the most reported type of food fraud.

In the food industry, technically, food manufacturers adulterate oil with other substances for the purpose of increasing the apparent value of the product or lowering the cost of its production [2, 9, 10]. In [11, 12], some refineries spike olive oil with cheaper oil while other refineries mix vegetable oils with natural food coloring (i.e. beta-carotene and chlorophyll) to give the look of green-gold color of olive oil and misbranded them as a fake olive oil. In 1993, the Food and Drug Administration (FDA) ordered a recall of Rubino U.S.A. Inc., (Cincinnati, Ohio) olive oils which were from pure canola oil [13]. In 2013, Greek police made several arrests on suspects that are accused of trying to sell soybean oil mixed with colorants as extra virgin olive oil [14]. In 2014, Wei Chuan Foods Corp. in Taiwan was accused of blending oil made from unsold pork scraps with an illegal substance —'gutter oil', and sold them as cooking oil [15]. Other than economically motivated purpose, oil adulteration can serve the purpose of inducing more desirable flavors and texture in food [16].

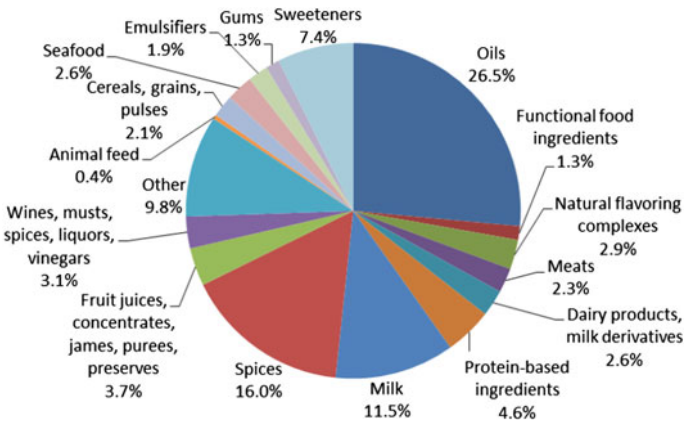

Fig. 1 Breakdown of food fraud being reported based on food ingredient category [2]

Figure 2, shows the breakdown of the world consumption for major fats and oils in 2015 as reported by IHS Inc [17]. It can be observed that animal-based fats and oils such butter, lard, tallow and grease ranked fourth most consumed fats and oil globally [17]. According to [16], animal fats were used immensely for domestic frying due to the desirable flavors they impart on some foods. For example, tallow and lard was added to french-fried potatoes and pie-crusts respectively, to enhance the flavor. In addition, animal fats are used as ingredient in the formulation of food products such as breads and cakes due to exhibiting good stability and economical [16, 18]. While both genuine and industrially-modified randomized lard are commercially available [19], they are also used to blend with vegetable oils to produce cost-effective margarines, shortenings and other oil-based foods [20].

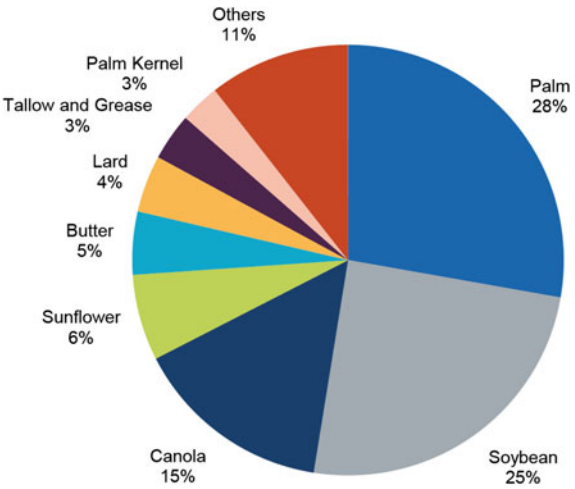

Fig. 2 Breakdown of world consumption of major fats and oil in 2015 [17]

In general, adulteration of edible oil causes two great concerns to the consumer. First, animal-based fats and oils adulteration in edible oil present great concern to followers of vegetarian diet such as Hindus or Buddhist [21]. In particular, lard adulteration prompt concern to followers of Islamic and Judaism religions as both religions prohibit the consumption of lard and pork [22, 23]. Several reported cases include shortening, butter, margarine and other specialty food oils made of vegetable oils blended with lard or tallow [24, 25], goat and pig body fat detected in vegetable ghee and cow/buffalo ghee respectively [26, 27] and recently, sunflower oil contaminated with chicken fat [28].

Second, health issues concern, which can be very vital to people who have allergies to a certain types of food as well as the relationship of dietary cholesterol and saturated fatty acid to coronary heart disease [29]. In 1997, European Commission reported that around 103,400 tonnes of olive oil adulterated with estimated 20,680 tonnes of hazelnut oil were to be placed on the market [30]. The presence of nut oils could cause complication for people with food allergies to nuts [2]. In [31], non-optimal intakes of polyunsaturated fat, trans fat and saturated fat each contribute to significant coronary heart disease.

It is clear that there is high dependency of consumers throughout the world to oils and fats. With the vast consumption of oils and fats, greedy manufacturers attempted to reap profits by illicitly adulterating original oils with alternative substances leading to numbers of food fraud cases. While in certain cases oil adulteration is intended to enhance food flavor or give stability as ingredient, these may cause serious health related issues or unable to be consumed by certain group of people. Thus, concern in adulteration in oils and fat should not be taken lightly or ignored. It is crucial to develop a verification system that can distinguish adulterated edible oils to combat food fraud. This thus can induce a healthier and safer eating lifestyle among the citizen of all ages, races and religions.

1.1 Conventional Techniques in Lard Detection

In the recent past, a number of verification techniques in differentiating and detecting lard in food products have been introduced. These methods can be categorized into two groups, which are labeling-based technology and spectral-based technology. Labeling-based technology includes polymerase chain reaction (PCR) techniques while spectral-based technology includes differential scanning calorimetry (DSC), electronic nose (E-Nose), gas chromatography, liquid chromatography and spectroscopy. Note that in the following examples, we also discussed the application of techniques used on pork as a derivative from pig aside from lard.

Labeling-based technology is a technique in lard detection that labels the sample with the observation of DNAs presence in them. PCR method has been used to analyze raw meats and fats of pigs and the identification of pork derivatives in food products like sausages, bread and biscuits [32, 33].

Spectral-based technology is the study of the interaction of electromagnetic radiation (EMR) with atoms and molecules to provide qualitative and quantitative chemical and physical information that is contained within the wavelength or frequency spectrum of energy that is either absorbed or emitted [34, 35]. Spectral-based technology in lard detection can be broken down into three categories namely DSC, chromatography and spectroscopy.

DSC is a thermoanalytical technique where the measurement of the change of the difference in temperature between the sample and the reference sample while they are subjected to a controlled temperature program [36]. DSC have been used in the study to detect lard and randomized lard as adulterant in palm oil in [37], to detect animal the presence of adulterated animal fat, i.e., chicken fat, in butter [38] and in the detection of lard in beef tallow and chicken fat [39].

Chromatography is a study of formation, change and movement of analyte chemical compounds of a studied sample in a flow of mobile phase with respect to solid or liquid stationary phases or particles [40]. Chromatography techniques can be further classified into gas chromatography and liquid chromatography. One example of gas chromatography is E-Nose. E-Nose has been used to analyze the aroma of food products such as cooked chicken meat, stored oysters, processed cheese and evaporated milk, stored vegetable oils, chocolates, edible oils, milk, honey, fruit, wheat, tea, corn and coffee [41]. While in the study of detection of lard adulteration in RBD palm olein, a detection limit of 1 % of lard in refined, bleached, deodorized (RBD) palm olein was achieved [42]. Another example of gas chromatography is gas chromatography mass spectrometry (GCMS). An investigation used GCMS coupled with elemental analyzer-isotope ratio mass spectrometry (EA-IRMS) to differentiate lard from chicken fat, beef fat and mutton fat [43]. Another study used different types of gas chromatography, a gas chromatography-flame ionization detector (GC-FID) to differentiate lard from other edible fats which are chicken and beef [44]. In [45], a gas chromatography hyphenated with time-of-flight (GC-ToF) mass spectrometry is used to detect lard by comparing the fatty acids profile with other animal fats like chicken, cattle and goat [45]. The study identified three fatty acid biomarker belonging specifically only to lard namely methyl trans-9, 12, 15-octadecatrienoate (C18:3 n3t), methyl 11, 14, 17-eicosatrienoate (C20:3 n3t) and methyl 11, 14-eicosadienoate (C20:2 n6). These fatty acid methyl ester (FAME) profiles could be used as a basis or biomarker to discriminate lard from other animal fats in food authentication process. An example of liquid chromatography is high-performance liquid chromatography (HPLC) that has been used to distinguish lard from other animal fats in admixtures of some vegetable oils [46].

Lastly, spectroscopy techniques utilize the electromagnetic radiation in obtaining electrical properties of the materials. Fourier transform infrared (FTIR) spectroscopy is one of the earliest lard detection technologies and it measures the electromagnetic absorption or emission of the material in an infrared spectrum. A number of investigations on lard detection using FTIR spectroscopy have been recorded, which analyze the potential of lard adulteration in chocolate and chocolate products [10], pork adulteration in beef meatball [47], lard adulteration in

Table 1 Summary of conventional techniques used in lard detection on several types of samples with different detection limit, and spectrum measured

Category	Techniques	Detection limit	Spectrum measured	Sample
Labeling-based	PCR	–	–	Raw meats and fats [32]
		–	–	Pork derivatives in sausages and the casings, bread and biscuits [33]
Spectral-based	Electronic Nose	1.0 %	Volatile compounds spectrum	RBD palm olein adulterated with lard [42]
	DSC	0.5 %	Thermal spectrum	Beef fat and chicken fat adulterated with lard [37]
	GCMS & EA-IRMS	–	Mass spectrum	Lard, chicken fat, beef fat and mutton fat [43]
	GCFID	0.5 %	Ion intensity spectrum	Beef fat and chicken fat adulterated with lard [44]
	GC-TOF-MS	–	Mass spectrum	Chicken fat, lard, goat fat and cattle fat [45]
	Liquid chromatography	2.0 %	Mass spectrum	Palm oil, palm kernel oil and canola oil adulterated with lard, beef tallow and chicken fat [46]
	FTIR	4.0 %[a]	Absorbance spectrum	Lard adulteration in chocolate and chocolate products [10]
		1.0 %[a]		Pork adulteration in beef meatball [47]
		1.0 %[a]		Cod-liver oil adulterated with lard [48]
		17.0 %[a]		Lard adulteration in cake formulation [49]
		1.0 %		Lard blended with mutton and cow body fats [50]
		10.0 %		Lard mixed with body fats of chicken, lamb and cow [51]
		–		Lard, beef, chicken and mutton fats, cod liver oil and other vegetable oil [20]

[a]assumed based on the lowest lard adulteration concentration investigated

cod-liver oil [48], lard adulteration in cake formulation [49], lard in mixture of body fats of mutton, cow and chicken [50, 51] and to differentiate lard from other edible oil [20]. Generally, these studies utilize the frequency region of 4000 cm^{-1} until 650 cm^{-1} which lies in the infrared spectrum of frequency. Table 1 summarizes all of the techniques that have been discussed with their respective samples.

1.2 Data Analysis in Lard Detection Approach

Aside from the data collected from measurements techniques discussed in previous topic, data analysis is important to enhance the detection ability. The main goal of this data analysis is to represent sample's data in a way that the differentiation between samples is significantly distinct.

Several examples of data analysis techniques that have been used in previous studies are partial least squares (PLS), discriminant analysis, principal component analysis (PCA), cluster analysis (CA), stepwise multiple linear regression (SMLR), least significant differences (LSD), analysis of variance (ANOVA), linear regression analysis, and Pearson's correlation analysis. Other statistical analysis techniques include mean difference (MD), standard deviation (SD), standard error (SE) and t-test. Some studies used one analysis technique while others used multiple analysis techniques at different stages during the data analysis process. Table 2 summarizes the different types of data analysis techniques and their respective functions.

As an example, a study to analyze the adulteration of lard in cod-liver oil utilized the PLS technique to develop a calibration model for quantitative measurement of

Table 2 Summary Of Data Analysis Techniques Used In Lard Detection

Category	Examples of data analysis techniques	Concept
Hypothesis testing	Analysis of variance (ANOVA)	Analyze variability in data in order to infer the inequality among population means [52]
	Pearson's correlation analysis	Measure the relation strength of two linear variable [53]
	T-test	Comparison two population means [54]
Clustering	Discriminant analysis	Determine which continuous variables discriminate between two or more naturally occurring groups [55]
	Principal component analysis (PCA)	Identify patterns in data, and expressing the data in such a way as to highlight their similarities and difference [56]
	Cluster analysis (CA)	Divides data into groups (clusters) that are meaningful, useful or both [57]
Modeling regression	Linear regression analysis	Predict scores on one variable from the scores of another variable [58]
	Partial least squares regression (PLS)	Constructing predictive models when the factors are many and highly collinear [59]
	Stepwise regression	Regressing multiple variables while simultaneously removing those that aren't important [60]
Validation	Mean difference (MD)	Measure variability [58]
	Standard deviation (SD)	
	Standard error (SE)	

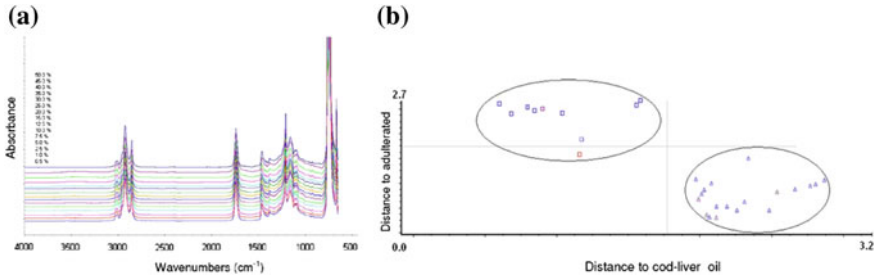

Fig. 3 **a** FTIR spectra of cod-liver oil adulterated with lard at different concentrations and **b** Coomans plot of pure cod-liver oil (*squares*) and cod-liver oil spiked with different proportion of lard (*triangles*) [48]

the adulterant, together with discriminant analysis method to classify cod-liver oil samples from other animal fats, beef, chicken, mutton and lard. Figure 3 shows the Coomans plot obtained from the discriminant analysis for the classification of pure cod-liver oil and the ones spiked with lard. From the plot, it is observed that there is clear group separation between pure cod-liver oil (squares) and the one that is spiked with lard (triangles). Other than that, the values of root mean standard error of cross validation (RMSECV) and coefficient of determination (R^2) were used as the validity criteria for the calibration model. The validation was further investigated using the MD and standard deviation of difference (SDD) for accuracy and reproducibility.

In this case, PLS is successfully used to detect the level of adulterant and discriminant analysis allows one to make a classification of cod-liver oil and potential adulterants of animal oils.

Figure 3a shows the data of FTIR spectra for different samples before data analysis was applied. Through naked eye, it is challenging to analyze, let alone to be able to detect the lard adulterated samples. A Coomans plot after discriminant analysis is applied in Fig. 3b showing the clear separation of lard adulterated with the original samples, thus enhance the detection ability. Multiple data analysis will not only enhance detection by developing a regression model but can also provide different information about the data collected from measurements like the accuracy, repeatability, significance difference among the samples by hypothesis testing and many more [61].

2 Dielectric Spectroscopy

A dielectric material is materials that are neither conductors nor insulators that can be polarized by an applied electric field [62]. A dielectric material does not have loosely bound electrons like a conductor material. When a dielectric material is

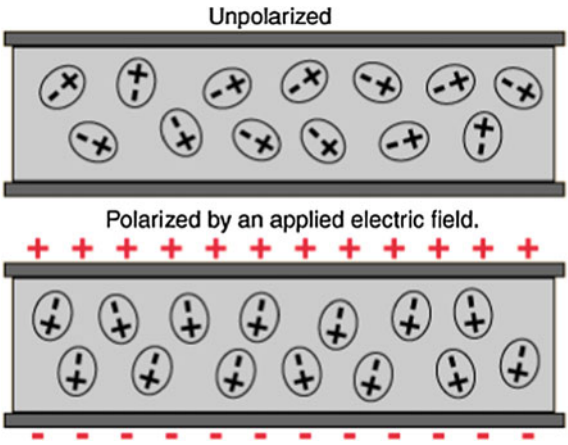

Fig. 4 The conditions of the molecule inside dielectric material when unpolarized and polarized by an applied electric field [67]

placed in an electric field, electric charges in the material slightly shift from their average equilibrium position. This cause a phenomenon called polarization, in which the positive charges was displaced towards the electric field, while negative charges shift on the opposite direction as illustrated in Fig. 4 [63]. The polarization creates internal electric field that reduces the overall field within and increases the capacitance. Dielectric spectroscopy or spectral permittivity is the measure of the ability of the material to resist (resistance) or store (capacitance) the electric field created [64]. Dielectric constant also known as relative permittivity is the permittivity of the material in relative to that of free space [65, 66].

According to [68], the dielectric parameter (Ɛ) can be calculated from the following equation

$$\varepsilon_r = \left(\frac{C_p}{C_0} - j\frac{1}{\omega C_0 R_p}\right) \tag{1}$$

where, ε_r is the complex permittivity, C_p is the capacitance of the material, C_0 is the capacitance of free space, R_p is the equivalent parallel resistance, ω is the angular frequency; $\omega = 2\pi f$ and f is the frequency.

ε_r of a dielectric material consists of two parts, a real part and an imaginary part as shown in Eq. (2). The real part, called dielectric constant, ε'_r, relates to the ability of the material to store electromagnetic energy (capacitance) and the imaginary part, called loss factor, ε''_r, relates to the ability of the material to resist the electric field, thus dissipates heat [62]:

$$\varepsilon_r = \varepsilon_r^{'} - \varepsilon_r^{''} \tag{2}$$

where, ε'_r is the relative dielectric constant and ε''_r is the dielectric loss.

Thus, dielectric constant can be defined as the ratio between the capacitance of the dielectric material, C_p, with the capacitance of that in free space or vacuum, C_0, as shown in Eq. (3) below:

$$\varepsilon_r = \frac{C_p}{C_0} \tag{3}$$

2.1 Measurement Principles

There are a number of methods available for dielectric measurement. According to [69], the methods relevant for any desired application depend on the nature of the dielectric material to be measured, both physically and electrically. This means a few variables should be taken into consideration to use a suitable method such as, the state of the material (i.e. solid, liquid or semisolid), the melting or boiling point of the material, the frequency of interest and the degree of accuracy required. A specific sample holder or probe design also plays an important part to justify with the nature of the material. The methods for dielectric property measurement include waveguide and coaxial transmission line methods [70, 71], short-circuited line technique [72, 73], open-ended probe technique [74, 75], time domain reflectometry (TDR) method [76], free-space transmission technique [77], microstrip transmission line [78], six-port reflectometer using an open-ended coaxial probe [79], colloid dielectric probe [80], test cell with Boonton RX-meter [81] and cavity perturbation technique [82]. Dielectric property measurement techniques is used in wide applications and materials includes; food and agriculture [83–85], biological tissues [86], wood and fibrous materials [87], resin and plastics [70, 88], ceramics [70, 89] and also soils and minerals [90].

2.2 Factors Influencing Dielectric Spectroscopy Measurement

Being a spectroscopy method, which relate the interaction of electromagnetic radiation with atoms or molecules [34, 35], dielectric spectroscopy depended on the nature of the atoms or molecule itself. This includes the characteristics of the material itself, i.e. dipole and ionic characteristics, and the behavior it possess upon external influences. The behavior of material's molecule is influenced by the frequency of the electric field introduced, temperature and moisture of the material. These factors affecting the measurement of dielectric spectroscopy will be discussed in this section below.

2.2.1 Frequency Dependence

Frequency dependence of dielectric properties of food relates the polarization of the molecules with the electromagnetic field. According to [69], the frequency dependence of the dielectric properties comes from the frequency dependence of dipolar and ionic food materials.

At low frequency, dipoles are able to follow the variations of the applied field, while at a very high frequency; the dipoles are unable to follow the rapid field reversal leading to higher and lower dielectric constant, respectively. Thus, in most of the dielectric measurements on dipolar food materials showed gradual decrease with frequency. Dipolar food materials can be in the form of polar or non-polar in which the molecules in the former have permanent dipole moment and the latter do not. For example, pure water, a very polar compound has a very high value of dielectric of 80.2, while that of oil, a non-polar compound, has a lower dielectric value of within 0–3 [69].

In ionic food materials, typical ionic compound like salt (i.e. NaCl) reduces the dielectric constant and increased the dielectric loss factor when compared to dipolar food material [91]. The reduction of ε'_r and increase in ε''_r is due to the binding of free water molecules by counter-ions and the addition of conductive charge carriers of dissolved salts, respectively.

2.2.2 Temperature Dependence

Temperature dependence also relates with the polarization of the molecules with the electromagnetic field in terms of viscosity and water phases of the food material. At low temperature, high viscosity leads to longer relaxation time and little dipole rotation and thus results in low dielectric constant [69, 92]. More on this will be discussed in the next section.

While in food materials with high water content, the dielectric constant highly dependent on the phase of the water in the food. Figure 5 illustrate the temperature dependence of dielectric value for various food materials from freezing to melting state [93]. The dielectric value of all the food materials experience abrupt change from very low to very high at around the melting point temperature of –5 to 0 °C, suggesting that no free water molecule is present during freezing and otherwise during melting. As temperature increases, the dielectric constant reduces following dielectric profile of water.

2.2.3 Moisture Dependence

Moisture content is one of the major influences in dielectric properties of food materials due to water is a polar compound and can easily absorb energy [69].

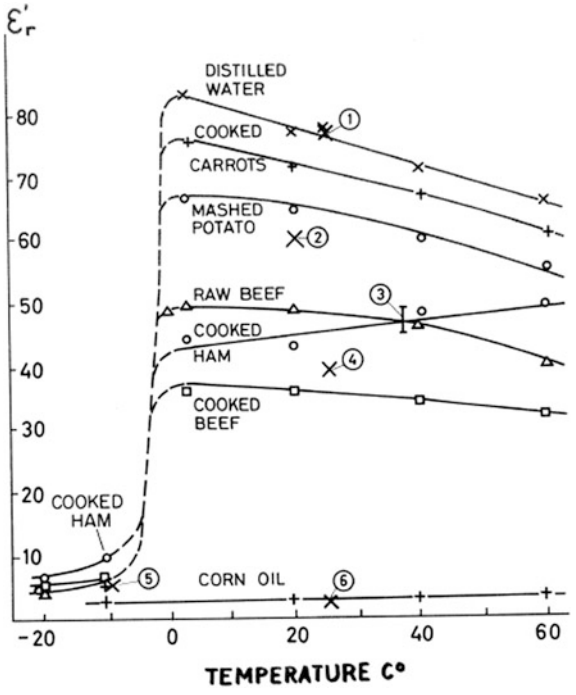

Fig. 5 Temperature dependence of dielectric value for various food substance at 2.8 GHz [93]

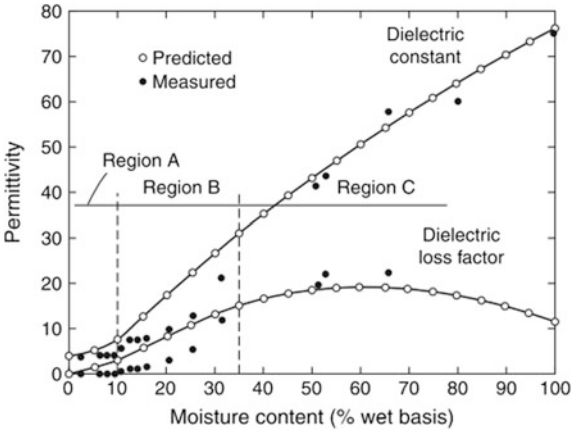

Fig. 6 Effect of moisture content on dielectric constant and loss factor in freeze-dried potato at 3 GHz [94]

Increase in moisture content increases the polarization, result in increase in dielectric constant and loss factor [69]. Figure 6 showed the effects of increase moisture content on the increase of both dielectric constant and loss factor of freeze-dried potato [94].

2.3 Dielectric Spectroscopy on Food Products

Dielectric spectroscopy has been applied to variety of agriculture and food products. The understanding of dielectric properties of food products becomes increasingly important for consistent and predictable product, process and equipment development [69]. Dielectric spectroscopy has been used to analyze and characterize fruits and vegetables, meat and seafood, milk and dairy products, oil and many more.

In [84], a study on the frequency dependence of the dielectric constant and loss factor of fresh fruits using a network analyzer in the range from 200 MHz to 20 GHz was conducted. The study also explored the possibility of sensing the maturity of fresh peaches. Investigation in [85] suggests that higher moisture content in fruit results in slightly higher dielectric constant, and decreased in dielectric constant with the increased of temperature or frequencies, for most fruits.

In [95], the permittivity and conductivity of various beef and chicken were measured within the frequency range of 1 Hz–1 MHz. The work observes the differences in fresh raw meat of commercially purchased with that after being cooked in microwave. Raw meat showed higher dielectric constant measurements than cooked meat, potentially due to high moisture content in raw meat.

A study on milk and dairy product in [96], investigated the dielectric properties of UHT skim, low fat and homogenized whole milk. The study concludes that the dielectric constant for all types of milk are close together in the high frequency region of 1–10 GHz, and display larger differences at lower frequency range. Figure 7 illustrate the dielectric constant of whole milk, low fat milk, skim milk and water at frequency range from 1–10 GHz. It can be observed that water gives the

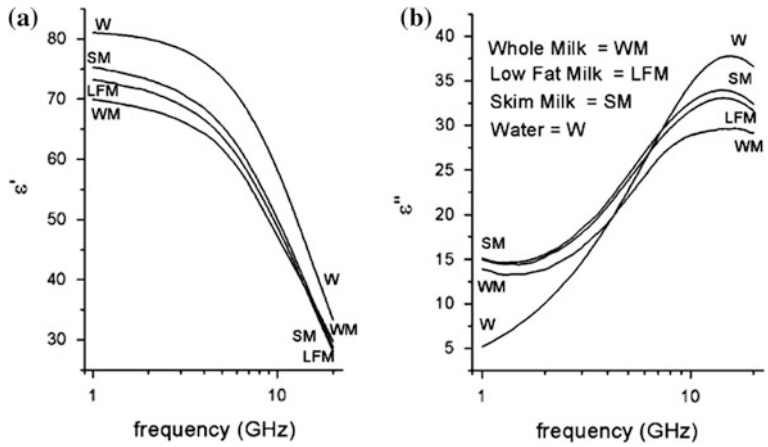

Fig. 7 Dielectric constant profile for whole milk, low fat milk, skim milk and comparison with water [96]

highest dielectric constant due to highest water content as compared to milk products. In addition, skim milk has higher water content than low fat and whole milk based on the dielectric constant profile.

2.4 Dielectric Spectroscopy on Oil and Fats

Several works have been reported on the usage of dielectric spectroscopy to study the dielectric properties of oils and fats. A research group from Japan investigated on discriminating olive oil adulterated with vegetable oil in the frequency range of 101 Hz–1 MHz [97]. The olive oil is spiked with other vegetable oils, soy, corn, canola, sesame and perilla oils with different concentration from 0 to 100 %. Figure 8 shows a PCA score plot for soy oil and perilla oil adulterated in olive oil, respectively. Leveraging on data analysis technique, the adulterated oil can be easily detected from the original oil as can be observed in Fig. 8.

A study edible oils and fatty acids as a function of frequency, temperature, moisture and composition has been reported in [92]. In this study, 10 edible oils and 6 fatty acids were used and the dielectric properties were measured over the frequency range 100 Hz–1 MHz. The effects of temperature (20–45 °C), moisture content (0.02–0.31 %), and fatty acid component on dielectric properties of oils were investigated. From the investigation, it can be concluded that the dielectric constant of oils affected by their fatty acid composition significantly, the dielectric constant of the oils increased with increasing moisture content, this effect diminished as frequency increases, and both dielectric constant and loss factor of edible oils demonstrated a gradual decrease with increasing temperature, as well as the dielectric constant of fatty acids.

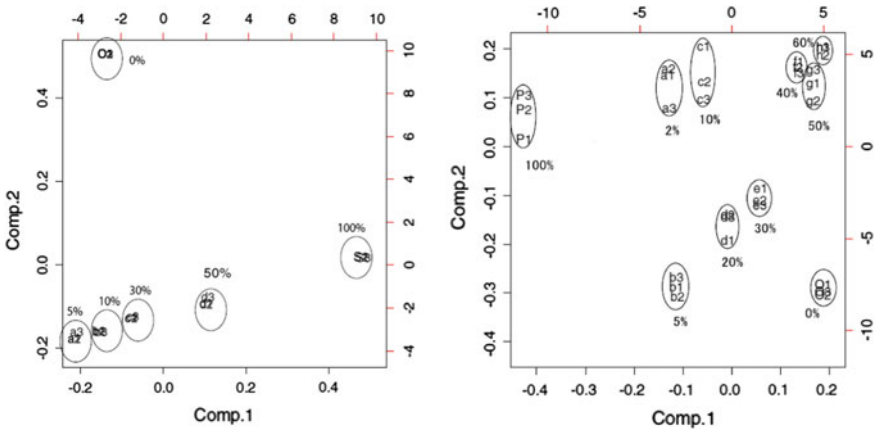

Fig. 8 PCA score plot for different concentration of soy oil in olive oil (*left*) and PCA score plot for different concentration of perilla oil in olive oil [97]

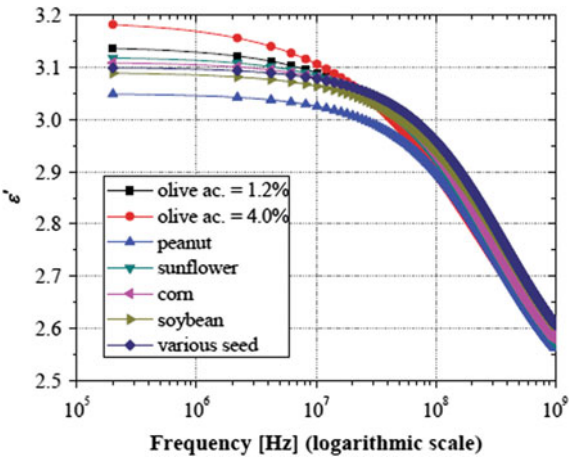

Fig. 9 Dielectric constant of the seven types of oil [99]

Another investigation on studying the dielectric properties of different varieties of rapeseed-mustard oil at different temperature [98]. The study suggests that the dielectric properties of rapeseed-mustard oil show dependence on different percentage of erucic acid content.

In [99], dielectric spectroscopy is used to study quality control of vegetable oil. This study observe a specific frequency ranges in which the permittivity of the different vegetable oils; olive, peanut, sunflower, corn, soybean and various seeds, can be discriminated. Figure 9 shows the dielectric constant of the seven different types of vegetable oil in the frequency range of 0.2–100 MHz. Table 3 summarizes previous dielectric spectroscopy studies and the frequency range used in the investigation.

2.4.1 Frequency Dependence in Oils and Fats

In most oil and fats, different frequencies result in little changes in the dielectric constant. Figure 10 shows the dielectric values dependency on frequencies for different fatty acids (i.e. caprylic, linolenic, linoleic, oleic, palmitic and stearic) and also of a few vegetable oils (i.e., sesame, soy, corn, canola, olive, safflower and

Table 3 Summary of previous studies on dielectric spectroscopy for oils and fats

Study	Sample	Frequency
Bansal (2001)	Rapeseed-mustard oil	100 kHz–8.93 GHz
Inoue (2002)	Soybean oil	1 kHz–100 kHz, 50 kHz–30 MHz
Lizhi (2008)	Vegetable oil & fatty acids	100 Hz–1 MHz
Cataldo (2009)	Vegetable oil	100 kHz–1 GHz
Lizhi (2010)	Olive oil adulterated with other vegetable oil	100 Hz–1 MHz

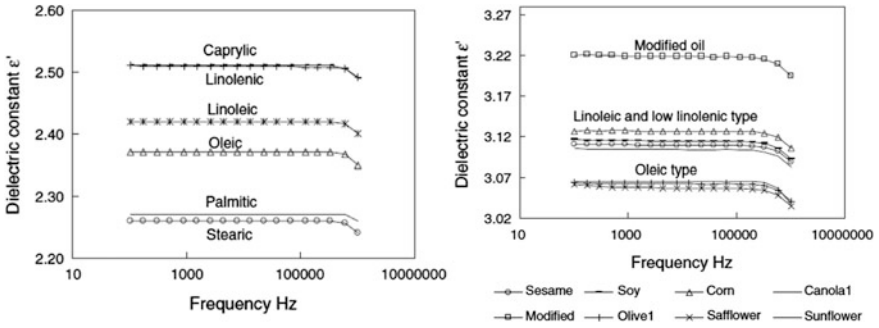

Fig. 10 Spectra of dielectric constant of saturated and unsaturated fatty acids at 75 °C (*left*) and of various oils at 25 °C (*right*) [92]

sunflower) [92]. It is explained that the dielectric spectra indicated general plateau and maximum value in frequency range between 100 Hz and 500 kHz suggesting that there exist equilibrium among the orientation of oil molecule and the electric field at low frequencies. At higher frequency, the dielectric spectrum is observed to decrease gradually. This is explained in [69] that at higher frequency, the dipoles are not reacting to the electric field as they are unable to follow the rapid field reversal.

2.4.2 Temperature Dependence in Oils and Fats

In [92], effects of temperature range between 20–45 °C were investigated. Figure 11 illustrate the effect of temperature on dielectric constant and loss factor of soybean oil. It can be observe from Fig. 11 that both dielectric constant and loss factor demonstrated a gradual decrease with increasing temperature.

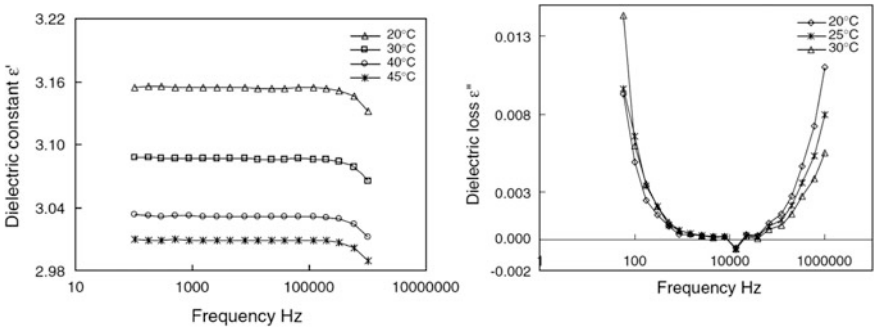

Fig. 11 Effect of temperature on dielectric constant (*left*) and loss factor (*right*) of soybean oil [92]

According to [90], at low temperature, high internal viscosity leads to longer relaxation time and little dipole orientation, thus result in low values of dielectric constant. As the temperature increased, the viscosity decrease causing the decrease of relaxation time and increase in dipole moment, thus decreasing the dielectric constant. This pattern can be observed for most of study on dielectric properties on food materials.

2.4.3 Moisture Dependence in Oils and Fats

Work in [92] also studied the effect of moisture on dielectric constant. The oil moisture content ranges from 0.02 to 0.31 % (w/w), was determined in accordance with Air Oven Method $1.4.1_{-2013}$ [100]. Figure 12 shows the effect of moisture content on dielectric constant of corn oil. As discussed earlier, water is a polar molecule with higher dielectric constant than water, thus lead to increase of dielectric constant with increasing moisture content [69].

3 Dielectric Spectroscopy for Lard Detection

The major animal fats, also termed meat fats, traded world-wide are produced from pigs (*Sus scrofa*), termed as lard or rendered pork fat, from cattle (*Bos Taurus*) or sheep (*Ovis aries*) termed tallow, and from poultry, primarily chickens (*Gallus gallus*) termed as poultry fat. Tallow from domestic cattle is known as beef tallow, whereas that from sheep is termed mutton tallow. "Acylglycerol" is the primary component of animal lipids, which may exist as either fat or oils. At room temperature, 24 °C, the former are primarily solid and the latter are liquid [16].

Lard is the fat rendered from fresh, uncontaminated, healthy fatty tissues from the meat of sound swine (Sus scrofa) at the time of slaughter, and hence, fit for

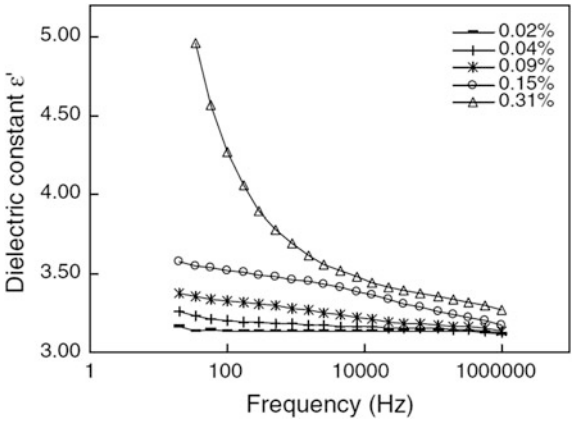

Fig. 12 Effect of moisture content on dielectric constant of corn oil at different frequencies [92]

human consumption. It is also imperative that the fat is pure and without the presence of bones, isolated skin, blood or any other viscera. Edible tallow (dripping), on the other hand, is the product obtained by rendering the clean, sound fatty tissues, including trimming and cutting fat, attendant muscles and bones of bovine and/or sheep in good health at the time of slaughter and fit for human consumption [101].

In our recent study, sample of animal fats which are lard, beef tallow, mutton tallow and chicken fat were extracted by rendering of adipose tissue of animals collected from local slaughter houses and market according to the method proposed by [37]. The rendering was done at 90–100 °C for two hours in the oven. The extracted fats was filtered through double-folded muslin cloth and dried over anhydrous sodium sulphate (Na2SO4) to remove residual moisture through filter paper. The filtered samples were stored in a freezer at –20 °C before further analysis. Before being used for analysis, all animal fats were thawed at 60 °C until they melted. As some of the animal fats are in solid form at room temperature, a solvent is needed for uniform sampling. Hexane is used as a standard oil-based solvent. Polar solvent dissolve polar compound, while non-polar solvents dissolve non-polar compounds [102]. As oil and fats are non-polar compounds, non-polar solvents are needed [103]. Common extraction solvents include hexane, methylene chloride, methy isobuthyl ketone (MIBK) and xylene [102]. Thus, the concentrations mentioned in the discussion of dielectric spectroscopy would indicate the concentration of each fat and oil in hexane.

Two works has been done for the lard detection in animal fats using dielectric spectroscopy. The first work utilizes the higher frequency region, 200 MHz–20 GHz [104], while the second study utilizes lower region frequency, 100 Hz–100 kHz [105].

3.1 High Frequency Dielectric Spectroscopy for Lard Detection

The investigation on high frequency range for dielectric spectroscopy on animal fats and plant oil was conducted at room temperature. The samples used in this study are beef tallow, chicken fat, lard, palm oil and soybean oil. Lard was spiked to beef tallow and palm oil respectively and dielectric profile are observed across the range of frequencies. 85070B dielectric probe kit and N5230A PNA-L Network Analyzer was used for dielectric data acquisition. Distilled water was used as the calibration fluid. 200 points of frequency was set from 200 MHz to 20 GHz.

Figure 13 shows the dielectric constant of individual fats; i.e., beef tallow, chicken fat, lard, palm oil and soybean oil. Based on Fig. 13, it is observed that the dielectric constant of the samples decreased as the frequency is increased from 200 MHz up until 15 GHz. As explained on the effect of frequency on oil and fat in the previous section, higher frequency results in the decrease of dielectric constant.

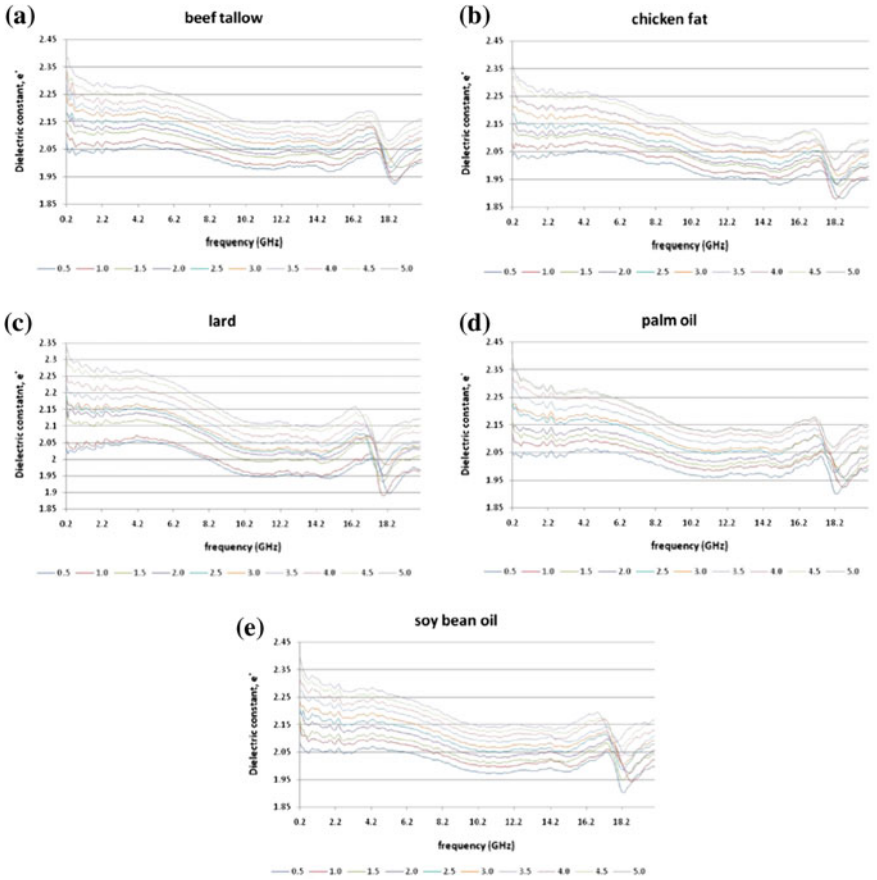

Fig. 13 Dielectric constant of individual fats; **a** beef tallow, **b** chicken fat, **c** lard, **d** palm oil and **e** soy bean oil [104]

Figure 14 shows the comparison on the dielectric constant and loss factor between beef tallow sample, lard sample and beef adulterated with lard sample. It can be observed that frequency between 8.2–14.2 GHz shows most clear separation of the dielectric constant between beef tallow and samples that contain lard, pure lard and beef adulterated with lard. While the loss factor shows separation in different frequency range, which is between 10.2–2.2 GHz.

It is concluded that the dielectric constant of all individual fats samples decreased as the frequency increased for all concentration. Lard adulterated sample can be distinguished from non-adulterated samples by its dielectric constant and loss factor spectral pattern at certain frequency range.

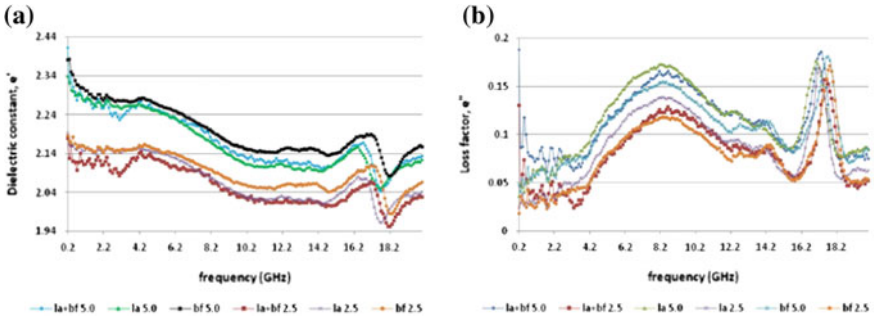

Fig. 14 Comparison of **a** dielectric constant and **b** loss factor between beef tallow sample, lard sample and beef adulterated with lard sample [104]

3.2 *Low Frequency Dielectric Spectroscopy for Lard Detection*

The study of the animal fats at low frequency was conducted at room temperature as well. Animal fats used in this study were beef tallow, chicken fat, mutton tallow and lard. An Agilent 16452A liquid dielectric test fixture was used as the probe and

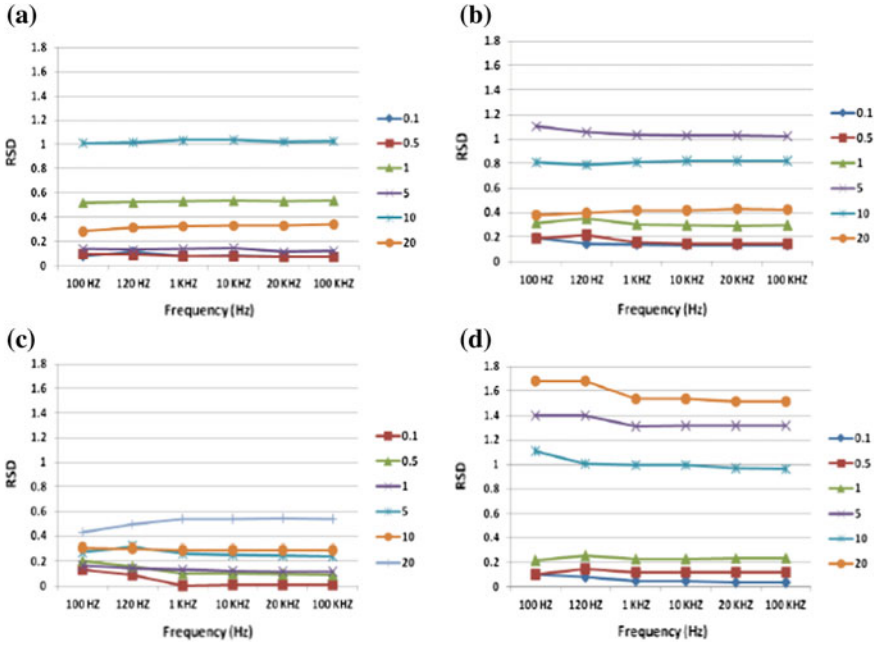

Fig. 15 RSD values for dielectric measurements at frequency range of 10 Hz–100 kHz for different animal fats: **a** chicken, **b** lard, **c** beef and **d** mutton [105]

Table 4 Anova results shows that the p-value at every frequency studied are less than 0.05

Frequency (Hz)	P-value
100	$2.47e^{-8}$
120	$1.93e^{-8}$
1 k	$1.68e^{-8}$
10 k	$1.76e^{-8}$
20 k	$3.44e^{-9}$
100 k	$3.76e^{-9}$

connected to an Agilent 4263B LCR meter. The dielectric values were measured at six discreet frequencies; 100 Hz, 120 Hz, 1 kHz, 10 kHz, 20 kHz and 100 kHz.

This study utilizes data analysis of Relative Standard Deviation (RSD), ANOVA, and PCA. Figure 15 illustrate the RSD values obtained from all of the animal fats.

It can observed that the RSD values of all samples are well below 1.8 %, which is very good for precision, as the minimum RSD required for normal analysis is around 10 % [106]. Table 4 shows the result from ANOVA analysis, which shows that at every frequency, the p-value is less than 0.05 indicating that different animal fat samples have significant difference at these frequencies. Figure 16 shows a PCA score plot for four different types of animal fats; i.e., beef tallow, mutton tallow, lard and chicken fat. From the observation on the PCA score plot, it is clearly depicted a well separation between different types of animal.

From this study, it is concluded that the dielectrics value is not a function of frequencies but a function of sample's concentration levels. Using ANOVA, it is statistically concluded that there is significant difference between different groups of

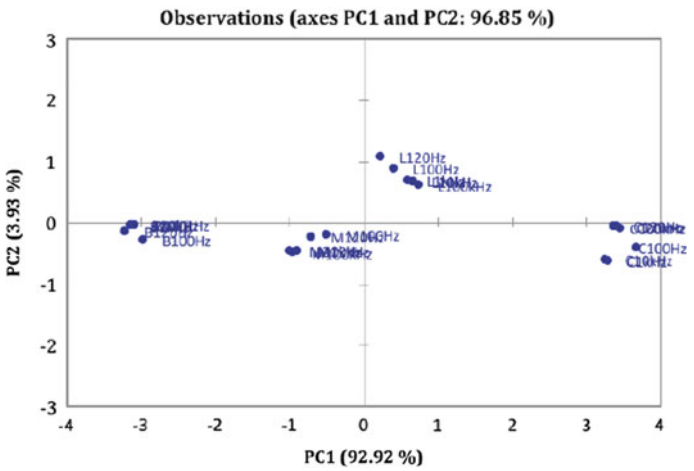

Fig. 16 PCA score plot for different types of animal fats in which B (beef tallow), M (mutton tallow), L (lard) and C (chicken fat) can be observe was well separated between each other [105]

sample, i.e., animal fats. PCA technique positively show clear group separation among different animal fats, thus highlight the ability of dielectric spectroscopy in lard detection.

4 Conclusion

This chapter has reviewed the motivation of detecting lard in lard adulterated food product such as edible oil, several conventional techniques that have been used in lard detection and a number of data analysis that have been applied on lard detection study. The factors influencing dielectric spectroscopy technique and use of dielectric spectroscopy on food products have been discussed. In addition to the applications presented on food products, the dielectric spectroscopy measurements on oil and fats was also discussed in detail with the factors influencing the dielectric constant and loss factor. Work has also been performed to distinguish lard from other animal fats by using the dielectric spectroscopy method with data analysis to help enhance lard detection ability.

References

1. J. Spink, D.C. Moyer, Background: defining the public health threat of food fraud. J. Food Sci. **76**(9), 1–7 (2011)
2. R. Johnson, Food Fraud and Economically Motivated Adulteration of Food and Food Ingredients, *Congr. Res. Serv. Rep.*, R43358, 1–40 (2014)
3. V. Lakshmi, Food adulteration. Int. J. Sci. Invent. Today **56**(2), 72–77 (2012)
4. S. Lauterbach ,J.A. Albrecht, NF94-186 functions of baking ingredients, *Hist. Mater. from Univ. Nebraska-Lincoln Ext.*, (1994)
5. R.V. Rios, M. Durigan, F. Pessanha, P.F. De Almeida, C.L. Viana, S. Caetano, Application of fats in some food products. Food Sci. Technol. **34**(1), 3–15 (2014)
6. *Vegetable Oils and Oilseeds: A Review* (The Commonwealth Secretariat, London, 1968)
7. C.J. Forde, M. Meaney, J.B. Carrigan, C. Mills, S. Boland, A. Hernon, Biobased fats (Lipids) and oils from biomass as a source of bioenergy, in *Bio-energy Research: Advances and Applications*, ed. by V.K. Gupta, C.P. Kubichek, J. Saddler, F. Xu, M.G. Tuohy (Elsevier, Amsterdam, 2014), pp. 185–201
8. F.D. Gunstone, Major edible uses of oils and fats, in *Oils and Fats in the Food Industry* (Wiley-Blackwell, 2008), pp. 113–135
9. P. He, X. Wan, C. Wang, Y. Jiao, Determination of Animal Oil Added in Vegetable Oil By Standard Chemical Method Coupled With Image Texture Analysis Technology. Int. J. Innov. Comput. Innnov. Control **10**(1), 67–80 (2014)
10. Y.B. Che Man, Z.A. Syahariza, M.E.S. Mirghani, S. Jinap, J. Bakar, Analysis of potential lard adulteration in chocolate and chocolate products using Fourier transform infrared spectroscopy, Food Chem. **90**(4), 815–819 (2005)
11. N. Blechman, Extra virgin suicide—the adulteration of italian olive oil (2014). http://www.nytimes.com/interactive/2014/01/24/opnion/food-chains-extra-virgin-suicide.html
12. N.H. Jenkins, *Virgin Territory—Exploring the World of Olive Oil* (Houghton Mifflin Harcourt, New York, 2015)

13. FDA: FDA Enforcement Reports (2011)
14. M. Tejada, Greek police make arrests in olive oil fraud ring, *Olive Oil Times*, 25 Jul 2013
15. M. Marino, Executive arrested in taiwan cooking oil scandal, *Olive Oil Times*, 24 Oct 2014
16. M.J. Haas, Animal Fats, in *Bailey's Industrial Oil and Fat Prodcuts*, ed. by F. Shahidi, vol. 1, no. C (John Wiley & Sons, Inc., Hoboken, NJ, USA, 2005), pp. 2005–2006
17. Houston, Despite FDA Phase-out of Partially Hydrogenated Oils, Global Outlook for Fats and Oils Remains Positive as Use Essential to Food and Nonfood Production, IHS Says, *IHS*, 22 Jan 2016
18. N.A. Fadzlillah, Y.B. Che Man, M.A. Jamaludin, S.A. Rahman, H.A. Al-Kahtani, Halal food issues from islamic and modern science perspectives, in *2nd International Conference Humaniy. History Social Science*, vol. 17 (2011), pp. 159–163
19. K.A. Al-Rashood, E.M. Abdel-Moety, A. Rauf, R.R. Abou-Shaaban, K.I. Al-Khamis, Triacylglycerols-profiling by high performance liquid chromatography: a tool for detection of pork fat (Lard) in processed foods, J. Liq. Chromatogr. **18**(13), 2661–2673 (1995)
20. Y.B. Che Man, A. Rohman, T.S.T. Mansor, Differentiation of lard from other edible fats and oils by means of Fourier transform infrared spectroscopy and chemometrics, JAOCS, J. Am. Oil Chem. Soc. **88**(2), 187–192 (2011)
21. J.A. Davidson, World Religions and the Vegetarian Diet. J. Advent. Theol. Soc. **14**(2), 114–130 (2003)
22. Al-Zamakhsyari, *Al-Kasysyaf*. Misr: Maktabah Al-'Abikan (1998)
23. M. Siddiqui, *The Good Muslim: Reflections on Classical Islamic Law and Theology mona siddiqui* (Cambridge University Press, New York, 2012)
24. M.T. Gillies, *Shortenings, Margarines, and Food Oils*. (Noyes Data Corporation, 1974)
25. N.O.V Sonntag, Fat splitting, esterification, and interesterification, in *Bailey's industrial oil and fat products*, vol. 2 (John Wiley & Sons, New York, 1982), pp. 134–135
26. P. Lambelet, O.P. Singhal, N.C. Ganguli, Detection of goat body fat in ghee by differential thermal analysis. J. Am. Oil Chem. Soc. **57**(10), 364–366 (1980)
27. P. Lambelet, N.C. Ganguli, Detection of pig and buffalo body fat in cow and buffalo ghee by differential scanning calorimetry. J. Am. Oil Chem. Soc. **60**(5), 1005–1008 (1983)
28. APK-Inform: FEDIOL reported on cases of Ukrainian sunflower oil adulteration, 18 Nov 2015
29. K. Jakobsen, Dietary modifications of animal fats: status and future perspectives. Fett-Lipid **101**(12), 475–483 (1999)
30. E. Commission, *Protection of the Communities' financial interests: The fight against fraud : annual report 2000* (May. 2001)
31. Q. Wang, A. Afshin, M.Y. Yakoob, G.M. Singh, C.D. Rehm, S. Khatibzadeh, R. Micha, P. Shi, D. Mozaffarian, M. Ezzati, S. Fahimi, J. Powles, I. Elmadfa, M. Rao, P. Wirojratana, S.S. Lim, R.E. Engell, K.G. Andrews, P.A. Abbott, M. Abdollahi, E.O. Abeyá Gilardon, H. Ahsan, M.A.A. Al Nsour, S.N. Al Hooti, C. Arambepola, H. Barennes, S. Barquera, A. Baylin, W. Becker, P. Bjerregaard, L.T. Bourne, N. Calleja, K. Castetbon, H. Chang, M.J. Cowan, S.De Henauw, E.L. Ding, C.A. Duante, P. Duran, I. Elmadfa, H.E. Barbieri, F. Farzadfar, D.N. Fernando, A.F. Hadziomeragic, R.M. Fisberg, S. Forsyth, D. Garriguet, J. Gaspoz, D. Gauci, B.N.V. Ginnela, I. Guessous, W. Hadden, D.J. Hoffman, A. HoushiarRad, I. Huybrechts, N.C. Hwalla, H.M. Ibrahim, M. Inoue, M.D. Jackson, L. Johansson, L. Keinan Boker, C. Kim, E. Koksal, H. Lee, Y. Li, N.I. Lipoeto, G. Ma, G.L. Mangialavori, Y. Matsumura, S.T. McGarvey, C.M. Fen, R.A. Monge Rojas, A.O. Musaiger, B. Nagalla, A. Naska, M.C. Ocke, M. Oltarzewski, P. Orfanos, M. Ovaskainen, W. Pan, D.B. Panagiotakos, G.A. Pekcan, S. Petrova, N. Piaseu, C. Pitsavos, L.G. Posada, L.M. Riley, L.M. Sánchez Romero, R.B.T. Selamat, S. Sharma, A.M. Sibai, R. Sichieri, C. Simmala, L. Steingrimsdottir, G. Swan, E.H. Sygnowska, L. Szponar, H. Tapanainen, R. Templeton, A. Thanopoulou, H. Thorgeirsdóttir, I. Thorsdottir, A. Trichopoulou, S. Tsugane, A. Turrini, S. Vaask, C. van Oosterhout, J.L. Veerman, N. Verena, A. Waskiewicz, S. Zaghloul, and G. Zajkás, Impact of Nonoptimal Intakes of

Saturated, Polyunsaturated, and Trans Fat on Global Burdens of Coronary Heart Disease. J. Am. Heart Assoc. **5**(1), e002891 (2016)
32. A.A. Aida, Y.B.C. Man, C.M.V.L. Wong, A.R. Raha, R. Son, Analysis of raw meats and fats of pigs using polymerase chain reaction for Halal authentication. Meat Sci. **69**(1), 47–52 (2005)
33. Y.B. Che Man, A.A. Aida, A.R. Raha, R. Son, Identification of pork derivatives in food products by species-specific polymerase chain reaction (PCR) for halal verification, Food Control, **18**(7), 885–889 (2007)
34. J. Sneddon, D.J. Butcher, *Advances in atomic spectroscopy*, 1st edn. (Elsevier Science, 2002)
35. J.M. Hollas, *Modern Spectroscopy*. (John Wiley & Sons, Inc., 2004)
36. G. Hohne, W.F. Hemmingher, H.J. Flammersheim, *Differential Scanning Calorimetry* (Springer-Verlag, Berlin Heidelberg, New York, 2003)
37. J.M.N. Marikkar, O.M. Lai, H.M. Ghazali, Y.B. Che Man, Detection of lard and randomized lard as adulterants in refined-bleached-deodorized palm oil by differential scanning calorimetry. J. Am. Oil Chem. Soc. **78**(11), 1113–1119 (2001)
38. E. Coni, M. Di Pasquale, P. Coppolelli, A. Bocca, Detection of animal fats in butter by differential scanning calorimetry: A pilot study. J. Am. Oil Chem. Soc. **71**(8), 807–810 (1994)
39. O. Dahimi, A.A. Rahim, S.M. Abdulkarim, M.S. Hassan, S.B.T.Z. Hashari, A. Siti Mashitoh, S. Saadi, Multivariate statistical analysis treatment of DSC thermal properties for animal fat adulteration. Food Chem. **158**, 132–138 (2014)
40. R.L. Wixom, C.W. Gehrke, V.G. Berezkin, J. Janak, Chromatography: A New Discipline of Science, in *Chromatography : A science of discovery*, vol. 1, ed. by R.L. Wixom, C.W. Gehrke, (John Wiley & Sons, Inc., Hoboken, NJ, USA, 2015)
41. H. Alam, S.H. Saeed, C. Engg, Electronic nose in food and healh applications: A review. Int. J. Comput. Corp. Res. **2**(6), 1–17 (2012)
42. M. Nurjuliana, Y.B. Che Man, D. Mat Hashim, Analysis of lard's aroma by an electronic nose for rapid Halal authentication, JAOCS. J. Am. Oil Chem. Soc. **88**(1), 75–82 (2011)
43. N.N. Ahmad Nizar, J.M. Nazrim Marikkar, D.M. Hashim, Differentiation of lard, chicken fat, beef fat and mutton fat by GCMS and EA-IRMS techniques. J Oleo Sci, **62**(7), 459–464 (2013)
44. O. Dahimi, M.S. Hassan, A.A. Rahimm, S.M. Abdulkarim, Differentiation of lard from other edible fats by Gas Chromatography-Flame Ionisation Detector (GC-FID) and Chemometrics, J. Food Pharm. Sci. **2**(2), 27–31 (2014)
45. D. Indrasti, Y.B. Che Man, S. Mustafa, D.M. Hashim, Lard detection based on fatty acids profile using comprehensive gas chromatography hyphenated with time-of-flight mass spectrometry. Food Chem. **122**(4), 1273–1277 (2010)
46. J.M.N. Marikkar, H.M. Ghazali, Y.B. Che Man, T.S.G. Peiris, O.M. Lai, Distinguishing lard from other animal fats in admixtures of some vegetable oils using liquid chromatographic data coupled with multivariate data analysis. Food Chem. **91**(1), 5–14 (2005)
47. A. Rohman, E. Sismindari, Y. Erwanto, Y.B. Che Man, Analysis of pork adulteration in beef meatball using Fourier transform infrared (FTIR) spectroscopy, Meat Sci. **88**(1), 91–95 (2011)
48. A. Rohman, Y.B. Che Man, Analysis of Cod-Liver Oil Adulteration Using Fourier Transform Infrared (FTIR) Spectroscopy. J. Am. Oil Chem. Soc. **86**(12), 1149–1153 (2009)
49. Z.A. Syahariza, Y.B. Che Man, J. Selamat, J. Bakar, Detection of lard adulteration in cake formulation by Fourier transform infrared (FTIR) spectroscopy. Food Chem. **92**(2), 365–371 (2005)
50. I. Jaswir, M.E.S. Mirghani, T.H. Hassan, M.Z.M. Said, Determination of Lard in Mixture of Body Fats of Mutton and and Cow by Fourier Transform Infrared Spectroscopy. J. Oleo Sci. **52**(12), 633–638 (2003)

51. Y.B. Che Man, M.E.S. Mirghani, Detection of lard mixed with body fats of chicken, lamb, and cow by fourier transform infrared spectroscopy. J. Am. Oil Chem. Soc. **78**(7), 753–761 (2001)
52. R. Peng, Analysis of Variance, in *Statistical Procedures* (2009), pp. 327–374
53. M.H. Katz, *Multivariable analysis: a practical guide for clinicians* (New York, 2011)
54. R. Shier, Paired t-tests. (Mathematics Learning Support Centre, 2004), pp. 1–3
55. J. Poulsen, A. French, Discriminant Function Analysis (DA). J. Forensic Sci. **56**(2), 297–301 (1996)
56. L.I. Smith, A tutorial on principal components analysis introduction, Statistics (Ber), **51**, 52 (2002)
57. P.-N. Tan, M. Steinbach, V. Kumar, Chap 8: cluster analysis: basic concepts and algorithms, in *Introduction to Data Mining* (2005), p. Chapter 8
58. D.M. Lane, D. Scott, M. Hebl, R. Guerra, D. Osherson, H. Zimmer, *Introduction to Statistics* (1974)
59. R.D. Tobias, An introduction to partial least squares regression, in *Proceedings. Annual SAS Users Group International Conference, 20th*, (Orlando, FL, 1995), pp. 2–5
60. SPSS: Stepwise linear regression, School of Geography, University of Leeds. http://www.geog.leeds.ac.uk/courses/other/statistics/spss/stepwise
61. S. Nielsen, Food analysis laboratory manual. J. Chem. Inf. Model. **53**, 160 (1989)
62. R. Simpson, *Engineering aspects of thermal food processing* (Taylor & Francis Group, Boca Raton, 2009)
63. C.G. Pearce, Polarization of Dielectrics, *EM Fields 2*, 196AD. http://www-users.aston.ac.uk/~pearcecg/Teaching/PDF/LEC2.PDF
64. J. Mijovic, B.D. Fitz, Dielectric spectroscopy of reactive polymers, Mater. Sci. **2**(5), pp. 1531–9 (1998)
65. S.E. Braslavsky, Glossary of terms used in photochemistry, 3rd edition. Pure Appl. Chem. **79**(3), 293–465 (2007)
66. Wave Propagation Standards Committee: *IEEE Standard Definitions of Terms for Radio Wave Propagation*, vol. 1997 (1997)
67. R. Nave, Dielectrics, *Hyperphysics*. http://www.hyperphysics.phy-astr.gsu.edu/hbase/hph.html
68. Agilent 16452A Liquid Test Fixture Operation and Service Manual (Japan, 2007)
69. A.K. Datta, G. Sumnu, G.S.V. Raghavan, Dielectric properties of foods, in *Engineering Properties of Foods*, 3rd edn., ed. by M.A. Rao, S.S.H. Rizvi, A.K. Datta (Taylor & Francis Group, Boca Raton, 2005), pp. 501–566
70. A.R. Von Hippel, *Dielectrics and Waves* (Cambridge, Mass., MIT. Press, Cambridge, 1954)
71. A.R. Von Hippel, *Dielectric Materials and Applications* (The Technology Press of MIT and John Wiley, New York, 1954)
72. S.O. Nelson, L.F. Charity, Frequency dependence of energy absorption by insects and grain in electric fields. Trans. Am. Soc. Agric. Eng. **15**, 1099–1102 (1972)
73. S. Nelson, L.E. Stetson, C.W. Schlaphoff, A general computer program for precise calculation of dielectric properties from short-circuited waveguide measurements, IEEE Trans. Instrum. Meas. **IM–23**(4), 455–460 (1974)
74. C. Gabriel, E.H. Grant, I.R. Young, Use of time domain spectroscopy for measuring dielectric properties with a coaxial probe. J. Phys. E. **19**(10), 843–846 (1986)
75. Y. Wang, T.D. Wig, J. Tang, L.M. Hallberg, Dielectric properties of foods relevant to RF and microwave pasteurization and sterilization. J. Food Eng. **57**(3), 257–268 (2003)
76. S. Mashimo, S. Kuwabara, S. Yagihara, K. Higasi, Dielectric relaxation time and structure of bound water in biological materials. J. Phys. Chem. **91**(25), 6337–6338 (1987)
77. A.W. Kraswzewski, S. Trabelsi, S.O. Nelson, Microwave dielectric properties of wheat, in *Proceedings of 30th Microwave Power Symposium* (1995), pp. 90–93
78. R.B. Keam, W.S. Holmes, Uncertainty analysis measurement of complex permittivity using microstrip transmission line, in *SBMO/IEEE MTT-S IMOC'95 Proceedings* (1995), pp. 137–142

79. F.M. Ghannouchi, R.G. Bosisio, Measurement of microwave permittivity using a six-port reflectometer with an open-ended coaxial line. IEEE Trans. Instrum. Meas. **38**(2), 505–508 (1989)
80. H. Wakamatsu, A Dielectric Spectrometer for Liquid Using the Electromagnetic Induction, Hewlett-Packard J. 1997, 1–10 (1997)
81. J.L. Jorgensen, A.R. Edison, S.O. Nelson, L.E. Stetson, A bridge method for dielectric measurements of grain and seed in the 50–250 MHz range. Trans. ASAE **13**(1), 18–20 (1970)
82. A.C. Metaxas, R.J. Meredith, *Industrial Microwave Heating* (Peter Peregrinus Ltd., London, 1983)
83. S.O. Nelson, Dielectric spectroscopy in agriculture, J. Non. Cryst. Solids, **351**(33–36) SPEC. ISS., 2940–2944, (2005)
84. S.O. Nelson, Dielectric properties of agricultural products-measurements and applications. IEEE Trans. Instrum. Meas. **41**(1), 385–387 (1991)
85. M.E. Sosa-Morales, L. Valerio-Junco, A.L. López-Malo , H.S. García, Dielectric properties of foods: Reported data in the 21st century and their potential applications, *LWT-Food Sci. Technol.* **43**(8), 1169–1179 (2010)
86. C. Gabriel, C. Gabriel, S. Gabriel, S. Gabriel, E. Corthout, E. Corthout, The dielectric properties of biological tissues: I. Literature survey. Phys. Med. Biol. **41**(11), 2231–2249 (1996)
87. R. Hollertz, *Dielectric properties of wood fibre components relevant for electrical insulation applications* (KTH Royal Institute of Technology, Stockholm, Sweden, 2014)
88. F. Liu, I. Turner, E. Siores, P. Groombridge, A numerical and experimental investigation of the microwave heating of polymer materials inside a ridge waveguide.pdf. J. Microw. Power Electromagn. Energy. **31**(2), 71–82 (1996)
89. M. Arai, J.G.P. Binner, G.E. Carr, T.E. Cross, High temperature dielectric measurements on ceramics, in *Sixth International Conference on Dielectric Materials, Measurements and Applications, 1992*, (IET, Manchester, 1992), pp. 69–72
90. P. Hoekstra, A. Delaney, Dielectric properties of soils at UHF and microwave frequencies. J. Geophys. Res. **79**(11), 1699–1708 (1974)
91. S. Ryyniinen, The electromagnetic properties of food materials: a review of the basic principles. J. Food Eng. **26**(4), 409–429 (1995)
92. H. Lizhi, K. Toyoda, I. Ihara, Dielectric properties of edible oils and fatty acids as a function of frequency, temperature, moisture and composition. J. Food Eng. **88**(2), 151–158 (2008)
93. N. Bengtsson, P. Risman, Dielectric properties of foods at 3 ghz as determined by a cavity perturbation technique–II measurements on food materials. J. Microw. Power **6**(2), 107–123 (1971)
94. R.E. Mudgett, S.A. Goldblith, D.I.C. Wang, W.B. Westphal, Dielectric behavior of a semisolid food at low, intermediate and high moisture content.pdf. J. Microw. Power **15**(1), 27–36 (1980)
95. B. Bodakian, F.X. Hart, The dielectric properties of meat. IEEE Trans. Dielectr. Electr. Insul. **1**(2), 181–187 (1994)
96. A.C. Nunes, X. Bohigas, J. Tejada, Dielectric study of milk for frequencies between 1 and 20 GHz. J. Food Eng. **76**(2), 250–255 (2006)
97. H. Lizhi, K. Toyoda, I. Ihara, Discrimination of olive oil adulterated with vegetable oils using dielectric spectroscopy. J. Food Eng. **96**(2), 167–171 (2010)
98. A.K. Bansal, P.J. Singh, K.S. Sharma, S. Kumar, P.R. Kumar, Dielectric properties of different varieties of rapeseed-mustard oil at different temperatures. Indian J. Pure Appl. Phys. **39**, 532–540 (2001)
99. A. Cataldo, E. Piuzzi, G. Cannazza, E. De Benedetto, L. Tarricone, On the use of dielectric spectroscopy for quality control of vegetable oils, in *19th IMEKO World Congr. 2009*, vol. 1 (2009), pp. 1–5
100. The JOCS Standard Methods for the Analysis of Fats, Oils and Related Materials Second English Edition. Japan Oil Chemists' Society (2013)

101. Codex Standard for Named Animal Fats (CODEX-STAN 211–1999), in *Codex Alimentarius Commission: Fats, Oils & Related Products* (Secretariat of the Joint FAO/WHO Food Standards Programme, Rome, 2001)
102. E.M.S.F., G.M.F.I.I. James W Robinson, Concepts of Instrumental Analytical Chemistry, in *Undergraduate Instrumental Analysis*, 6th ed., New York: Taylor & Francis Group, 2005, pp. 1–1107
103. R.J. Stokes, D.F. Evans, *Fundamentals of Interfacial Engineering* (Wiley Inc, New York, 1997)
104. N.H.A. Latiff, Lard detection using dielectric spectroscopy (Universiti Putra Malaysia, 2010)
105. M.A. Sairin, N. Naquiah, A. Nizar, S.A. Aziz, D.M. Hashim, A. Samples, Potential of Dielectric Spectroscopy Measurement for Lard Detection, pp. 1–6
106. V. Thomsen, D. Schatzlein, D. Mercuro, Limits of detection in spectroscopy. Pure Appl. Chem. **18**(12), 112–114 (2003)

Optical-Based Interference Cancellation in Wireless Sensor Networks

Matthew P. Chang, Jingyi (Jenny) Sun, Monica Lu, Eric Blow and Paul R. Prucnal

Abstract One of the biggest challenges facing the widespread implementation of wireless sensor networks is wireless interference and radio-frequency (RF) spectrum crowding. Even today, wireless networks are already straining under society's relentless demand for higher data rates and constant connectivity. For wireless sensor networks to become a reality, research on increasing network capacity and allocating spectral resources must necessarily involve new techniques for handling wireless interference scalably and efficiently. This chapter focuses on analog interference cancellation using optical signal processing as a path towards operating in the presence of wireless interference. Canceling interference before it enters a receiver allows wireless sensor networks to conserve scarce spectral resources and relax system requirements, resulting in robust operation, increased battery life, and reduced size and cost. Through its unique physics, optics enables new RF functionalities that are extremely valuable to canceling interference in the RF front-end, chief among them being wide processing bandwidth. The wideband nature of optics is key to anticipating the rise in data rates, bandwidths, and channel counts of future networks, and endows optics with the potential to realize true multiband radio transceivers. Our goal in this chapter is to present an overview of optical-based RF interference cancellation and discuss the key characteristics that make optics an outstanding technology platform for the job. We then show several system architectures and a sample of their experimental performance. We leave the readers with a discussion on the future prospects for this technology, focusing specifically on photonic integrated circuits.

1 Introduction

Wireless sensor networks can provide valuable insight into the patterns and processes of our surroundings that we were formerly unaware of. Yet, connecting thousands or millions of wireless devices in a seamless network brings a unique set of challenges

M.P. Chang · J. (Jenny) Sun · M. Lu · E. Blow · P.R. Prucnal (✉)
Lightwave Communications Research Laboratory, Electrical Engineering Department, Princeton University, Princeton, NJ 08540, USA
e-mail: prucnal@princeton.edu

S. Mukhopadhyay et al. (eds.), *Sensors for Everyday Life*, Smart Sensors, Measurement and Instrumentation 23, DOI 10.1007/978-3-319-47322-2_13

that must first be overcome before this promise can be fulfilled. Chief among them are the problems of wireless interference and RF spectrum crowding.

Wireless interference is the greatest problem in wireless communications because of the very nature of our shared transmission medium. Interference mitigation techniques involve sharing other radio resources such as time (time-division duplexing, TDD), codes (code-division duplexing, CDD), and frequency (frequency-division duplexing, FDD). These techniques have successfully permitted multiple users to communicate without interfering with each other, but they come at a cost: RF spectrum, the universal currency of wireless communications. As data rates and the number of connected devices continue to rise exponentially [1], the limited RF spectrum has grown extremely crowded, and the price for bandwidth worldwide has soared into the billions of U.S. dollars for 10s of MHz of spectrum. Similarly, the number of communication bands and the market for RF front-end components, particularly filters, the gateways to different bands, has followed suite (see Fig. 1).

Adding more bands and filters may seem like a solution, but this trend is not sustainable. Most RF components, like filters, operate in a single, fixed frequency band, meaning each band requires a dedicated chain of RF components. As a result, RF front-ends, like those in Fig. 2, have grown complex, bulky, and expensive. Meanwhile, limited circuit board real estate (and profit margins) in size-sensitive platforms like handsets mean that hardware designers have to sacrifice functionality for the expanding RF front-end. Finally, no amount of additional filters actually creates capacity, it only divides it up further.

New methods of operating in the presence of interference will be required in widescale wireless sensor networks, as well as in the larger scope of 5G. These methods will need to work in tandem with the traditional TDD, FDD, and CDD techniques. Furthermore, any new hardware must be tunable and wideband, lest they be vulnerable to the same scaling limitations of existing front-ends and risk facing irrelevance in 5G.

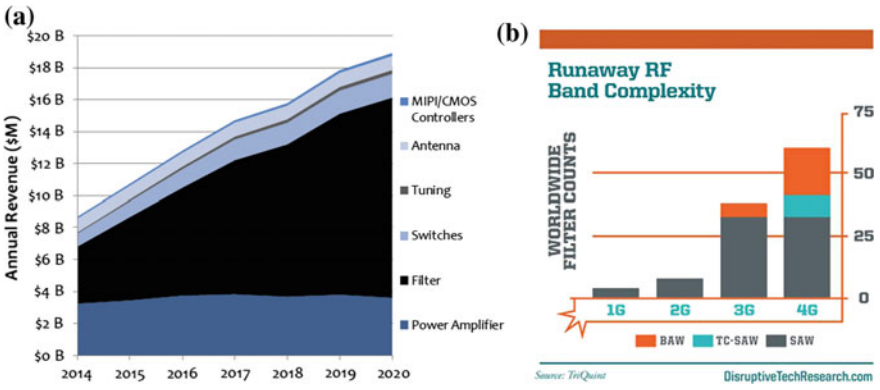

Fig. 1 **a** The projected growth of revenue for RF front-end components, dominated by filters. Taken from [2]. **b** The rise in the number of different band filters. *Source* Triquint

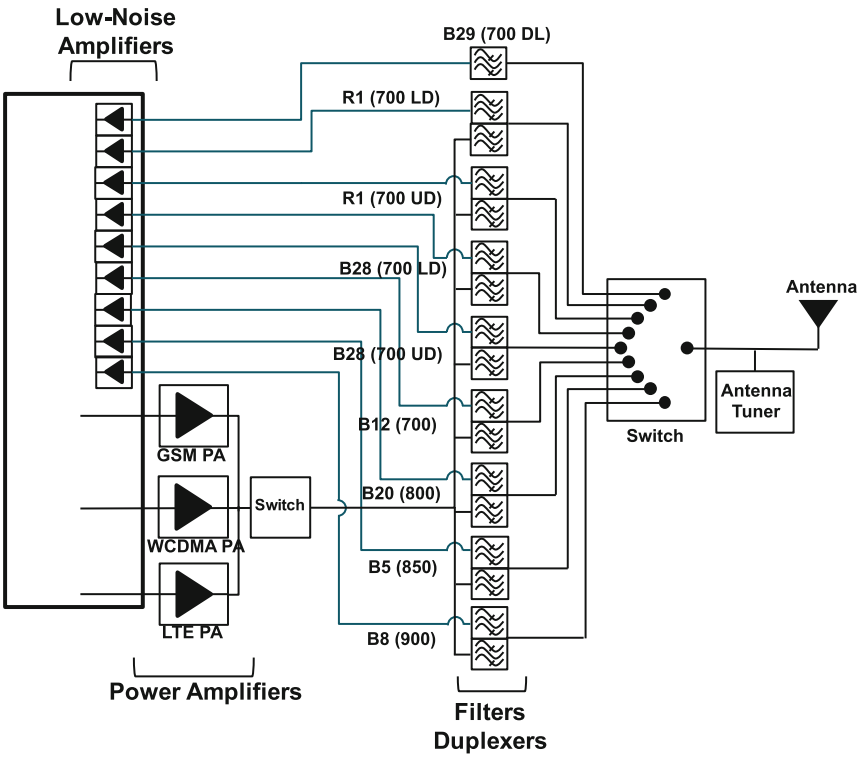

Fig. 2 RF front-end architecture for the 700–900 MHz bands, showing the front-end complexity

In this chapter, we discuss the importance of interference cancellation in future wireless communication systems. In particular, we present our vision for using optical signal processing techniques, instead of traditional RF approaches, to cancel interference. Optics possesses the key property that it can operate over extremely wide bandwidths and frequencies, which is necessary to not only cancel interference over wide bandwidth channels, but also to enable a true multiband transceiver and future-proof them to newly defined bands and frequencies. This latter point is especially important to stem the expansion of RF front ends. The chapter is organized as follows: we first give an overview of interference cancellation and determine the key characteristics of an interference canceller. We then turn our attention to optical interference cancellation, particularly as it pertains to self-interference cancellation. We discuss how optical cancelers meet the key characteristics and then present various system architectures with their experimental results. Last, but not least, we discuss the feasibility for optical technology in commercial markets via photonic integrated circuits.

2 Interference Cancellation in Wireless Sensor Networks

Interference cancellation refers to the process of actively nulling interference by subtracting the interference signal from the corrupted signal. This is in contrast to other interference mitigation techniques, which use some form of temporal, spectral, spatial, or code-based isolation to protect the desired signal from interference; some examples are provided in Fig. 3. The need for interference cancellation arises because these methods are not perfect and in some cases not applicable. For example, in in-band full-duplex communications, or simultaneous transmit and receive on the same frequency, filters are no longer applicable and circulators, which typically provide 20 dB of isolation, are insufficient to protect the receiver.

Interference cancellation is often confused for spectral filtering, but the two techniques are different and should be used together, rather than as substitutes, to address different components of interference. The key differences between cancellation and filtering are summarized in Table 1. The main advantages of interference cancellation are (1) its ability to address in-band interference and (2) its frequency-independence. With regard to the first advantage, interference cancellation nulls interference without harming the desired signal regardless of the spectral characteristics of either signal. In contrast, filters indiscriminately reject (pass) signals outside (inside) of its passband, regardless of whether it is the desired signal or the interference. With regard to the second advantage, cancellation can occur at any frequency, assuming that the hardware performing the cancellation can operate at that frequency. On the other hand, the majority of RF filters operate only over a fixed frequency range at any given time. However, the advantages of cancellation can only be leveraged if the system has prior knowledge of the interferer, and this often translates into increased system complexity and processing power.

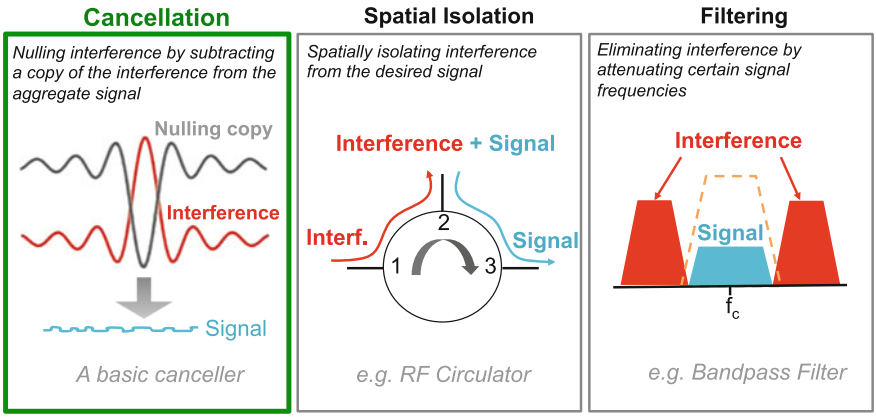

Fig. 3 Different forms of interference mitigation techniques: (*left*) cancellation, (*middle*) spatial isolation, (*right*) spectral isolation or filtering

Table 1 Interference cancellation versus filtering

Characteristic	Cancellation	Filtering
Interference spectrum	In-band and out-of-band	Out-of-band only
Operational bandwidth	Wideband (practically limited)	Narrowband (fundamentally limited)
Interference knowledge	Required	Not required

2.1 Interference Cancellation Model

The ability of a system to cancel interference depends strongly upon the source of the interference, the coupling channel between the interference source and the receiver, herein called the *interference channel*, and any apriori knowledge about the interference and the desired signal. In a general interference cancellation scenario, the received signal consists of a signal of interest, $s(t)$, corrupted by an unknown interference signal, $n(t)$, which is assumed to be strong enough to block the receiver (Eq. 1). The purpose of the interference cancellation system is to extract the interference from the aggregate signal and subsequently subtract the extracted interference, $n_p(t)$, from the aggregate signal, recovering the signal of interest. The output is given by Eq. 2, where the term in brackets represents the residual interference.

$$r(t) = s(t) + n(t) \tag{1}$$

$$y(t) = s(t) + \{n(t) - n_p(t)\} \tag{2}$$

Apriori knowledge can consist of anything from the waveform of the interference to its statistical nature and will in general dictate the signal processing that is required to extract the interference from the aggregate signal.

Interference can be divided into two categories: known and unknown. When the interference signal is unknown, statistical methods must be used to distinguish the interference from the desired signal. This is known as *blind source separation*. Assuming that the signal of interest and the interference are statistically independent, techniques such as principal component analysis (PCA) and independent component analysis (ICA) are often employed. These techniques aim to separate the aggregate signal into two or more components, demarcated by their statistical properties. An interference canceller would then eliminate the components related to the interference. Much research has been devoted to the topic of blind source separation, and we refer the readers to these sources [3–5]. Herein, we focus on the situation where the interference signal is either known or has been successfully extracted.

2.2 *Self-interference*

A specific type of known interference is self-interference. Self-interference is unintentionally generated by one's own system, and therefore, a reference of the interference is locally available. Examples of self-interference are shown in Fig. 4. As adjacent bands move closer together and communication platforms are required to support more and more transceivers, the growth of self-interference is hindering efforts to increasing capacity. As a specific example, in in-band full-duplex communications, a transmitter and a receiver purposefully operate on the same frequency band at the same time and can theoretically halve spectrum usage [6]. The self-interference generated by a full-duplex system is enormous because the receiver has no protection against the strong transmitter operating in close proximity. Receiving a desired signal at −90 or −100 dBm when the transmitter is outputting at +30 or +40 dBm would require >130 dB of self-interference cancellation!

A model for self-interference is shown in Fig. 5. In self-interference cancellation, because a reference of the interferer is available, the purpose of the interference cancellation system's signal processing is to estimate the interference channel that the transmitted signal propagates through prior to combining with the received signal. To first order, the interference channel will attenuate and delay the transmitted sig-

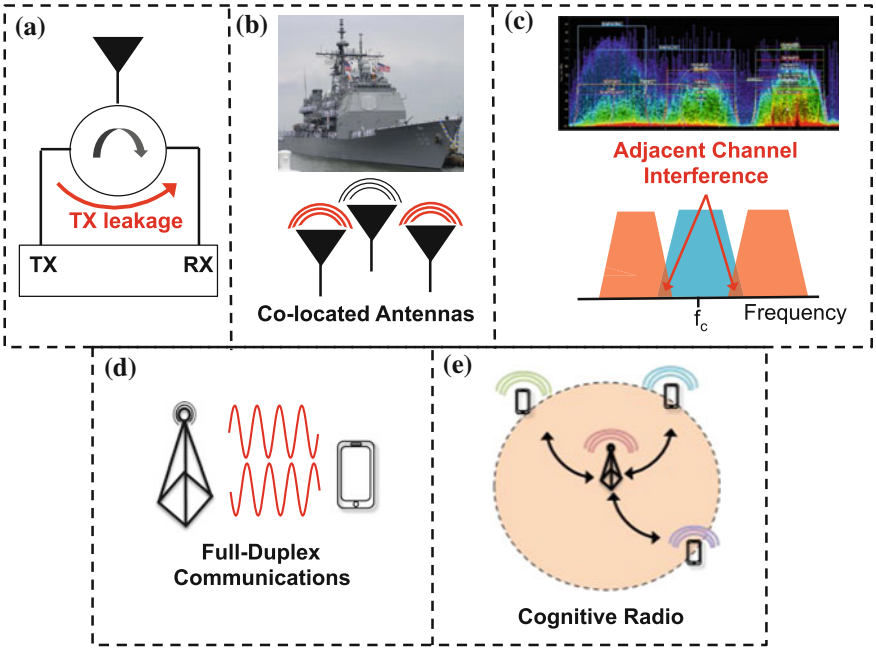

Fig. 4 Examples of self-interference: **a** Transmitter leakage, **b** Co-located antenna systems, **c** Adjacent channel interference, **d** Self-Interference from full-duplex communications, **e** Cognitive radio and dynamic spectrum access [7]

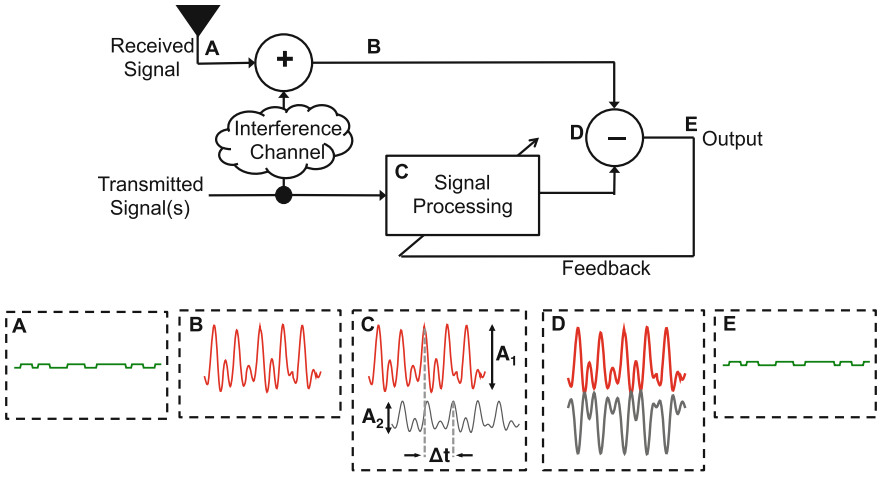

Fig. 5 A general model for self-interference cancellation

nal, but more complex channel effects, such as multipath, reflections within the RF circuitry, amplifier noise, and nonlinear distortion are also present [8, 9]. The self-interference at the receiver can be given by

$$n(t) = \sum_{n=1}^{\infty} (\alpha_n n_0(t - \tau_n)) + w(t) + n_{nl}(t) \tag{3}$$

where $n_0(t)$ represents the original interferer at the transmitter, α_n and τ_n are the channel attenuation and delay for the *nth* multipath component, $w(t)$ represents wideband amplifier noise, and $n_{nl}(t)$ represents all nonlinear byproducts. The ability of the system to estimate and mimic these effects determines the maximum amount of interference cancellation achievable.

2.3 *Key Characteristics of an Interference Canceller*

An interference canceller must emulate the interference channel as closely as possible to maximize interference cancellation. To quantify how closely one must match the interference channel to achieve a certain level of cancellation, consider the cancellation of a sinusoidal interferer by subtracting from it another sinusoid with slightly different phase and amplitude. The phase and amplitude mismatch between the two signals represent the error of the interference canceller and its signal processing. Cancellation, or the relative reduction in the interferer power from its original power, is shown in Fig. 6. We will call these curves *mismatch curves*.

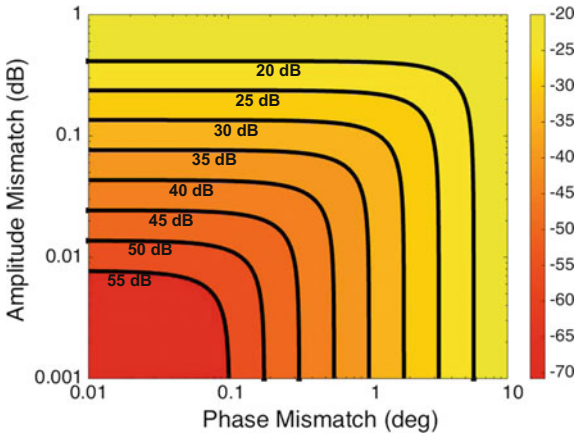

Fig. 6 Mismatch curve: the maximum interference cancellation of a sinusoid that can be achieved given a certain amplitude and phase mismatch

Figure 6 shows that achieving levels of interference cancellation above 40 dB requires less than 0.4° of phase mismatch and 0.04 dB of amplitude mismatch between the two sinusoids. This level of precision is a formidable task, and grows even more demanding for higher cancellation depths. Hence, the first key characteristic of an interference canceller, perhaps intuitively, is extremely precise control of the amplitude and phase. The mismatch curves provides insight into the precision requirement.

Although the mismatch curves are useful, they only indicate the cancellation achievable at a single frequency. Actual cancellation will depend upon the bandwidth of the interfering signal, as well as the frequency responses of the interference canceller and the interference channel. Even if the cancellation conditions are met perfectly at a single frequency, it is unlikely that these same conditions will be met at other frequencies. This creates an important tradeoff between average cancellation depth and bandwidth of cancellation. The second key characteristic is therefore wideband operation of the canceller and the RF front end. The flatter the frequency responses of the canceller, RF front-end, and interference channel, the wider the achievable cancellation bandwidth for a fixed cancellation depth.

The third key characteristic of an interference canceller is low latency tunability. Practical RF environments are dynamic, even ones that are physically fixed. Wind effects on antennas, temperature drifts, and objects moving around the antennas all affect the RF environment and the interference channel. Any practical canceller must be able to adapt to changes, and sufficiently quickly, to minimize system down-time.

Finally, the fourth key characteristic of an interference canceller is extremely wide dynamic range. An interference canceller must not only be able to accept high powers from an interferer, but simultaneously be able to resolve weak signals of interest. Interference cancellers which cannot process high powers will generate unacceptable harmonics and intermodulation products, which will also mask the desired signal. Conversely, interference cancellers which cannot resolve low power signals will lose the desired signal under the noise floor.

3 Interference Cancellation Using Optical Signal Processing

In this section, we give a brief introduction to analog optical signal processing and make a case for using optics to perform interference cancellation based on its ability to satisfy the four key characteristics of an interference canceller:

- Wideband operation
- Precise amplitude and delay (phase) control
- Low latency tunability
- High dynamic range

3.1 Analog Optical Signal Processing and Microwave Photonics

Despite the omnipresence of digital electronics in our world, there has recently been a strong resurgence of interest in RF analog signal processing. This is because converting an analog RF signal into a digital signal with high fidelity is extremely demanding. It requires a large number of bits to achieve high dynamic range and a large sampling rate to represent high bandwidths. These tall technical requirements make it cost prohibitive, if not impossible, to implement a truly software-defined radio (SDR) today.

Following the development of the laser and the optical fiber in the late 1960s, researchers began investigating the potential of optics to perform high-fidelity transmission, distribution, and processing of analog RF signals [10]. In this process, the RF signal is first modulated onto an optical carrier (historically 1310 and 1550 nm because of propagation characteristics in optical fiber), which was generated by a laser or an LED. The modulated optical carrier is transmitted through an extremely low-loss optical fiber over long distances to a destination, where it is converted back into an RF signal by a photodetector. The goal was to capture the natural advantages of optical fiber, namely very low propagation loss and RF frequency-independent propagation (i.e. wide bandwidths). Today, optical fiber exhibits losses as low as 0.5 dB/km and carries aggregate data rates over 1 Tbps; in contrast, RF cables have losses of 360 dB/km at 2 GHz [11] and gets even lossier at higher frequencies. Military and other weight sensitive platforms also sought lightweight optical fibers to replace heavy RF cables (1.7 kg/km vs. 80–600 kg/km) [12].

Soon after data transmission using fiber-optics had proven successful, researchers turned towards using optics to perform actual RF signal processing functions (see. Fig. 7). In 1991, the term *microwave photonics* was coined [13] to describe the general field of analog RF signal processing, distribution, and generation using optics and photonics, and has since continued to captivate the research community. Microwave photonics seeks to leverage the physics of optics to achieve functional-

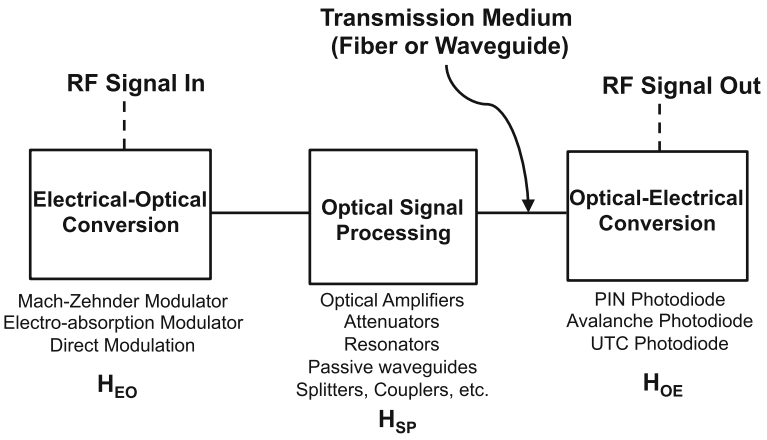

Fig. 7 A general analog optical link, showing RF input and output, and optical signal processing and distribution in the middle

ity and performance that is impossible to obtain using RF components. These key performance advantages include high dynamic range, low loss fiber, low susceptibility to electromagnetic interference, ease of reconfigurability, and perhaps most importantly wide bandwidth [11, 14–16].

The performance of a microwave photonic link, generically shown in Fig. 7, is determined by three main parts: the electrical-optical (EO) conversion, the intermediate optical signal processing, and the optical-electrical (OE) conversion. To speak a common language with RF engineers, microwave photonic links are often characterized using traditional RF figures of merit: link loss, noise figure, and dynamic range. Because the EO and OE conversions determine the fidelity of the signal as it transitions between the electrical and optical domains, the modulators and detector devices that perform this conversion have a dominant effect on the link loss (or gain), noise figure, and dynamic range. Over the years, microwave photonic links have shown consistent improvement in all three figures of merit and commercial products are now on the market [17–19]. The intermediate optical signal processing architecture determines the actual photonic circuit function. Microwave photonic implementations of FIR (or matched) filters [20–22], beamformers [22–25], wideband phase shifters [21, 26, 27], true-time delays [16, 21, 28], and interference cancellers [7, 29–33] have all been demonstrated.

3.2 Wide Bandwidth Operation

The wide bandwidth of optics is one of the primary reasons why optics is the de facto carrier of the Internet, and these benefits apply to wideband interference cancellation as well. Optics is able to process extremely wide bandwidth signals because

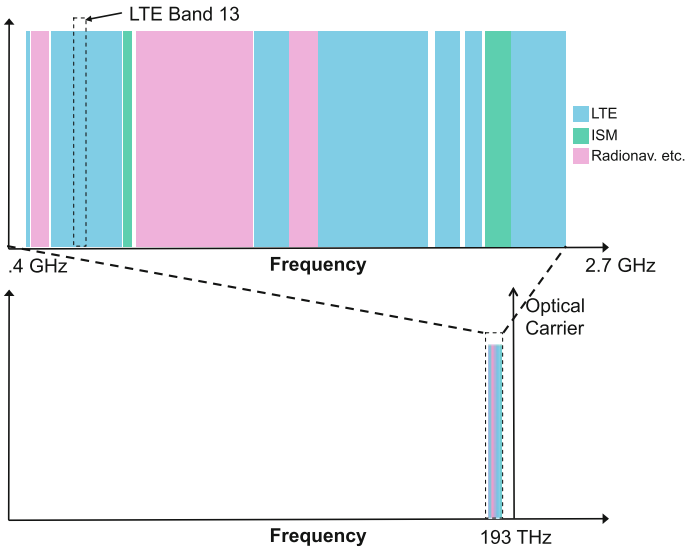

Fig. 8 A standard RF signal is essentially narrowband when modulated onto an optical carrier

of the tiny fractional bandwidth of an RF signal on an optical carrier. Whereas a single 20 MHz LTE channel may represent a significant bandwidth when modulated onto a 700 MHz RF carrier, it is virtually narrowband when modulated onto a 193 THz (1550 nm) optical carrier (Fig. 8). Modern optical devices can easily process RF signals from DC to 20 GHz, offering unprecedented flexibility to process wideband channels and tune freely between bands throughout the entire cellular spectrum and beyond. Innovations such as traveling wave electrodes [34] and uni-traveling carrier photodiodes have pushed the limit of RF frequencies that can be processed by optics well into the millimeter-wave regime [25, 35–37]. In contrast, RF front-end components are typically designed for a single frequency band and a relatively small instantaneous bandwidth (e.g. 20 MHz). Generally, *RF is narrowband and fixed, whereas optical circuits is wideband and tunable*. The wideband and tunable advantages of optics can enable enormous cost-savings by consolidating the RF front-end and create a path toward a true multiband radio.

3.3 Precise Amplitude and Delay Control

The precision of amplitude and delay control achievable by an interference canceller determines the maximum amount of cancellation that can be realized, per Fig. 6. The physics of optics enables relatively simple control of these two parameters so that continuous tunability and high precision can be obtained.

To effect amplitude control, mirror and semiconductor based devices with tunable gain or insertion loss are commonly used. Commercial mirror-based variable optical attenuators (VOAs) can achieve an RF attenuation resolution better than 0.01 dB/mV over a range of 30 dB, which is sufficient to obtain 50 dB of cancellation given sufficient phase matching. Semiconductor optical amplifiers (SOA) and electroabsorbers use a bias current or voltage to change a semiconductor's optical gain or absorption coefficient, respectively. SOAs can achieve similar gain resolution as a mirror-based VOA, but it is typically not a linear function of the SOA bias current and is also dependent on the input optical power. Additionally, memory and cross-gain saturation effects within the SOA can induce crosstalk between RF signals modulated onto different wavelength-division multiplexed optical carriers.

Tunable optical delay lines have been researched intensively for their important role in applications such as wideband true-time delays, FIR filters, beamforming, and optical buffers [16, 38–41]. They have been implemented through a variety of mechanisms such as mechanical positioning of mirrors, thermally-tuned refractive index spiral waveguides, microring resonators, Bragg gratings, and switching delays. Sub-picosecond delay resolution can be readily achieved by multiple delay technologies. At 10 GHz RF frequency, this corresponds to a phase shift of 0.01°, which is sufficient to meet high cancellation depths.

3.4 Low Latency Tunability

The minimum acceptable latency of an interference canceller is determined by the coherence time of the interfering channel, or how long it takes for the channel's response to change significantly. This depends strongly on the RF environment; as an example, a typical indoor office environment has a coherence time of about 100 ms [9]. Therefore, the chosen amplitude and delay tuning technologies must exhibit millisecond or shorter latencies to reduce system overhead. This rules out mechanical and thermal methods, which typically require at least 10s of milliseconds to settle down. The preferred tuning methods are therefore current/voltage controlled or switch-based. For amplitude control, current and voltage control mechanisms are either based on stimulated emission and absorption for III-V compounds or the free-carrier plasma dispersion effect in silicon [42, 43]. These effects are currently used in high-speed III-V and silicon modulators to achieve data rates of well over 10 Gbps. Therefore, they can easily satisfy the low latency requirements to track an interference channel as it dynamically evolves. For tunable delay and phase control, switching delays typically exhibit 10s of microseconds of latency, whereas tunable delays based on tuning resonances and wavelengths will depend on the semiconductor carrier and photon cavity lifetimes. Both of these are in the domain of nanoseconds and less.

3.5 High Dynamic Range

Lastly, an interference canceller must be able to both resolve weak signals of interest and deal with strong interferers simultaneously. Many microwave photonic links have demonstrated experimental dynamic ranges surpassing 120 dB/Hz$^{2/3}$ [19] (here we use third-order intermodulation spurious-free dynamic range or SFDR as the representative metric), which meets the stringent requirements of many analog RF applications.

In a microwave photonic link, the ceiling on the dynamic range is often set by the optical modulator, because of its nonlinear transfer function. With direct modulation (modulating the laser bias current using the RF signal), dynamic range is maximized by using a laser with as linear a light-current relationship as possible, maximizing gain, and minimizing relative intensity noise (RIN) [19, 44]. In direct modulation, the dynamic range is also a strong function of frequency, declining sharply as the operating frequency approaches the laser relaxation oscillation frequency [19, 45].

External modulators have the benefit of operating a continuous-wave laser and therefore, do not have the dynamic range degradation with respect to frequency that directly modulated links exhibit. However, both Mach-Zehnder modulators (MZM) and electro-absorption modulators (EAM) exhibit nonlinear transfer functions, which limit the link's dynamic range at high powers. Because an MZM's transfer function is predictable, it can be linearized by pre-distorting the input RF signal to eliminate the third-order intermodulation product [46]. Such linearized links have demonstrated SFDRs larger than 130 dB/Hz$^{4/5}$ [19], albeit at limited frequencies. Other techniques, such as low-biasing the MZM to lower noise and using dual-parallel MZMs to cancel third-order intermodulation products, have also been used to increase SFDR [13, 47, 48]. Overall, microwave photonic links can exhibit extremely large dynamic ranges. However, careful consideration of the link application requirements must be taken in account, as there is almost always a tradeoff between dynamic range, gain, noise figure, and bandwidth.

4 Optical Interference Cancellation System Architectures

An optical interference canceller can achieve unprecedented performance in terms of wide instantaneous bandwidth, tunable operating frequency range, and cancellation depth. The canceller architecture and components determine the canceller's capabilities and the tradeoffs between key parameters. We now present several system architectures that have been experimentally demonstrated, and analyze their performance. This section culminates in the demonstration, for the first time, of a monolithic photonic integrated circuit for interference cancellation, which has the potential to catapult the benefits of optical interference cancellation into cost-sensitive and commercial markets.

4.1 Two-Tap Manual Canceller with Balanced Photodetector

A two-tap discrete optical interference canceller architecture is shown in Fig. 9 [29]. The canceller propagates the corrupted received signal, $r(t) = s(t) + n(t)$, on one fiber path of the system, while the interference reference, $n_0(t)$, is processed and propagates on a second fiber path, which we call the cancellation path. With a single cancellation path, this canceller is designed to remove the dominant source of self-interference, which is usually either the line-of-sight signal in the case of a two-antenna communication system or the strongest leakage signal (e.g. circulator leakage or antenna return loss) in a duplexed single-antenna system. The optical modulation devices are two electro-absorption modulators (EAMs), which each receive a +10 dBm optical carrier from the same C-band (i.e. 1550 nm) laser source. The optical-to-electrical converter is a balanced photodetector, which also performs the subtraction. The overall system has a bandwidth of 10 GHz, limited by the EAMs.

To match the interference channel, a MEMS variable optical attenuator (VOA) and two manual tunable delay lines (TDL) based on free-space mirrors are used in the cancellation path. The MEMS VOA has attenuation resolution of 0.01 dB/mV with a range of 30 dB, while the combined TDL has sub-picosecond resolution with a full range of 375 ps. To subtract the processed interference reference from the corrupted received signal, a balanced photodetector is used, which outputs an electrical current proportional to the difference between the optical intensities incident on two separate photodiodes. To characterize the system, a wideband interference signal was combined with a much weaker, single-tone signal of interest. Interference cancellation was optimized by observing the output of the system on a spectrum analyzer and manually tuning the VOA and TDL until interference power was minimized.

Experimental results (Fig. 10) show that the system can cancel interference in both the 900 MHz and 2.4 GHz ISM (industrial, scientific, and medical) bands. All of these results were obtained by the same optical canceller by simply tuning the VOA

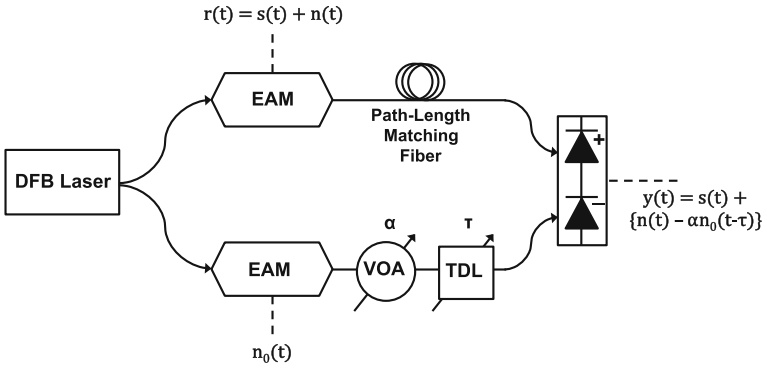

Fig. 9 Architecture of a two-tap canceller. $s(t)$ = signal of interest, $n(t)$ = self-interference, $n_0(t)$ = tap of original transmitter signal

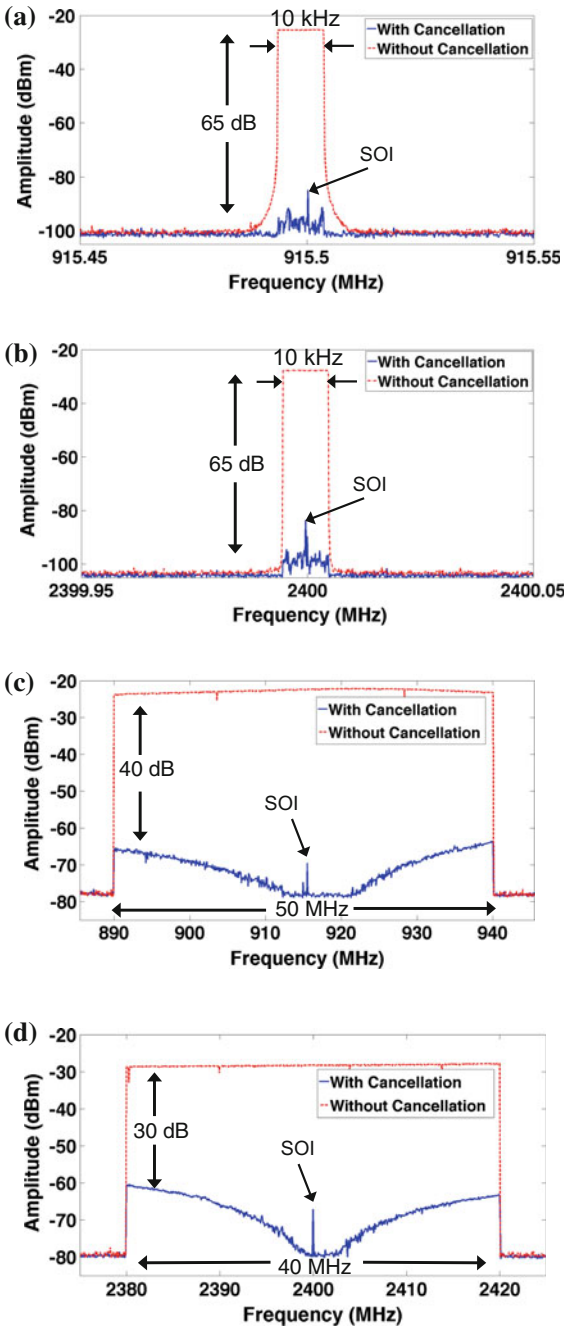

Fig. 10 Experimental results of interference cancellation in the (*top*) 900 MHz band and (*bottom*) 2.4 GHz band for broadband (*left*) and narrowband (*right*) interfering signals. SOI = signal of interest. Taken from [29]

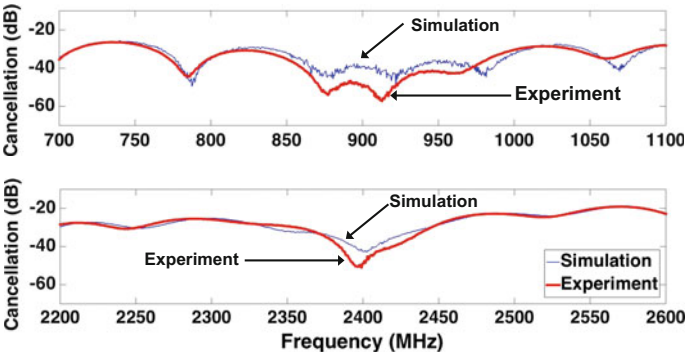

Fig. 11 Interference cancellation measured over 400 MHz in both the (*top*) 900 MHz band and (*bottom*) 2.4 GHz band. Taken from [29]

and TDL to account for the interference channel's frequency response, illustrating the wide tunability of the optical canceller. In fact, any system operating frequency from DC to 10 GHz can be selected by the VOA and TDL. The system achieves greater than 65 dB of cancellation of a narrowband interferer, demonstrating the high amplitude and delay precision of the optical components. For broadband cancellation, the system achieves better than 40 and 30 dB of cancellation for a 50 MHz and 40 MHz signal in the 900 MHz and 2.4 GHz bands, respectively. In all cases, the signal of interest is recovered, despite the in-band interference, which is a key advantage of interference cancellation over filtering. Because the cancellation system operates on the RF-level of the communication system, the results are completely independent of either signal of interest or interference signal modulation format.

The tradeoff between cancellation depth and bandwidth (see Sect. 2.3) can be studied by observing cancellation for a fixed system state across a wide bandwidth, as shown in Fig. 11. Cancellation degrades with bandwidth because of the inability of a two-tap system to model the interference channel's response at every frequency. Nonetheless, the optical system has clearly demonstrated the ability to operate over an extremely wide bandwidth.

4.2 Adaptive Canceller Using a Semiconductor Optical Amplifier

A limitation of the previous system was that the optical delay line was tuned mechanically, and therefore could not adapt to rapidly changing RF environments. The architecture featured in Fig. 12 utilizes similar principles to the interference canceller in the previous section; however, unlike the previous architecture, a semiconductor optical amplifier (SOA) is inserted into the cancellation path to provide a fast and fully electronic control interface. The SOA performs three key signal-processing

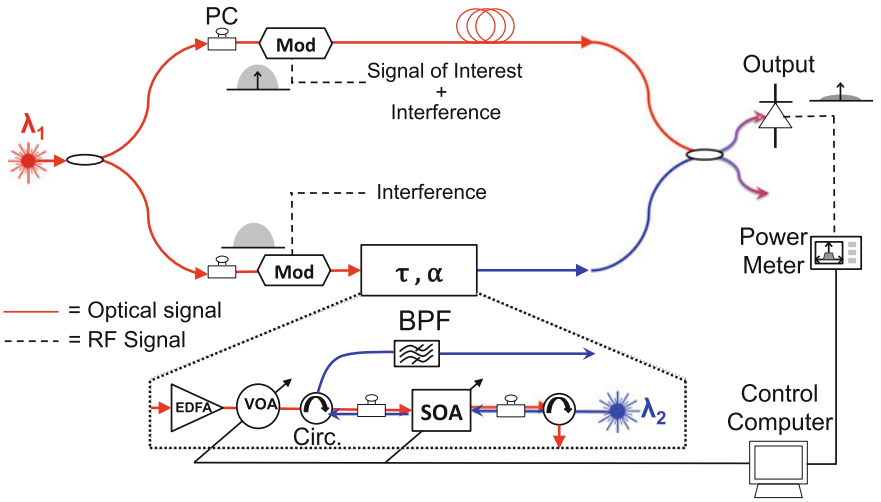

Fig. 12 Architecture of an adaptive canceller using a semiconductor optical amplifier based tunable delay line and variable optical weight. BPF = Bandpass Filter, EDFA = Erbium-Doped Fiber Amplifier, Mod = Modulator, PC = Polarization Controller

functions related to interference cancellation: amplitude control, delay control, and signal inversion. The SOA achieves a tunable optical delay by controlling the group velocity of the propagating signal through both the SOA bias current and input optical power. Controlling the group velocity of optical semiconductors has been coined slow and fast light, and has been investigated thoroughly for its applications in microwave photonic filters, beamformers, and optical buffers. [26, 40, 49, 50].

In addition to setting a time delay, the SOA bias current and input optical power also affect the SOA gain; therefore, the SOA can also be used to control the RF signal amplitude. Simultaneous and independent control of the signal amplitude and delay is realizable because two independent control variables (SOA bias current and input optical power) are used to drive the SOA. The relationships between SOA bias current, input optical power, RF gain, and RF time delay are shown in Fig. 13. The SOA can be operated in constant-gain mode, constant-delay mode, or variable gain and delay mode [38].

Finally, the SOA is also used to invert the RF signal by counter-propagating a second, continuous-wave optical signal of different wavelength through the SOA and subjecting it to cross-gain modulation in the SOA. The second optical signal exits the SOA with the RF signal imprinted onto it, except inverted. The subtraction occurs in a 50/50 optical coupler, which combines the received signal path with the processed and inverted cancellation path. The output is detected by a photodetector.

The SOA-based architecture achieves similar performance to the previous architecture: 40 dB cancellation over 60 MHz at 900 MHz band and 56 dB narrowband cancellation [30]. The narrowband cancellation is reduced by 9 dB compared to the previous architecture because the noise floor rises with the addition of the SOA. The

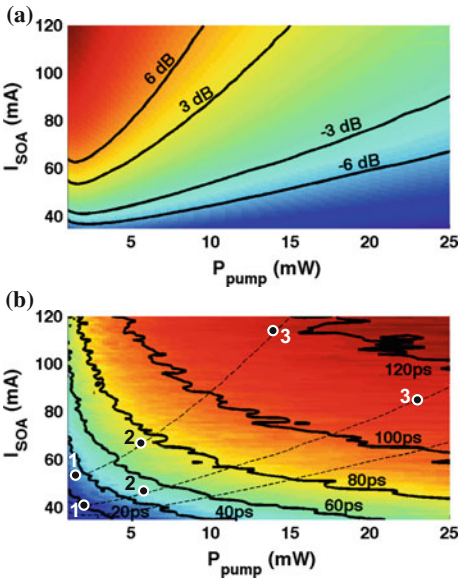

Fig. 13 Relationship between SOA bias current (I_{SOA}) and input optical power (P_{pump}) on **a** RF gain, and **b** RF delay. *Curves* correspond to constant-gain lines and constant-delay lines. Taken from [38]

9 dB rise in noise floor is in agreement with estimated SOA noise figure, and is one tradeoff of using the SOA.

The SOA's fully electronic control variables are used to implement a computer-controlled optimization algorithm to adaptively cancel interference. An example experimental run of the algorithm is shown in Fig. 14a. A map of the output residual interference power as a function of the SOA control variables is retroactively superimposed. Figure 14b demonstrates that the algorithm converges to the global minimum solution over a delay mismatch range of 83 ps (the maximum SOA-induced delay range was 120 ps). We note that 120 ps is not a sufficient delay range to account for delay variations in most RF environments, particularly if antennas are subject to movement. Indeed, additional coarse delays (either optical or RF) will be required to account for large delay variations. With regards to speed, the settling time of the SOA corresponds to the inverse of the modulation bandwidth of the SOA, which is about 1 μs for these devices. This can be improved by selecting SOAs designed for high modulation bandwidths. The SOA-based tunable delay is thus well-suited to react to rapid but small changes in delay, such as antenna vibrations.

As a bit of foreshadowing, the SOA-based interference canceller sheds light on a possible path to achieving a fully-integrated interference canceller, by designing the signal-processing functions of amplitude control, delay control, and signal inversion into a semiconductor.

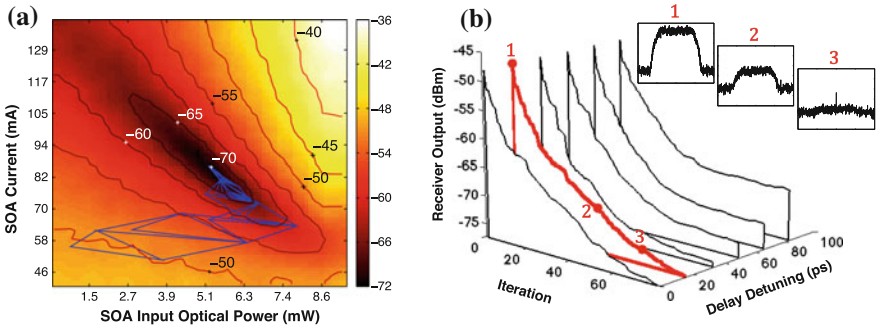

Fig. 14 **a** The SOA-based interference canceller adaptively canceling interference using the SOA bias current and input optical power as control knobs. **b** The system converges to the global minimum over a range of 83 ps. Insets show the output spectra as the algorithm progresses. Taken from [30]

4.3 Adaptation to Wireless Environments

In practical wireless environments, multipath propagation introduces multiple copies of self-interference, each with a different set of attenuation and delay (see Eq. 3). Therefore, any practical implementation of an interference cancellation system will need to consider multipath components as additional interference sources.

Here, we examine the architecture of an optical self-interference canceler for a co-located transmitter-receiver in an outdoor environment [51]. This architecture boasts a scalable method of canceling multiple copies of self-interference. Figure 15 shows the architecture of the optical canceler and how it interfaces with the RF front end of a communication system, complementing the following system description.

The system takes two inputs: (1) the reference interference signal from a tap of the transmitter output, $x_{\mathrm{TX}}(t) = n_0(t)$, and (2) the corrupted received signal, $x_{\mathrm{RX}}(t) = s(t) + \sum_{i=1}^{N} n_i(t)$, where $s(t)$ is the signal of interest (SOI) and $n_i(t)$ is the *ith* multipath component of $x_{\mathrm{TX}}(t)$. For example, $n_1(t)$ is the line-of-sight self-interference and $n_2(t)$ is the strongest multipath component etc. The reference interference is tapped from the transmitter using a balun, which provides an inverted copy of the reference interference for the optical canceler (see Fig. 15)

The RF input signals are then each separately modulated onto two optical carriers at 1552.56 and 1550.55 nm using electroabsorption modulated lasers. The modulated self-interference reference signal is split into N cancellation paths using a 1:N optical splitter, one for the line-of-sight and the rest for multipath components. Here, we use $N = 2$ cancellation paths.

The receive antenna picks up a sum of distorted multipath components of the transmit interference signal, $\sum_{i=1}^{N} n_i(t)$, which underwent channel effects of attenuation, delay, other front end components, and noise. Because of these effects, the N interference reference copies in the cancellation paths, $n_{0_{copy(i)}}(t)$, do not exactly match the interference signals in the receiver, $n_i(t)$, and must be adjusted in ampli-

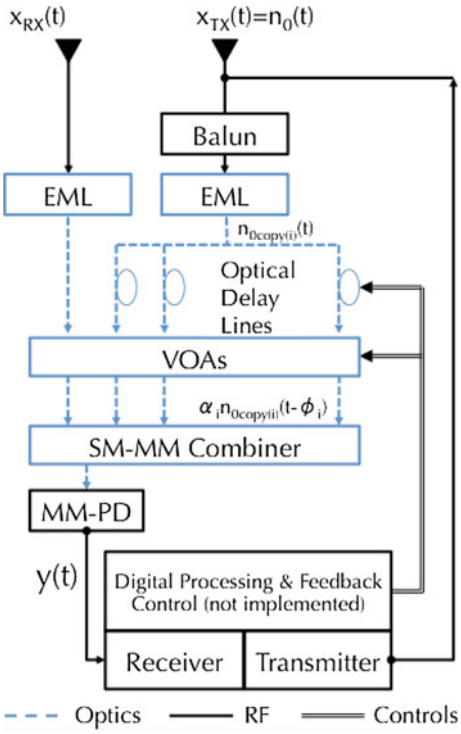

Fig. 15 Simplified diagram of the scalable optical cancellation system connected to two directional antennas [51]. EML = Electroabsorption Modulated Laser, VOA = Variable Optical Attenuator, SM-MM = SingleMode to MultiMode, and MM-PD = MultiMode Photodetector. Fiber delay lines are represented by *blue loops*

tude and phase to match. The goal of the optical canceller is to delay and attenuate each interference reference copy $n_{0_{copy(i)}}(t)$, with unique parameters ϕ_i and α_i, respectively, such that it resembles each $n_i(t)$ as closely as possible, thereby achieving the maximum cancellation. To perform these adjustments, each cancellation path undergoes delay matching using fixed optical fiber lengths and tunable optical delay lines, and amplitude matching using variable optical attenuators, yielding $\alpha_i n_{0_{copy(i)}}(t-\phi_i)$.

After tuning adjustments, both the cancellation and received signals are fed into separate inputs of a custom-built 8×1 singlemode to multimode combiner (SM-MM) combiner. The SM-MM combiner maps each singlemode input onto orthogonal spatial modes of a multimode fiber [52]. Since each optical signal resides in an orthogonal spatial mode, all optical carriers can share wavelengths without suffering coherent beat noise. This eliminates the need for a separate optical source for each multipath component as well as the associated multiplexers/demultiplexers/modulators that would be necessary otherwise. Specifically, without the SM-MM combiner, this system, with $N = 2$ taps, would require three distinct optical sources and modulators. Although this allows each laser and modulator to be tailored to optimize different trade-offs, its scalability is limited.

Finally, the combined optical signal is detected by a multimode photodetector. Because each optical signal resides in a different spatial mode of the multimode fiber,

the photodetector incoherently sums each optical signal in the output RF photocurrent. This operation results in the subtraction of the self-interference copies from the received signal, since the self-interference copies were initially inverted by a balun. The system output can be represented as:

$$\begin{aligned} y(t) &= x_{\mathrm{RX}}(t) - \sum_{i=1}^{N} \alpha_i \, n_{0_{copy(i)}}(t - \phi_i) \\ &= s(t) + \left\{ \sum_{i=1}^{N} n_i(t) - \sum_{i=1}^{N} \alpha_i \, n_{0_{copy(i)}}(t - \phi_i) \right\} \end{aligned}$$

where our goal is to reduce the term in brackets to 0 such that $y(t) \rightarrow s(t)$.

Figure 16 shows the results of the optical canceller used in an outdoor environment to uncover a weak signal of interest [51]. The canceller, wielding two cancellation paths, canceled the line-of-sight component of self-interference and the strongest multipath component of the same self-interference. The system achieved 34 dB of narrowband cancellation and >29 dB of cancellation across 20 MHz of instantaneous bandwidth. Multipath cancellation contributed more than 10 dB of additional cancellation. This additional cancellation enabled the system to uncover a weak sigal of interest received at 5 dB above the noise floor [51].

4.4 A Monolithically Integrated Optical Canceller

Although discrete optical cancellers achieve impressive performance, they are impractical for cost-sensitive commercial applications due to their large size, high cost, and power hungry nature. Miniaturizing the optical canceller into a monolithic photonic integrated circuit (PIC) can offer a panacea to these issues and pave avenues to new applications. A PIC is compact and mobile, since it is a single semiconductor chip; scalable and low cost, since it can leverage the economies of scale of the semiconductor industry; and robust to thermal and vibrational shock, since it is purely solid-state. With these advantages, the PIC canceller creates a win-win situation for both performance and cost. Here, we introduce the design and demonstration, for the first time, of a monolithically integrated PIC canceller.

4.4.1 Integrated Circuit Architecture and Design

The PIC canceller is designed to mimic the functionality of the discrete optical canceler while eliminating its weaknesses. First, the PIC canceller is optically self-contained, meaning that it has monolithically integrated lasers and photodetectors so that the electrical-optical and optical-electrical conversions are all performed on-chip. This eliminates the expensive and tedious fiber-coupling process that drives

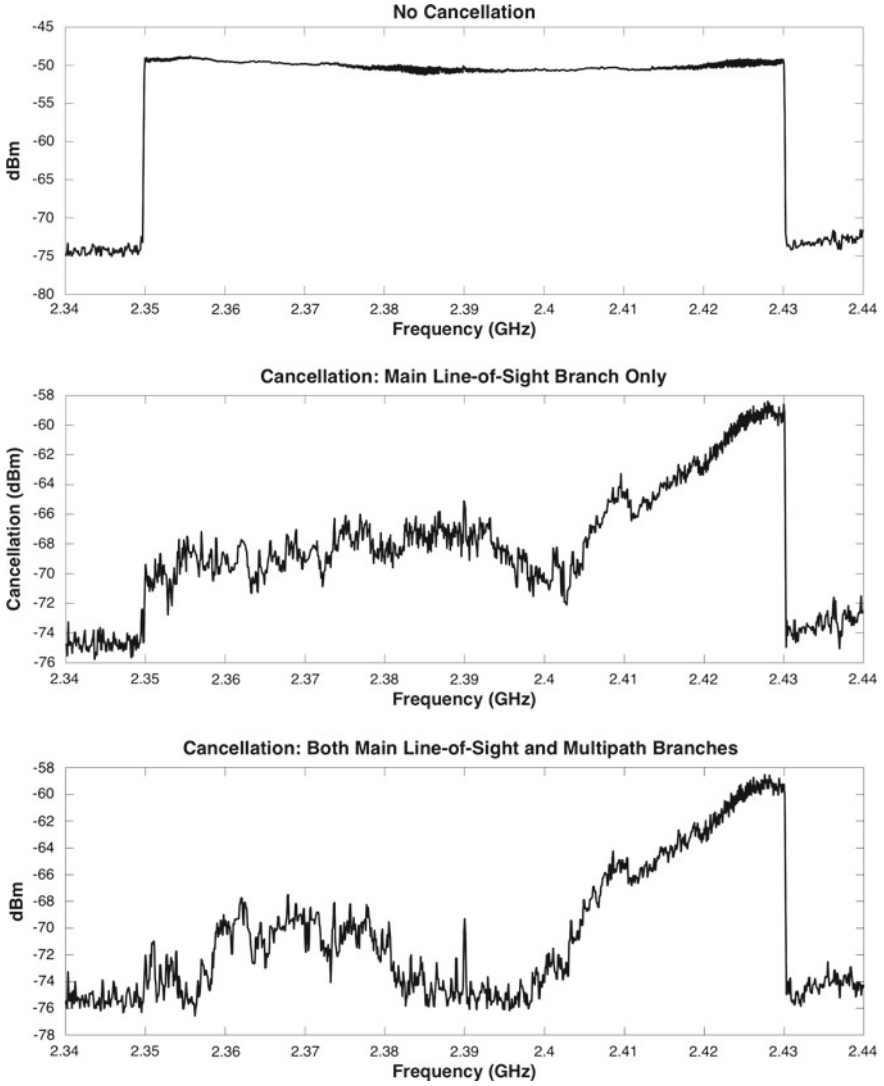

Fig. 16 A weak signal of interest received at 5 dB above the noise floor is uncovered with the help of the multi-tap optical canceller. The spectrum analyzer plots show the output of the canceller (*top*) without cancellation, (*middle*) with cancellation using only the line-of-sight cancellation path, and (*bottom*) with cancellation using both the line-of-sight and the multipath cancellation paths. Only the last configuration is able to uncover the weak SOI

packaging costs in optical components and other PICs. Instead, the PIC can be packaged using standard IC packaging technology. Second, instead of optical fiber, semiconductor optical waveguides carry the optical signal from one optical device to the next (Fig. 17), greatly reducing the loss caused by cascaded fiber-couplings between discrete optical components. This loss can be 1–2 dB *per fiber-coupling*, which results in 2–4 dB of RF loss due to the square law relationship between optical and RF power. Link designers now have more margin in the loss budget and can make tradeoffs to improve dynamic range, noise figure, or bandwidth.

As with the discrete optical canceller, the optical modulators are critical to the performance of the PIC canceller. The PIC canceller erforms electrical-optical conversion via direct modulation of etched facet Fabry-Perot lasers as the optical modulator (see Fig. 18). Although, distributed feedback (DFB) lasers are usually the monolithic laser source in PICs, the etched-facet laser design eliminates the requirement for complicated electron-beam or stepper lithography, as well as one regrowth step, which adds cost and reduces yield. The etched facet is created by dry-etching a trench to produce a vertical sidewall that is sufficiently smooth to act as a reflective laser

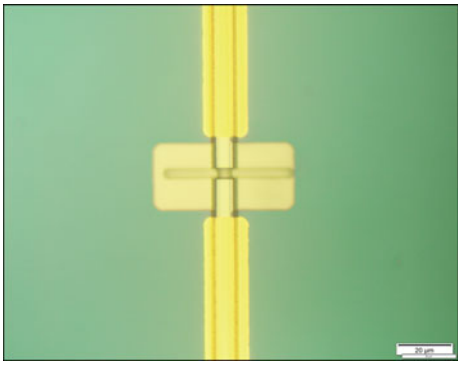

Fig. 17 Mode-matched ridge

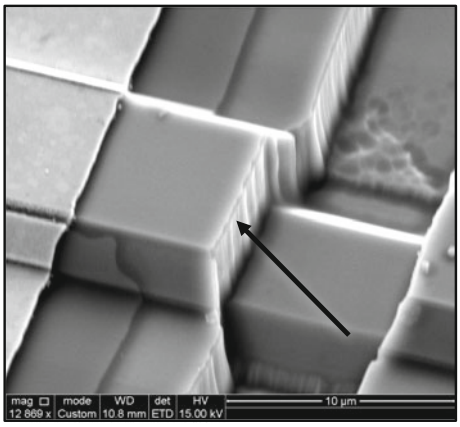

Fig. 18 Etched facet laser

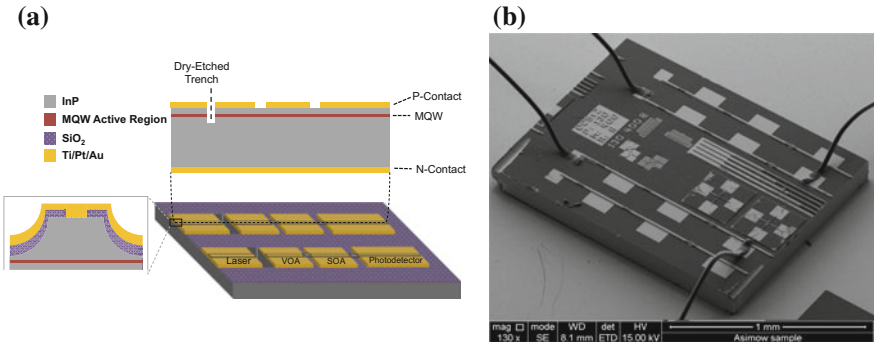

Fig. 19 **a** Schematic of the chip layout and composition. **b** Scanning Electron Microscope image of a fabricated PIC

facet. The 5 μm wide trench is etched 3 μm deep into the existing ridge waveguide, which connects the laser to the remainder of the photonic circuit. The lack of an external modulator also reduces insertion loss and the need for an additional device; however, further research on alternative laser and modulator devices is ongoing.

Architecturally speaking, each PIC canceller is composed of two paths: one for the propagation of the reference interference signal (the cancellation path) and one for the propagation of the corrupted received signal (see Fig. 19a). Both paths have tunable amplitude and phase devices to maximize tunability range. All elements on the PIC canceller are connected by integrated waveguides, which carry the optical/RF signal from one element to the next with minimum loss. Both paths consists of a monolithic laser, tunable delay line, semiconductor optical amplifier (SOA), and photodetector. As with the architecture presented in Sect. 4.2, the SOA plays a critical role in the functionality of the canceller. It overcomes the speed bottleneck that is present in the discrete optical canceller while also implementing amplitude matching of the RF signal via current injection. A waveguide photodetector converts the processed optical signal back into an RF signal. Gold wirebonds are used to transfer the RF signals to and from the PIC. Finally, the subtraction mechanism is performed by using a differential transimpedance amplifier following the photodetectors.

The PIC is fabricated on a 1550 nm multiple quantum well laser-diode epitaxial wafer. The active region of the wafer consists of 5 InGaAlAs quantum wells grown on a semi-conducting InP substrate; the photoluminescence spectral peak of the wafer is 1542 nm. The fabrication of the PIC requires five mask layers: ridge definition, electrical isolation, trench etch, contact window opening, and p-contact deposition. Following fabrication, the PICs are lapped, cleaved, and mounted to a silicon submount, which facilitates electrical contact and testing. Each cleaved die, which also includes test structures and other elements, is 2.5 mm × 2 mm. A scanning electron microscope image of a single PIC die is shown in Fig. 19b.

PICs were characterized for both DC optical performance and interference cancellation. Self-interference cancellation tests were conducted by generating an interfer-

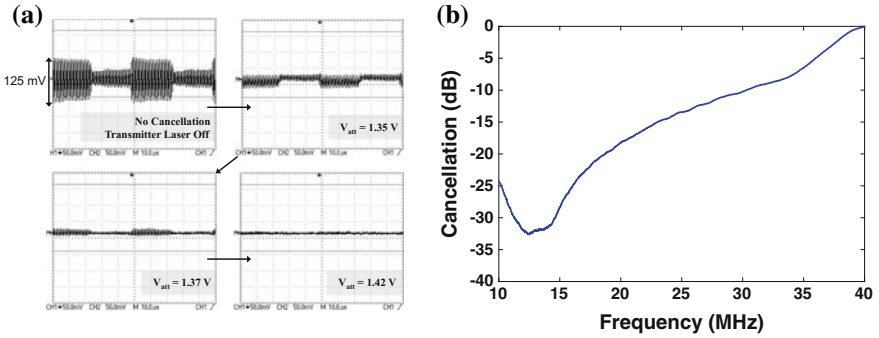

Fig. 20 **a** Oscilloscope plots of the PIC dynamically reducing AM self-interference. **b** Cancellation versus bandwidth

ence signal using a signal generator and modulating it onto both paths of the PIC. The system was then tuned to optimize cancellation of the self-interference by adjusting the laser and photodetector bias voltages to amplitude match the reference interference with the interference in the corrupted received signal.

Preliminary results of the experiment are shown in Fig. 20a and demonstrate the convergence of the PIC from zero cancellation to maximum cancellation. In these experiments, the delay is matched ahead of time, and the amplitude is tuned from completely unmatched (i.e. cancellation path is off) to optimum matching. As the PIC improves the amplitude matching between the interference reference and the actual interference signal, the residual interference at the PIC output is slowly reduced until it hits the noise floor. The cancellation versus bandwidth tradeoff for the PIC is shown in Fig. 20b, indicating that optimum cancellation is achieved over about 5 MHz instantaneous bandwidth and degrades sharply outside that bandwidth. The degradation is a result of deviations between the frequency responses of the two different paths of the PIC. We believe that the deviation results from significant differences in parasitics, such as wirebond lengths and the traces on the silicon submount. Fabrication adjustments to improve the chip bandwidth are currently underway.

5 Integrated Microwave Photonics and Future Prospects

For the past few decades, research on microwave photonics has primarily focused on discrete fiber-optic systems. These systems were built to address niche applications, such as military and defense, where performance is the top priority over cost. However, the recent years have witnessed a flurry of interest in high data rate (Gbps) telecommunications, such as wireless sensor networks, broadband public access points, and small cell and picocell backhaul. These applications are much more cost-sensitive and are not appropriate for discrete fiber systems. The emerging field of *integrated microwave photonics* is poised to address these high data rate

applications, while also meeting their price-point. The high volume demand of these applications can also serve as the catalyst to generate the capital needed to propel the integrated microwave photonic infrastructure to commercial readiness.

Integrated microwave photonics seeks to package the advantages of optics, such as wide bandwidth and frequency-agnostic performance, into an integrated circuit, where it can leverage the economies of scale of the semiconductor industry. The primary barriers to the commercial viability of such systems are the economics (yield) and the fabrication of materials and devices, which must satisfy stringent application requirements. As opposed to electronic ICs, where the transistor is the dominant device, multiple optical devices are needed per photonic integrated circuit (PIC), leading to a more difficult fabrication process. Unlike discrete microwave photonics, where each device can be optimized on separate materials, integrated microwave photonics compromises this degree of freedom for manufacturing simplicity. Yet, great strides have been made in recent years to increase the number of devices integrated on one PIC and reduce the killer defect density to increase yield (see Fig. 21). Infinera, the first widely successful PIC company, has led the charge by fabricating a PIC with over 400 devices, capable of aggregate data rates of 500 Gbps [53]. Indeed, a Moore's Law of Photonics has already been declared.

Photonic integrated circuits (PICs) are primarily being built in three core material platforms: InP and GaAs (III-V), silicon-on-insulator, and silicon nitride. Each platform has its unique advantages and disadvantages and should be selected based on the application requirements; a review for each platform is provided in [55]. Multi-Project Wafer (MPW) consortia for standardized PIC development, such as IMEC and JeppiX in Europe, have made PIC research much more accessible to researchers and developers worldwide. These initiatives consolidate resources and know-how to make it affordable for industry and academic researchers to experiment with PICs. A standard software ecosytem (layout, verification, extraction) and simulation platform is also needed to unite the PIC community in a similar fashion to what was achieved in silicon. Companies such as PhoeniX and PhotonDesign have begun this effort.

It is an exciting time to be involved in integrated microwave photonics research because manufacturing technology maturity, device performance, and market demand

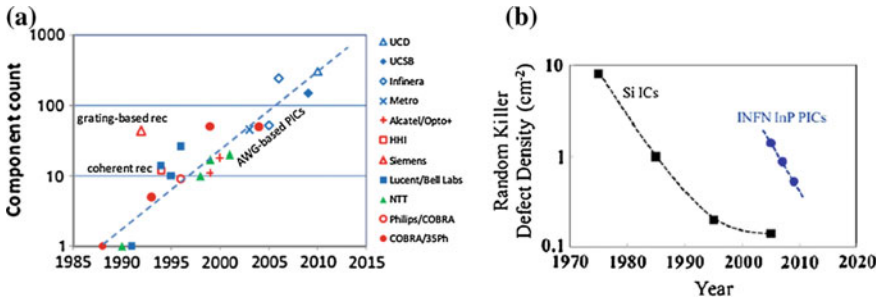

Fig. 21 **a** Device count per PIC. Taken from [54]. **b** Killer defect density. Taken from [53]

for high-performance RF analog signal processing have arrived at a common intersection. Wireless sensor networks and interference cancellation will certainly benefit from the progress being made in these fields, and we expect that they will be but one of many.

References

1. Cisco, Cisco Visual Networking Index: Global Mobile Data Traffic Forecast Update, 2015–2020 (2016)
2. Resonant Inc., Radically reducing the cost and size of cellphone RF filters to fuel the mobile revolution, Tech. Rep. (2015)
3. S. Choi, A. Cichocki, A. Beloucharni, Second order nonstationary source separation. J. VLSI signal Process. Syst. Signal, Image Video Technol. **32**(1–2), 93–104
4. S. Lee, S. Choi, A. Cichocki, H.M. Park, Blind source separation and independent component analysis: a review, Jan 2005
5. G. Fabrizio, A. Farina, Blind source separation with the generalised estimation of multipath signals algorithm. IET Radar Sonar Navig. **8**(9), 1255–1266 (2014)
6. S. Hong, J. Brand, J. Choi, M. Jain, J. Mehlman et al., Applications of self-interference cancellation in 5G and beyond. IEEE Commun. Mag. **52**(2), 114–121 (2014)
7. M.P. Chang, P.R. Prucnal, Full-duplex spectrum sensing in cognitive radios using optical self-interference cancellation, in *2015 9th International Conference on Sensors and Technology* (IEEE, 2015), pp. 341–344
8. M. Jain, J.I. Choi, T. Kim, D. Bharadia, S. Seth et al., Practical, real-time, full duplex wireless, in *Procedings of 17th Annual International Conference on Mobile Computing Networks—MobiCom '11* (ACM Press, New York, New York, USA, 2011), p. 301
9. D. Bharadia, E. McMilin, S. Katti, Full duplex radios, in *Proceedings of ACM SIGCOMM 2013 Conference—SIGCOMM '13*, vol. 43, no. 4 (ACM Press, 2013, New York, New York, USA), p. 375
10. R.C. Williamson, R.D. Esman, RF photonics. J. Light. Technol. **26**(9), 1145–1153 (2008)
11. J. Capmany, D. Novak, Microwave photonics combines two worlds, in *National Photonics*, vol. 1, no. 6, June 2007, pp. 319–330
12. E. Granot, R. Weber, S. Tzadok, G. Gertel, N. Narkiss, Fibers vs. coax for RF delay line applications, in *2009 IEEE International Conference on Microwaves, Communications, Antennas and Electronics System* (IEEE, Nov 2009), pp. 1–2
13. D. Marpaung, *High Dynamic Range Analog Photonic Links: Design and Implementation* (2009)
14. J. Yao, Microwave photonics. J. Light. Technol. **27**(3), 314–335 (2009)
15. A.J. Seeds, K.J. Williams, Microwave photonics. Light. Technol. J. **24**(12), 4628–4643 (2006)
16. R.A. Minasian, Photonic signal processing of microwave signals. IEEE Trans. Microw. Theory Tech. **54**(2), 832–846 (2006)
17. C.H. Cox, Gain and noise figure in analogue fibre-optic links, pp. 238–242 (1992)
18. C.H. Cox, E. Ackerman, R. Helkey, G.E. Betts, Techniques and performance of intensity-modulated direct-detection of analog optical links. IEEE Trans. Microw. Theory Tech. **45**(8), 1375–1383 (1997)
19. C. Cox, E. Ackerman, G. Betts, J. Prince, Limits on the performance of RF-over-fiber links and their impact on device design. IEEE Trans. Microw. Theory Tech. **54**(2), 906–920 (2006)
20. J. Capmany, B. Ortega, D. Pastor, A tutorial on microwave photonic filters. J. Light. Technol. **24**(January), 201–230 (2006)
21. R.A. Minasian, Ultra-wideband and adaptive photonic signal processing of microwave signals. IEEE J. Quantum Electron. **52**(1), 1–13 (2016)

22. J. Chang, M.P. Fok, R.M. Corey, J. Meister, P.R. Prucnal, Highly scalable adaptive photonic beamformer using a single mode to multimode optical combiner. IEEE Microw. Wirel. Components Lett. **23**(10), 563–565 (2013)
23. J. Chang, J. Meister, P.R. Prucnal, Implementing a novel highly scalable adaptive photonic beamformer using "blind" guided accelerated random search. J. Light. Technol. **32**(20), 3623–3629 (2014)
24. S. Fathpour, Silicon-photonics-based wideband radar beamforming: basic design. Opt. Eng. **49**(1), 018201 (2010)
25. T.P. McKenna, J.A. Nanzer, T.R. Clark, Photonic beamsteering of a millimeter-wave array with 10-Gb/s data transmission. IEEE Photonics Technol. Lett. **26**(14), 1407–1410 (2014)
26. J. Sancho, J. Lloret, I. Gasulla, S. Sales, J. Capmany, Fully tunable 360 microwave photonic phase shifter based on a single semiconductor optical amplifier. Opt. Express, **19**(18), 17–421 (2011)
27. W. Xue, S. Sales, J. Capmany, J. Mørk, Wideband 360 degrees microwave photonic phase shifter based on slow light in semiconductor optical amplifiers. Opt. Express **18**(6), 6156–6163 (2010)
28. K.L. Deng, K.I. Kang, I. Glask, P. Prucnal, A 1024-channel fast tunable delay line for ultrafast all-optical TDM networks. IEEE Photon. Technol. Lett. **9**(11), 1496–1498 (1997)
29. M.P. Chang, M. Fok, A. Hofmaier, P.R. Prucnal, Optical analog self-interference cancellation using electro-absorption modulators. IEEE Microw. Wirel. Compon. Lett. **23**(2), 99–101 (2013)
30. M.P. Chang, C.-L. Lee, B. Wu, P.R. Prucnal, Adaptive optical self-interference cancellation using a semiconductor optical amplifier. IEEE Photonics Technol. Lett. **27**(9), 1018–1021 (2015)
31. J. Chang, P.R. Prucnal, A novel analog photonic method for broadband multipath interference cancellation. IEEE Microw. Wirel. Compon. Lett. **23**(7), 377–379 (2013)
32. C. Cox, Transmit isolating photonic receive links: a new capability for antenna remoting, in *Optical Fiber Communication Conference on Fiber Optic Engineers 2011* (OSA, Washington, D.C., Mar 2011), p. OThA1
33. C. Cox, E. Ackerman, Demonstration of a single-aperture, full-duplex communication system, in *2013 IEEE Radio Wireless Symposium* (IEEE, Jan 2013), pp. 148–150
34. R. Alferness, Waveguide electrooptic modulators. IEEE Trans. Microw. Theory Tech. **30**(8), 1121–1137 (1982)
35. J.-W. Shi, C.-B. Huang, C.-L. Pan, Millimeter-wave photonic wireless links for very high data rate communication. NPG Asia Mater. **3**(4), 41–48 (2011)
36. M. Fice, E. Rouvalis, F. Van Dijk, A. Accard, F. Lelarge et al., 146-GHz millimeter-wave radio-over-fiber photonic wireless transmission system. Opt. Express **20**(2), 1769–1774 (2012)
37. A. Hirata, H. Ishii, T. Nagatsuma, Design and characterization of a 120-GHz millimeter-wave antenna for integrated photonic transmitters. IEEE Trans. Microw. Theory Tech. **49**(11), 2157–2162 (2001)
38. M.P. Chang, N. Wang, B. Wu, P.R. Prucnal, A simultaneous variable optical weight and delay in a semiconductor optical amplifier for microwave photonics. J. Light. Technol. **33**(10), 2120–2126 (2015)
39. P.A. Morton, J. Cardenas, J.B. Khurgin, M. Lipson, Fast thermal switching of wideband optical delay line with no long-term transient. IEEE Photonics Technol. Lett. **24**(6), 512–514 (2012)
40. F. Xia, L. Sekaric, Y. Vlasov, Resonantly enhanced all optical buffers on a silicon chip, in *2007 Photonics Switch. PS* (2007), pp. 7–8
41. J.K.S. Poon, L. Zhu, G.A. DeRose, A. Yariv, Transmission and group delay of microring coupled-resonator optical waveguides. Opt. Lett. **31**(4), 456–458 (2006)
42. B. Jalali, S. Fathpour, Silicon Photonics. J. Light. Technol. **24**(12), 4600–4615 (2006)
43. R. Soref, The past, present, and future of silicon photonics. IEEE J. Sel. Top. Quantum Electron. **12**(6), 1678–1687 (2006)
44. G. Bodeep, T. Darcie, Semiconductor lasers versus external modulators: a comparison of nonlinear distortion for lightwave subcarrier CATV applications. IEEE Photonics Technol. Lett. **1**(11), 401–403 (1989)

45. K.Y. Lau, A. Yariv, Intermodulation distortion in a directly modulated semiconductor injection laser. Appl. Phys. Lett. **45**(10), 1034 (1984)
46. R. Childs, V. O'Byrne, Multichannel AM video transmission using a high-power Nd:YAG laser and linearized external modulator. IEEE J. Sel. Areas Commun. **8**(7), 1369–1376 (1990)
47. L.M. Johnson, H.V. Roussell, Reduction of intermodulation distortion in interferometric optical modulators. Opt. Lett. **13**(10), 928 (1988)
48. S. Korotky, R. de Ridder, Dual parallel modulation schemes for low-distortion analog optical transmission. IEEE J. Sel. Areas Commun. **8**(7), 1377–1381 (1990)
49. J. Capmany, I. Gasulla, S. Sales, Microwave photonics: Harnessing slow light. Nat. Photonics **5**(12), 731–733 (2011)
50. J.B. Khurgin, Slow light in various media: a tutorial. Adv. Opt. Photonics **2**(3), 287 (2010)
51. J. Sun, M. Chang, R.P. Paul, Scalable optical self-interference cancellation system for over-the-air multipath interference, IEEE Photonics J. (2016)
52. M.P. Fok, Y. Deng, K. Kravtsov, P.R. Prucnal, Signal beating elimination using single-mode fiber to multimode fiber coupling. Opt. Lett. **36**(23), 4578–4580 (2011)
53. F.A. Kish, D. Welch, R. Nagarajan, J.L. Pleumeekers, V. Lal et al., Current status of large-scale InP photonic integrated circuits. IEEE J. Sel. Top. Quantum Electron. **17**(6), 1470–1489 (2011)
54. M. Smit, J.V.D. Tol, M. Hill, *Moore's law in photonics*, vol. 13, no. 1 (2012), pp. 1–13
55. D. Marpaung, C. Roeloffzen, R. Heideman, A. Leinse, S. Sales, J. Capmany, Integrated microwave photonics. Laser Photonics Rev. **7**(4), 506–538 (2013)

Traffic Adaptive Channel Access Scheme for IEEE802.15.4 Cluster-Based WSNs Under Spatial Non-uniform Traffic Condition

Akiyuki Yamauchi, Kazuo Mori and Hideo Kobayashi

Abstract Difference in transmission performance arises between cluster heads (CHs) involved in inter-cluster communication on IEEE 802.15.4 cluster-based wireless sensor networks (WSNs) under spatial non-uniform traffic condition where the CHs have various amount of traffic. In this chapter, we first quantitatively-clarify appearance of the performance difference between different traffic loaded CHs under such traffic condition, and then proposes traffic adaptive channel access scheme to mitigate this performance difference. In the proposed scheme, introducing autonomous traffic adaptive priority access control, the CHs adjust their backoff exponent *BE*, which is one of key control parameters in IEEE 802.15.4 MAC, based on their estimated traffic status relative to other CHs. Through performance evaluation by computer simulation, this chapter shows that the proposed scheme can reduce the performance difference between CHs with different traffic loads in inter-cluster communication under spatial non-uniform traffic conditions.

1 Introduction

Due to limited network resources such as battery capacity and processing capability, wireless sensor networks (WSNs) absolutely require lower energy consumption and simpler processing mechanism to achieve long network lifetime under limited network resource condition [1, 2]. To satisfy these requirements, duty cycle mechanism, under which sensor nodes (SNs) periodically put their communication functions in inactive state, and cluster-based network topology, under which neighbouring SNs form a cluster and each SN transmits its measured data to its cluster head (CH) and then the CH sends the aggregated data to a sink node (or a parent CH), are deeply investigated in recent years [3, 4].

A. Yamauchi · K. Mori (✉) · H. Kobayashi
Mie University, Tsu, Japan
e-mail: kmori@elec.ie-u.ac.jp

S. Mukhopadhyay et al. (eds.), *Sensors for Everyday Life*, Smart Sensors, Measurement and Instrumentation 23, DOI 10.1007/978-3-319-47322-2_14

As a practical example of medium access control (MAC) mechanisms for WSNs, IEEE802.15.4 MAC [5] specifies beacon enabled mode, and this mode provides energy saving operation based on the duty cycle mechanism. The beacon enabled mode adopts superframe structure in time axis on communication channels and achieves active/inactive alternative operation at SNs based on the superframe, leading to lower energy consumption in WSNs. On the other hand, the cluster based topology also contributes to reduction of energy consumption in WSNs due to reduced transmission power at SNs and traffic load dispersion. Hence, previous studies have investigated clustering mechanisms to achieve low energy WSNs [6–8].

In cluster-based WSNs, the data communication consists of two parts; intra-cluster and inter-cluster communications. CHs collect measured data from their subordinate SNs in the intra-cluster communication, whereas in the inter-cluster communication, child CHs (CCHs), which are lower level CHs in a network and generally located near the periphery of the network, send the data received from their SNs to their parent CH (PCH) which is a higher level CH and located near the center of the network. We focus on the inter-cluster communication and investigate its transmission performance in this chapter.

For network characteristic, on the other hand, the WSNs indicate different characteristics from other wireless networks, such as cellular and wireless local area networks (WLANs). These characteristics include spatial (geographical) non-uniform traffic, where the traffic volume generating in a given area differs from that in other geographical areas. For example, for the event-driven WSNs, event generation might concentrate in a particular area, and such event generation leads to spatial non-uniform traffic. Under this traffic condition, introducing cluster topology into the WSN, the traffic volume generated within a cluster is different between clusters. As a result, in the inter-cluster communication where some CCHs transmit their data to the same PCH with a shared communication channel, the difference in the transmission performance, such as packet dropping probability and transmission delay, might arise among CCHs with different cluster traffic. For several applications including environmental monitoring, it is undesirable to have non-uniformity in quality of data collected from clusters (or regions), such as the difference in accuracy and instantaneity. Hence, WSNs need to mitigate such non-uniformity in data quality between clusters by suppressing the different transmission performance between CCHs with different cluster traffic.

For this issue, a priority channel access is one of promising solutions which can suppress the different transmission performance between CCHs. As an example of the priority channel access schemes, WLAN systems adopt the MAC scheme specified in IEEE 802.11e [9] to provide quality of service (QoS) support [10]. In this scheme, the priority control based on enhanced distributed channel access (EDCA) is performed to offer required QoS to multi-medium services, such as speech, video streaming, and so on. The EDCA is an extended form of distributed coordination function (DCF) specified in IEEE 802.11, and achieves QoS provision by means of classification of transmitting information into several access categories (ACs). For the QoS provision in WSNs, the recent studies have investigated its application to WSNs in order to handle their multimedia traffic [11–13].

From above background, focusing on the inter-cluster communication in cluster-based WSNs employing IEEE 802.15.4 beacon enabled mode under spatial non-uniform traffic, the objectives in this work are to (1) clarify non-uniformity in transmission performance between CCHs with different cluster traffic in a quantitative way, and then (2) provide mitigation scheme against this performance non-uniformity between CCHs in order to achieve better uniformity in data collected from the WSN under such traffic condition. To achieve latter objective, this chapter proposes a traffic adaptive channel access scheme in which each CCH autonomously controls channel access priority based on its current cluster traffic. The proposed scheme achieves traffic adaptive priority access by adjusting a control parameter, backoff exponent *BE*, for backoff operation in slotted carrier sense multiple access/collision avoidance (CSMA/CA), specified in IEEE 802.15.4 MAC. The performance for the proposed scheme is evaluated through computer simulation and its effectiveness is demonstrated.

This chapter is organized as follows. Section 2 briefly describes previous work related to this chapter. In Sects. 3 and 4, the system model under our consideration and the problem to be solved in this chapter are discussed, respectively. Section 5 proposes an autonomous traffic adaptive channel access scheme to mitigate non-uniformity in transmission performance between CCHs. In Sect. 6, the simulation condition used in our evaluation is described, and then, Sect. 7 shows various simulation results and demonstrates the effectiveness of the proposed scheme. Finally Sect. 8 concludes the chapter.

2 Related Work

Shared communication channel access in cluster-based WSNs is focused on in this chapter and the objective is to provide priority channel access scheme for shared channels according to current traffic load in each cluster. The typical work related to shared channel access in WSNs and priority channel access in wireless networks are as follows.

2.1 IEEE 802.15.4 MAC

IEEE 802.15.4 [5] specifies physical (PHY) and MAC protocols for low-rate wireless personal area networks (LR-WPANs) and is often employed to lower layer protocol in WSNs, such as ZigBee [14, 15], due to its lower energy consumption. The beacon enabled mode specified by IEEE 802.15.4 MAC provides power saving operation based on duty cycle mechanism by using superframe structure. The superframe is divided into active and inactive periods, and its active period is also divided into two periods: contention access period (CAP) and contention free

period (CFP). This chapter focuses on shared channel access with slotted CSMA/CA in the CAP, and dedicated channel access in the CFP is out of scope.

The slotted CSMA/CA channel access normally adopts backoff operation to prevent signal collisions on shared communication channel. Before transmitting data, each sender randomly selects access delay interval from a backoff window (BW) defined by a range of [0, 2^{BE}-1]. The backoff exponent *BE* is initially set to $BE_{\min}$ and is increased up to $BE_{\max}$ when clear channel assessment (CCA) detects busy channel after a timeout of selected access delay interval. The transmitting data is discarded after the number of the backoffs exceeds a predefined value ('*macMaxCSMABackoffs*' in IEEE 802.15.4).

Equal transmission opportunity is generally given to all the nodes willing to transmit their data in the slotted CSMA/CA access with normal backoff operation. This is because the above control parameters such as $BE_{\min}$, $BE_{\max}$, and *macMaxCSMABackoffs* commonly take the same values for all nodes. However, this parameter setting and thus equal transmission opportunity for all nodes, is undesirable to the cluster based WSNs with spatial non-uniform traffic.

2.2 IEEE 802.11e EDCA

IEEE 802.11e EDCA [9] is a typical well-known priority access scheme for shared communication channels in WLANs, and can offer QoS provision to multi-medium communication services in WLANs by utilizing backoff operation in CSMA/CA mechanism.

The EDCA defines multiple access categories (ACs) depending on required QoSs, such as transmission delay and so on. Transmission data is categorized into one of these ACs based on its required QoS and is stored separately in the transmission queue corresponding to each AC. The EDCA selects the transmission data from one of the AC queues based on their priority order and then transmit wireless frame containing selected data.

To offer priority channel access depending on the required QoS, the control parameters, arbitration inter-frame space (AIFS) and contention window (CW) are set to an adequate value for each AC according to its priority order. Specifically, the AIFS and CW take smaller values for the AC with higher priority, and larger ones for lower priority AC. Thus, the EDCA provides priority operation by adjusting access delay interval before data transmission, and enables the QoS provision required by each communication service.

3 System Model

Let us consider a cluster-based WSN with one PCH and N_{cch} CCHs subordinating some SNs, as illustrated in Fig. 1. All nodes in the WSN operate with duty cycle mechanism in accordance with IEEE 802.15.4 beacon enabled mode, and the different time period in the IEEE 802.15.4 superframe is assigned as an active period for intra-cluster communication to different cluster in order to avoid interference between any intra-cluster communications. The active period for inter-cluster communication is also assigned different time period from those for any intra-cluster communications, as shown in Fig. 2. Therefore, this active period

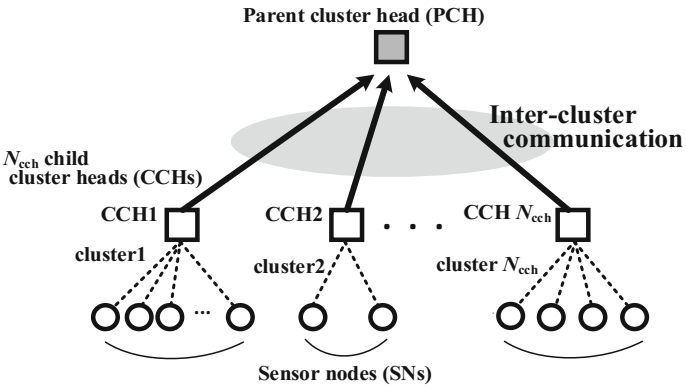

Fig. 1 Topology model

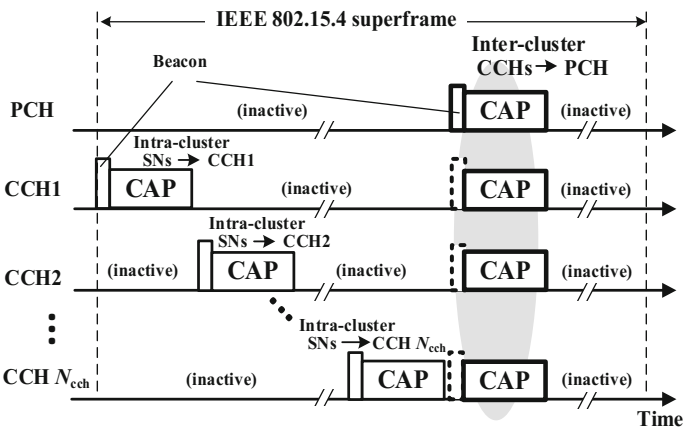

Fig. 2 Frame structure model

assignment causes no interference between inter-cluster and any intra-cluster communications.

Every CCH receives data from its SNs during the CAP in its active period assigned to intra-cluster communication, and then transmits the data to its PCH during the CAP in the active period assigned to inter-cluster communication. Hence, the CAP for the inter-cluster communication can be considered as a shared communication channel, where N_{cch} CCHs compete to transmit their data. IEEE 802.15.4 beacon enabled mode employs the slotted CSMA/CA with backoff operation as a channel access scheme for the shared communication channel. In this channel access, every CCH normally employs the same parameter setting for its control parameters as others.

Considering spatial non-uniform traffic conditions, each cluster has different traffic load from others, for example having different number of subordinate SNs as illustrated in Fig. 1.

4 Motivation

Normal slotted CSMA/CA fundamentally provides fair channel access among CCHs regardless of their traffic load. This characteristic results from control parameter settings common to all CCHs for the backoff operation, such as BE_{min}, BE_{max}, and *macMaxCSMABackoffs*. This common setting is preferable for the channel access where the CCHs having the same traffic load compete with each other for the shared channel.

Under the spatial non-uniform traffic condition, however, common parameter setting causes negative effect to the system performance, that is non-uniform transmission performance between CCHs with different traffic, because each CCH has different traffic load. For example, frequent buffer overflow occurs at high traffic CCHs due to insufficient transmission opportunity for their traffic load. This leads to high packet dropping probability and long transmission delay. In contrast, low traffic ones can obtain too much opportunity for their traffic, and therefore, enjoy quite low packet dropping probability and also short delay.

This performance difference might cause non-uniform quality in the data collected at a sink node (center node). The non-uniform quality in collected data might bring negative impact on application services offered by the sink node utilizing the collected data. Hence, each CCH should retain uniform transmission performance to provide higher quality application services. Then priority channel access scheme should be required for the inter-cluster communication involving the CCHs with various traffic loads, such as under spatial non-uniform traffic conditions.

5 Autonomous Traffic Adaptive Backoff Control Scheme

This section proposes a countermeasure technique to the above-mentioned problem appearing on the inter-cluster communication in cluster-based WSNs with spatial non-uniform traffic. The proposed scheme aims to supress the performance non-uniformity among CCHs with various traffic loads on the inter-cluster communication.

5.1 Requirements for Proposed Mechanism

Contemplating the causes raising the above problem, the proposed scheme requires two basic functions: traffic adaptive channel access control and autonomous distributed control.

For the traffic adaptive channel access, the CCHs with high/low traffic should operate with high/low priority for shared channel access to supress the performance difference between CCHs with different traffic. In addition, this priority control should be achieved by using autonomous distributed control mechanism since WSNs should avoid additional control signal exchange due to their limited network resources, such as communication capacity, computational and battery power.

5.2 Pruority Channel Access Based on Cluster Traffic Status

In the traditional priority access mechanism in WLAN systems, IEEE 802.11e, each mobile terminal (MT) decides the channel access priority by selecting the size of AIFS and CW in backoff operation for CSMA/CA channel access, as mentioned before in Sect. 2.2. IEEE 802.15.4 MAC employs the same kind of backoff operation as IEEE 802.11 WLAN systems, and the BW for IEEE 802.15.4 MAC corresponds to the CW for IEEE 802.11e. The size of both BW and CW is given by the same control parameter of backoff exponent *BE*. Therefore, the proposed scheme also controls the access priority by adjusting the *BE*.

The proposed scheme sets different access priority to the CCHs according to the traffic conditions in their clusters. The priority control can be achieved by setting different value to this *BE* at each CCH with different traffic load. Figure 3 illustrates a conceptual diagram of the proposed autonomous traffic adaptive backoff control scheme.

In the proposed priority control, as a basic framework, the high traffic loaded CCHs obtain high priority state, being able to get more transmission opportunity, by setting a smaller value to their *BE*. The smaller *BE* brings a shorter waiting interval before channel accesses, leading to high priority in the shared channel access. The low traffic loaded CCHs, on the other hand, take a larger value to their

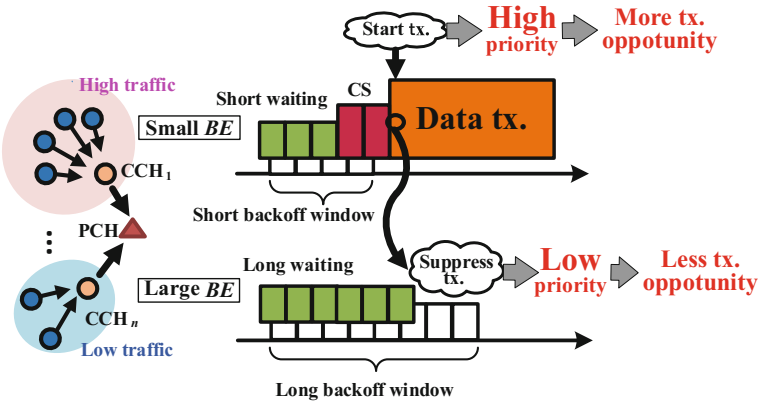

Fig. 3 Priority control based on backoff operation

BE in order to increase the BW size and this parameter setting forces them to wait for a larger interval, leading to low priority state, being hard to get more transmission opportunity. From these *BE* setting, the CCHs with higher traffic can obtain more transmission opportunity than the CCHs with lower traffic, as illustrated in Fig. 3. As a result, each CCH can transmit the data received from its SNs in proportion to its own traffic load, and then, WSNs can suppress the non-uniform transmission performance between CCHs, resulting in system performance improvement.

IEEE 802.15.4 MAC defines two control parameters for the *BE*; $BE_{\min}$ and $BE_{\max}$. The $BE_{\min}$ adjustment could impact the access priority at the earlier stage of backoff operation. $BE_{\max}$ adjustment, however, cannot influence at the earlier stage, do only at the final stage. Therefore, in this work, we employ the $BE_{\min}$ to control the priority levels for CCHs.

5.3 *Traffic Status Estimation*

To achieve the above-mentioned priority access, each CCH needs to know its current traffic status relative to other CCHs competing the same CAP. Therefore, as an indicator of the relative traffic status, the proposed scheme introduces the length $L_{\text{queue}}^{\text{CAPend}}$ (packets) of transmission queue at the end point of the CAP assigned to the communication from the CCHs to their PCH.

At the end point of a given CAP, the data stored in the transmission queue shows the data which the CCH cannot complete to transmit during that CAP. Monitoring the amount of the non-completed data allows each CCH to recognize its transmission status, good or poor status, reflecting the competition for the CAP with

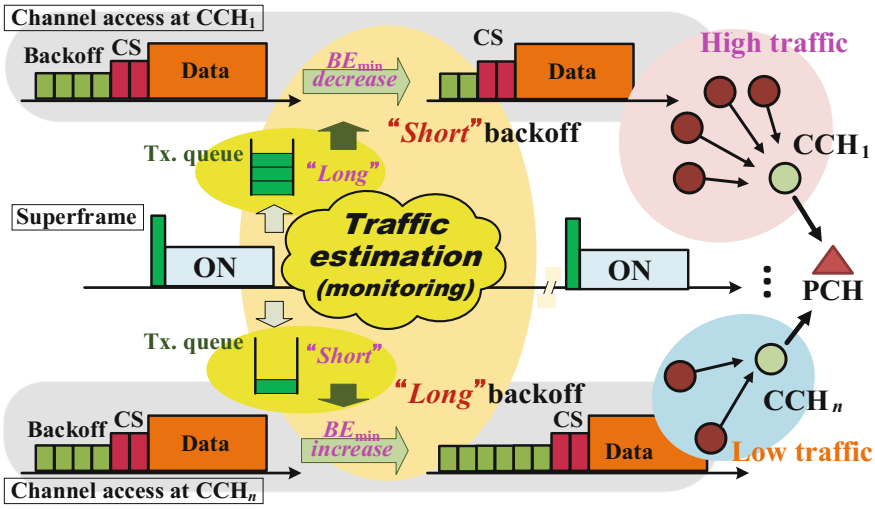

Fig. 4 Backoff exponent *BE* adjustment based on traffic status estimation

other CCHs. Hence, each CCH can estimate its traffic status relative to other CCHs by observing the transmission queue length $L_{\text{queue}}^{\text{endCAP}}$.

Figure 4 partly illustrates an example for the proposed traffic status estimation, where the CCH_1 (upper one) with many SNs detects a long $L_{\text{queue}}^{\text{CAPend}}$ at the end of the current CAP. Then, the CCH_1 can estimate its traffic status at high traffic condition, where it obtain insufficient transmission opportunity compared with its current load. Conversely, the CCH_n (lower one) with a small number of SNs has a short $L_{\text{queue}}^{\text{CAPend}}$ which shows it can get sufficient transmission opportunity during that CAP. Therefore the CCH_n can cognize that it is in low traffic status. From these considerations, the transmission queue length $L_{\text{queue}}^{\text{CAPend}}$ at the end of the CAP is useful for estimating traffic status relatively to other CCHs.

5.4 Control Procedure

In the proposed scheme, the backoff exponent BE_{min} is adjusted by a following procedure, as illustrated in Fig. 4.

In every superframe, the CCHs observe the transmission queue length $L_{\text{queue}}^{\text{CAPend}}$ at the end of the CAP used for data transmission to their PCH, and then estimate their traffic status based on the observed $L_{\text{queue}}^{\text{CAPend}}$. After the traffic estimation, they adjusts their BE_{min} value which will be applied in the next superframe (CAP).

As criteria for traffic status estimation, the proposed scheme introduces a pre-defined constant threshold TH_{queue} for evaluating the observed $L_{\text{queue}}^{\text{CAPend}}$. The CCHs

estimate high traffic status relative to others when detecting the observed $L_{\text{queue}}^{\text{CAPend}}$ is greater than the threshold TH_{queue}. In contrast, they estimate their low traffic status after detecting N_{up} consecutive $L_{\text{queue}}^{\text{CAPend}} \leq TH_{\text{queue}}$.

For the specific procedure for controlling the BE_{min}, the CCHs under the high traffic status decrease the value of BE_{min} by a decrement step ΔBE_{down} in order to increase their access priority, whereas CCHs with the low traffic status increase the BE_{min} by an increment step ΔBE_{up} to lower their access priority. These adjustment steps ΔBE_{down} and ΔBE_{up} are predefined and constant control parameters. The detailed controlling procedure for the BE_{min} and its adjustment range is given by:

$$BE_{\text{min}}^{\text{after}} = \begin{cases} BE_{\text{min}}^{\text{before}} + \Delta BE_{\text{down}} & ; L_{\text{queue}}^{\text{CAPend}} > TH_{\text{queue}} \\ BE_{\text{min}}^{\text{before}} + \Delta BE_{\text{up}} & ; L_{\text{queue}}^{\text{CAPend}} \leq TH_{\text{queue}} \text{ in consecutive } N_{\text{up}} \\ BE_{\text{min}}^{\text{before}} & ; \text{ otherwise,} \end{cases} \quad (1)$$
$$\text{subject to } BE_{\text{min}}^{\text{lower}} \leq BE_{\text{min}} \leq BE_{\text{min}}^{\text{upperr}},$$

where $BE_{\text{min}}^{\text{lower}}$ and $BE_{\text{min}}^{\text{upper}}$ are a minimum and maximum value for BE_{min}. The optimal settings for N_{up}, ΔBE_{down} and ΔBE_{up} will be discussed in Sect. 7.2.

6 Performance Evaluations

The performance for the proposed autonomous traffic adaptive backoff control is evaluated through computer simulation with following assumptions. The statistics are collected from the inter-cluster communication involving one PCH and its N_{cch} subordinate CCHs, as illustrated in Fig. 1.

6.1 Wireless Channel Model

The radio channels are assumed to be ideal without any consideration of propagation loss, shadowing and fading fluctuation in this evaluation. Packet transmission error occurs only due to packet collision caused from simultaneous transmission from multiple CCHs. The CCA at each CCH is perfect without impact of hidden terminal problem.

6.2 Traffic Model

The packets are continuously generated at each CCH following Poisson distribution with an average cluster traffic load of G_x (packets/L_{pkt}), which corresponds to

cluster traffic load. The L_{pkt} is a packet length and is same for all generated packets. After the packet generation, the packet is stored in transmission buffer with a length of L_{buffer} (packets) at each CCH. The packet is discarded due to buffer overflow when the buffer is full. At the buffer overflow the oldest packet is discarded.

Three different cluster traffic loads, G_x (x = 'low', 'mid', or 'high') are defined to simulate spatial non-uniform traffic condition. N_{cch} CCHs are equally separated into three CCH groups, and each CCH group has one of G_x without duplication each other. Defining the ratio ($R_{\mathrm{low}} : R_{\mathrm{mid}} : R_{\mathrm{high}}$) for traffic loads (low : mid : high), the traffic load G_{x} for the cluster in group x is given by using average network traffic load G (packets/L_{pkt}):

$$G_x = \frac{R_x}{\sum_{x=\mathrm{low,\,mid,\,high}} R_x} \cdot G/N_{\mathrm{CCH}} \tag{2}$$

For transmission failure, the packets are retransmitted following IEEE 802.15.4 MAC specification.

6.3 Evaluation Metric

We evaluate the packet dropping probability P_{drop} and transmission delay D_{tx} as transmission performance, where P_{drop} and D_{tx} are given by a ratio of the number of dropping packets due to transmission failure or buffer overflow at CCHs to that of generated packets, and a time duration elapsed from packet generation at CCHs to successful reception at the PCH, respectively. We also evaluate standard deviations (SDs) σ_{drop} and σ_{delay} for the packet dropping probability P_{drop}s and the transmission delay D_{tx}s observed at all the CCHs as an indicator showing uniformity in the transmission performance among CCHs with different cluster traffic.

In the performance evaluation, we compare the above each performance for the proposed scheme with that for the system employing fixed BE_{min} setting of 5, which is called 'standard system' in this evaluation.

7 Evaluation Results

Using the parameter settings listed in Table 1, we evaluated the system performance for the proposed scheme, comparing with the standard system. Note that MAC parameter settings except shown in Table 1 employ their default values specified in the IEEE standard.

Table 1 Simulation Parameter Settings

	Symbol	Value	
Transmission rate	R_{rate}	250	(kbps)
aUnitBackoffPeriod	UBP	0.32	(ms)
Duration of *aUnitBackoffPeriod*	T_{UBP}	48	(UBPs)
Beacon order	*BO*	8	
Superframe order	*SO*	3	
Beacon interval	*BI*	12288	(UBPs)
CAP length	L_{CAP}	384	(UBPs)
Beacon frame length	L_{bcon}	5	(UBPs)
Data packet length	L_{pkt}	8	(UBPs)
ACK frame length	L_{ack}	2	(UBPs)
macMaxCSMABackoffs		5	
Initial *BE*	BE_{min}, BE_{max}	5, 8	
Range of BE_{min}	$BE_{\text{min}}^{\text{lower}}$, $BE_{\text{min}}^{\text{upperr}}$	2, 5	
Threshold for BE_{min} adjustment	TH_{queue}	0	
Tx. buffer length	L_{buffer}	10	(packets)

7.1 *Non-uniform Performance Between CCHs with Different Traffic Loads*

This section clarifies the non-uniformity in transmission performance between CCHs with different cluster traffic loads for inter-cluster communication under non-uniform traffic condition with the number of CCHs $N_{\text{cch}} = 6$ (thus, every CCH group has 2 CCHs) and the traffic ratio of $(R_{\text{low}} : R_{\text{mid}} : R_{\text{high}}) = (1.0 : 1.5 : 2.0)$.

Figure 5 shows the packet dropping probability P_{drop} for each CCH group with low, middle, or high cluster traffic load. Each CCH group shows quite different P_{drop} performance in the network traffic G of over around 0.01, and the P_{drop} for high traffic CCHs clearly degrades compared with that for lower traffic ones. This result clarifies that the transmission performance has clear non-uniformity between CCHs with different traffic loads for such spatial non-uniform traffic. Hence, this non-uniformity caused from different cluster traffic should be mitigated even under spatial non-uniform traffic condition in order to improve overall system performance.

7.2 *Optimal Parameter Settings for* $\mathbf{N}_{up}$, $\Delta\mathbf{BE}_{up}$, *and* $\Delta\mathbf{BE}_{down}$

Before evaluating the performance of the proposed scheme by comparing with the standard system, optimal parameter settings for N_{up}, ΔBE_{up}, and ΔBE_{down} should be obtained to achieve better system performance for the proposed scheme.

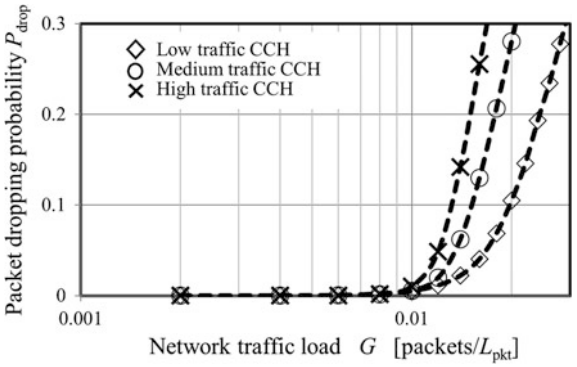

Fig. 5 Performance non-uniformity between CCHs with different cluster traffic loads

Therefore, their optimal values are derived through computer simulation. Here, we employ, as an evaluation metric, an average packet dropping probability $P_{\text{drop}}^{\text{ave}}$ over all CCHs in the network traffic region of $0.002 \leq G \leq 0.03$, and its standard deviation $\sigma_{\text{drop}}^{\text{ave}}$ for N_{cch} CCHs.

Firstly we determine an optimum value for the number of detection times N_{up} required for estimating low traffic status. Figure 6 shows the $P_{\text{drop}}^{\text{ave}}$ and $\sigma_{\text{drop}}^{\text{ave}}$ performances for various N_{up} under the same conditions as Fig. 5. The packet dropping probability $P_{\text{drop}}^{\text{ave}}$ in Fig. 6 is slightly better for smaller N_{up}. However, the standard deviation $\sigma_{\text{drop}}^{\text{ave}}$ degrades at Nup of 1 and is better for $N_{\text{up}} \geq 2$. In addition it is almost the same for $N_{\text{up}} \geq 2$, and thus, N_{up} of 2 is concluded to be optimum value from these observations.

Next, Fig. 7 shows the $P_{\text{drop}}^{\text{ave}}$ and $\sigma_{\text{drop}}^{\text{ave}}$ performances for varying the increment step ΔBE_{up}, to discuss its optimal value. The $\sigma_{\text{drop}}^{\text{ave}}$ performance degrades with increasing ΔBE_{up}, while the $P_{\text{drop}}^{\text{ave}}$ is almost equal for all ΔBE_{up}s. Therefore, these results show the ΔBE_{up} should be set to 1 as its optimum value.

Then, for optimization of the decrement step ΔBE_{down}, Fig. 8 shows the $P_{\text{drop}}^{\text{ave}}$ and $\sigma_{\text{drop}}^{\text{ave}}$ performances for various ΔBE_{down} setting. Roughly speaking, both the $P_{\text{drop}}^{\text{ave}}$ and $\sigma_{\text{drop}}^{\text{ave}}$ indicate almost the same performance regardless of ΔBE_{down} value,

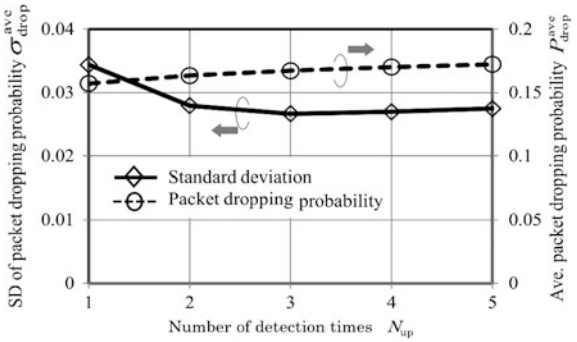

Fig. 6 Packet dropping probability for varying N_{up}

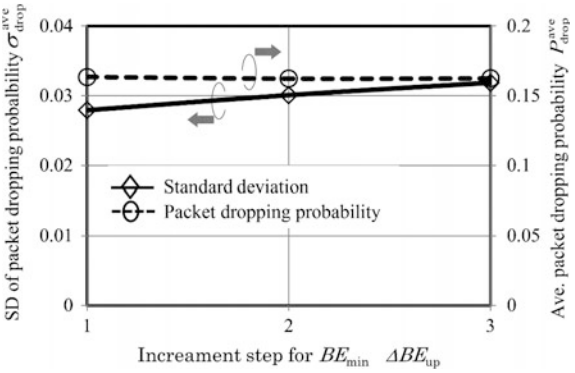

Fig. 7 Packet dropping probability for varying ΔBE_{up}

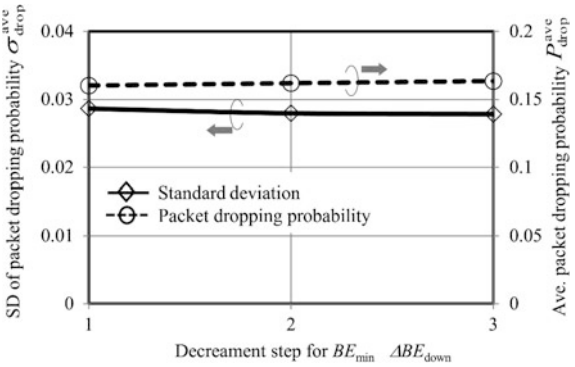

Fig. 8 Packet dropping probability for varying ΔBE_{down}

however, the larger ΔBE_{down} gives slight better σ_{drop}^{ave} performances. From these results, therefore, we conclude ΔBE_{down} of 3 as its optimal setting.

Setting the optimum values derived above to N_{up}, ΔBE_{up}, and ΔBE_{down}, Fig. 9 shows the BE_{min} behaviour for varying network traffic load G, under the same conditions as Fig. 5. From Fig. 9, each CCH can adjust the BE_{min} to a smaller value with higher traffic load and a larger value with lower traffic load in middle and high network traffic load regions. This BE_{min} behaviour proves the proposed scheme works well according to the traffic load estimated at each cluster.

7.3 Transmission Performance Comparison

The transmission performances P_{drop} and D_{tx} are shown in Figs. 10 and 11 for the proposed scheme (referred as 'Traffic adaptive BE' in Figs.) and the standard system under the same conditions as Fig. 5. The performance for each traffic group,

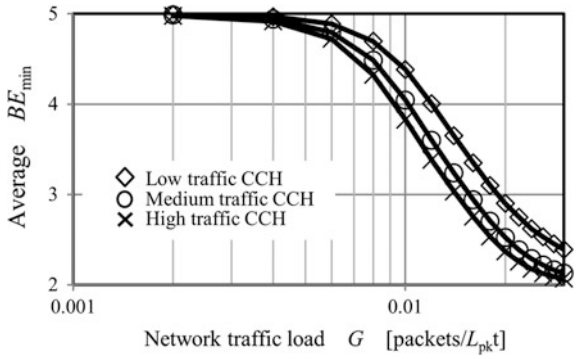

Fig. 9 BE_{min} behaviour for each CCH group (low, mid, and high)

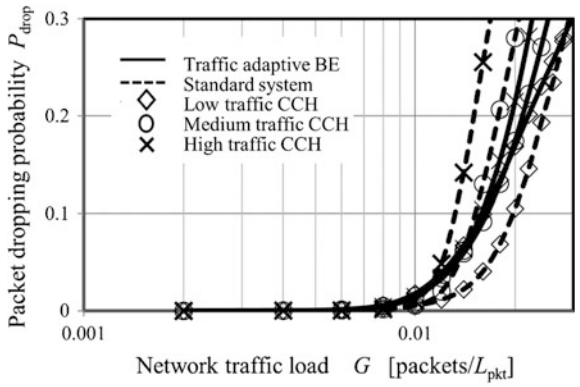

Fig. 10 Packet dropping probability P_{drop} performance

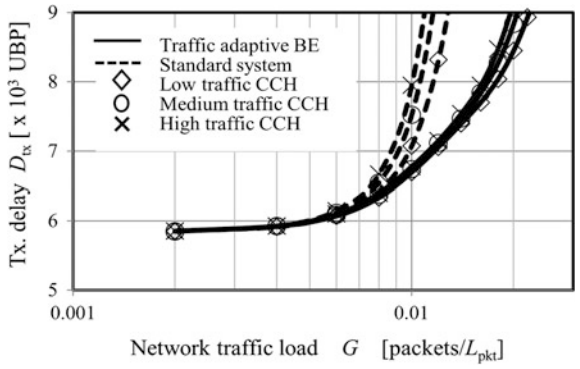

Fig. 11 Transmission delay D_{tx} performance

low, middle or high traffic, is separately shown when varying the network traffic load G in these figures.

In Fig. 10, the packet dropping probability P_{drop} is nearly equal between different traffic groups of CCHs for the proposed scheme, despite the standard system with different P_{drop} performance, and thus, the proposed scheme can suppress

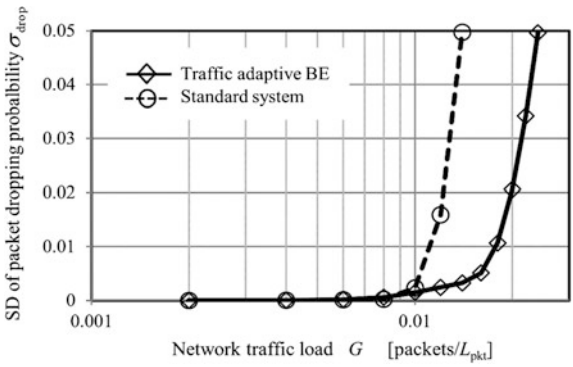

Fig. 12 Standard deviation of packet dropping probability P_{drop}

non-uniformity in P_{drop} across CH groups with different cluster traffic. For the transmission delay D_{tx}, almost the same behaviour can be found in Fig. 11 as the P_{drop}. Hence, the non-uniformity in the transmission performances can be reduced for all network traffic load regions, applying the proposed scheme.

To provides quantitative analysis of the uniformity in transmission performance between CCH groups with different cluster traffic, Figs. 12 and 13 show the standard deviations σ_{drop} and σ_{delay} of P_{drop}s and D_{tx}s observed at all the N_{cch} CCHs. In Comparison with the standard system, both the standard deviations σ_{drop} and σ_{delay} are largely reduced for high network traffic load regions by applying the proposedscheme, and we can find in Figs. 12 and 13 significant reduction against the transmission performance non-uniformity, provided by the proposed scheme. This performance improvement is given by proper BE_{min} control based on current cluster traffic offered to each CCH, which is a new mechanism provided by the proposed scheme and is a main contribution of this work.

From the above results and their considerations, applying the proposed scheme can provide quite effective mitigation against the non-uniformity in the transmission performance between different traffic loaded CCHs on the inter-cluster communication in cluster-based WSNs under spatial non-uniform traffic.

7.4 Performance for Various Network Conditions

In the previous section the effectiveness of the proposed scheme is basically presented for the typical network condition. Since the network has various operating condition, this section examines the performance for the proposed scheme under for various network operating conditions.

First, we examine the performance under various spatial non-uniform traffic conditions, and then the packet dropping probability P_{drop} is evaluated for the conditions with spatial non-uniform traffic of (R_{low} : R_{mid} : R_{high}) = (1.0: 1.0: 1.0), (1.0: 1.25: 1.5), (1.0: 1.5: 2.0), (1.0: 2.0: 3.0), (1.0: 2.5: 4.0), and (1.0: 3.0: 4.0). The

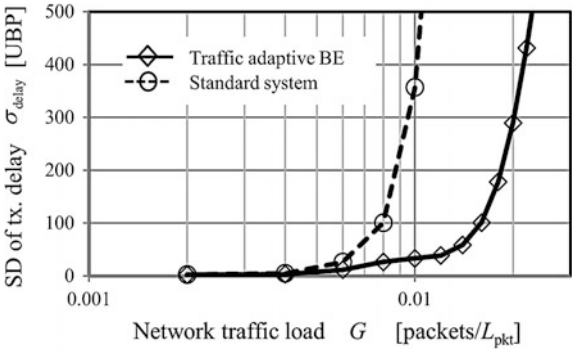

Fig. 13 Standard deviation of transmission delay D_{tx}

standard deviation $\sigma_{traffic}$ in offered cluster traffic loads under these traffic conditions is 0.0, 0.2, 0.41, 0.82, 1.2, and 1.6, respectively, which indicates degree in non-uniformity of the offered cluster traffic. Figure 14 shows the standard deviation σ_{drop}^{ave} of the P_{drop}^{ave}s at the CCHs, which is the same evaluation metric as shown in Fig. 6, for varying the standard deviation $\sigma_{traffic}$ of offered traffic. We can see from Fig. 14 that the proposed scheme provides superior σ_{drop}^{ave} performance to the standard system for any $\sigma_{traffic}$ (spatial non-uniform traffic conditions). Moreover, the performance improvement obtained by the proposed scheme increases with the $\sigma_{traffic}$. This result concludes that the proposed scheme can provide the effectiveness under various spatial non-uniform traffic conditions, and the effectiveness gets larger for the larger spatial non-uniform traffic conditions.

Next, we examine the transmission performance for various network scale, which includes the number of CCHs N_{cch} competing the CAP in the inter-cluster communication. The proposed scheme adjusts the BE_{min} according to the traffic load offered to each CCH, and higher traffic CCHs tend to use smaller BE_{min} to achieve higher priority in the channel access. However, the smaller BE_{min} likely increases the possibility of channel access collision between competing CCHs, and thus, the impact of smaller BE_{min} setting to the performance should be clarified for

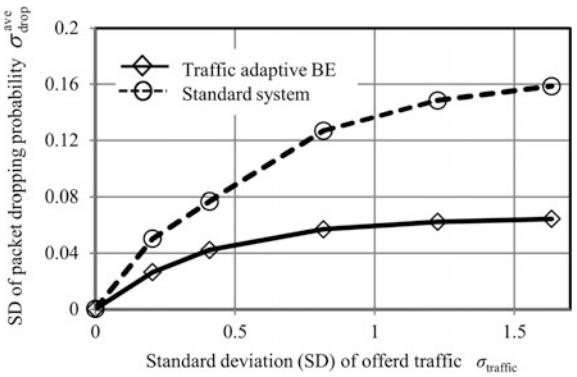

Fig. 14 Packet dropping probability for various spatial non-uniform traffic conditions

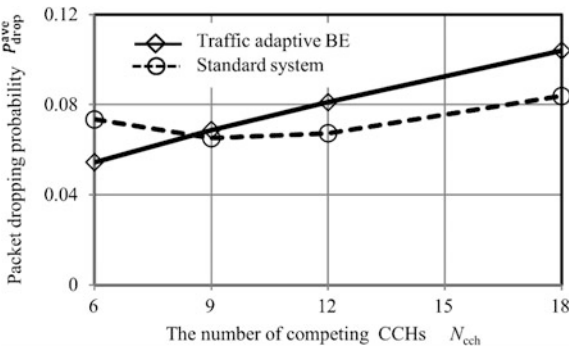

Fig. 15 Standard deviation of packet dropping probability for varying the number of competing CCHs

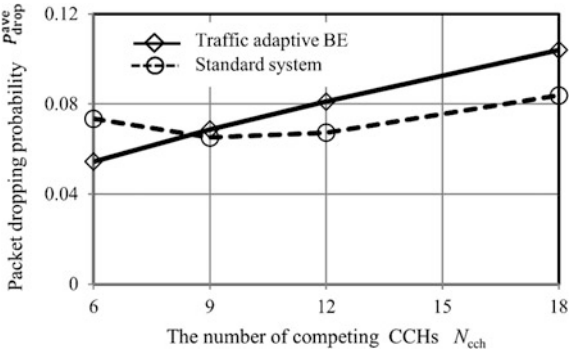

Fig. 16 Packet dropping probability performance for varying the number of competing CCHs

the proposed scheme. Figures 15 and 16 show the packet dropping probability performance for various number of competing CCHs. From the standard deviation σ^{ave}_{drop} shown in Fig. 15, the proposed scheme show better performance and can achieve a reduction in the performance non-uniformity compared with the standard system for any values of the N_{cch}. Therefore, an effectiveness of reducing the performance non-uniformity can be obtained even under the conditions with larger N_{cch}. However, the improvement is getting smaller with increasing N_{cch}, and thus, the effectiveness gradually disappears with increasing N_{cch}. Additionally, the packet dropping probability P^{ave}_{drop} for the proposed scheme is slightly getting worse with increasing N_{cch}, compared with the standard system, and therefore, the network scale, such as the N_{cch}, gives no small impact to the transmission performance for the proposed scheme. Hence, the proposed scheme has to pay some cost to achieve uniformity in the transmission performance and requires countermeasure against this drawback, which is left as our future work.

8 Conclusion

This chapter has discussed non-uniformity in transmission performance between CCHs with various cluster traffic loads on inter-cluster communication in cluster-based WSNs employing IEEE 802.15.4 MAC. This chapter has firstly quantitatively-clarified appearance of the performance non-uniformity among different traffic loaded CCHs under spatial non-uniform traffic condition, and then has proposed the countermeasure technique, the autonomous traffic adaptive channel access, which controls the backoff exponent $BE_{\min}$ in backoff operation based on the current traffic status estimated at each CCH, in order to mitigate such performance non-uniformity.

The transmission performances, packet dropping probability, transmission delay and their standard deviations as an indicator showing performance uniformity, have been evaluated for the proposed scheme through computer simulation under various network conditions. These simulation results prove that the proposed scheme can significantly reduce the performance non-uniformity between different traffic CCHs, and thus, can achieve fairer transmission performance under spatial non-uniform traffic conditions.

Consequently, the proposed autonomous traffic adaptive channel access scheme is quite effective for cluster-based WSNs under spatial non-uniform traffic conditions.

Acknowledgments This work is partly supported by Japan Society for the Promotion of Science (JSPS), Grant-in-Aid for Scientific Research (c) 25420366, 2013–2015.

References

1. I.F. Akyildiz, W. Su, Y. Sankarasubramaniam, E. Cayirci, Wireless sensor network: a survey. Comput. Netw. **38**(4), 393–422 (2002). doi:10.1016/S1389-1286(01)00302-4
2. R. Verdone, D. Dardari, G. Mazzini, A. Conti, Wireless sensor and actuator networks: technologies analysis and design. Academic Press (2008)
3. M. Arzamendia, K. Mori, K. Naito, H. Kobayashi, Traffic adaptive MAC mechanism for IEEE802.15.4 cluster based wireless sensor networks with various traffic non-uniformities. IEICE Trans. Commun. **E93-B**(11), 3035–3047 (2010). doi:10.1587/transcom.E93.B.3035
4. K. Kubo, K. Mori, K. Naito, H. Kobayashi, Enhanced 2-level traffic adaptive active period control for IEEE802.15.4 cluster-based wireless sensor networks. IEICE Trans. Commun. **E94-B**(9), 2521–2531 (2011). doi:10.1587/transcom.E94.B.2521
5. IEEE 802.15.4, Part 15.4: Low-Rate Wireless Personal Area Networks (LR-WPANs) (2011)
6. W.R. Heinzelman, A. Chandrakasan, H. Balakrishnan, Energy-efficient communication protocol for wireless microsensor networks. Proc. HICSS (2000). doi:10.1109/HICSS.2000.926982
7. O. Younis, S. Fahmy, Distributed clustering in ad-hoc sensor networks: a hybrid energy-efficient approach. Proc. IEEE INFOCOM **2004**, 629–640 (2004). doi:10.1109/INFCOM.2004.1354534

8. R. Mizutani, K. Mori, K. Naito, H. Kobayashi, Traffic-distributed clustering scheme for cluster-based WSNs with various non-uniform traffic fluctuations. Int. J. Commun. Netw. Syst. Sci. **6**(2), 109–118 (2013). doi:10.4236/ijcns.2013.62013
9. IEEE 802.11e-2005—Part 11: Wireless LAN Medium Access Control (MAC) and Physical Layer (PHY) Specifications—Amendment 8: Medium Access Control (MAC) Quality of Service Enhancements (2005)
10. S. Mangold, C. Sunghyun, G.R. Hiertz, O. Klein, B. Walke, Analysis of IEEE 802.11e for QoS support in wireless LANs. IEEE Wirel. Commun. **10**(5), 40–50 (2003). doi:10.1109/MWC.2003.1265851
11. H. Touil, Y. Fakhri, M. Benattou, MAC queue size and energy-efficient of IEEE 802.11e EDCA in wireless multimedia sensor networks, in *Proceedings of International Conference on Innovative Computing Technology (INTECH)* 2012, pp. 97–101 (2012). doi:10.1109/INTECH.2012.6457758
12. J. Zhang, J. Zhang, Y. Tan, A hybrid-measure IEEE 802.11e backoff scheme in wireless mesh sensor networks, in *Proceedings of International Conference on Multimedia Information Networking and Security (MINES) 2011*, pp. 150–154 (2011). doi:10.1109/MINES.2011.100
13. H. Touil, Y. Fakhri, M. Benattou, Contention window MAC parameters tyning for wireless multimedia sensor networks, in *Proceedings of ACS International Conference on Computer Systems and Applications (AICCSA)* 2013, May 2013. doi:10.1109/AICCSA.2013.6616509
14. ZigBee Standards Organization, ZIGBEE SPECIFICATION ZigBee Document 053474r17 (2008)
15. G. Ding, Z. Sahinoglu, P. Orlik, J. Zhang, B. Bhargava, Tree-based data broadcast in IEEE 802.15.4 and ZigBee networks. IEEE Trans. Mobile Comput. **5**, 1561–1574 (2006). doi:10.1109/TMC.2006.172

Author Index

S. Mukhopadhyay et al. (eds.), *Sensors for Everyday Life*, Smart Sensors, Measurement and Instrumentation 23, DOI 10.1007/978-3-319-47322-2